A STUDY OF OPEN-CELL NICKEL-CHROME METALLIC FOAM FOR AN ABRADABLE COMPRESSOR SEALING

Martyn Lindop, MEng

Thesis submitted to the University of Nottingham

for the degree of Master of Philosophy

2015

ABSTRACT

This thesis documents the investigation of open-cell Ni-Cr metallic foams, analysing the mechanical properties of the material as well as the properties of brazed samples. Also investigated was the effectiveness of an ultrasound non-destructive evaluation technique used to analyse braze quality.

The anisotropic structure of the foam sheets resulted in anisotropic properties, with a 'dark band' that was found to run through the longitudinal length of the material acting as the initial deformation site. Higher compressive strength samples corresponded with higher density areas, but strength is higher for relatively thinner strut samples where Cr has been able to fully diffuse, whereas tensile strength was found to be more dependent upon the defects within the struts of the foam. The shear failure of the foam was characterised by the collapse and subsequent densification of the cells at the point closest to the shear incursion face.

Investigation of the machinability of the foams confirmed that fast tool speed, at low depth of cuts produced the best results.

Areas of some brazed samples had poor, even no, braze material coverage due to the wicking of the braze material by the struts. B, present in the braze layer, had diffused out forming Cr-B phases in the struts and the plate, as well as Ni-B phase within the braze. This left voids that weakened the braze bond, and the areas of Cr-B

phase within the struts were found to be the most susceptible to corrosion

The largest areas of good bond, determined by the ultrasound method, corresponded with higher strength samples. However the performance of the braze layer bond had less to do with the amount of braze, and more to do with the quality of the bond, with the quality increased with the right amount of wicking to bond the strut, but not too much that would cause the area bonded to the Ni plate to diminish.

ACKNOWLEDGEMENTS

I would first like to thank my supervisor Dr Andrew Kennedy, for his invaluable support, advice and patience throughout this research, and without whom this thesis would not have been possible. Thanks also to the staff in the Wolfson building; Keith Dinsdale and Tom Buss for their help during testing, Rory Screaton and Graham Malkinson for their help with sectioning the material, and Julie Thornhill for her help with the SEM and microCT work.

This project was sponsored by Rolls Royce, and I wish to thank John Gent and Glen Pattinson for their assistance, as well as Ian Collison for his help with regards to the NDE work.

I wish to express my deepest gratitude to my parents Peter and Elizabeth Lindop, for their loving support and encouragement, not only during the course of my research, but throughout my academic studies. A big thank you also too my brother Tim and sister-in-law Eleanor, as well as all of my family and friends. Your support meant a lot to me.

Dedicated to the memory of Emma Lindop

TABLE OF CONTENTS

1 INTRODUCTION 1

2 LITERATURE REVIEW 6

2.1 Abradable Seals 6

2.2 New Seal Design 10

2.3 Metal Foam Overview 11

2.4 Rolls Royce Abradability Trials 17

2.5 Nickel-Chrome Open-Cell Foam Manufacture 22

2.5.1 Ni-Cr Material Properties 22

2.5.2 Methods Of Production For Open-Cell Ni-Cr Foam 27

2.5.3 Electro-Deposition Method of Production 30

2.6 Mechanical Properties of Open-cell Foams 42

2.6.1 Compressive Properties 42

2.6.2 Tensile Properties 46

2.6.3 Shear Properties 50

2.6.4 Machinability 51

2.7 Joining Metallic Foam 53

2.7.1 Brazing Nickel-Chrome Material 54

2.7.2 Brazing Open-Cell Nickel-Chrome Foam 55

3 EXPERIMENTAL PROCEDURES 59

3.1 Sample Material 59

3.1.1 As Supplied Non-Brazed Foam 59
3.1.2 Brazed Foam 61
3.2 Microscopy 65
3.2.1 Optical Microscopy 65
3.2.2 Scanning Electron Microscopy (SEM) 66
3.2.3 X-Ray Micro-Tomography (µCT) 67
3.2.4 Ultrasonic Inspection Of Braze 68
3.3 Density 69
3.3.1 Bulk Density 69
3.3.2 Pycnometry 70
3.4 Mechanical Testing 71
3.4.1 Compression Testing 72
3.4.2 Tensile Testing 75
3.4.3 Shear Testing 78
3.4.4 Machinability Testing 81
3.5 Chemical Analysis 82
3.5.1 Energy Dispersive X-Ray Spectroscopy (EDX) Analysis 82
3.5.2 Spark Atomic Emission Spectroscopy (AES) 83
3.6 Corrosion Analysis 84
4 ANALYSIS OF AS SUPPLIED NON-BRAZED FOAM 85
4.1 *S*heet Properties and Macrostructure Analysis Of As Supplied Foam 85

4.1.1 Optical and Scanning Electron Microscopy (SEM) Analysis 85
4.1.2 X-Ray Micro-Tomography (μCT) Analysis 92
4.1.3 Density 99
4.1.4 Atomic Emission Spectroscopy (AES) Chemical Analysis 102
4.2 Microstructure Analysis Of As Supplied Foam 104
4.2.1 Optical and Scanning Electron Microscopy (SEM) of the Microstructure 104
4.2.2 EDX Chemical Analysis Of Supplied Foam Microstructure 106
4.3 Mechanical Testing of The As-Supplied Foams 111
4.3.1 Compression Testing 111
4.3.2 Tensile Testing 128
4.3.3 Comparison of Compression and Tensile Strengths ...141
4.3.4 Machinability 143
4.4 Conclusions 146
5 ANALYSIS OF BRAZED FOAM MATERIAL.....150
5.1 Optical and Scanning Electron Microscopy of Brazed Foam 150
5.2 EDX Chemical Analysis of Brazed Foam 162
5.3 Braze NDE Analysis 165
5.4 X-Ray Micro-Tomography (μCT) Analysis of Braze Foam..169

5.5 Mechanical Testing of Brazed Foam 171
5.5.1 Compression Testing of Brazed Foam 171
5.5.2 Tensile Testing of Brazed Foam 172
5.5.3 Shear Testing of Brazed Foam 187
5.6 NDE Braze Analysis 206
5.7 Conclusion 209
6 DIGITAL IMAGE CORRELATION 211
6.1 Initial Trials 211
6.2 Secondary Trials 212
6.2.1 Compression Testing 1723 Foam 212
6.2.2 Compression Testing 1116 Foam 214
6.2.3 Tensile Testing 1116 Foam 218
6.3 Conclusions 220
7 CORROSION 221
7.1 Non-Brazed Foam 221
7.2 Corrosion of the Brazed Foam 223
7.3 Conclusion 228
8 ANALYSIS OF FILLED FOAM MATERIAL 229
8.1 Modelling Filled Foam Mechanical Properties 230
8.2 Analysis of the Filled Foam 231
8.3 Mechanical Testing of the Filled Foam 234
8.4 Conclusions 237

9 FINAL CONCLUSIONS 240

10 FUTURE WORK.....242

11 REFERENCES 244

12 APPENDIX 253

12.1 APPENDIX 1 – Tensile Rig Drawings.....253

12.2 APPENDIX 2 – Density Sheet Layout 256

12.3 APPENDIX 3 – Pycnometry Results 258

12.4 APPENDIX 4 – EDX Ananlysis 259

12.4.1 Non-Brazed Foam Second Phase.....259

12.4.2 Braze Layer.....260

12.5 APPENDIX 5 – 1723 Compressive Stress Layout Plots 263

12.6 APPENDIX 6 – 1116 Compressive Stress Layout Plots 270

12.7 APPENDIX 7 – 1116 ST Compressive Stress-Strain 273

12.8 APPENDIX 8 - 1116 LL Compressive Stress-Strain 274

12.9 APPENDIX 9 – NDE Analysis.....275

12.9.1 Sample 1 275

12.9.2 Sample 2 277

12.9.3 Sample 3 279

12.9.4 Sample 4 280

12.9.5 Sample A 282

12.9.6 Sample B 284

12.10 APPENDIX 10 – Brazed Foam Stress-Strain Plot.....287

12.11 APPENDIX 11 - Brazed Foam Stress-Incursion Plot 289

12.12 APPENDIX 12 – Corrosion Analysis Images 291

12.13 APPENDIX 13 – Young's Modulus 294

12.13.1 Experimental Procedure 294

12.13.2 Results 295

12.14 Appendix 14 – Material Supply Issues 299

LIST OF TABLES

Table 2-1. Summary of results from the investigation into compressive yield of Ni-Cr foam by Choe, *et al.*[4]..... 45

Table 4-1 Table showing estimated average pore sizes for 1723 and 1116 foam samples, along with the variance percentages..... 95

Table 4-2. Calculated average densities (g/cm3), for 1116 and 1723 samples as well as for a localised area of 1723 samples. 99

Table 4-3. Average volume and density for 1116 and 1723 samples 101

Table 4-4. Average volume of samples taken from columns in the 1723 material 101

Table 4-5. Chemical composition estimation derived from AES results. 102

Table 4-6. 1723 top surface strut EDX chemical analysis. 108

Table 4-7. 1116 top surface strut EDX chemical analysis. 108

Table 4-8. 1116 below surface strut EDX chemical analysis.....108

Table 4-9. 1116 mid-section strut EDX chemical analysis. 108

Table 4-10. Average compressive stresses (MPa), over the entire sheet area, for the three strains. 112

Table 4-11. Average compressive stresses (MPa) for the three strain areas. All samples are from a localised area.....112

Table 4-12. Compression stresses (MPa) for 1116 samples in the ST axis. 114

Table 4-13. Compression stresses (MPa) for 1116 samples in the longitudinal axis 114

Table 4-14. Tensile test results for 1723 samples. 128

Table 4-15. Tensile test results for 1723 samples, with the removal of AC3 data. 128
Table 4-16. Tensile test results for 1116 samples in the ST axis. .131
Table 4-17. Tensile test results for 1116 samples in the LL axis...131
Table 5-1. Estimated areas of "good" braze quality for the tensile test samples. 168
Table 5-2 Estimated areas of "good" braze quality for shear test samples. 168
Table 5-3. Tensile results for brazed foam samples, with the proof stress and UTS calculated using both the foam sample cross-sectional area and the NDE derived area. 174
Table 5-4. Shear test results for the brazed foam samples.....188
Table 12-1. Complete results of the density and volumes determined by the Pycnometer. 258
Table 12-2. Average Young's Modulus derived from compressive cyclic loading. 297
Table 12-3. Average Young's Modulus derived from tensile cyclic loading.....297
Table 12-4. Average Young's Modulus derived from the combined compressive and tensile cyclic loading data. 297

LIST OF FIGURES

Figure 2-1. Schematic of an abradable seal [8]. 7

Figure 2-2. Microstructure of abradable coating (Metco 320)[9]. 7

Figure 2-3. Illustration of a side view of a blade passing over the abradable surface and its effects on the particles [8] 8

Figure 2-4. Illustration of the new abradable seal design[9]. 10

Figure 2-5. Images of foam material; (a) is an open cell Ni foam, (b) is a closed cell aluminium foam and (c) is a hollow sphere foam[10]. 11

Figure 2-6 Taxonomy of cellular metal manufacturing processes [10] 12

Figure 2-7. Relative density vs. cell size for various manufacturing processes[10]. 15

Figure 2-8. Young's Modulus vs. density for various commercial foams [10] 16

Figure 2-9. Compressive strength vs. density for various commercial foams[10] 16

Figure 2-10. Illustration and photograph of the Sulzer Innotec abradability test rig [9]..... 17

Figure 2-11. Abradability results from a low incursion rate [9] 20

Figure 2-12. Abradability results from a high incursion rate [9]..... 20

Figure 2-13. Abradability results for various disc velocities and incursion [9]. 21

Figure 2-14. Image of the effect of intergranular corrosion on a Ni-Cr sample[18]. 24
Figure 2-15. Plot of Cr content against average pore diameter for Recemat foams[24]. 26
Figure 2-16. Cr-Ni phase diagram[25]. 26
Figure 2-17. Image of Ni based foam produced by templated transient liquid phase bonding, showing where some pores are filled (a). Image (b) shows the course ligaments, with image (c) a magnified image of one of them[28]. 29
Figure 2-18. Electro-deposition method for manufacture of metal foams[13]. 30
Figure 2-19. Illustration of the pentagonal dodecahedron shaped cell in its open and closed form [14]. 31
Figure 2-20. Continuous foam slab stock production method [31]... 32
Figure 2-21. Illustration of the rotary peeling technique and cell orientation[32]. 33
Figure 2-22. Foam loop slitting machine[32]. 33
Figure 2-23. Longitudinal density profile comparison between a loop slit foam and a horizontally peeled bun (HPB) foam [32]. 33
Figure 2-24. Illustration of a thermal reticulation vessel [31]. 35
Figure 2-25. Caustic bath used for chemical (quenching) reticulation [31]. 35
Figure 2-26. Illustration showing the variation in coating thickness, from a strut at the top surface to one in the mid-section. 38
Figure 2-27. Schematic representation of Ni-Cr diffusion, during homogenisation heat treatment[2]. 39

Figure 2-28. Polyurethane eruption during the burn out process[26]. 40
Figure 2-29. SEM images of etched strut cross sections showing grains (a), and imperfectly formed walls (b)[3]..... 41
Figure 2-30. Image showing grains with uniform composition on the strut wall [2]. 41
Figure 2-31. Theoretical stress-strain curve for cellular materials[14]. 43
Figure 2-32. Illustration of a cubic model for an open-cell foam (a), showing elastic buckling in the struts (b), and the formation of plastic hinges (c)[14]. 43
Figure 2-33. Relative yield strength against relative density[4]. 46
Figure 2-34. Alignment of struts during tensile loading[14]. 47
Figure 2-35. Propagation of a crack through an open-cell foam [14]. 48
Figure 2-36. Tensile stress-strain curves for several Alulight open-cell foams in both the ST and LL directions[14]. 48
Figure 2-37. Necking failure in a Ni-Cr open-cell strut wall[3]. 49
Figure 2-38. Unzipping failure in a Ni-Cr open-cell strut wall[3]. 50
Figure 2-39. Images of tantalum based open-cell foams. Image (a) is of the foam prior to machining. Image (b) is an of the foam following machining, showing signs of smearing[44]. 52
Figure 2-40. SEM image of a Ni brazed bond microstructure, with the borides diffused out of the Isothermal Solidified Zone (ISZ) [52]. 55

Figure 2-41. Experimental set-up of the Ultrasound NDE equipment [56]. 57
Figure 2-42. The amplitude vs. time plot for averaged sample results is shown in image (a). The plots following Fourier transformation which can be used assess the quality of the braze is shown in image (b) [56]. 57
Figure 2-43. Signal intensity map of brazed foam[57]. 58
Figure 3-1. Grid layouts for the 1723 (left) and 1116 (right) supplied material. The red highlights the area of samples used for localised testing. 60
Figure 3-2. Illustration indicating the notation used for the orientation of the foam samples. 61
Figure 3-3. Images of the brazing method. The foam, with a ground face, is placed on the braze tape upon the grit blasted surface of the plate (a). The material is the placed in a furnace basket, between two ceramic tiles (b-c). Weights are placed on top of the ceramic tiles (d). 62
Figure 3-4. Illustration of how the braze material fills the troughs created by the polishing and grit blasting of the Ni-Cr foam and the Ni plate. 63
Figure 3-5. Illustration of location diagrams used for images of samples. The black square indicates the plane of the image. Arrows indicate whether image is from: (i) near the surface, (ii) below the surface, or (iii) the mid-section. 65
Figure 3-6. Illustration of how the sample size was determined for compression testing[64]. 73

Figure 3-7. Illustration of the method for determining the zero deformation point[64]. 74
Figure 3-8. Illustration of the samples used for compression testing of the brazed foam. 75
Figure 3-9. Image showing a sample prepared for tensile testing. 76
Figure 3-10. Illustration of the brazed material cross-sectional geometry, for tensile testing. 77
Figure 3-11. Image of a brazed tensile sample clamped to the tensile testing rig. The rig is designed with adjustable clamps to help with imperfectly manufactured samples. 78
Figure 3-12. Shear testing sample dimensions. 79
Figure 3-13. Image of the shear testing rig showing the direction of force, and the point of shear. 79
Figure 3-14. Illustrates how the shear rig works and the terminology used (a), and sample lengths used to calculate the reducing area (b). 80
Figure 3-15. Illustration of the channel cuts milled for machinability analysis..... 81
Figure 4-1. Images of 1116 sample (a) and 1723 sample (b) showing difference in pore size. 85
Figure 4-2. Images of 1116 sample (a) and 1723 sample (b) showing the 'dark band' deformed region. 86
Figure 4-3. SEM images of the deformed region in a 1116 foam sample, showing bent struts in images (a-b) and unzipping in (c-d) 88

Figure 4-4. SEM images of pores above (a) and below (b) the deformed region 89
Figure 4-5. SEM images showing variation between thicknesses of strut walls near the surface (a) and at the mid-section (b). 90
Figure 4-6. SEM images of illustrating the larger strut sizes of 1116 samples (a) compared to 1723 (b) 90
Figure 4-7. SEM image of 'exhaust' hole on a strut wall in a 1723 sample. 91
Figure 4-8. SEM image of debris impact on a 1723 sample strut causing peeling. 91
Figure 4-9. SEM images showing the microstructure of the Ni-Cr struts. (a) shows the predominantly fine-grained microstructure. (b) shows a large grain. 92
Figure 4-10. 3D rendered model of a 1116 sample using X-Ray Micro-Tomography 93
Figure 4-11. Slice made through the cross-section of the rendered 3D model, with the new face coloured red, and highlighting the deformed area. 93
Figure 4-12. Plot of the relative area against depth of a 1723 foam sample. 96
Figure 4-13. Plot of relative area against depth of a 1116 foam sample. 97
Figure 4-14. Line and circular methods for determining pore size. 98
Figure 4-15. Density layout plot for (a) the 1723 samples showing higher density towards the edge of the sample, and (b) the localised area. (Edited version of full plot seen in Appendix 2) 100

Figure 4-16. Chemical composition layout plot as measured by AES. 104
Figure 4-17. Etched samples of 1723 material, showing a strut from the top of the sample with grains (a), and from the middle section showing 2-phases (b). 105
Figure 4-18. Etched images from an 1116 sample. Image (a) shows a strut from the top, with Cr along the edges. Image (b) is from a strut in the middle of the sample, showing the second phase present, as well as a wall defect. 105
Figure 4-19. 1116 top surface strut EDX line scan with Cr and Ni profiles.....109
Figure 4-20. 1723 top surface strut EDX line scan with Cr and Ni profiles.....109
Figure 4-21. 1116 Mid-section strut EDX line scan with Cr and Ni profiles.....110
Figure 4-22. 1723 mid-section strut EDX line scan with Cr and Ni profiles.....110
Figure 4-23. SEM image of the secondary phase present in the strut walls. Showing the location and results of an EDX analysis (a Pt coating had been applied). 111
Figure 4-24. Compressive stress-strain plots for 1723 samples, showing variation between samples across the whole sheet area.113
Figure 4-25. Compressive stress-strain plots comparing the short-traverse and longitudinal-length axis for the 1116 foam samples.115

Figure 4-26. Images taken of a 1116 sample during compression testing in the ST axis, showing the deformation occurring initially in the 'dark-band' region.....116
Figure 4-27. Images taken of a 1116 sample during compression testing in the longitudinal axis, showing the deformation occurring more uniformly throughout.....116
Figure 4-28. Average compressive stress-strain plots comparing the 1723 and 1116 samples, showing their maximum and minimum values.....117
Figure 4-29 Average proof stress and compressive stress at 25% and 60% strain (in the ST orientation), plotted against the average pore size of the samples.....119
Figure 4-30 Compressive stress plotted against the chromium content for the 1723 foam.....120
Figure 4-31 Plots of the compressive stresses against density for the 1723 foam samples.....121
Figure 4-32 Plot of the relative yield strength against relative density for the 1116 and 1723 foam samples, with the theoretical model line plotted as well.....125
Figure 4-33 Plot of the relative yield strength against relative density for the 1116 and 1723 foam samples, as well as the plots of the Choe, *et al*. samples.....127
Figure 4-34. Tensile stress-strain plots for 1723 foam samples. ..129
Figure 4-35. Tensile stress-strain plot comparing the ST and LL orientations for 1116 foam samples.....132

Figure 4-36. Images taken of 1116 sample during tensile testing in the ST axis, showing the deformation occuring initially in the 'dark band' region. 133
Figure 4-37. Images taken of a 1116 sample during tensile testing in the LL axis, showing the deformation occuring more uniformly throughout. 133
Figure 4-38. Images of the failed tensile test 1116 LL axis foam samples, (a) 1F, (b) 4F and (c) 7F, showing the path of fracture failure. 133
Figure 4-39. SEM images of failure sites formed during tensile testing. Images (a-b) show areas where bent struts have torn apart. Images (c-d) show struts where necking has occurred. 134
Figure 4-40. Etched images of struts from samples that have undergone tensile testing. Image (a) show the cross-section of necked strut with a second phase present. Image (b) shows a strut through which a crack has past. 135
Figure 4-41 Average proof stress and UTS, plotted against the average pore size of the 1723 and 1116 samples 136
Figure 4-42 Tensile stress plotted against the chromium content for the 1723 foam 137
Figure 4-43 Plots of the tensile stresses against density for the 1723 foam samples 138
Figure 4-44. Tensile stress-strain plot comparing the 1723 and 1116 foam samples in the ST axis. 140

Figure 4-45. Average stress-strain plots for the 1723 ans 1116 foam samples, from both compressive and tensile loading, and in both the ST and LL orientations. 142
Figure 4-46. Images of the resulting finishes from cuts made at, low tool speed high cut depth (LSHD), high tool speed low cut depth (HSLD), high tool speed high cut depth (HSHD) and low tool speed low cut depth (LSLD). The flash produced by the cuts are also highlighted. 143
Figure 4-47. Cross-section images taken of the cut faces of the channel walls, machined at high speed. Images (a-b) are cut struts from the side walls of the material cut at low depth, and high depth, respectively. Image (c) is a cut strut from the base of the base of the high depth cut. Image (d) shows cut and deformed struts from a high depth. 144
Figure 4-48. Cross section images of the channel after machining at low speed, at both high and low depths. Images (a-b) show struts from the side walls of the channel at low depth and high depth, respectively. Image (c) is an image from the base of the channel, with the cut plane highlighted. Image (d) is an image from the side wall at high depth showing misalignment. 146
Figure 5-1. Ni plate with braze layer showing several large indentations in the braze layer. 150
Figure 5-2. Images of samples manufactured for shear testing. Image (a) shows the overlap of the braze layer. Image (b) shows the gap in the bond between the foam and Ni plate. 151

Figure 5-3. Images of foam and plate section region of no bond in Figure 5-2. Showing the braze on the struts (a), and the predominantly "dull" area seen, along with a small strip of "shiny" along the edge of the Ni plate (b). 152
Figure 5-4. Image foam and Ni plate from sample with a poor bond. It has a "dull" and a "shiny area" on the plate ~ 50/50 split. 152
Figure 5-5. Etched images of the braze layer on the Ni plate with a fine grain structure (a). A secondary phase is seen within the braze layer as well as a needle-like phase below the braze (b).....153
Figure 5-6. SEM image of the indentation edge, with larger grains visible on the upper most surface. 154
Figure 5-7. Image the etched braze layer close to the edge of the indentation area, showing the secondary phase crowding the braze layer. 154
Figure 5-8. Etched image of the centre of the indentation. There is no braze and unlike the braze layer either side there is no needle-like phase either.....155
Figure 5-9. SEM images of the indentation area. (a) shows the area of no braze which shows no secondary phase. (b) shows the area of braze just before the no braze area with several phases visible. ..155
Figure 5-10. Image of an etched Ni plate from a brazed foam sample, showing a large grain structure. 156
Figure 5-11. Image of a strut that has bonded well to the Ni plate with the braze. Several phases are visible but no needle-like phase below the braze layer.....157

Figure 5-12. Images of two struts from roughly 2mm away from the foam surface; (a) is from a sample not brazed and (b) is from a sample that is, and contains material within its void. 157
Figure 5-13. Surface of a brazed foam sample that has been sectioned, showing braze concentrated around a strut along with a "dull" area of no braze close by. 158
Figure 5-14. An image of a brazed foam sample showing a void within the braze layer. 158
Figure 5-15. Image of a brazed foam strut, which has a void within the braze layer next to the strut. 159
Figure 5-16. Illustrations of the wicking behaviour of the braze material (a-b), and the various bonds created such as; no wicking (c), a little wicking (d), a large amount of wicking (e), and wicking depleting material from other struts (f). 160
Figure 5-17. Image of a brazed layer from a brazed foam sample that had not bonded well. The needle-like phase is present below the braze layer as well as a darkening of the contrast in the immediate grain boundary vicinity. 161
Figure 5-18. Image of an etched strut in the middle of a brazed foam sample. 162
Figure 5-19. SEM image of the phases present in and around the braze layer, showing the locations and results of two of the EDX analyses. 163
Figure 5-20 An EDX line scan with Cr and Ni profiles of a brazed foam sample. The line intersects through the strut, braze layer and Ni plate. 164

Figure 5-21. An EDX line scan with Cr, Ni and Si profiles of a brazed foam sample with a wicked braze centre. 165
Figure 5-22. Process for quantifying the good braze area. (a) is the NDE C-scan image along with the percentage intensity threshold. (b) is the "green" colour split of the image. (c) is the binary image created from the "green" image. 167
Figure 5-23. MicroCT image slice through the 3D rendered model of the sample in (b). Areas of poor bond are visible at the edges of the sample. 169
Figure 5-24. Relatively large area of no braze bond found in the NDE C-scan image. 170
Figure 5-25. MicroCT 3D rendered image of the area of no bonding seen in Figure 5-24 (a). Images (b)-(d) are slices taken through the image increasingly further back from the front face, and show the area of no bonding from within the sample. 170
Figure 5-26. Image of a brazed foam sample undergoing compression testing, with the collapse in the deformed mid-section visible. 171
Figure 5-27 Plot of the compressive stress against compressive strain for the average brazed and un-brazed 1116 ST foam sample 171
Figure 5-28. SEM image of the braze bond layer of a foam strut after compression testing, showing no signs of damage to the braze layer 172

Figure 5-29. Image of a tensile test sample clamped to the rig, with the foam sample aligned as best possible. Showing bending of the plate during testing. 173
Figure 5-30. Images of the tensile failures for brazed samples AA2 (a), BA7 (b), BA4 (c) and the front and rear of AA1 (d).....176
Figure 5-31. Average tensile stress-strain plot for the brazed foam samples, showing the variance between the maximum and minimum sample plots. 177
Figure 5-32. Tensile stress-strain plots for samples AA2, BA4 and BA7. 178
Figure 5-33 Plot of the maximum load against the NDE derived area for the brazed tensile samples 179
Figure 5-34 Plots of the UTS against NDE derived area, with the UTS calculated using the foam cross-section and the NDE derived area 180
Figure 5-35. Images of two struts that have bonded well, showing no signs of damage to the braze bond layer after tensile testing..181
Figure 5-36. Image from the edge of a sample showing a strut above the braze layer. 181
Figure 5-37. SEM images from an area of good bonding in a tensile brazed foam sample. Image (a) shows struts coated in braze material. Image (b) shows the bottom of a strut with braze material at two different depths. Image (c) shows the fracture surface on the braze layer. Image (d) shows a strut with a braze layer that has fractured through the thickness.....182

Figure 5-38. SEM images from an area of poor bonding in a tensile brazed foam sample. Image (a) shows struts with little, and on some no, braze material. Image (b) shows the bottom of a strut with a small amount of braze on the tip, which has fractured. Image (c) shows the braze layer on the bottom of a strut which has fractured through its thickness. Image (d) shows a strut with no braze material, which has previously been ground flat during manufacture. 184
Figure 5-39. SEM images from a Ni plate pulled from a brazed foam sample during tensile testing showing; a well bonded strut (a-b); an area previous strut bond which has undergone fracture (c-d); areas of wicked braze which has not bonded well (d-e); areas of gaps in the braze layer (f). 186
Figure 5-40. Shear stress-incursion plots for the areas derived from the cross-section of the foam samples. 190
Figure 5-41. Shear stress-incursion plots for the areas derived from the NDE area%. 191
Figure 5-42. Sequence of images taken from the 4B1 sample shear test showing the deformation of the foam when there is a good bond. 192
Figure 5-43. Sequence of images taken from the C sample shear test showing the deformation of the foam when there is a medium quality bond. 192
Figure 5-44. Two images of the 4B2 sample taken during shear testing. Image (a) is from the begining of the test and (b) is from the point of failure. 193

Figure 5-45. Images of foam samples and there corresponding Ni plates, after shear testing. With the braze sides showing and the direction of shear upwards.....195
Figure 5-46. 2D slices of a 3D rendered microCT model of sample 4B1. Top slice (a) is at the top surface of the sample with each slice from deeper within until reaching close to bond area (d). 196
Figure 5-47. Shear stress-incursion plots for 4B1 sample, where the stress is calculated using the cross-section of the foam sample, and by an area reduced by the incursion amount.....198
Figure 5-48 Plots of the maximum shear stress against NDE derived area, where the shear stress is calculated using the foam cross-section, the NDE derived area, and the reducing area 199
Figure 5-49. Images of the Ni plates braze layer for samples 4A1 (a) and sample B (b).....200
Figure 5-50. SEM images the foam sample after shear testing. All images are from the previously bonded surface. Images (a-b) show the fracture struts, (c) shows a braze fractured surface, and (d) shows cracking in a strut wall. 201
Figure 5-51. Images of etched foam samples after undergoing shear tests. Images (a-b) show the compacting of the struts which were closest to the bond area. Images (c-d) show magnified images of the struts and the failed brazed layer.....203
Figure 5-52. SEM images of the Ni plate braze layer following shear testing, showing sites of struts that have remained bonded (a-e), sites where the strut/bond has failed (f-g).....205

Figure 5-53. Etched cross-section images of the Ni plate braze layer, of the 4B2 sample following shear testing. 206
Figure 5-54. Comparison of real and NDE scan images of the brazed plate for samples A (a) and B (b). 207
Figure 5-55. Comparison of microCT scans of non-brazed (a) and brazed (b) foam material, with the thickness of the struts in the brazed sample possibly due to wicking. 208
Figure 6-1 Images from the initial trials of the DIC method showing the small area that the system could recognise (a), and the incomprehensible reconstruction (b) 212
Figure 6-2 Images of the DIC analysis of the 1723 foam sample, ST orientation compression test, with displacement plots (mm) of the Y-axis (a) and X-axis (b). 214
Figure 6-3 Images of the DIC analysis of the 1116 foam sample, ST orientation compression test, with displacement plots (mm) of the Y-axis (a) and X-axis (b). 216
Figure 6-4 Images of the DIC analysis of the 1116 foam sample, LL orientation compression test, with displacement plots (mm) of the Y-axis (a) and X-axis (b). 217
Figure 6-5 Images of the DIC analysis of the 1116 foam sample, ST orientation compression test, with displacement plots (mm) of the Y-axis (a) and X-axis (b). 219
Figure 7-1. Images of an 1116 sample taken at labelled times, showing the location and progression of corrosion during salt spray testing. 222

Figure 7-2. Images of two samples which have undergone corrosion testing for 200 hours. Highlighted are the areas where corrosion is visible. 223
Figure 7-3. Images of brazed samples taken before and after 900 hours of salt spray testing. Samples were orientated with the Ni pates at the top and bottom (a), and with the plates at the sides (b). 225
Figure 7-4. Etched sample images after 900 hours of salt spray testing. Showing the corrosive effects on a strut within the bulk of a sample (a), the braze layer (b-d), the strut wall (e), and a strut that had not bonded to the Ni plate (f). 227
Figure 8-1 Illustration of the model used for determining the contribution to strength by the filler.....230
Figure 8-2 Stress-strain plot showing the five regions exhibited by the filled Al foam compared to the three of the unfilled. 231
Figure 8-3. SEM images of struts in a filled sample. 232
Figure 8-4. SEM image of a filled foam sample, showing a large void in the filler material. 232
Figure 8-5. Micro- CT 2D slices from CT analysis of a filled foam sample with a 4mm hole drilled through it. Image (a) is the original image, (b) is an image with colour and contrast manipulation 233
Figure 8-6. SEM images of the machined channels in a filled foam sample, showing crushed glass spheres in the corners (a), and crack at the edge of a strut (b).....234
Figure 8-7. Compressive stress-strain plots for filled foam samples. 236

Figure 8-8. Images taken during compression testing of the filled foam material, showing voids present in the material (a-b), as well as the filler material pushing out through the pores (c). 237
Figure 8-9. Image of a compressed filled sample showing tearing and push-out. 237
Figure 8-10. Cross-sectional images of a filled foam sample after compression testing, showing voids through the centre of the sample. 237
Figure 12-1. Drawings for the T-section for the tensile rig. 254
Figure 12-2. Drawing for the clamp of the tensile rig.....255
Figure 12-3. Density layout plot for the 1723 samples. 256
Figure 12-4. Key to the density layout plot. 257
Figure 12-5. EDX spot spectrum analysis of a 1116 sample. The image shows the site from where the spectrum was located, and the table shows the results. 259
Figure 12-6. EDX spot spectrum analysis of a 1116 sample. The image shows the site from where the spectrum was located, and the table shows the results. 260
Figure 12-7. EDX spot spectrum analysis of a 1116 sample. The image shows the site from where the spectrum was located, and the table shows the results. 260
Figure 12-8. EDX spot spectrum analysis of a brazed sample. The image shows the site from where the spectrum was located, and the table shows the results. 261

Figure 12-9. EDX spot spectrum analysis of a brazed sample. The image shows the site from where the spectrum was located, and the table shows the results. 261
Figure 12-10. EDX spot spectrum analysis of a brazed sample. The image shows the site from where the spectrum was located, and the table shows the results. 261
Figure 12-11. EDX spot spectrum analysis of a brazed sample. The image shows the site from where the spectrum was located, and the table shows the results. 262
Figure 12-12. EDX spot spectrum analysis of a brazed sample. The image shows the site from where the spectrum was located, and the table shows the results. 262
Figure 12-13. EDX spot spectrum analysis of a brazed sample. The image shows the site from where the spectrum was located, and the table shows the results. 262
Figure 12-14. Layout plot for the 1723 samples at 0.2% Proof Stress. 264
Figure 12-15. Key to the layout plot for the 1723 samples at 0.2% Proof Stress. 265
Figure 12-16. Layout plot for the 1723 samples at 25% strain. ...266
Figure 12-17. Key to the layout plot for the 1723 samples at 25% strain. 267
Figure 12-18. Layout plot for the 1723 samples at 60% strain. ...268
Figure 12-19. Key to the layout plot for the 1723 samples at 60% strain. 269

Figure 12-20. Layout plots for the 1116 foam samples in the ST axis, at the proof stress (a), at 25% strain (b) and at 60% strain (c).....271
Figure 12-21. Layout plots for the 1116 foam samples in the LL axis, at the proof stress (a), at 25% strain (b) and at 60% strain (c). .272
Figure 12-22. 1116 foam, ST compression stress-strain plot. 273
Figure 12-23. 1116 foam, LL compression stress-strain plot. 274
Figure 12-24. Sample 1 Side A ultrasound C-scan image (a), and binary image created using ImageJ to calculate the area% (b)....276
Figure 12-25. Sample 1 Side B ultrasound C-scan image (a), and binary image created using ImageJ to calculate the area% (b)....276
Figure 12-26. Image showing how the material was sectioned and the subsequent sample codes. 277
Figure 12-27. Sample 2 ultrasound C-scan image (a), and binary image created using ImageJ to calculate the area% (b). 278
Figure 12-28. Image showing how the material was sectioned and the subsequent sample codes. 278
Figure 12-29. Ultrasound C-scan images, and binary images (created using ImageJ to calculate the area%), for Samples A, B and C.....279
Figure 12-30. Sample 4 Side A ultrasound C-scan image (a), and binary image created using ImageJ to calculate the area% (b)....280
Figure 12-31. Sample 4 Side B ultrasound C-scan image (a), and binary image created using ImageJ to calculate the area% (b)....281
Figure 12-32. Image showing how the material was sectioned and the subsequent sample codes. 282

Figure 12-33. Sample A Side A ultrasound C-scan image (a), and binary image created using ImageJ to calculate the area% (b)....283
Figure 12-34. Sample A Side B ultrasound C-scan image (a), and binary image created using ImageJ to calculate the area% (b)....283
Figure 12-35. Image showing how the material was sectioned and the subsequent sample codes. 284
Figure 12-36. Sample B Side A ultrasound C-scan image (a), and binary image created using ImageJ to calculate the area% (b)....285
Figure 12-37. Sample B Side B ultrasound C-scan image (a), and binary image created using ImageJ to calculate the area% (b)....285
Figure 12-38. Image showing how the material was sectioned and the subsequent sample codes. 286
Figure 12-39. Tensile stress-strain plots for the brazed foam samples. 288
Figure 12-40. Shear stress-incursion plots for the brazed foam material, with the area calculated using the reducing area method. 290
Figure 12-41. Images of 1723 foam samples after 900 hours in the salt spray cabinet. 291
Figure 12-42. Images of 1116 foam samples after 900 hours in the salt spray cabinet. 293
Figure 12-43. Stress-strain plot of a sample undergoing compressive cyclical loading, showing good conformity after initial load.....296
Figure 12-44. The second-cycle compressive stress-strain plot for a sample, showing the equation of linear best fit and the correlation coefficient. 296

NOMENCULTURE

PPI = Pores per inch

1116 = Recemat material code for samples with 11-16 PPI

1723 = Recemat material code for samples with 17-23 PPI

X-1723 = Recemat material code for samples with 17-23 PPI, with a higher Cr content than the ordinary 1723.

FH = Material supplied by the Fraunhofer Institute

wt.% = Weight percent

MSRR9500/700 = Code for the braze tape with composition (wt.%): Ni(bal)-2.9B-4.5Si

MSRR7036 = Code for the Ni plate with composition (wt.%): Ni(bal)-20Cr-20Co-5.8Mo-2.1Ti-0.7(max)Fe-0.6(max)Al-0.6(max)Mn-0.4(max)Si-0.2(max)Cu-0.007(max)S-0.005(max)B-0.002(max)Pb-0.0005(max)Ag-0.0001(max)Bi

P500 = Grit size with an average diameter of 30.2 μm

P1200 = Grit size with an average diameter of 3 μm

ST = Short-Traverse

LL = Longitudinal Length

X-Sec = Cross-sectional area

TDR	=	Thickness deposition ratio
t_e	=	The thickness of the surface layer
t_l	=	The thickness of the mid-section layer
σ_*	=	Yield stress of the foam
E^*	=	Young's Modulus of the foam
E_s	=	Young's Modulus of the solid material
σ_s	=	Yield stress of the solid material
ρ_*	=	Density of the foam
ρ_s	=	Density of the solid material
F	=	Force/Load applied
G	=	Shear Modulus
σ_{ys}	=	Yield stress of the solid material
MP	=	mega pixel
d_{ave}	=	Average pore diameter
W	=	Width of the sample
H	=	Height of the sample
V	=	Test speed
UTS	=	Ultimate tensile stress
0.2% proof	=	Proof stress, defined at 0.2% strain.

Mean = Mean average

Standard Dev = Standard deviation

Variance = Coefficient of variance

R^2 = Correlation Coefficient

SCC = Stress Corrosion Cracking

HAZ = Heat affected zone

ISZ = Isothermal solidification zone

EDX = Energy dispersive X-ray spectroscopy

AES = Spark atomic emission spectroscopy

NDE = Non-destructive evaluation

DIC = Digital Image Correlation

SEM = Scanning electron microscopy

μCT = X-ray Micro-Tomography

2D = 2-Dimensional

3D = 3-Dimensional

EDM = Electrical discharge machining

PVD = Physical Vapour Deposition

CVD = Chemical vapour deposition

SFC = Specific fuel consumption

LSHD = Low tool speed, high depth of cut

LSLD = Low tool speed, low depth of cut

HSHD = High tool speed, high depth of cut

HSLD = High tool speed, low depth of cut

1 INTRODUCTION

This research project was undertaken (in collaboration with Rolls Royce) in order to evaluate the materials that are to be used as abradable seals in a newly designed compressor seal. The new seal design is part of an overall bigger project to design a new turbine engine, the F136, for the F35 Lightning II (a.k.a. the Joint Strike Fighter). The F136 project is a joint venture between General Electric and Rolls Royce (a venture called the Fighter Engine Team) and was, during this thesis project, going through system development and demonstration. Rolls Royce had produced a design that consisted of metal foam, machined with grooved channels, brazed to a Ni backing plate that would be secured into the casing of the engine.

Metal foams are a relatively new category of material in which pores are deliberately integrated into the structure of the metal. Metal foams have combinations of properties that cannot be obtained by other material forms, such as their strength, stiffness and energy absorption with respect to their weight, as well as their surface area to size ratio. Several foams were considered by Rolls Royce including both open-cell and closed-cell foams. Closed-cell foams have been mostly used in load bearing applications due to their good mechanical properties, whereas open-cell foams, having an open porosity and large surface area, have been used for applications such as heat exchangers, catalysts and electrodes [1].

Rolls Royce conducted some preliminary research, which included erosion and abradability of several foams to determine which foam material they would like to use. They decided upon using the open-cell Ni-Cr foam after initial trials, and the tiles manufactured for engine trials were made using 1116 (11-16 pores per inch (PPI)) material supplied by Recemat, as it was the only material available with a thickness that met the requirements of the design. Because of the porous nature of the foam, it was required to be sealed using a filler material. Whilst a filler material was investigated and ultimately used by Rolls Royce, a comprehensive understanding of the underlying foam properties was not known. Data on the mechanical properties of the foam being used, as well as the testing methods, was sparse, and was needed not only for future modelling purposes, but also to work as benchmark from which to assess future material considerations. Even less was known of the braze bond, and the effectiveness of the NDE methods used.

To date there has been little literature published on Ni-Cr foams. This can be attributed to the relatively short time that this class of material has been around for, the fact that only now are current applications presenting themselves for development (for example fuel cells), and due to the fact that they can be hard to manufacture. There have been even fewer reports and other literature published that are directly related to the material the author has researched, i.e. Ni-Cr foams of similar composition, pore size and foam thickness, as well as those made by a similar manufacturing route [2-4].

Although literature on metal foams has mentioned the anisotropic structure, little published work has related it to the mechanical properties. As multiple tiles were manufactured from a single foam sheet, and several sheets were needed to manufacture the required number of parts, there would inevitably be variations in properties, but to what extent was unknown.

The initial manufacturing of the tiles for engine trials also required the development of a non-destructive evaluation (NDE) technique to analyse the brazed bond. Initial work done by Rolls Royce allowed comparisons to be made between the manufactured tiles, but the relationship between the scans performed and the actual properties had not been fully researched. One issue that had arisen was that there were several areas within the tiles that appeared to have poor bond, or even no bond, and the reason for this was unclear.

Although there is literature available on the machinability of foams, much is dedicated to Al foams. The ability to machine the foams to high precision is important for the application. Any deformation of the foam, rather than cutting/removal of the material, will impact upon the sealing material when filled, affecting the geometry of the grooved channels and ultimately the performance.

Two foam material sheets were researched, both of which were manufactured by Recemat. As the 1116 sheets had been used to produce the tiles for the engine trials little was left for analysis, and so a 1723 sheet was used to analyse the variation in properties throughout a sheet. This also allowed for comparison between small

and large pores. Analysis of the brazed foam was performed on the 1116 material used in the engine trial.

The aims of the research undertaken for this thesis were therefore; to analyse the mechanical properties of the metallic foam and the relationship of these properties to the sheets anisotropic nature; to analyse the braze bond of the material (shear and tensile), and evaluate the effectiveness of the NDE process; to assess the corrosion resistance that the foam has (both brazed and non-brazed), and to determine whether any significant issues may arise in service; and finally to perform a preliminary assessment of the machinability of the metal foam, in order to assess whether problems might arise.

Reported in this thesis for the first time is data for the 1723 and 1116 foam produced by Recemat, including analysis; of a 'dark band' region previously un-reported in the literature; of variation in density and composition across the produced sheet; of the machinability; of the compressive properties with respect to the area from which the samples are sections from the sheet, and with respect to orientation; of the tensile properties in both the short-traverse and longitudinal-length, which requires developing a method to test samples without creating a 'dog-bone' test sample; of the machinability of the Ni-Cr foam material. New data was also produced to allow for comparison of the relative yield against relative density.

Further to the new data for the Recemat foam, this thesis is also reports for the first time on the analysis of brazed Ni-Cr foam, including; the use of ultrasonic C-scan NDE analysis, to analyse braze quality; the testing of brazed foam material under tensile and shear loads, which required the designing of new testing rigs and testing procedures.

New data was also reported by this thesis which complements the existing data on corrosion of Ni-Cr foams, and reported for the first time is corrosion analysis of brazed Ni-Cr foams.

2 LITERATURE REVIEW

2.1 ABRADABLE SEALS

In order to increase the efficiency of gas turbine engines, there is a need to reduce the clearance between the blade tip and the casing shroud, and thus reduce the air leakage over the blade tips. Improvements in reducing the seal leakage throughout the engine by 4% can improve the Specific Fuel Consumption (SFC) by 2%, which can create huge savings on fuel costs. [5-6]. Rolls Royce has therefore decided that no future military fans will run without tip treatment [7].

Reducing the blade-casing clearance can result in blades rubbing against the shroud. If an abradable coating is used, then the rubbing between blade and casing can be tolerated. Figure 2-1 shows a schematic of an abradable seal. As the blade passes over the surface of the abradable, the tip makes contact with any material protruding from the abradable coating. The force of the impact pushes protruding particles into the coating, after which they rebound and de-bond through the built-up elastic energy. The energy is derived from the blade tip. If there is a stronger particle bond, then more energy is required from the blade tip. Therefore by reducing the energy for detachment, abrasion will be easier. Current abradables, such as the one in Figure 2-2 made by Metco, are a composite of a metal matrix material, a polymer to generate porosity (it is burnt out), as well as lowering coating stresses during thermal spraying, and solid lubricants or release agents to act as

dislocators within the coating [8]. Figure 2-3 shows the process of particle detachment.

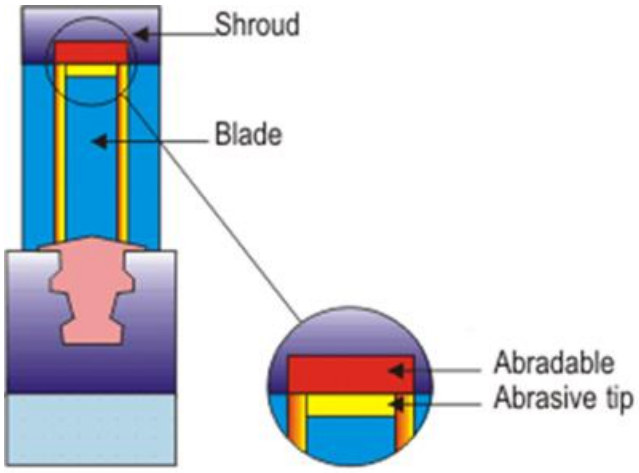


Figure 2-1. Schematic of an abradable seal [8].

`

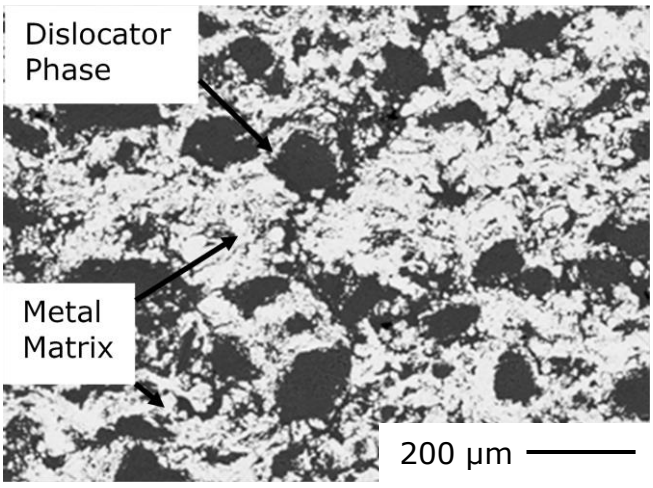
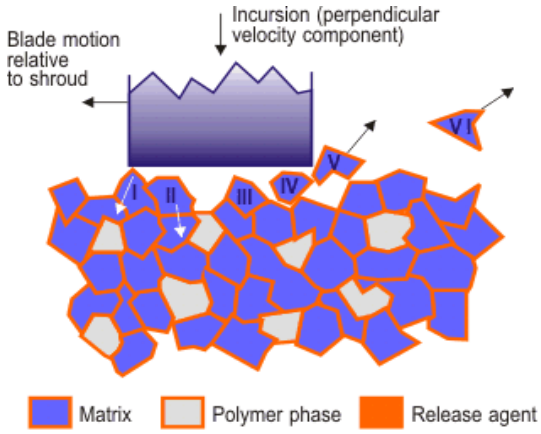


Figure 2-2. Microstructure of abradable coating (Metco 320)[9].



- Particle I was struck by the blade and through momentum transfer accelerates downwards into the coating.
- Particle II was impacted earlier and is still travelling downwards elastically deforming the neighbouring particles and itself.
- Particle III has transferred all the energy it absorbed during the impact into elastic energy.
- Particle IV was accelerated out of the coating because of the release of the stored elastic energy and tore itself free from surrounding particles.
- Because of the thin blade tip, particle V is able to leave the surface of the abradable coating.
- Particle VI has broken free and passed though the engine. The small size of the wear debris causes no collateral damage to the following blades and vanes.

Figure 2-3. Illustration of a side view of a blade passing over the abradable surface and its effects on the particles [8]

As well as the sacrificial properties required, several other attributes are needed in order to be effective in maintaining the sealing properties during operation. Resistance to erosive nature of the environment is important, as if the seal is eroded the clearance between tip and coating will increase resulting in efficiency loss. The erosive resistance properties are not just against the high-speed gas flowing through the engine but also the particles ingested into the engine during operation.

The abradable material is often exposed to moisture during operation; this can lead to corrosion, which it needs to resist. The aluminium-based abradables are particularly susceptible to galvanic corrosion, with a cell being created between them and the substrate. Graphite dislocators also increase the conductivity, which can accelerate the process. Corrosion can lead to delamination or swelling of the coating, even material fall out.

As with all materials used in gas turbine engines, the abradable needs to withstand the high temperatures involved in operation. In addition to the high temperatures, cyclic thermal gradients are also experienced during the flight cycle. These imposed stresses are due to the differences in thermal expansion between the coating and the substrate. Over a number of cycles the coating can begin to form cracks, known as 'mud-flat' or 'crazed' cracking, which propagate perpendicularly from the coating surface to the substrate. Although small cracks, which are small enough not to affect the sealing efficiency, can act as stress relievers, once they grow they can cause loss of coating material which will greatly affect the clearance.

Friction is another property that the abradable must be able to overcome by wearing efficiently. If wear is not efficient, i.e. material is not removed easily, friction will expose the blade tip to higher than normal temperatures. Higher temperatures can cause pick-up of the material by the blade from the abradable, which can solidify. This solidified pick-up can cause grooving in the coating on continuing rotations during the engine cycle. Grooving can have

some serious repercussions such as hung starts, engine stalls and engine surges [8].

2.2 NEW SEAL DESIGN

The requirement for a new type of abradable seal material has been due to the new shape that the seal will form. Figure 2-4 illustrates the new design. This seal tile is brazed to a Ni-alloy carrier plate, which is mechanically fastened to the Ti-alloy engine casing. As can be seen, the abradable seal, unlike conventional seals, has a slotted and grooved geometry. The walls of the grooves are relatively thin structures and due to the brittle nature and low structural strength of current thermally sprayed materials, it is likely that the walls would collapse. However metal foams at 20mm thickness and having better ductility and structural strength than traditional seal materials are better suited to this design [9].

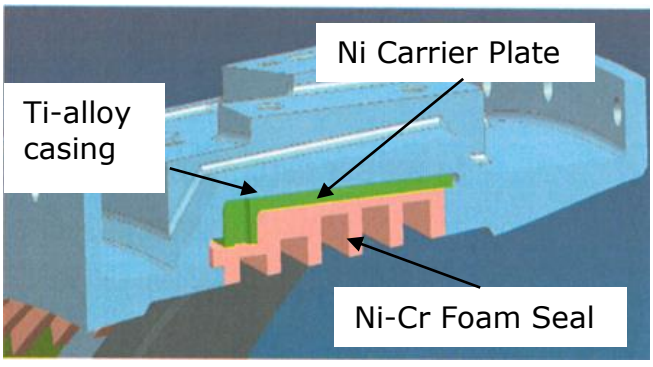


Figure 2-4. Illustration of the new abradable seal design[9].

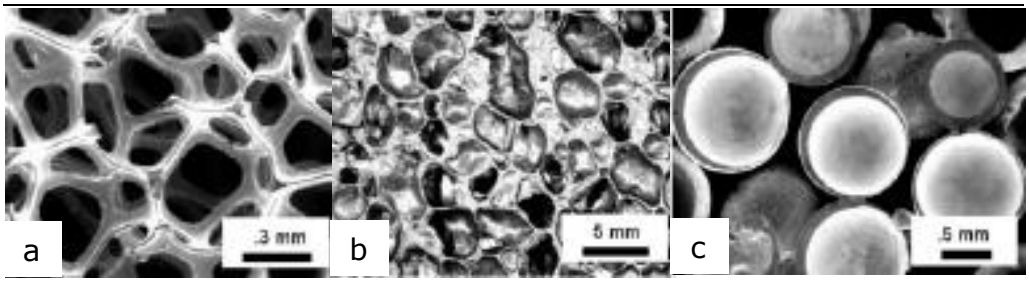


Figure 2-5. Images of foam material; (a) is an open cell Ni foam, (b) is a closed cell aluminium foam and (c) is a hollow sphere foam[10].

2.3 METAL FOAM OVERVIEW

Metal foams are metals with pores integrated into their structures. These structures possess unique properties that cannot be obtained with dense polymers, metals and ceramics or polymer and ceramic foams. They are stronger, have higher stiffness and energy absorption capabilities as well as being electrically and thermally conductive compared to polymer foams. Compared to ceramic foams they have the ability to deform plastically to absorb energy.

Metallic foams can be characterized structurally in many ways: based on whether they are relatively homogeneous or heterogeneous structures, their pore size and shape, whether they have open porosity, closed cells or are made from hollow spheres (Figure 2-5 (a),(b) and (c) respectively) and the relative density. They can be made from a variety of metals including Al, steel, Ti and Ni, with Al being the most prolific in terms of commercial availability. The chart in Figure 2-6 illustrates the manufacturing process routes (divided into liquid, solid and vapour phase) that are currently used to produce the metallic foams which can be seen at the bottom [10].

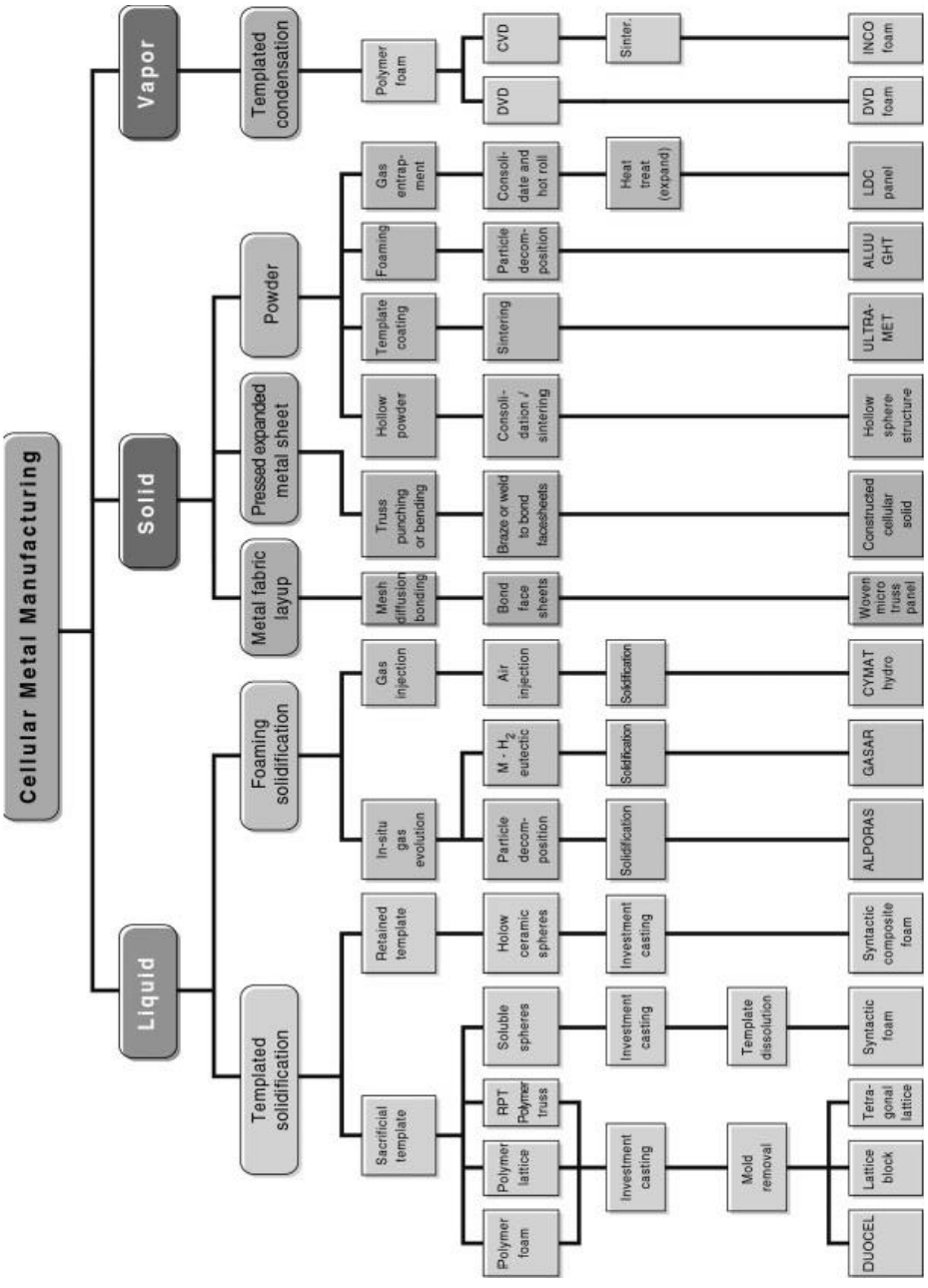


Figure 2-6 Taxonomy of cellular metal manufacturing processes [10]

The liquid process route was one of the first to be developed to make Al foams. Typically metal hydride particles are decomposed within the molten Al alloy to create a hydrogen gas to form the cells. Alporas is a closed-cell foam that is produced this way. Another method to produce closed-cell aluminium foam, such as Cymat, is to add silicon carbide, aluminium oxide, or magnesium oxide particles into the molten aluminium and blowing a gas into the mix using rotating impellers. To produce an open-cell foam, such as Duocel, an investment casting technique can be used. An open-cell polymer foam is coated in a heat-resistant material, from which the polymer is burned out and the molten metal is cast in the mold, followed by the removal of the mold material [10 - 13].

The solid process route uses powder metallurgy that also exploits the decomposition of metal hydrides. A mixture of the powdered metal alloy and powdered metal hydride are compacted and formed into a precursor. The formed part is placed within a hollow mold where it is heated above the decomposition temperature of the hydride, causing the expansion of the foam into the mold shape. Aluminium foams, such as Alulight, are the most common produced by this method although other metals such as tin and brass have been used as well [10 - 13].

Hollow metal sphere foams can be created by either a liquid or solid process. The spheres can be created by deposition of the metal onto polymer spheres (polymer spheres are removed in a later stage), or blowing metal powder, metal oxide powder or metal hydride powder

slurries up to micro-spheres using coaxial nozzles, and drying the spheres in a drop tube. Once formed the spheres are packed into the required shape and then densified and sintered. Hollow metal sphere foams have been manufactured from stainless steel, titanium and Ni [10 - 13].

The vapour phase deposition process uses an open-cell polymer foam as a scaffold. The polymer is dipped in a graphite solution or is coated by metal vaporization to make it electrically conductive. The metal is then electroplated onto the foam, followed by the burning out of the polymer scaffold. This technique is used typically with Ni and Cu foams [10 - 13]. This process is discussed in more depth later.

Metal foams also have a wide range of porosities spanning from as low as 2% to as high as 98%. Relative density, foam morphology and pore size depend on the method of manufacture. Relative density directly affects the cell size, cell wall thickness and pore diameter and consequently affects the mechanical and thermal properties of the foam. Figure 2-7 shows the relationship between relative density and cell size for the range of manufacturing processes.

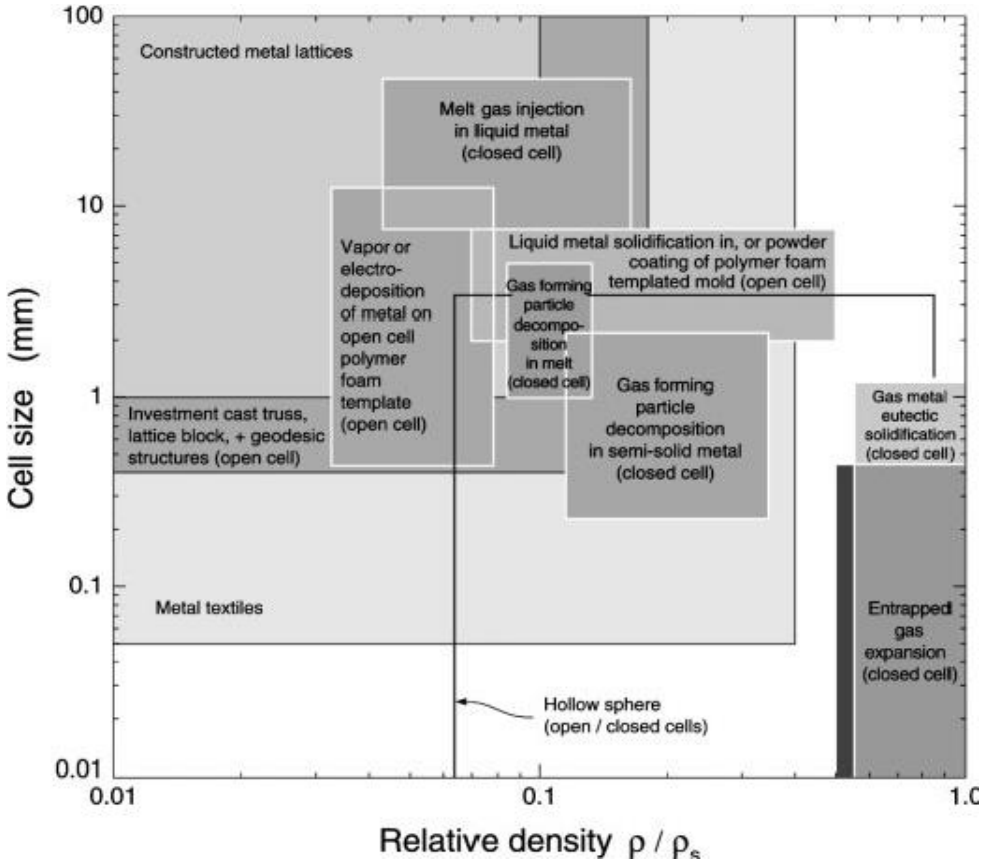


Figure 2-7. Relative density vs. cell size for various manufacturing processes[10].

Figure 2-8 and Figure 2-9 show foam property charts with a selection of commercially available foams plotted. These charts show the range of properties able to be produced by the various manufacturing processes as well as being helpful for selecting the specific foam required for a given application [14].

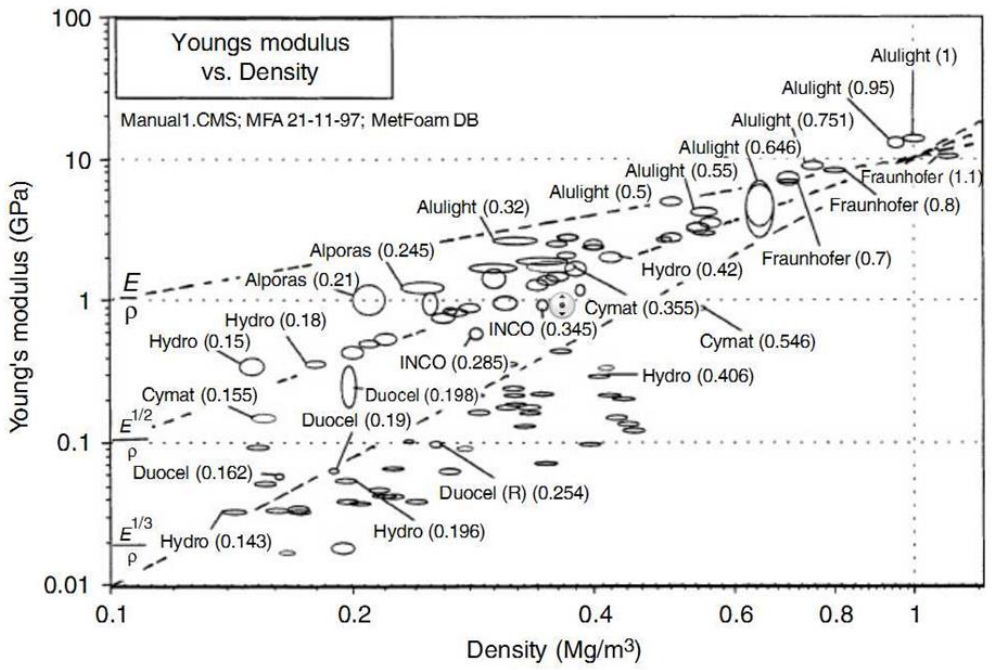


Figure 2-8. Young's Modulus vs. density for various commercial foams [10]

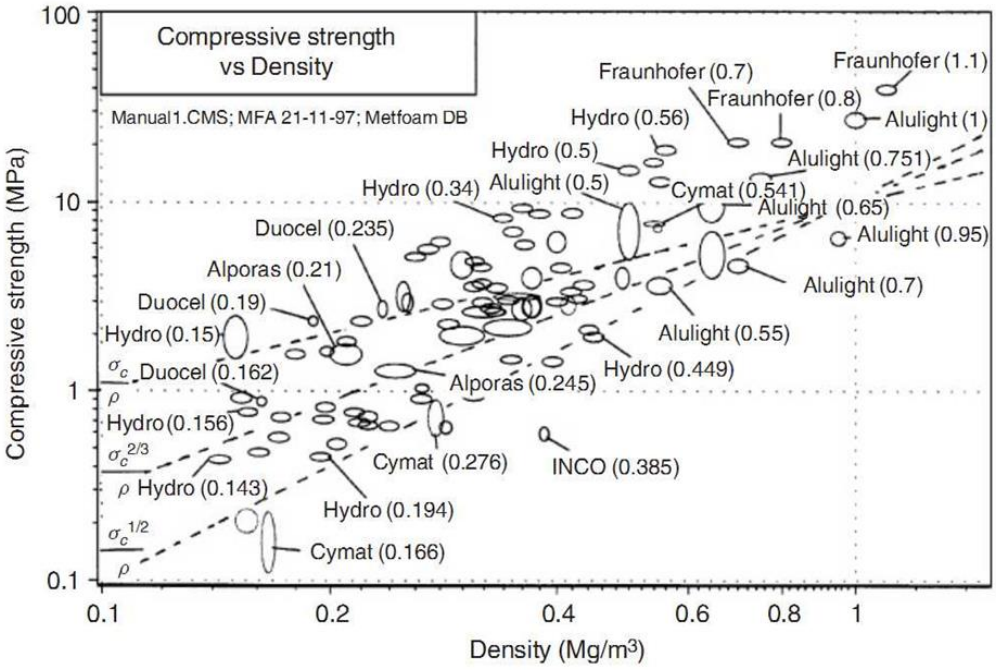


Figure 2-9. Compressive strength vs. density for various commercial foams[10]

2.4 ROLLS ROYCE ABRADABILITY TRIALS

To determine which foam would be most suitable for the newly designed seal, Rolls Royce subjected several metallic foams to an abradability test using a Sulzer Innotec abradability test rig. Figure 2-10 illustrates the rig set up. The foam samples were held in place whilst a spinning disc comparable to an engine disc with blades is moved into the foam. The velocity of the disc and the incursion rate were pre-determined and the blade wear and blade tip temperatures were recorded.

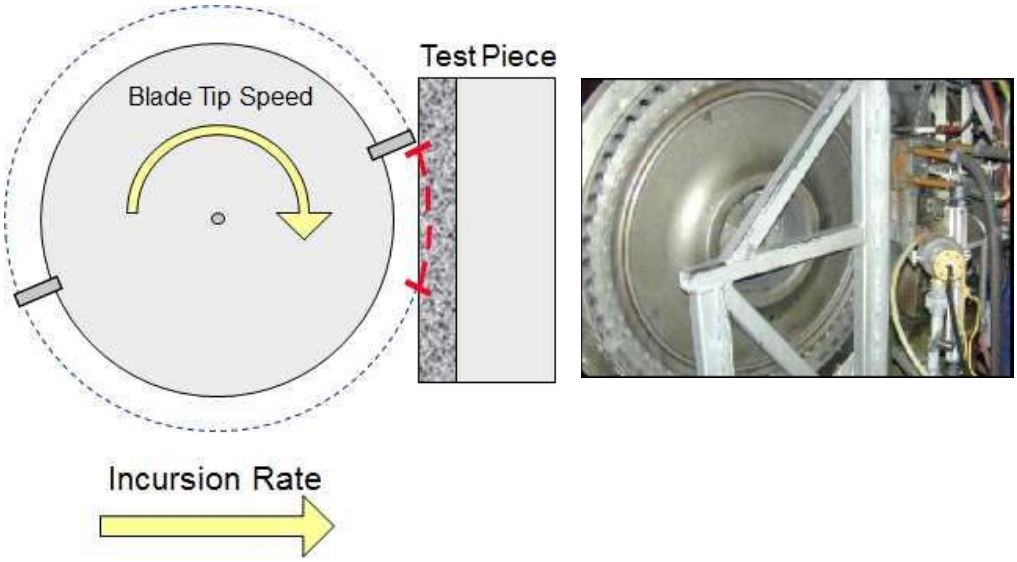


Figure 2-10. Illustration and photograph of the Sulzer Innotec abradability test rig [9].

The foams subjected to the test were; several steel sintered hollow sphere materials supplied by the Fraunhofer Institute, several closed cell aluminium foams, and some open-cell Ni-Cr foams with 17-23PPI and 27-33PPI supplied by RECEMAT.

Figure 2-11 illustrates the results of the abradability tests performed with a low incursion rate. It can be seen that the FeCrAl sintered hollow sphere sample and the aluminium closed-cell foam sample both exceeded the acceptable blade wear limit with smearing visible on the surfaces.

Figure 2-12 illustrates the results of the tests performed on the same samples as Figure 2-11 but with a higher incursion rate. Here once again the FeCrAl sintered hollow sphere sample well exceeds the acceptable limit for blade wear. Also of note was the X-1723 Ni-Cr (the X denotes a higher Cr content) which only just stayed below the acceptable limit.

Following the results of the first set of samples further tests were performed on the Ni-Cr and steel sintered hollow sphere samples. Figure 2-13 shows the chart of results of the various samples at the various disc velocities and incursion rates. It can be seen that the NiCr 1723, FH 0.32/2 and FH 0.55/2 all were able to remain within the acceptable limits of blade wear. However when a grooved geometry sample of each material was tested (Grooved (Recemat) and Grooved (FH)) the steel sintered hollow sphere samples exceeded the limit.

From these abradability trials it was determined that the 1723 Ni-Cr open-cell foam would be best suited for as an abradable material. However the 1723 was not an ideal candidate for the new seal design, as unlike the close-cell foam it would need to be filled to create a seal. The dimensions of the seal also meant that the 1723

material was not thick enough. For this reason a 1116 Ni-Cr (also supplied by Recemat) was selected, as it was twice as thick as the 1723 samples, had a similar composition, and was the only 20mm thickness foam on the market available and in sufficient quantities. The larger pore size that it contained also meant that it would be easier to fill [9].

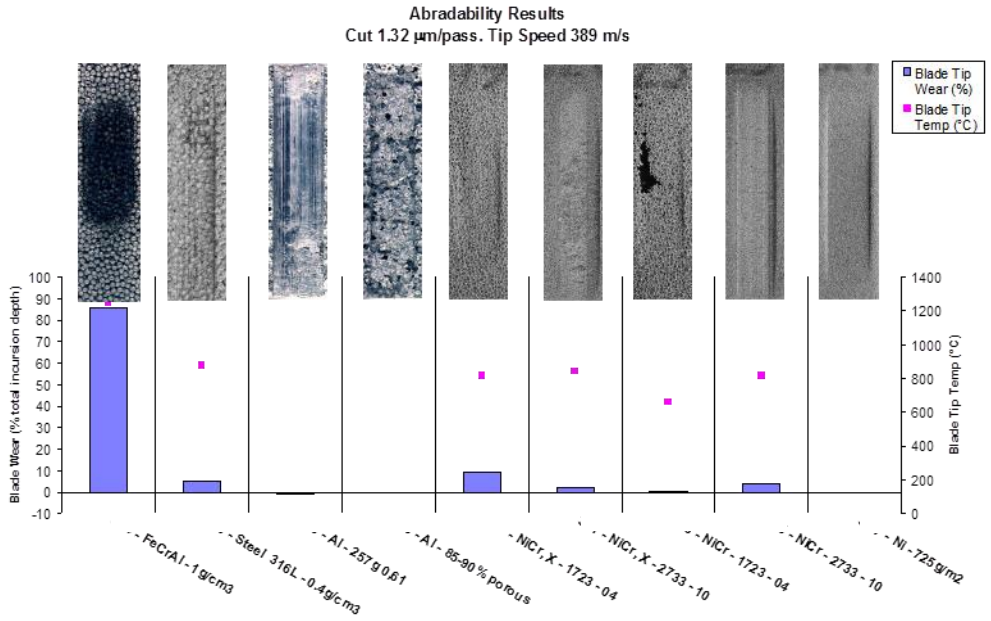


Figure 2-11. Abradability results from a low incursion rate [9]

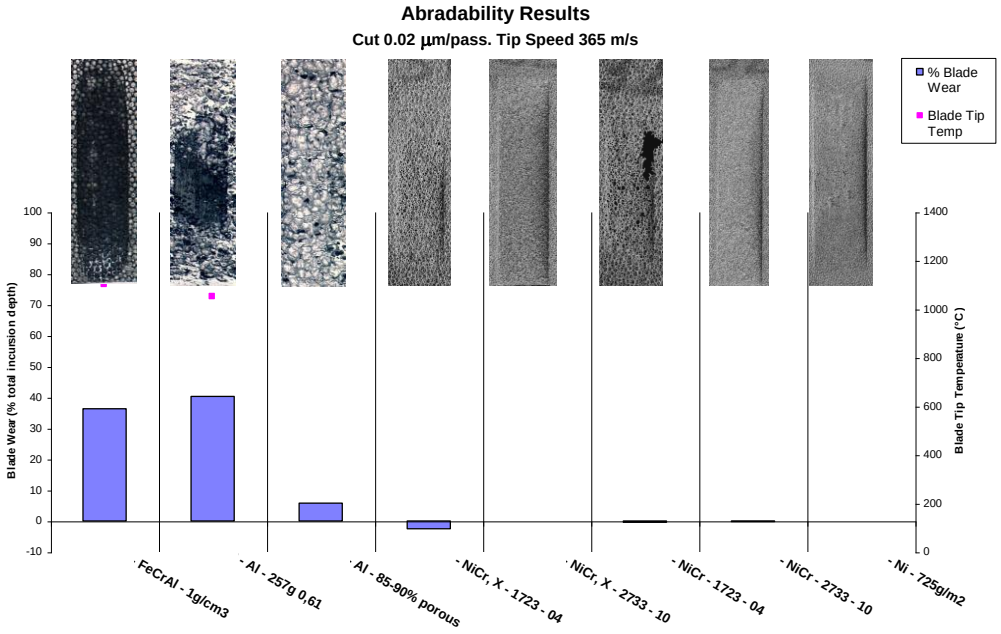


Figure 2-12. Abradability results from a high incursion rate [9].

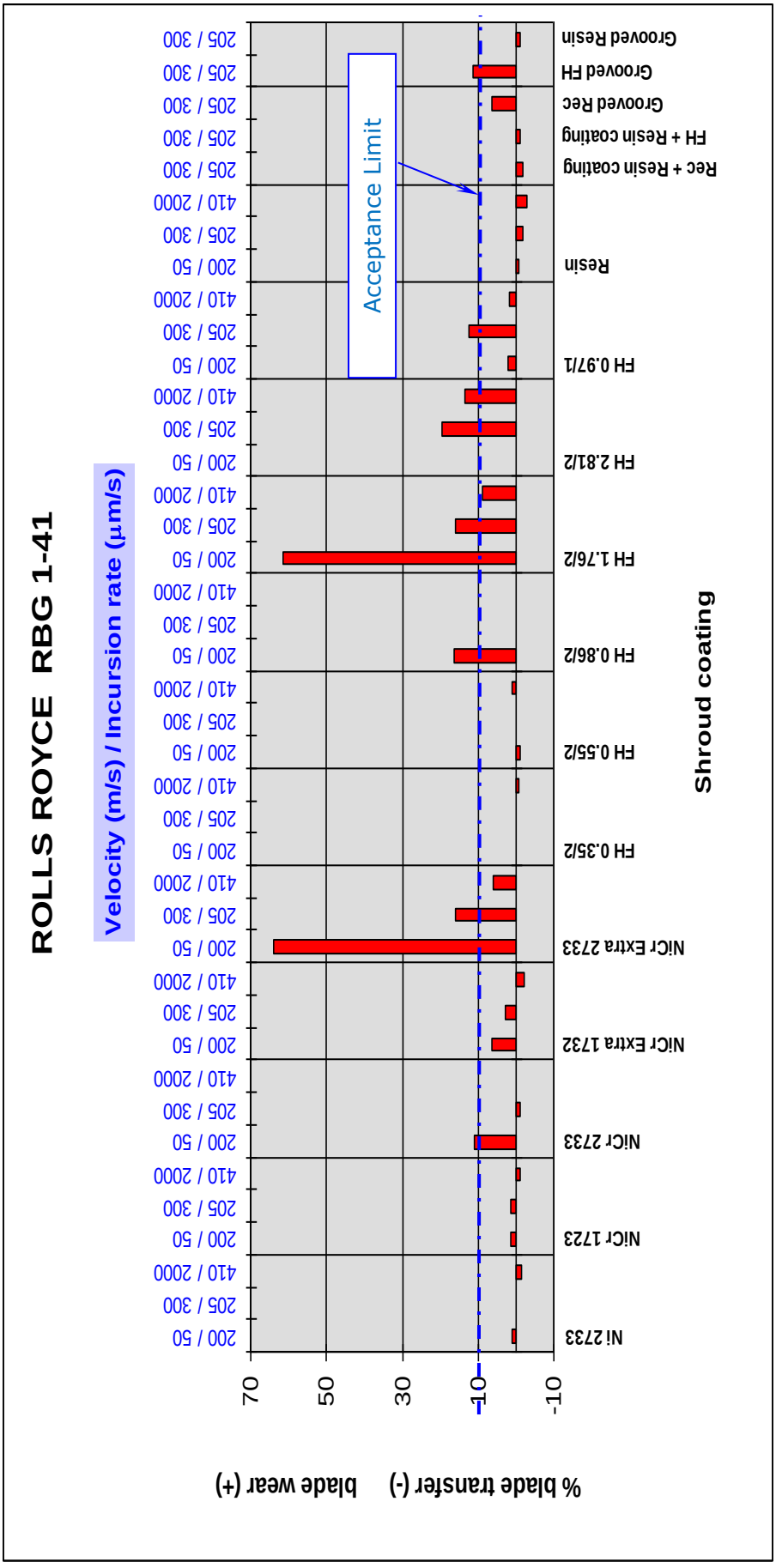


Figure 2-13. Abradability results for various disc velocities and incursion [9].

2.5 NICKEL-CHROME OPEN-CELL FOAM MANUFACTURE

2.5.1 Ni-Cr Material Properties

Ni-based alloys combine good corrosion resistance with excellent mechanical properties at high temperatures. The addition of Cr to Ni enhances the strength, as well as the resistance to corrosion and hot corrosion within carburising, sulfidising and oxidising environments. High Cr alloys are also resistant to highly oxidizing aqueous solutions such as nitric acid and nitric-hydrofluoric acid mixtures. The good corrosion resistance properties are a result of the passive oxide film, which spontaneously forms in all Ni-alloys. At high corrosion potentials, when entering the transpassive state and the Cr-rich passive films cannot be maintained, the addition of ~1% Si can extend protection by forming a more stable Si-oxide film. These properties make Ni-Cr an ideal material for use in jet turbine engines.

The greater the content of Cr within the alloy, the greater the resistance to oxidation. The improvement is significant when the Cr content exceeds 15-20%; this is attributed to the very adherent, dense Cr-oxide layer [15]. The research by Choe, *et al.* [4], found that the oxidation kinetics of Ni-Cr foams is similar to that of bulk Ni-Cr material.

There are several corrosion mechanisms that Ni-Cr alloys are susceptible too: pitting, crevice, general, intergranular and stress corrosion cracking.

Pitting corrosion occurs when aggressive anions such as chloride or bromide can penetrate into the passive oxide film. Initiation points are at surface defects, localised change in composition, or damage to the passive film surface. The anions depassivate the area causing it to become anodic, whilst the surrounding area becomes cathodic, creating a galvanic cell [16-18].

Crevice corrosion is similar to that of pitting corrosion. It is a localised mechanism initiated by the stagnation of fluid from the environment. The micro-environment created leads to a different local chemistry being formed, causing it to become anodic with respect to the cathodic surroundings and creating a galvanic cell. This could be an issue with regards to the structure of foams, which have a hollow interior [19-20].

In contrast to pitting and crevice corrosion, general corrosion is the result of a general instability in the oxide layer, and therefore the corrosion attacks the entire surface. General corrosion happens when none of the alloy components can form a protective oxide film such as during the active and transpassive dissolution of material [18].

Intergranular corrosion (sensitisation) occurs at high temperature in the range of 649-871°C. The mechanism is the precipitation of chromium carbides at the grain boundaries, resulting in chromium depleted areas surrounding them. These chromium depleted areas are less resistant to corrosion than the grains themselves, and can cause grains to become separated if the grain boundary is corroded

away. Figure 2-14 shows an image of a Ni-Cr sample which has undergone intergranular corrosion, with the grain boundaries depleted [18] [21].

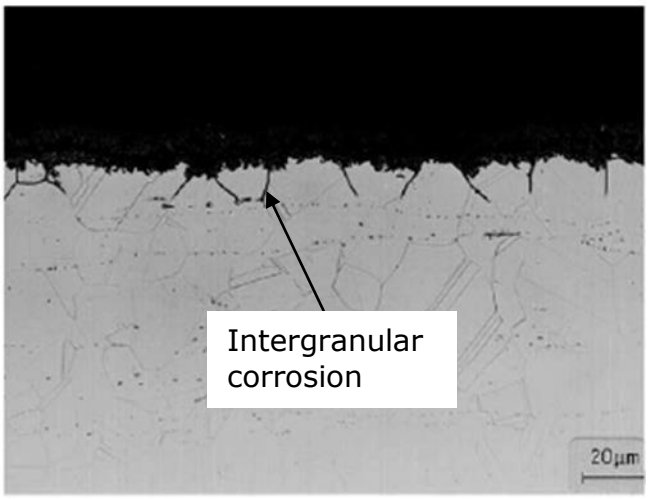


Figure 2-14. Image of the effect of intergranular corrosion on a Ni-Cr sample[18].

Stress corrosion cracking (SCC) can be observed along the grain boundaries (inter-granular) or through the grains (trans-granular). SCC needs both a chemical and mechanical component. With higher stresses the aggressiveness of the corrosive environment does not need to be as high. Conversely highly aggressive environments will result in failure at lower stresses [18] [21].

When sectioning Ni-Cr foams wire-electrical discharge machining (EDM) is usually employed, as it results in less damage to the foam structure. The machining process involves a pulsed voltage difference between a wire electrode and a conductive workpiece initiating a spark, which erodes the workpiece material. The

remaining workpiece material rapidly re-solidifies to form a recast layer. This recast layer contains an altered microstructure (with a depleted Cr composition), tensile stresses, micro cracks and impurities, all of which can be detrimental to the corrosion resistance of the material [22-23].

The estimated Cr content for Recemat supplied foams can be seen in Figure 2-15. According to the plot, the 1116 foam has between 20-25wt.%Cr, whereas the 1723 foam has between 20-32wt.%Cr [24]. The large variation in Cr content is due to the manufacturing limitations associated with the deposition of Cr (described later in the electrodeposition section) but as a Recemat standard will have a minimum of 20wt.%Cr regardless of pore size. The supplier also states that their foams can also contain <8wt.%Fe and <2wt.%C. Upon review of the Cr-Ni phase diagram (Figure 2-16) the foams should exhibit a single phase. However, the phase diagram does show that the formation of a secondary phase is possible at around 500-540°C [25].

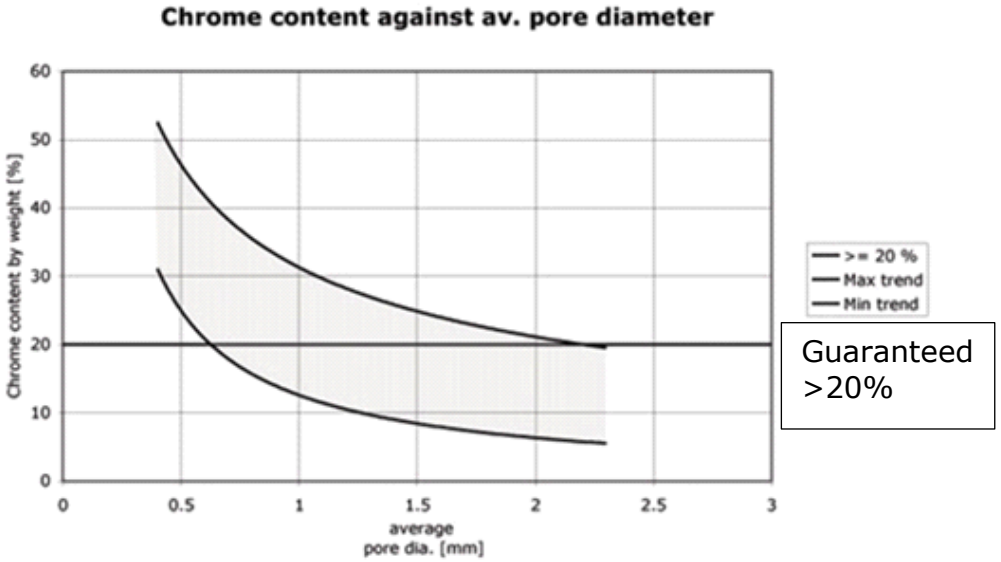


Figure 2-15. Plot of Cr content against average pore diameter for Recemat foams[24].

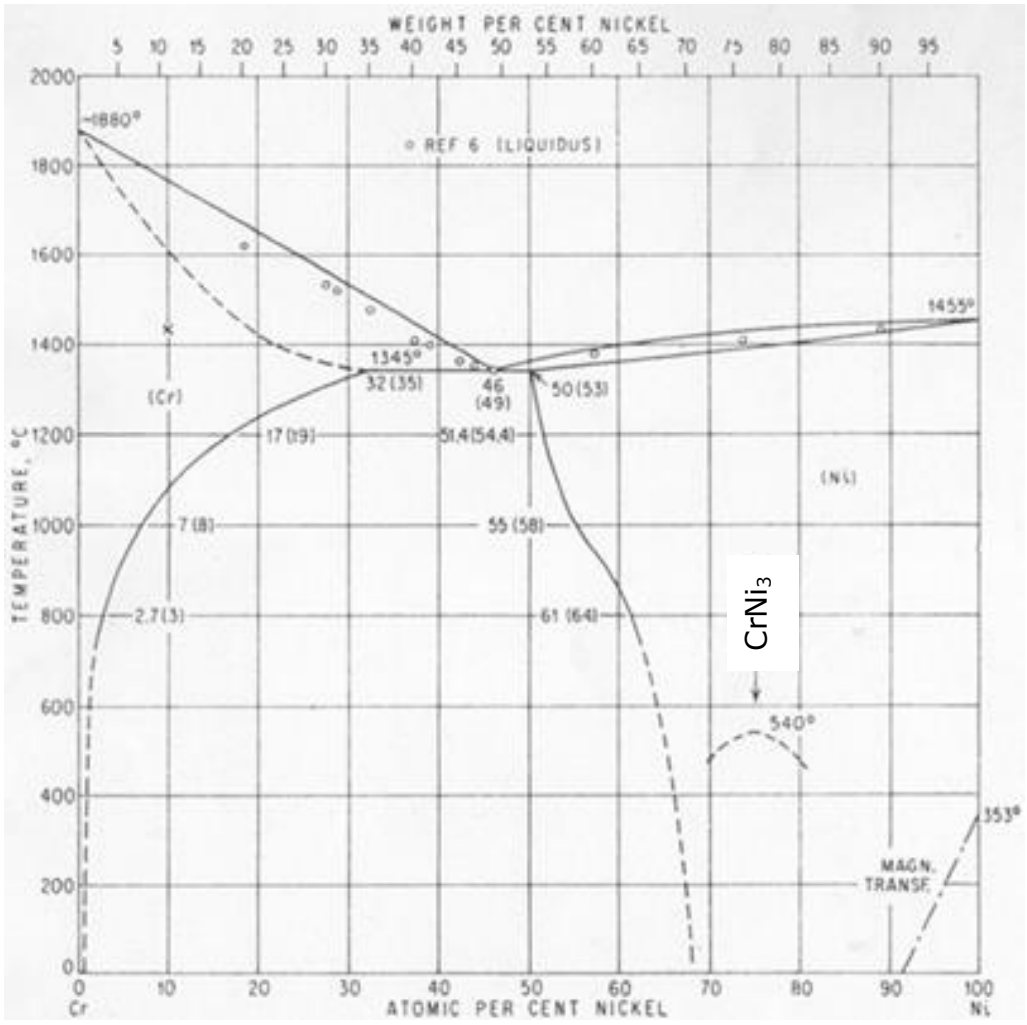


Figure 2-16. Cr-Ni phase diagram[25].

2.5.2 Methods Of Production For Open-Cell Ni-Cr Foam

There are several methods that are used to produce Ni-Cr foams; chemical vapour deposition (CVD), pack-chromizing, template transient liquid phase bonding and electro-deposition. The following sections give a brief overview of the methods, with the exception of the electro-deposition method which is described in detail as it is the method by which the foams investigated for this study were made.

2.5.2.1 Foam Manufacture by Chemical Vapour Deposition Method of Production

IncoFoam is manufactured by Inco and uses a chemical vapour deposition method (CVD), where by Ni carbonyl is decomposed and condensed coating the open-cell polyurethane substrate. The coating of pure Ni uses a cold-wall CVD reactor with a spool-spool winding mechanism which guides the porous substrates through a series of deposition chambers. These foams are of high purity (99.97% Ni) and are used widely in the battery manufacturing market. A further process of vapour deposition of Cr can be then carried out upon the Ni substrate, which then requires heat treatment to induce thermal interdiffusion. However, currently production of sheets is only up to a maximum thickness of 3.3mm [26]. For this reason the method, and product, is not utilised by Rolls Royce for the abradable seal.

2.5.2.2 Pack-Chromizing Method of Production

Choe, *et al.* [27], developed a method to create reticulated Ni–Cr foams, with a chromium content of 9.2–32.0 wt.%. These were created by the pack-chromizing of pure Ni foams procured from Porvair (manufactured by investment casting [10]). The pack, consisting of 5 wt.% NH4Cl activator, 25 wt.% Cr powder, and 70 wt.% Al_2O_3 filler powder, was mechanically mixed in a tumbling device for 20 minutes. The pure Ni Porvair foam was embedded within 40 g of pack contained in a high-chromium stainless-steel bag which was placed in the central zone of a tube furnace with flowing argon as cover gas. Heating and cooling to the process temperature of 1000 ◦C. Following chromizing, the samples were homogenized at 1200 ◦C for 48 h under flowing Ar, followed by furnace-cooling. The final structural characteristics of the foam, such as PPI, are dependent on the pure Ni Porvair foam (or whichever pure Ni foam used) used as the substrate. Currently there is no commercially available foam produced this way [4, 27].

2.5.2.3 Templated Transient Liquid Phase Bonding Method of Production

Queheillalt, *et al.* [28], developed a production method for synthesizing open-cell Ni based alloy foams by template transient liquid phase sintering. Vitreous carbon foams were produced by polymerizing infused polyurethane foam, followed by heat treating to carbonize it. This provides a stable high temperature template

which are then dipped in a binder solution and lightly shaken to remove excess binder. The binder coated foams are then suspended in a fluidized airbed containing a mixture of a Ni based alloy (Ni–21Cr–9Mo–4Nb) and brazing alloy (Ni–25Cr–10P). The powder coated carbon foam is then sintered, densifying the powder coating. The resulting foam, whilst open-cell, does contain some filled pores which can be seen in Figure 2-17 (a), as well as having coarser ligament surfaces which can be seen in image (b) and enhanced in (c).

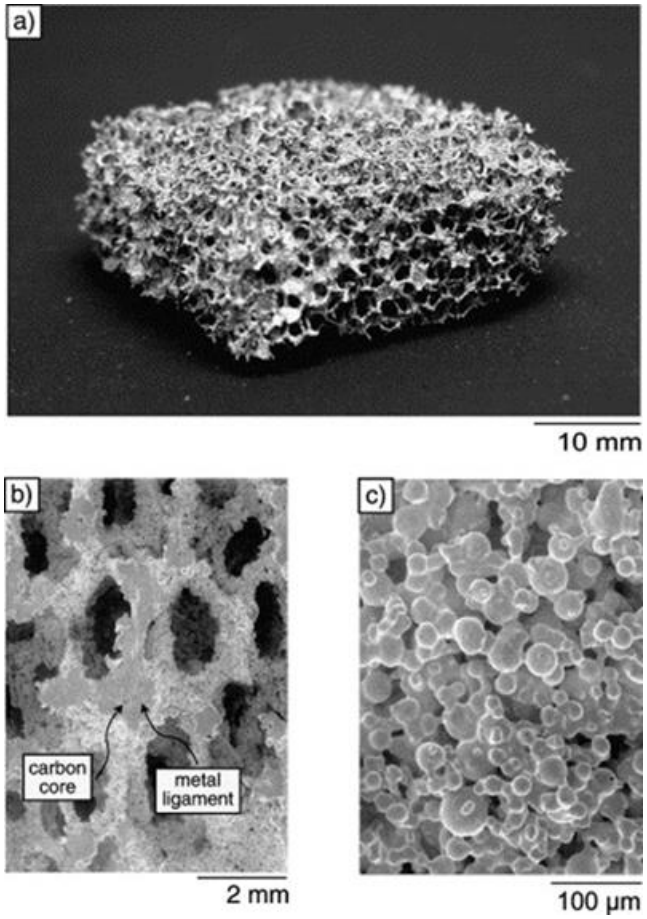


Figure 2-17. Image of Ni based foam produced by templated transient liquid phase bonding, showing where some pores are filled (a). Image (b) shows the course ligaments, with image (c) a magnified image of one of them[28].

2.5.3 Electro-Deposition Method of Production

The electro-deposition method involves electroplating an open-cell polymer foam and then removing the polymer afterwards (Figure 2-18). This method is utilised by several companies for commercial sales under the names Retimet (Dunlop, GB), Celmet (Sumito Electric, Japan) and Recemat (SEAC, The Netherlands). The following sections will describe in detail the manufacturing process [13].

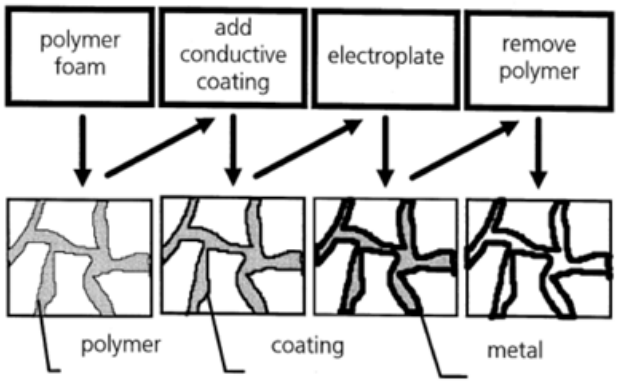


Figure 2-18. Electro-deposition method for manufacture of metal foams[13].

2.5.3.1 Reticulated Polyurethane Production

Reticulated polyurethane is used as a substrate to deposit the Ni-Cr onto. This substrate determines the size and shape of the struts as well as the pore size of the final Ni-Cr foam.

Reticulated polyurethane is produced from initially closed-cell foam, with cell structured polyhedron of pentagonal dodecahedrons (Figure 2-19). These are produced by the reaction of a polyisocyanate with a polyol (usually ester) in the presence of a blowing agent (water), surfactant and a catalyst. Silicon surfactants are often used in

polyurethane production, higher concentrations of which can result in faster nucleation (formation of bubbles) resulting in finer celled foams. The presence of dissolved gas such as entrained air in the mixture may also result in faster nucleation. Cell size is dependent mainly upon the proportion of gas molecules that diffuse through the liquid into existing bubbles to those that diffuse through the liquid to a nucleating site. It is also dependent upon the concentration and effectiveness of the nucleating agents [29- 30].

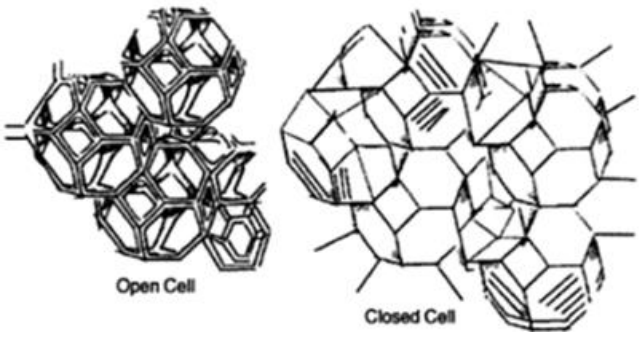


Figure 2-19. Illustration of the pentagonal dodecahedron shaped cell in its open and closed form [14].

Commercially the closed cell polyurethane foam is produced in continuous slabs, which are cut-off into segments known as buns. The process is illustrated in Figure 2-20, in which it can be seen how the material rises from the bottom of the mould. This creates anisotropy of the foam structure through the sheet as, due to gravity and the generation of carbon dioxide, the cells near the bottom are smaller and more spherical, compared to the more elongated and larger cells near the top. This type of structure will show physical properties that will depend on direction. [31].

Once the bun has been created it is then further cut to create sheets. A rotary peeling operation is used to perform this, such as can be seen in Figure 2-21. However due to the variation in cell size and shape there are periodic differences, which are more pronounced in log foams but which are still noticeable in bun foams. It is also shown how the bun can be peeled as well as the orientation of the cells when cut. Figure 2-22 illustrates a method peeling known as loop slitting; it is a method where by a foam bun of ~60m length is bonded into a loop. The loop is then continuously slit as it is rotated around. Loop slitting can remove the large periodic density variation within the longitudinal direction of the foam (Figure 2-23) [32].

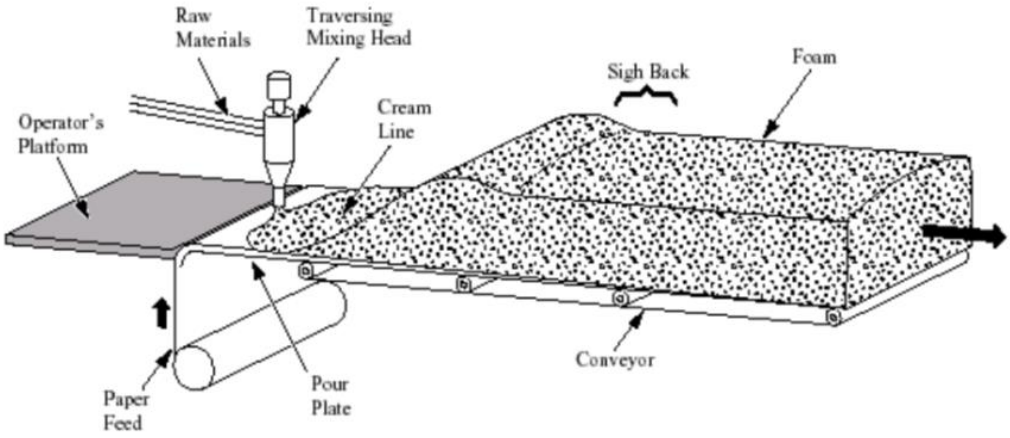


Figure 2-20. Continuous foam slab stock production method [31].

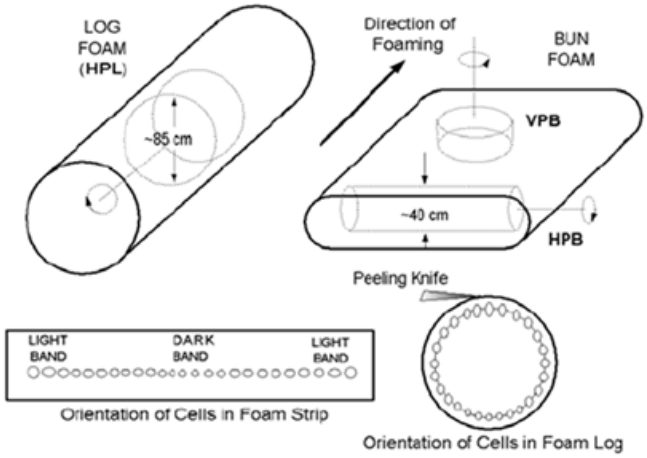


Figure 2-21. Illustration of the rotary peeling technique and cell orientation[32].

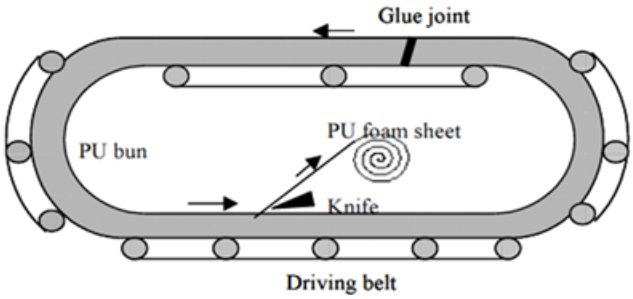


Figure 2-22. Foam loop slitting machine[32].

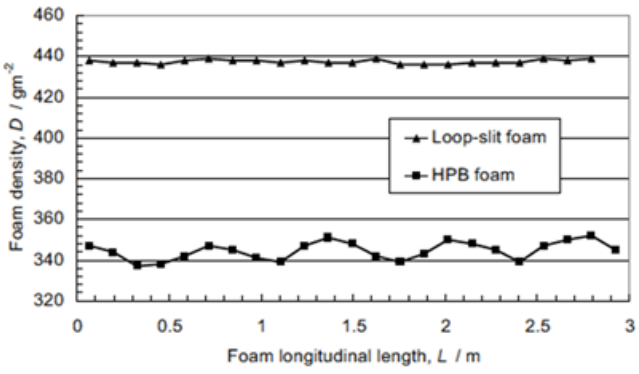


Figure 2-23. Longitudinal density profile comparison between a loop slit foam and a horizontally peeled bun (HPB) foam [32].

There are two methods to create reticulated polyurethane foams from formed closed-cell polyurethane foams. The first is a thermal reticulation process whereby the foam is placed within a pressure vessel, such as the one that can be seen in Figure 2-24. A vacuum is pulled followed by the introduction of an explosive mixture of hydrogen and oxygen gases. When ignited, a flame front passes through the foam at sub-sonic speed causing the foam membranes to melt and volatilise leaving the flame-polished skeletal strand structure. [31].

The alternative method is that of a chemical (quenching) process. In this process the foam is passed through a caustic bath (Figure 2-25). The caustic solution dissolves the membranes leaving a rough skeletal structure. The rough surface is detrimental to the final Ni-Cr foam as, once coated, the metal foam inherits the rough surface on the internal walls of the strut. These rough surfaces can act as crack initiation sites and have been found to contribute to lower strength values. As such the thermal reticulation process is the preferred method. [31-32].

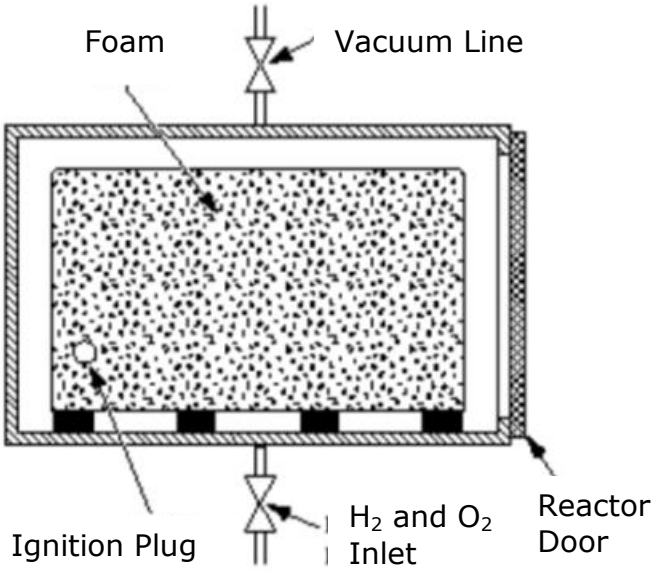


Figure 2-24. Illustration of a thermal reticulation vessel [31].

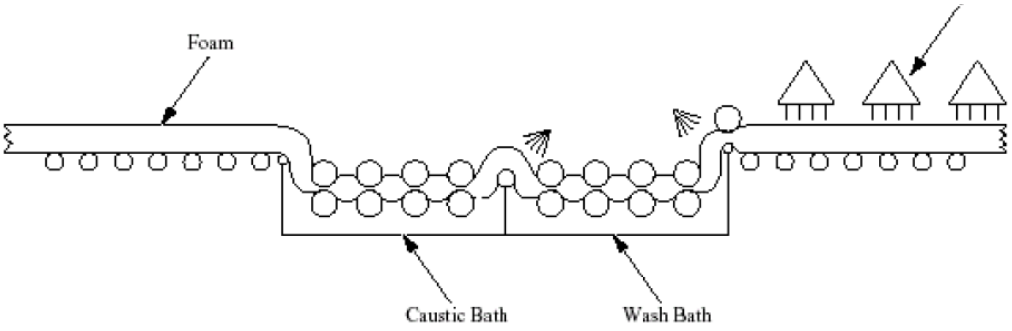


Figure 2-25. Caustic bath used for chemical (quenching) reticulation [31].

2.5.3.2 Electro-deposition

Electro-deposition of Ni onto the polyurethane substrate requires electrical conductivity of the polyurethane. In order to achieve this the polyurethane can be either dipped into a conductive slurry of graphite or carbon black, coated with Ni by using a cathode sputtering method, or by an electroless Ni plating method (this method still requires the further electroplating of Ni).

The conductive layer can contain various defects, such as vacancies, voids and micro-steps, which are caused by irregular arrangements of carbon micro-particles, or Ni grains. These defects promote irregular nucleation and growth of grains during the electro-deposition process

One method to produce the Ni-Cr foams, involves alternate coatings of Ni and Cr being electroplated onto the conductive polyurethane substrate. The foam is then heat treated to create the alloy by thermally inducing interdiffusion of the two metals. The interdiffusion occurs in two ways simultaneously; vapour phase transfer and solid-state diffusion. The Cr content between the middle and the edge of the foam is inhomogeneous due to the poor plating power of the Cr, which is the main shortcoming of the method.

Alternatively the Cr can be deposited onto the Ni foam by a separate vapour deposition stage, with a similar heat treatment afterwards. However, it is difficult to control the Cr content by way of this process, but it is the preferred route chosen by Recemat. [2, 13, 33-34].

The electrodeposited layers are not uniform throughout the thickness of the foam. The electrodeposition technique is intrinsically associated with a thickness deposition ratio (TDR=t_e/t_l, where t_e = the thickness of the surface layer and t_l = the thickness of the mid-section layer) that varies from unity. The actual thickness of the deposited material at any point on the surface of a shaped article is

dependent on the current density at that point, which in turn is determined by how the current is distributed over the surface. The shape of the part (to be deposited on), the relative placement with respect to the anode, how the parts are placed on the racks (within the coating chamber) and the dimensions of the system will all effect the current distribution. Struts closest to the surface of the sheets will have a greater current density, as they have a shorter anode-to-cathode distance and therefore a lower resistance to current flow. The result is a profile that has a thicker layer near the surface of the foam compared with the mid-section, illustrated in Figure 2-26 [35-36].

In addition to the geometric factors, metal deposition throwing power is influenced by the cathode polarization, the cathode efficiency – current density relationship, and the electrical conductivity of the solution. The electroplating of Cr onto the Ni substrate suffers from this low throwing power and the porous geometry of the foam which promotes hydrogen bubble formation and inhibits the mass transfer of Cr. Physical vapour deposition of Cr is feasible, although deposition of material on thicker foams is severely limited by the line-of-sight limitations of PVD techniques [36-37].

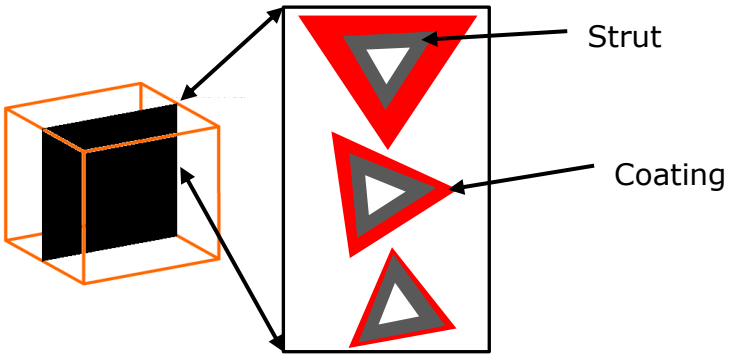


Figure 2-26. Illustration showing the variation in coating thickness, from a strut at the top surface to one in the mid-section.

The Ni-Cr foams, produced by electrodeposition, by Duan, *et al.* [2], showed that there large Cr content coating on the surface of the strut could be diffused by heat treatment. Figure 2-27 (a) shows a schematic representation of the Cr content through the Ni strut thickness, with 100wt.% Cr on the surface and under 20wt.% within the strut. With increasing time of heat treatment it was possible to homogenise the strut, so that there was 20wt.% Cr at the surface of both walls Figure 2-27 (b), although there is a drop in Cr content towards the centre of the strut wall. The heat treatment is carried out during the removal of the polyurethane substrate.

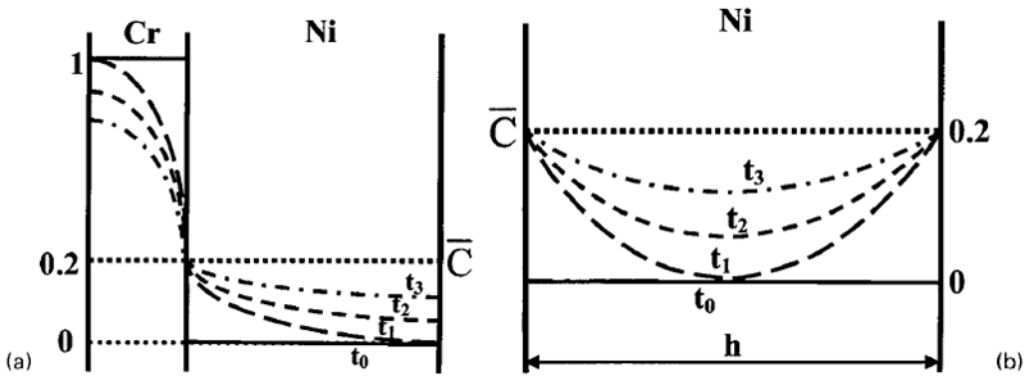


Figure 2-27. Schematic representation of Ni-Cr diffusion, during homogenisation heat treatment[2].

The supplied Recemat material for testing is the non-age-hardened variety. This means that a second heat treatment that would enable complete dissolution of the Cr does not occur. Therefore samples may have Cr layer coating on the struts which will result in localised variation in properties when compared to a fully homogenised sample material.

2.5.3.3 Removal of the Polyurethane Substrate

There are two methods for removal of the polyurethane substrate and conductive layer, a two-step and a one-step method. The two-step method removes the polyurethane matrix by burning it out in air at ~600°C. The burning process can cause eruption of the polyurethane material not only out of the ends of the metal struts, but along the struts as well, an image of which can be seen in Figure 2-28. Both the polyurethane and the carbon based conductive materials react with O_2 to form CO_2, H_2O and other gases, which can escape through the plated layer. This process can also create NiO on the surface. By subjecting the foam to a sintering process (at 850°C

and 980°C) in a reductive atmosphere (NH_3) the surface oxide is reduced to Ni metal. The sintering process also reduces the surface energy, advancing the surface diffusion, resulting in shrinkage, the disappearance of small pores and the reduction of excess voids and dislocations within the crystal lattice.

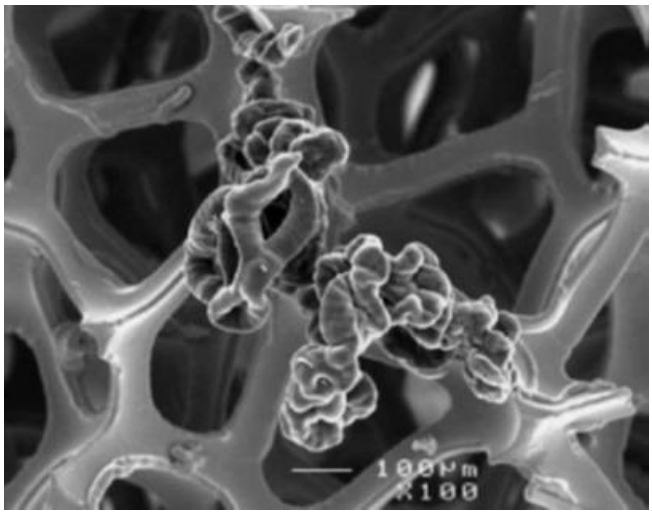


Figure 2-28. Polyurethane eruption during the burn out process[26].

The one-step method is similar to the two-step but does not involve NiO reduction. Instead the polyurethane and conductive layer are subjected to pyrolysis in the same reductive atmosphere that is used in the two-step method. During pyrolysis the polyurethane decomposes into small gaseous molecules such as CH_4 and C_2H_6. Whether the heat treatment was at 850°C or 980°C, the same foam morphology to that of the two-step method is created. [33].

2.5.3.4 Final Ni-Cr Reticulated Foam Product

As can be seen in Figure 2-29, the final cross-section of a strut has taken on the triangular shape inherited from the polyurethane. The etched sample shown clearly shows the grains (a), which are the width of the strut. Figure 2-29 (b) is an image taken from the same material where it is visible that there is an imperfection in the strut wall, probably related to the location of the grain boundaries meeting at the corner. [3]. Figure 2-30 shows the grains that are on the strut wall, which show a single Ni-Cr solid solution of uniform composition [2].

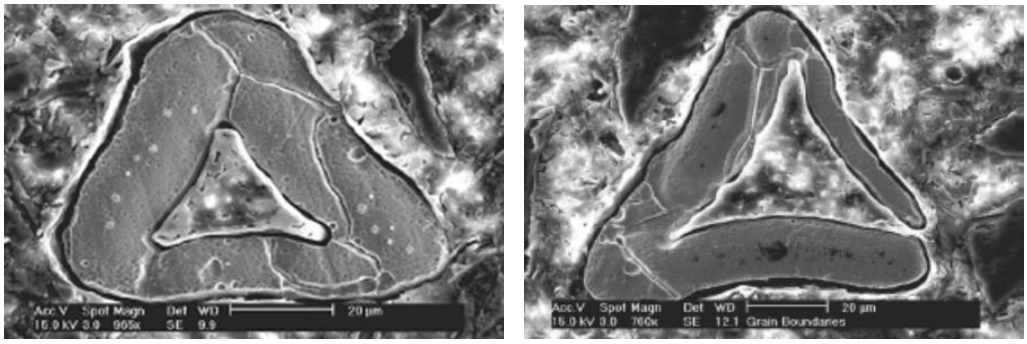


Figure 2-29. SEM images of etched strut cross sections showing grains (a), and imperfectly formed walls (b)[3].

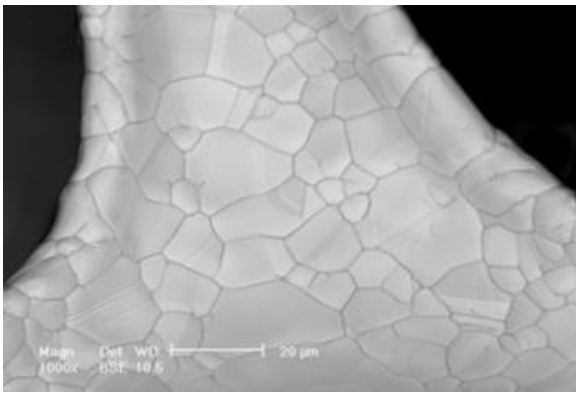


Figure 2-30. Image showing grains with uniform composition on the strut wall [2].

2.6 MECHANICAL PROPERTIES OF OPEN-CELL FOAMS

There has been much research published about the mechanics of cellular structures. In addition to these data, models exist allowing for prediction of properties such as yield strength and Young's Modulus, as well as the failure mechanics for the various types of foam. Gibson & Ashby have published the two most widely cited publications associated with the mechanics of foams [14, 38]. The following sections outline the theoretical mechanical properties of open-cell foams, which are determined to be relevant to the application.

2.6.1 Compressive Properties

During compression, three regions define the compressive behaviour of the foam. Figure 2-31 shows a theoretical stress-strain curve for cellular materials. In the image it can be seen that in the first region the material undergoes linear-elastic deformation, until the initial maximum yield stress is met. After this the material undergoes plastic collapse at a near constant stress, which gives a long horizontal plateau region to the stress-strain curve. During this period, plastic collapse propagates from one cell band to another. Densification of the foam occurs when all the bands have collapsed. This causes a rapid rise in the stress, which indicates passage into region III. Typically this is reached at 60% strain.

By using a cubic model to represent the open-cell foam, such as can be seen in Figure 2-32 (a), it is possible to illustrate how the foam

deforms. During the linear elastic region, the strut walls begin to buckle, modelled in Figure 2-32 (b). Plastic collapse occurs when the moment exerted on the cell walls exceeds the fully plastic moment, creating plastic hinges at the strut joints. This can be modelled such as in Figure 2-32(c). Once the cell walls have buckled and been crushed, the large strains begin to compress the material itself. This leads to the large stress increases.

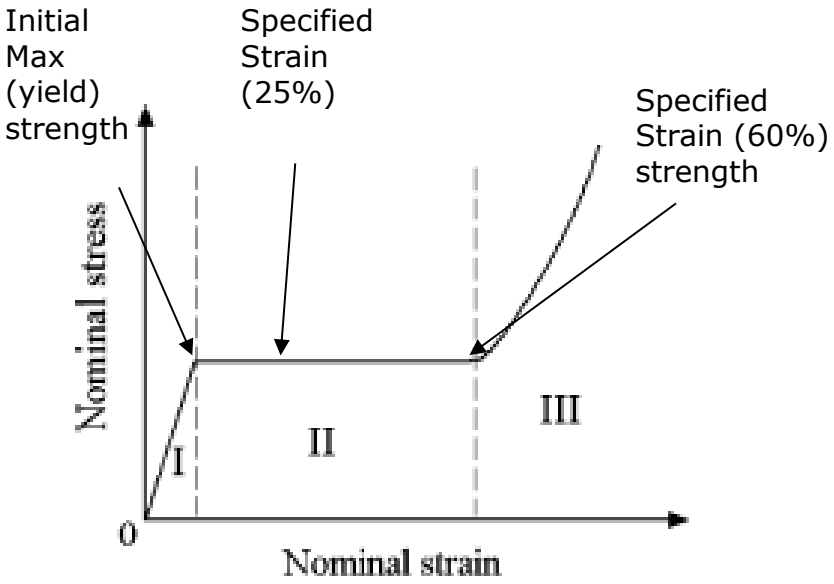


Figure 2-31. Theoretical stress-strain curve for cellular materials[14].

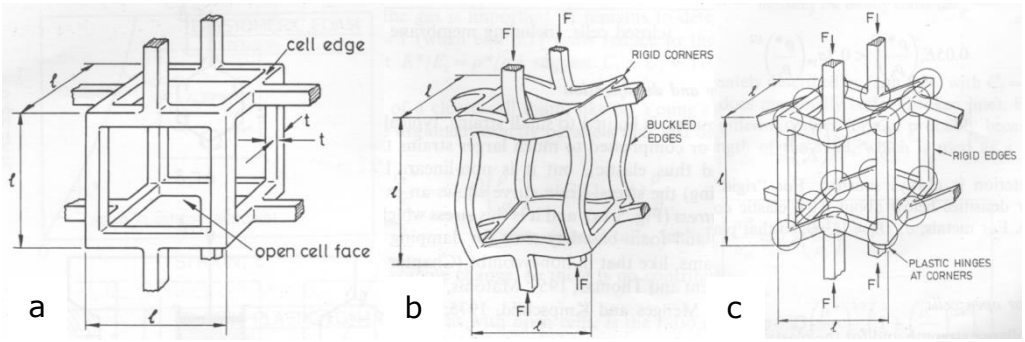


Figure 2-32. Illustration of a cubic model for an open-cell foam (a), showing elastic buckling in the struts (b), and the formation of plastic hinges (c)[14].

Equation 2-1 is derived from the cubic models and defines the relationship between the relative yield and relative density of open-cell metal foams. Equation 2-2 is also derived from the cubic models, and defines the relationship between the relative Young's Modulus and relative density of open-cell foams.

$$\frac{\sigma^*}{\sigma_s} = \boldsymbol{C}\left(\frac{\rho^*}{\rho_s}\right)^n \quad \text{- Eqn 2-1.}$$

σ^* = Yield stress of the foam
σ_s = Yield stress of the solid
ρ^* = Density of the foam
ρ_s = Density of the solid
C = Constant (~0.3)
n = Constant (~1.5)

$$\frac{E^*}{E_s} = \left(\frac{\rho^*}{\rho_s}\right)^2 \quad \text{- Eqn 2-2.}$$

E^* = Young's modulus of the foam
E_s = Young's modulus of the solid
ρ^* = Density of the foam
ρ_s = Density of the solid

The work of Choe, *et al.* [4], found that the data they collected from compression tests on Ni-Cr foams was in general agreement with the theoretical data derived from the equation, considering that there is a large experimental error for the relative yield (conservatively estimated at ±20%).

The work by Badiche, *et al.* [35], into the compression deformation of open-cell Ni foams has highlighted several aspects. The first being that due to the anisotropy of the structure an elongated cubic model

is required to accurately model the failure. This anisotropy has also been attributed to the lower yield strength for the foam compressed through its thickness than in the other direction. The stress-strain curve shows the common features, however the plateau region isn't horizontal, instead having a slight gradient. There is also a short plateau region at the very beginning of the curves, attributed to the lack of flatness of the material preparation for testing. It was also observed that during deformation the slightly less dense core of the foam sheets fail earlier. The work of Choe, *et al.* [4], which investigated the compressive yield of Ni-Cr foam, found that by increasing the Cr content the yield strength was also increased (Table 2-1). This was attributed to both the increase in relative density and the increase in strut yield strength by solid solution strengthening. The samples that they manufactured were also heat treated until complete dissolution of the Cr had taken place.Their work also reported that their data diverged from the theoretical model (Equation 2-1) with a gradient n=2.5 and within the limit of constant C=0.3-0.6 (Figure 2-33).

	Pure Ni	Ni-12.2Cr	Ni-19.2Cr	Ni-22.3Cr	Ni-27.2Cr
Relative Density ρ* /%	2.2	2.7	2.9	3.0	3.2
Measured foam yield stress σ*/MPa	0.11	0.29	0.39	0.55	0.91
Alloy yield stress σ / MPa	90	180	220	235	255
Yield ratio σ^*/σ_s	0.0012	0.0016	0.0018	0.0023	0.0036

Table 2-1. Summary of results from the investigation into compressive yield of Ni-Cr foam by Choe, *et al.*[4].

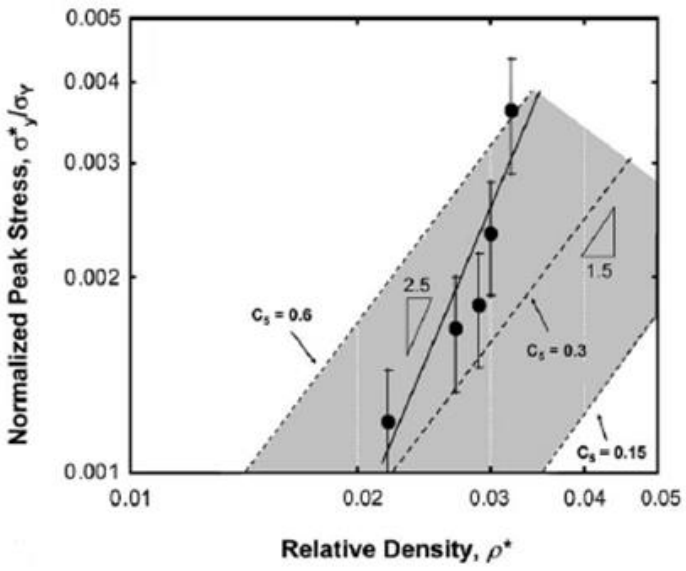


Figure 2-33. Relative yield strength against relative density[4].

2.6.2 Tensile Properties

Foams subjected to tensile stress will experience similar deformation mechanisms as those for compressive stresses, but will experience them in different directions. The exception to this is fracture. Tensile stress can cause a fast, brittle fracture whereas compression causes progressive crushing.

When subjected to a small tensile stress, the linear-elastic modulus is the same as that in compression, as the mechanism is still strut bending. During plastic collapse the foam yields in tension by the same mechanism and at roughly the same stress as in compression. Post-yield however, the compression and tension mechanisms differ. In compression the bending moment created by the rotation of the cell walls remains constant (or slightly increases), creating a horizontal plateau. However, in tension the rotation reduces the

bending moment, aligning the struts with the tensile axis (Figure 2-34). Therefore further strain requires plastic extension of the strut itself, which creates necking and eventual failure. An alternative failure mechanism in tension is that of crack propagation, illustrated in Figure 2-35. Once a crack forms within the foam it extends in a discrete way. Each time the row of struts along a crack front fractures, the crack advances by one cell width.

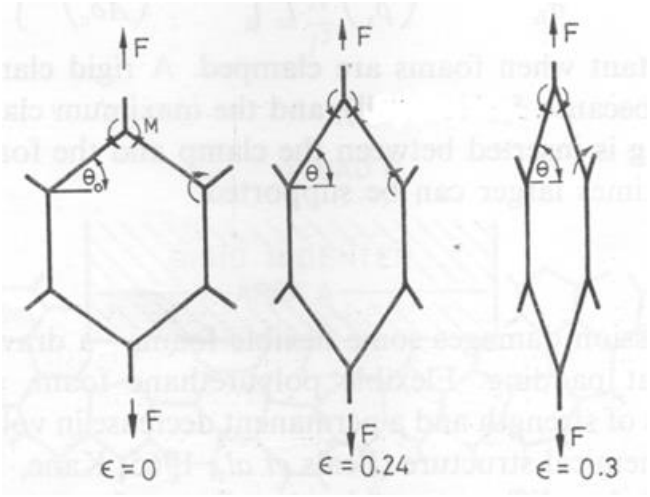


Figure 2-34. Alignment of struts during tensile loading[14].

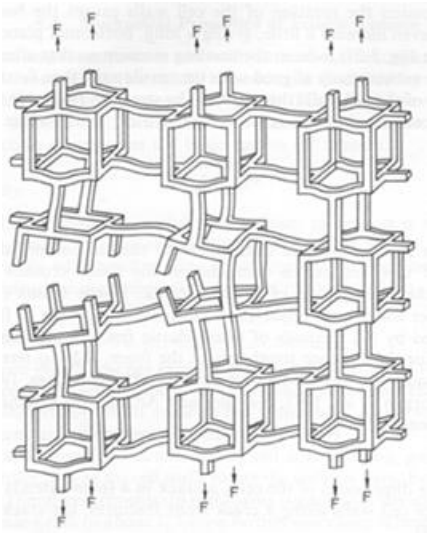


Figure 2-35. Propagation of a crack through an open-cell foam [14].

Figure 2-36 shows several tensile stress-strain curves for an Alulight foam. It can be seen how the curves vary in shape dependent upon the direction of testing. The ST has a plateau region, whilst the LL direction is able to obtain a higher maximum tensile stress, provided strut failure due to defects does not occur [14].

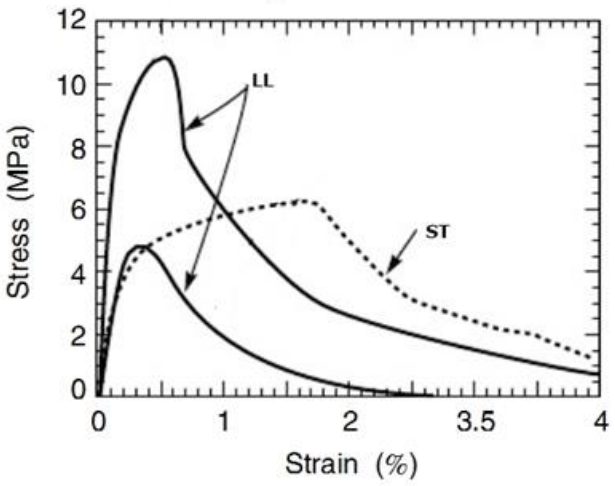


Figure 2-36. Tensile stress-strain curves for several Alulight open-cell foams in both the ST and LL directions[14].

The work of Onck, *et al.* [3], investigating the fracture of Ni-Cr foam, tested some Recemat 4753 foams samples. The sample had been heat treated prior to testing and no embrittling phases were reported. The work concluded that the failure is initiated by the onset of necking in the strut walls (Figure 2-37), although evidence of some brittle fractures was found. The process is very ductile, with almost all the energy dissipated through plastic deformation during necking. Another damage mechanism reported was that of strut 'unzipping'. Figure 2-38 shows an image of an unzipped strut, which thought to be related to the imperfections in the strut wall caused by grain boundaries meeting at the corners of the strut.

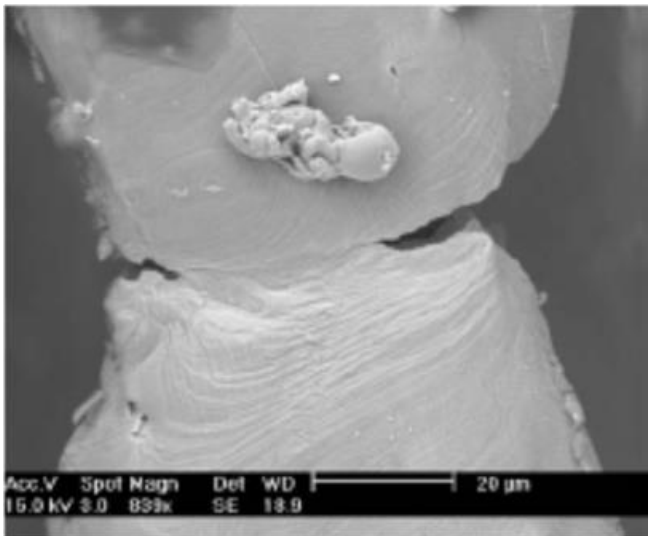


Figure 2-37. Necking failure in a Ni-Cr open-cell strut wall[3].

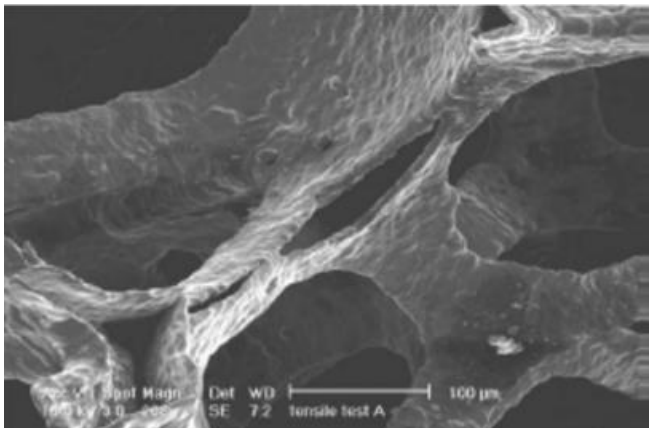


Figure 2-38. Unzipping failure in a Ni-Cr open-cell strut wall[3].

2.6.3 Shear Properties

There has been much research into the shear behaviour of metallic foam structures. However they have been predominantly based on aluminium closed-cell foam core sandwiches [14, 38-40]. The findings of these investigations have shown that shear force is carried mainly by the foam core of the sandwich, wherein the structure undergoes a compressive deformation between the two sandwich plates as the cells align in the shear direction. The failure of the foams was found to be similar to that of tensile failure and exhibits a similar stress-strain relationship. The work of Jarvis, *et al.* [41], which was commissioned by Rolls Royce to research the brazed bond of the Ni-Cr foam to a Titanium plate, is the only published work that has performed shearing on Ni foams. Whilst the report concluded that the foam failed before the braze bond it was beyond the scope of that investigation to analyse the foam failure.

The shear modulus of metal foam can be defined by Equation 2-3, which has been found to accurately model experimental data [42]. For isotropic foams the shear modulus is about 3/8 the value of the Young's Modulus and has a Poisson's ratio of 1/3.

$$\frac{G^*}{E_s} = C\left(\frac{\rho^*}{\rho_s}\right)^2 \quad \text{- Eqn 2-3.}$$

G* = Shear modulus of the foam
E_s = Young's modulus of the solid material
ρ* = Density of the foam
ρ_s = Density of the solid
C = Constant (3/8)

2.6.4 Machinability

Whilst literature of specific research into the machinability of open-cell Ni-Cr foam is not available, the machinability of foams in general is mentioned in the oft cited Metal Foam: A Design Guide [14]. Whilst it has been found that it is possible to machine metal foams using conventional techniques, such as a band saw, miller, etc. EDM or diamond sawing methods are preferred as cell damage and surface distortions are minimised.

The thin cell walls/struts offer little internal support against machining forces; forces which can cause cell wall/strut collapse and compromise the surface porosity through smearing. Figure 2-39 shows the smearing of an open-cell tantalum based foam caused by machining. Smearing is dependent on several key factors including material plasticity, pore size and machining parameters [43-45].

The work of Chen, *et al.* [46], found that tool geometry and cutting edge radius variation are the main machining factors influencing smearing and distortion of the foam. Machining with high cutting speed, low feed rates and low cut depth was found to result in the best surface finish.

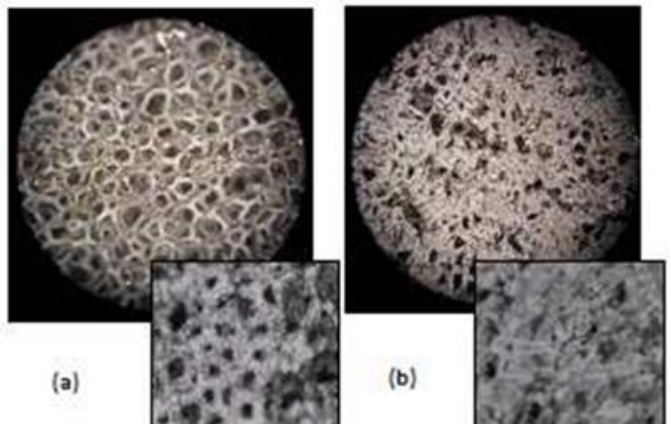


Figure 2-39. Images of tantalum based open-cell foams. Image (a) is of the foam prior to machining. Image (b) is an of the foam following machining, showing signs of smearing[44].

2.7 JOINING METALLIC FOAM

Metal foams are able to be joined, to other cellular materials or to solid material, by a variety of technologies, such as mechanical joining, adhesive bonding, brazing and welding.

A mechanical joint can be created by using fasteners, such as bolts that are placed between pre-drilled holes, or through the use of self-tapping screws. It is also possible to use built-in elements to join foam material. These are parts that are anchored within the foam during the production of the foam itself. These methods are usually used for closed-cell foams with surface 'skins', and with low porosity as self-tapping screws need material to bore into and built-in elements require the material to prevent shifting within the foam [14, 47-48].

Adhesive joints can be made using the same adhesives used to bond solid metals, and can create joints that are stronger than the foam itself. Adhesive joints have some disadvantages, such as low thermal stability, mismatch of expansion coefficients and the creation of a thermal and electrical isolation barrier [14, 47-48].

Brazing, welding and soldering have all been used to join metallic foams. One of the primary problems with brazing and soldering is that the fluxes used can lead to oxidation of the material if it penetrates the foam. Therefore, careful selection of material is required. Laser welding has been investigated as an option for

joining foam to solid material, with the main disadvantage currently being the high cost of machinery [14, 47-49].

2.7.1 Brazing Nickel-Chrome Material

Ni superalloys, such as Ni-Cr, are relatively difficult to weld due to their high susceptibility to micro-fissuring in the heat affected zone (HAZ) during welding and post-welding heat treatment. To overcome this, furnace vacuum brazing has become the main process for joining these materials, by the fusion of pre-located braze alloy between the two parts to be joined.

BNi-4 is a Ni-based filler braze material that is commonly used. It is available in forms such as powder and paste; however it is the tape form that Rolls Royce has used in their trials. It contains melting point depressants such as B and Si. The presence of B also decreases the liquid metal surface tension and, therefore, strongly increases wetting and flow as well.

B rapidly diffuses in the solid base material, which decreases the amount left in the joint which can form Cr borides in the joint eutectic. The B depletion assists joint isothermal solidification, as insufficient diffusion will result in persistence of the liquid phase along the joint region. However B is practically insoluble intergranularly in highly alloyed materials and segregates at the base material grain boundaries thus making them prone to brittle failure. It also depletes the base material grain boundary interface zones in Cr and concentrates Cr in Cr_xB_y which reduces the corrosion

and oxidation resistance. The microstructure created by the brazing of two Ni-alloy plates (composition Ni13.5Cr-9.5Co-4.75Ti-3.3Al-3.8W-1.53Mo-2.7Ta-0.23Fe-0.09C-0.01B) with a BNi-4 tape is shown in Figure 2-40. The image shows that the boron has diffused out of the isothermal solidification zone (ISZ) and has formed borides with the Ni and Cr. These problems can be corrected via careful selection and optimization of the heat treatment process during the joining process [50-53].

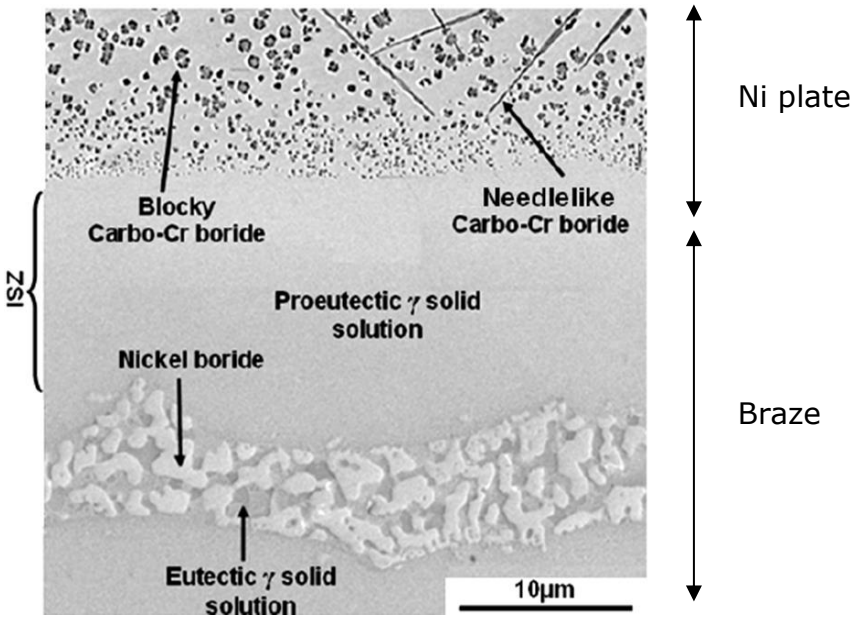


Figure 2-40. SEM image of a Ni brazed bond microstructure, with the borides diffused out of the Isothermal Solidified Zone (ISZ) [52].

2.7.2 Brazing Open-Cell Nickel-Chrome Foam

There is very little published work currently available on brazing open-cell Ni-Cr foams. The work published by Jarvis, *et al.* [41], which was commissioned by Rolls Royce, investigated the shear behaviour of the Ni-Cr foam which had been brazed to a Ti backing plate. The report concluded that the foam failed, and not the braze.

However, it did not analyse the base/braze/foam interface. That report was based on previous work performed by Rolls Royce (but not published) that ran trials on the feasibility and manufacturing process required to braze open-cell Ni-Cr foams to a Ni backing plate [54]. A BNi-4 brazing tape was used and shown, in cross-section, that a bond was made. No further microstructural characterisation was undertaken, however a mention was made of several sample sites where the struts has caused wicking of the braze material. This is similar to what was reported by the only other similar published work, which investigated the brazing of a Ni honeycomb structure [55]. The investigation also found that similar problems to solid-solid brazing could be experienced with intermetallic compound formation in the braze layer if heat treatments weren't chosen correctly.

In order to assess the braze quality quantitatively; Rolls Royce has been developing an experimental non-destructive evaluation (NDE) technique with ultrasound [56]. Figure 2-41 illustrates the NDE experimental set-up. It works by the pulser-reciever generating ultrasound waves in the metal substrate. The received signal is then amplified and sent to the oscilloscope which captures the data. Figure 2-42 (a) shows a plot of the data received for 4 trial samples, 3 with varying quality bonds and a metal plate with no foam attached to act as a broken bond test sample. Single wave forms were captured at 20 random positions on each sample to obtain an average result. The signals then undergo a Fourier Transform and are re-plotted (Figure 2-42 (b)). When viewed as a frequency

response plot, relative peak magnitudes represent a quantitative measure of bond line integrity. By deciding on a pass-fail gate position (an arbitrary position is shown for illustrative purposes), the quality of the brazed foam tiles can be assessed.

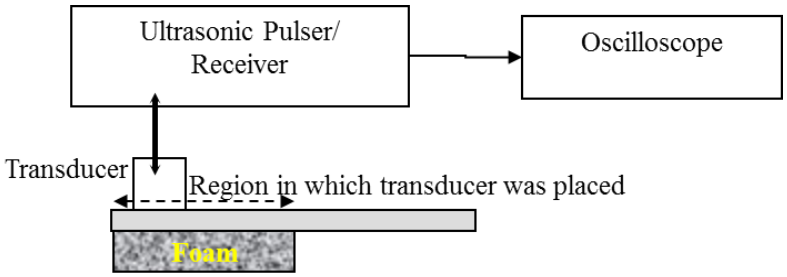


Figure 2-41. Experimental set-up of the Ultrasound NDE equipment [56].

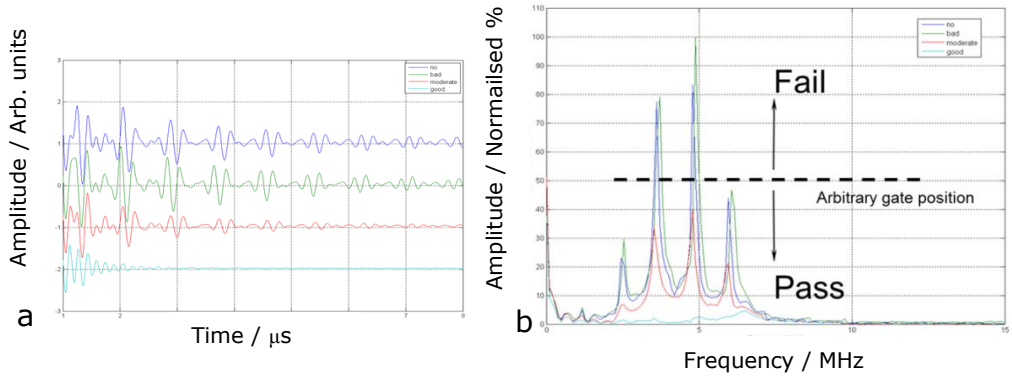


Figure 2-42. The amplitude vs. time plot for averaged sample results is shown in image (a). The plots following Fourier transformation which can be used assess the quality of the braze is shown in image (b) [56].

Rolls Royce have also used the same NDE equipment to analyse flaws and defects within the braze bond. By using the C-scan presentation capability of the equipment, it is possible for the intensities of the received signal to be mapped on a plan view of the sample, images produced this way allow for qualitative analysis of

the braze [57]. Figure 2-43 shows an example of a C-scan image created by Rolls Royce of one of their engine tiles, a brazed foam on a Ni plate and including the 6 inserted connection pins. The grey around the edges of the image is the background, the dark blue areas are from high intensity signal and correspond to areas of good contact, lighter blue areas correspond to a weaker signal/ weaker contact, and the green areas represent the weakest signal/ weaker contact areas. It can be seen how on the right hand side even though there is no plate or braze, the foam struts are visible and are returning a strong signal indicating good contact. Obviously this isn't a good contact area, and shows that high intensity signals aren't necessarily indicative of a good bond and contact between the foam and the Ni plate.

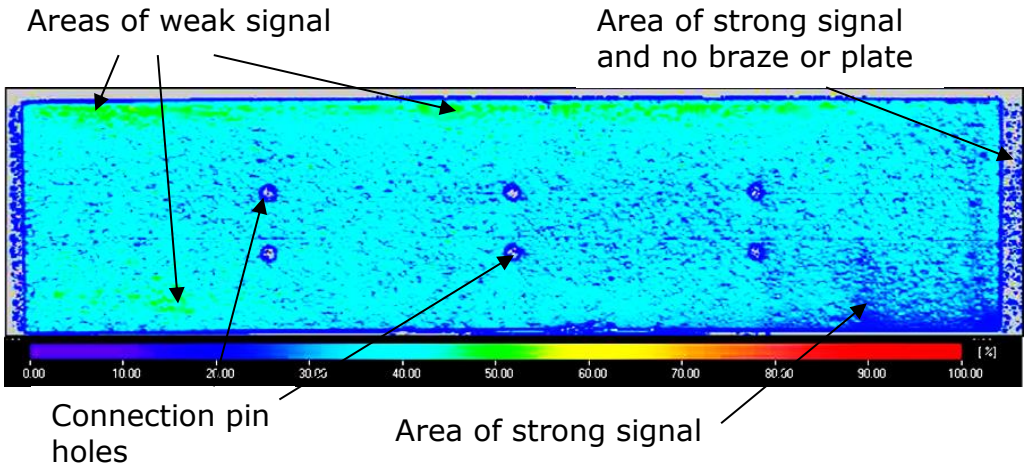


Figure 2-43. Signal intensity map of brazed foam[57].

3 EXPERIMENTAL PROCEDURES

3.1 SAMPLE MATERIAL

3.1.1 As Supplied Non-Brazed Foam

In order to investigate the variation in properties across a sheet, the as-supplied material was broken down into a grid of samples, which are coded (Figure 3-1). The 1723 sheet was 600 x 900mm, and was supplied to the author as it had been to Rolls Royce. Due to the limited amount of 1116 grade available, Rolls Royce was only able to supply a cut strip of material, 45 x 720mm. The samples taken from these were of 20 x 20mm dimensions (cut using a band-saw unless otherwise stated), and were grouped in threes (four for 1116). These groups were assumed to be of similar enough composition that any variation was negligible. This then allowed for group areas to be investigated by both non-destructive (microscopy and analysis) and destructive methods (mechanical and corrosion testing). Further to this a localised area of samples were also tested to compare their variation in properties against that of the whole sheet.

In order to measure the variation in properties due to anisotropy, different orientations of the 1116 material were also investigated. Figure 3-2 illustrates the notations used to describe the directionality of the foams. The Short-Traverse (ST) is the direction through the thickness of the material. The Longitudinal Traverse (LT), sometimes referred to in literature as the rolling direction, is

the direction the polyurethane foam was rolled along during formation. Longitudinal-Length (LL) is the third direction and displays isotropic qualities with the LT, unlike the anisotropy between ST and LT.

The following sections describe the experimental procedures and equipment used for the investigation of the Ni-Cr foams, in the brazed and non-brazed condition.

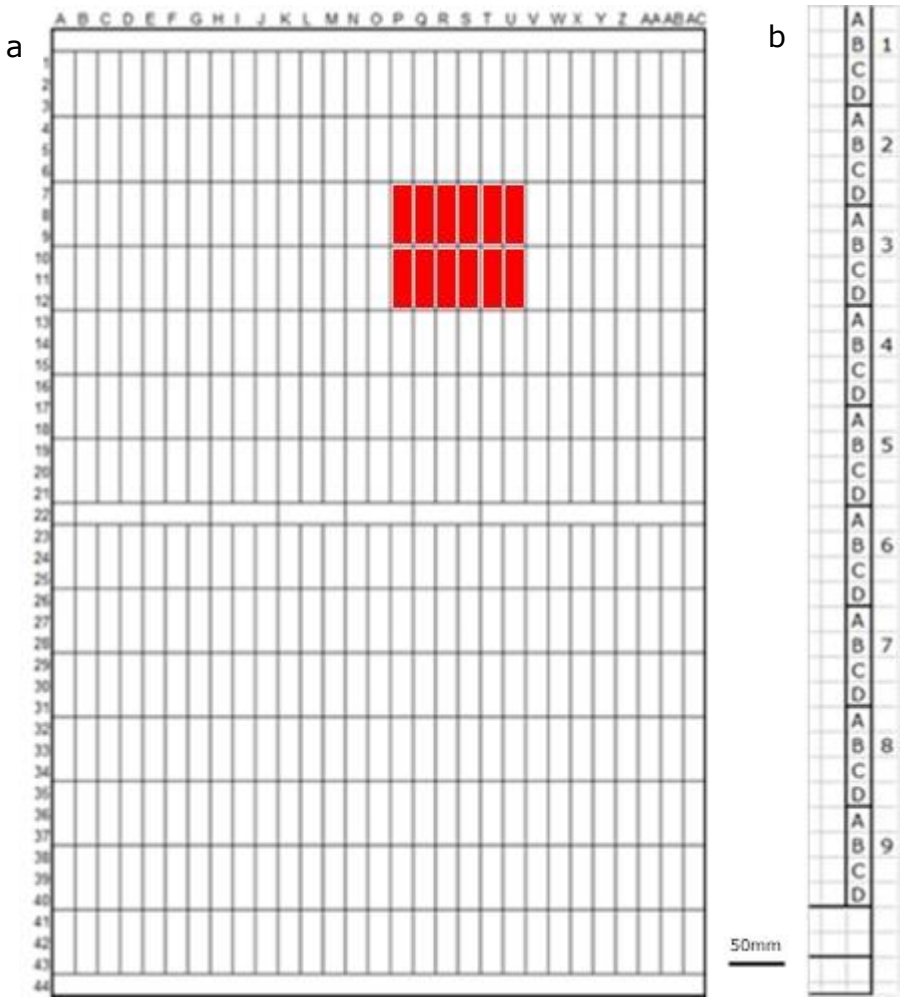


Figure 3-1. Grid layouts for the 1723 (left) and 1116 (right) supplied material. The red highlights the area of samples used for localised testing.

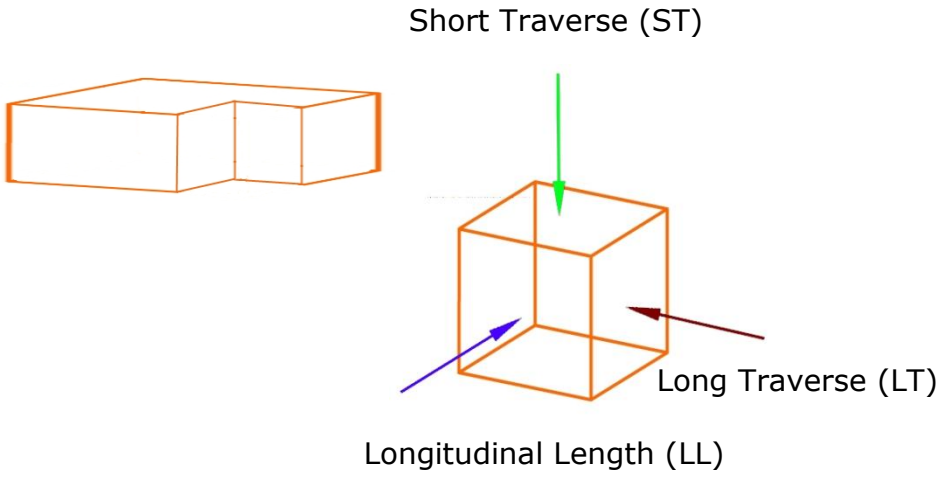


Figure 3-2. Illustration indicating the notation used for the orientation of the foam samples.

3.1.2 Brazed Foam

Brazed material used for analysis was supplied, as described in the relevant sections, by Rolls Royce. The braze used was MSRR9500/700 tape which has a composition Ni-2.9B-4.5Si and a has a thickness of 102μm. The Ni plate that the foam was brazed to was 2mm MSRR7036 (C263), which has a nominal composition of Ni(bal)-20Cr-20Co-5.8Mo-2.1Ti-0.7(max)Fe-0.6(max). The method used by them to manufacture the samples was the same as that which had been used to manufacture the engine tiles for trials.

The faces of the foam sections were ground wet on a polishing wheel using P500 grade SiC paper (~30.2μm grit diameter), and the plates were grit blasted with Al_2O_3 grade P1200 (~2.5-3.5μm), which created a flat clean faying surface for brazing. They were then washed in de-ionised water and then rinsed in methanol and allowed to air dry.

The braze tape was cut to give a 3mm overlap on all four sides of the blocks (Figure 3-3 (a)). The tape was supplied with a release film on both sides and hence was not given additional cleaning. The tape was self-adhesive on one side.

Two layers of braze tape were pre placed onto the plates and the foam sections mounted, ground face down, onto the braze tape. To maintain a close contact between the blocks and the plates they were weighted down. The weight was such that the foam blocks were loaded at approximately 25g/cm^2. Ceramic tiles were used to prevent contact between the foam and the metal weights used. The samples were then placed in a basket to be interned in the furnace (Figure 3-3 (b-d)).

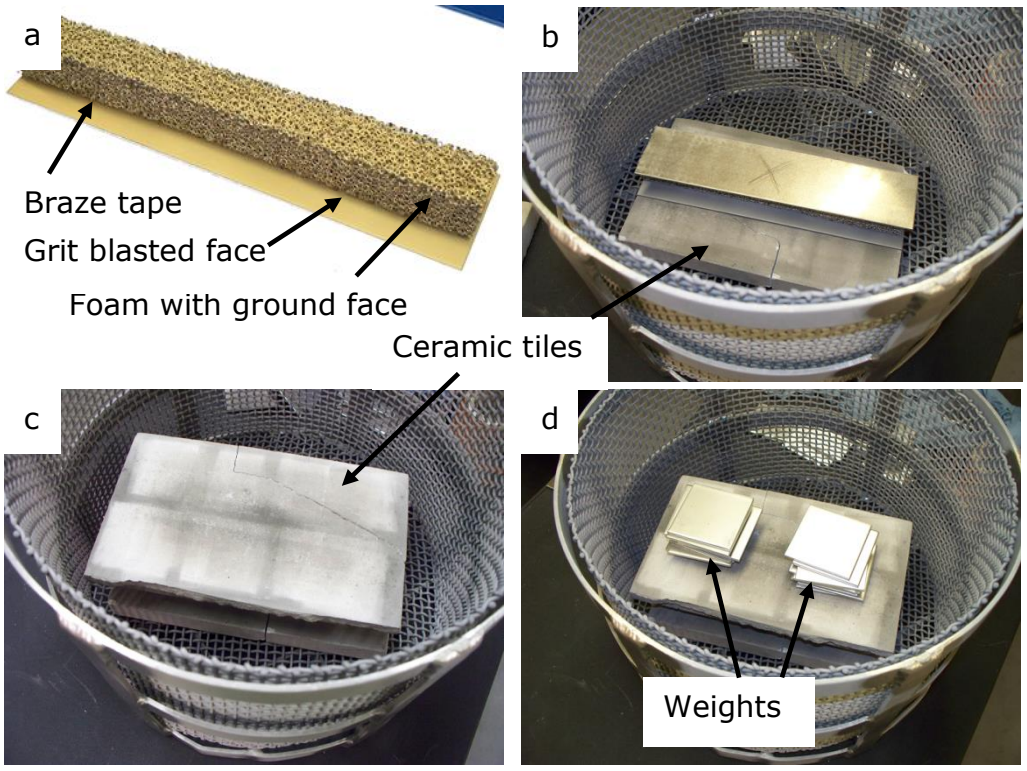


Figure 3-3. Images of the brazing method. The foam, with a ground face, is placed on the braze tape upon the grit blasted surface of the plate (a). The material is the placed in a furnace basket, between two ceramic tiles (b-c). Weights are placed on top of the ceramic tiles (d).

All the tape specimens were brazed in a single furnace run at 1125°C for 5 minutes. The heating rate was approximately 10°C per minute. The specimens were vacuum cooled to 900°C and gas fan quenched to room temperature.

The size relationship between the depths of the troughs in the polished and grit blasted surfaces compared to the thickness of the braze tape allowed for complete filling of the voids, at maximum penetration of the strut through the braze and onto the plate (Figure 3-4). The excess material, which is greater than twice thickness of the troughs, allows for the braze tape to fill the troughs in both the plate and foam strut even if they are not touching, and with small variations in distances between them if the plate and foam aren't level, such as curvature of the plate.

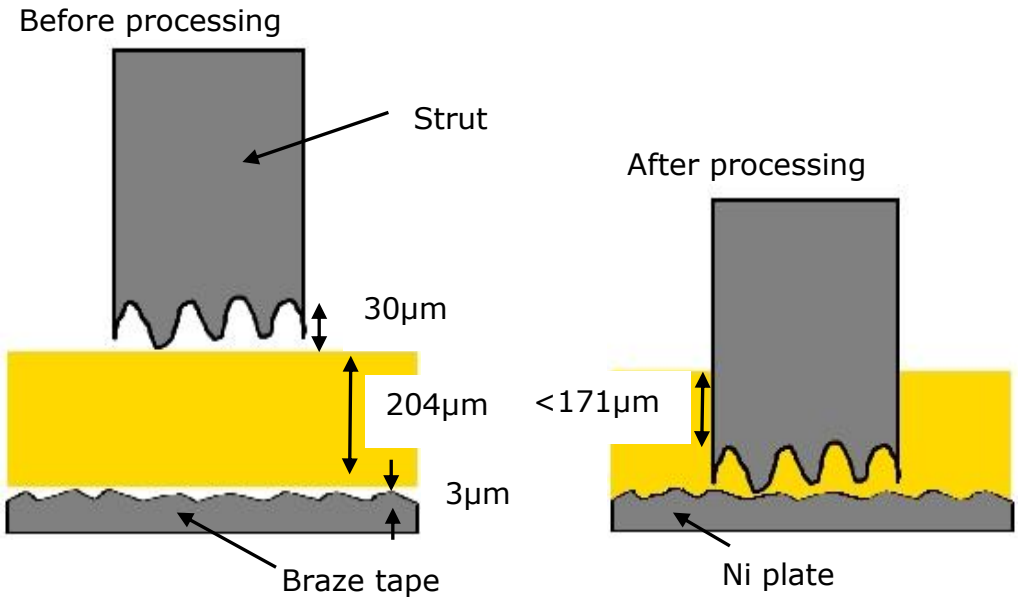


Figure 3-4. Illustration of how the braze material fills the troughs created by the polishing and grit blasting of the Ni-Cr foam and the Ni plate.

The positions from where the sections of foam used had come from, with regards to the as supplied sheets, were unknown, and samples were only supplied for the 1116 grade foam material. Brazed material was sectioned using EDM, to prevent deformation caused by impact of cutting blades on the overhanging backing plate sections.

3.2 MICROSCOPY

Analysis using several microscopy techniques was used to investigate the material and structures both before and after mechanical and corrosion testing. Locations of sites imaged are described using the notation that can be seen within Figure 3-5 as reference.

Etched samples required an initial embedding of the foam within a two-part epoxy resin. Following curing, the samples were then polished to 1μm, using grinding and polishing wheels. The samples were then etched by an electro etch method in a solution of 4 parts H_3PO_4 and 3 parts distilled water, at 4 volts.

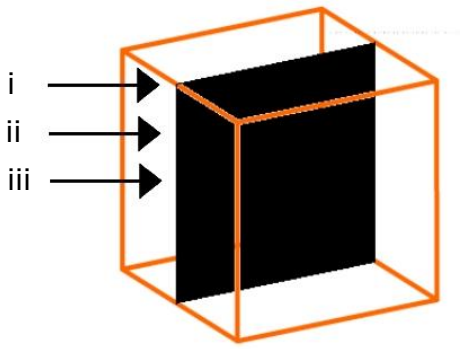


Figure 3-5. Illustration of location diagrams used for images of samples. The black square indicates the plane of the image. Arrows indicate whether image is from: (i) near the surface, (ii) below the surface, or (iii) the mid-section.

3.2.1 Optical Microscopy

Visual analysis was performed to identify irregularities in the samples that can be seen by eye, as well observing how the

samples deform during mechanical testing. Observations of etched samples were performed in order to analyse the grain structure of the struts, as well as the braze bond layer. Analysis was predominantly qualitative with images being captured using a 12 mega pixel (MP) Kodak EasyShare Z1285 camera and a Nikon Optiphot optical microscope.

3.2.2 Scanning Electron Microscopy (SEM)

Analysis of the strut structures and the materials and topology was performed using scanning electron microscopy (SEM). SEM allows visual analysis of the samples at high resolutions (~>5nm for secondary electron image analysis and ~>100nm for backscattered images), at high magnifications (< 350,000 x magnification) and with larger depth of fields than optical microscopy. The SEM creates images by firing a beam of electrons and rastering it across the sample, releasing electrons from it. These electrons are then detected and the energies analysed which can be displayed as an image on a monitor. Two types of electrons can be detected, secondary and backscattered. Secondary electrons originate from in elastic collisions between the high-energy beam electrons and the sample electrons near the surface and produce high-resolution topographical images. A JEOL 2000 FX SEM instrument was used and prior to testing the samples were cleaned by using a gas canister to blow dirt from the surface, followed by being washed with acetone.

3.2.3 X-Ray Micro-Tomography (μCT)

X-ray Micro-Tomography (μCT) creates 2D slice images throughout the thickness of the sample, which can then be analysed with computer software and a 3D model created. An X-ray beam being focused onto the sample, which is rotated through 360°, creates X-ray 'shadows' which are detected by a highly sensitive camera. The detector creates images at each rotation position, that are subsequently analysed and displayed as the slice images. This allows for analysis of slices taken through a sample without destroying it.

Much work has been done into using microCT models to analyse foams and derive the 3D pore dimensions. They have been more focused on increasing the accuracy with which to determine pore volume and dimensions, by creating more complex shapes to model the pores mathematically. [48, 59-61]. For the purposes of this study these methods were determined to be overly complex and time-consuming, when all that is needed is a comparison between the cell sizes from one area of the foam sheets and another. For this reason only a few 3D models were created to analyse qualitatively whether irregular pore shapes are formed from the cutting process or are inherent throughout the foam. Further to this, 2D slices were taken throughout the thicknesses of several samples to compare the average pore sizes between samples and through the thickness.

In order to determine the average pore size from the 2D slice images obtained. Line intercept methods, used for determining grain

sizes and adhering to ASTM standards, were used [62]. Lines are superimposed over the image and the number of pores counted. Lines were required to be of long enough length in order to yield 50 intercepts. Equation 3-1 is used to estimate the average pore size. Both linear and circular intercept methods were used, and consisted of more than one line, in order to compensate for irregular shapes and orientation of the pores. As the pore cell boundaries are not clearly defined, for estimation purposes the pores are considered to be circular.

$$Average\ pore\ diamter\ = \frac{Intercept\ line\ length}{Number\ of\ pore\ intercepts} \quad \text{- Eqn 3-1}$$

The machine used was a Scanco Medical μCT 40. The resolution of the machine is related linearly to the size of the sample. In order for enough pores to be analysed, the samples need to be 20x20 mm which is at the higher end of the sample sizes that can imaged, and therefore has a resolution of 20μm (the thinnest strut walls are ~50 μm).

3.2.4 Ultrasonic Inspection Of Braze

Qualitative analysis of the braze bond was performed using the NDE ultrasonic method developed by Rolls Royce. Pulse-echo instruments create a burst/ pulse of sound when a transducer is struck with an electric pulse. The sound wave propagates through the transducer and into the material being tested. The sound pulse continues until

it encounters a sudden increase in acoustical impedance, such as when it reaches an air interface (an area of no bond). The air acts as a transmission barrier, causing the sound pulse to echo or return. C-Scan profile maps are then made from the amplitude of the return sound and the position from where it is received [57].

C-Scan profile maps were created with a 0.5-1mm pitch, depending on the size of the sample, from a signal of 7dB and 10MHz. Scans were performed prior to testing the brazed samples, and allowed areas of good and bad brazing to be pinpointed.

3.3 DENSITY

Two methods were used to calculate the density of the foams. To calculate the relative density of the foams the density of solid Ni-Cr is required. The assumptions are therefore made that solid material density for the 1116 composition is 8.4g/cm^3 (based on a 80:20 Ni-Cr alloy), and the 1723 composition is 8.2 g/cm^3 (based on a 70:30 Ni-Cr alloy) [63]. These values are based on solid material that has had complete dissolution of the Cr content that, something that the foam samples will likely not have, therefore some error in the calculated relative density is to be expected.

3.3.1 Bulk Density

The bulk density can be calculated using Equation 3-2. The volume is calculated from the dimensions of the sample measured with a

micrometer and the mass is measured using a digital set of scales (accurate to 2 decimal places). This method allows for estimation of the density of the foam samples relatively quickly, and also allows large samples to be analysed.

$$\rho = \frac{mass}{volume} \quad \text{- Eqn 3-2.}$$

Sectioned samples had their density calculated by this method, as well as several large pieces taken from the sheet. This allowed for a large average measurement to be made.

3.3.2 Pycnometry

Pycnometry allows for a more accurate measurement of the volume and therefore density. The pycnometer can only measure samples less than 10mm in diameter and is a much more time consuming process than the one previously described. This method was therefore only used in order to compare with the estimation of the simple bulk density analysis.

The pycnometry measuring process is based on Boyle's law that for a given mass at constant temperature, the pressure of the gas times its volume is constant. The sample is placed in a calibrated chamber of known volume and helium gas is forced into it. The volume of the gas is equal to the difference between the volume of the cell and the volume of the specimen, with the helium filling the space between the pores. By inputting the mass of the sample during the set-up of

each test, the volume of the specimen can be calculated and the actual density of the material of the skeletal foam structure determined. However this method cannot compensate for any trapped porosity within the struts. The pycnometer used was a Micrometrics AccuPyc-1330.

3.4 MECHANICAL TESTING

Mechanical tests were performed to determine compressive, tensile and shear strengths of the foams. Compression and tensile tests were performed in both the ST and LL directions for the 1116 foam, and just the ST direction for the 1723 foam. As has been previously stated the samples were cut using a band saw. The cutting process usually leaves burred edges and so samples were filed before testing in order to make them as level as possible prior to being loaded.

1116 Foams brazed to 2mm Ni plates were run in identical compression and tensile tests (although only in the ST orientation) to the non-brazed foam samples. Along with the shear test samples they were sectioned using EDM.

Sample dimensions were measured using a micrometer. In order to estimate the relative yield strengths of the samples the following solid material yield strengths were assumed; 280 MPa for the 1116 composition and 565MPa for the 1723 composition. The Young's Modulus was assumed to be 221GPa and 212GPa, for the 1116 and 1723 compositions respectively [63]. Like the density, these values are based on samples that have complete dissolution of the Cr

content, therefore errors in the calculated relative yield are to be expected.

3.4.1 Compression Testing

The compression test method adheres to the guidelines laid out by the Japanese Standards Association (there are currently no BS or ASTM standards for compression testing of porous materials) [64]. The standard states that, "The length of the shorter side in the cross section normal to the compressive direction shall be no less than either 7 times the average pore size (d_{ave}). The height of the test specimen shall be within 1 to 2 times the shorter side of the cross section" (Figure 3-6).

With a pore size of 1.4mm in the 1116 foam, the minimum cross-section a sample could have is ~10mm. It was determined that 20mm would be more suitable dimensions for the samples, as this way when loaded in either the ST and LT directions they would be similar. A 1723 foam sample could have a cross-section as small as ~7mm, but 20mm was decided upon. This size was as it would allow samples to be cut more easily and safely. It would also allow for a more direct comparison with the 1116 foam in the ST direction when tensile tested as there would be a similar adhesive plate surface.

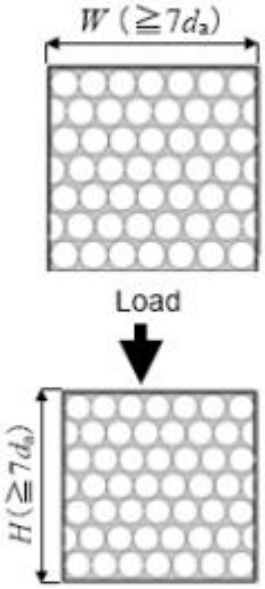


Figure 3-6. Illustration of how the sample size was determined for compression testing[64].

$$V = \mathrm{A.H} \qquad \text{- Eqn 3-3.}$$

V = test speed (mm/min)
H = test specimen height (mm)
A = 0.1 min^{-1}

The compression testing speeds were determined by the use of Equation 3-3. The 1116 samples were compressed at a speed of 2mm/min in both ST and LT directions, whilst the 1723 were compressed at a speed of 1mm/min. All samples were tested and data recorded until 80% compressive strain was reached, as this included all the data that was of interest. Four sets of data were extracted from the test, the zero deformation point (point adjusted to correct for the initial plateau region caused by unevenness of samples and defined by the method illustrated in Figure 3-7), the proof-stress (defined as 0.2% compressive strain), the stress

corresponding to 25% plastic strain within the plastic collapse region, and the densification stress. As the specific densification stress is likely to be hard to define, instead a 60% strain (which is a typical value for densification) was defined to allow comparison. All stress calculations used the original cross sectional area measured. The results allow the determining of the mean average, standard deviation and variable coefficient as per the guidance of the testing standard.

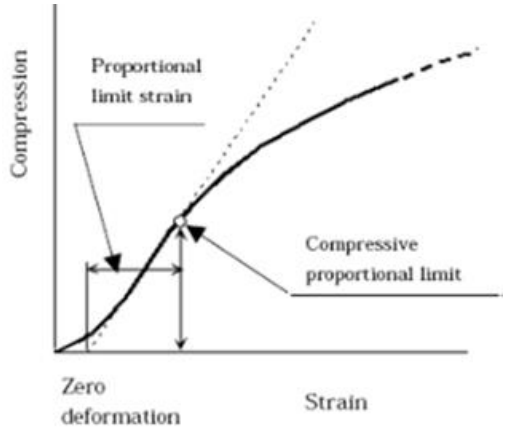


Figure 3-7. Illustration of the method for determining the zero deformation point[64].

Testing of the compressive properties of the brazed foam was performed using identical parameters as the non-brazed material. Figure 3-8 illustrates the brazed foam samples tested, which consisted of plates brazed to two sides of the foam. This enabled twice the area of observable braze to be investigated per test.

The compression tests were carried out on an Instron Compression Testing Machine, with data compiled by Blue Hill/Instron software.

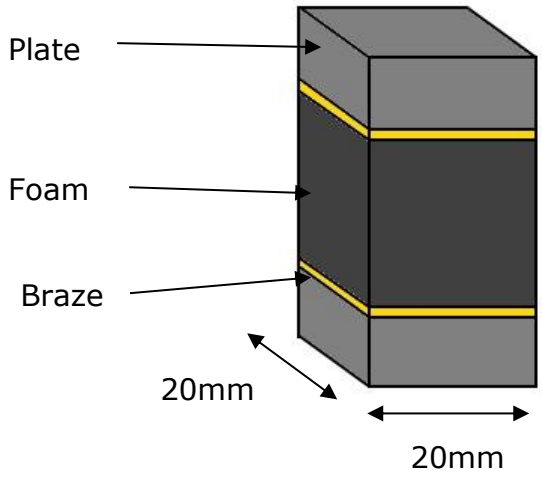


Figure 3-8. Illustration of the samples used for compression testing of the brazed foam.

3.4.2 Tensile Testing

There are currently no standards for tensile testing of foams, although Ashby, *et al.* [14], recommend sample sizes of no less than 7 times the cell size (similar to the Japanese Standards). As such sample sizes and testing speeds were taken from the compression testing standards. Normally tensile testing of materials requires a 'Dog Bone' shaped sample, but due to the geometry size limit in the ST direction, this was not possible. Therefore cube samples identical to the compression testing samples were used and were glued to tabs that facilitated convenient gripping.

Preliminary trials were performed using various adhesives to determine which adhesive was to be used, as it had been found that some high tensile rated adhesives failed at lower stresses than the foam, through strut pull-out from within the adhesive layer and peeling. A two-part Araldite 2011 epoxy, cured at 40°C for 16 hours,

was found to be of sufficient strength and foam samples were bonded, as illustrated in Figure 3-9, to two Al T-shape tabs.

The tabs were grit blasted prior to application of the adhesive, to increase the surface area and improve the quality of the bond, followed by cleaning of the surface with degreaser. The adhesive was applied in a thin layer of less than 1mm thickness, to allow sufficient contact to be made around the base of the foam struts.

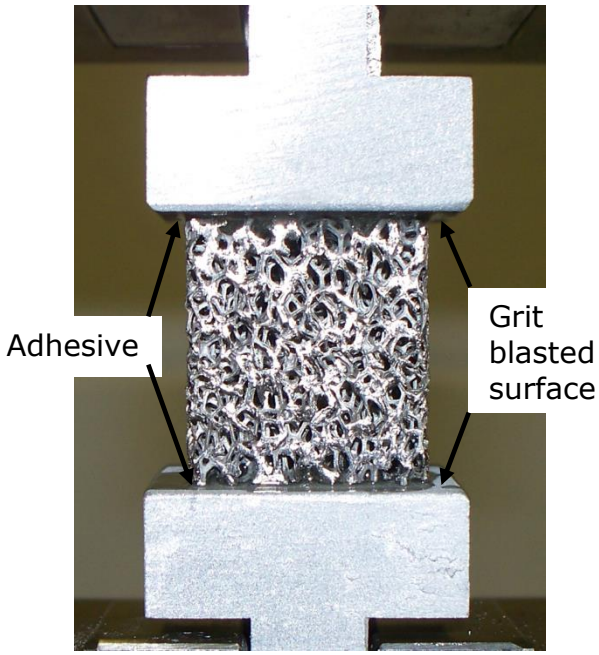


Figure 3-9. Image showing a sample prepared for tensile testing.

Two sets of data were extracted from the tests, the proof-stress (defined as 0.2% tensile strain) and the ultimate tensile stress (UTS). All stress calculations used the original cross sectional area, the respective results used to determine the mean average, standard deviation and variable coefficient.

Tensile tests of the brazed foam material required a different set-up, in order to avoid any errors that could be caused by bonding the base of the Ni plate to the tabs. Figure 3-10 illustrates the design of the sample cross-sectional geometry. This design was created to allow for the clamping of the Ni plate without affecting the braze bond. Two sections of material were manufactured this way, both with a length of 200mm, from which samples were sectioned using EDM.

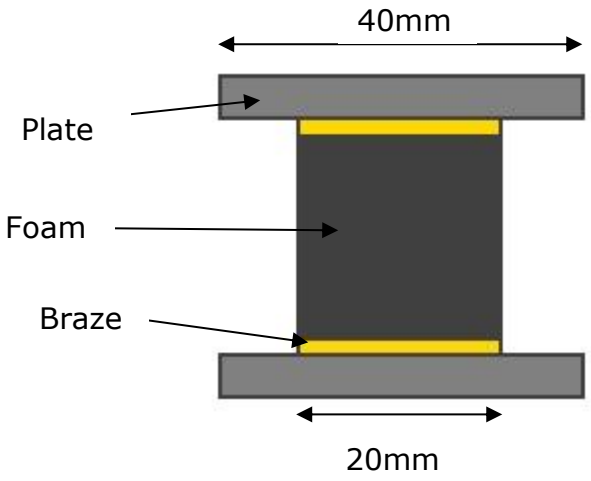


Figure 3-10. Illustration of the brazed material cross-sectional geometry, for tensile testing.

Figure 3-11 shows an image of the specially designed rig, and illustrates how the samples are clamped for testing (Appendix 1 contains the full design specifications). The adjustable clamps allowed for any non-parallel plate samples to be clamped, and orientated (as best possible) in the tensile direction. The testing parameters for the brazed material were the same as those for the non-brazed material.

The tensile tests were carried out on an Instron Tensile Testing Machine, with data compiled by Blue Hill/Instron software.

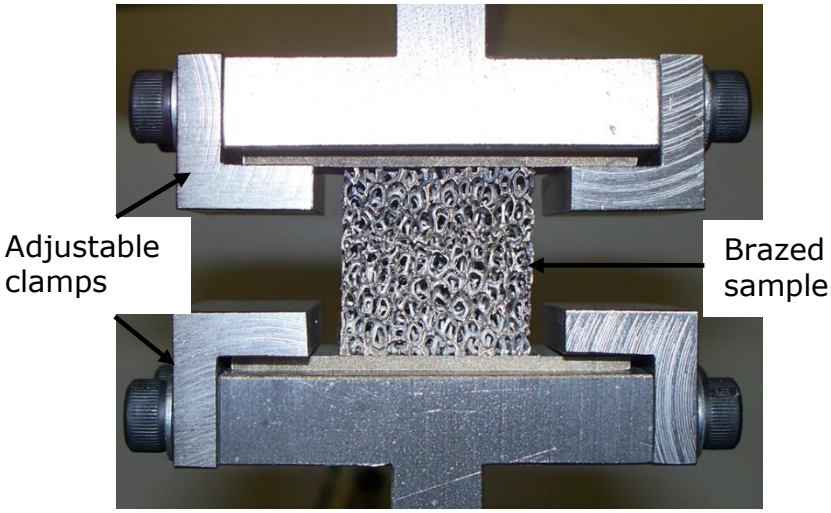


Figure 3-11. Image of a brazed tensile sample clamped to the tensile testing rig. The rig is designed with adjustable clamps to help with imperfectly manufactured samples.

3.4.3 Shear Testing

Unlike for tensile and compression testing there is a standard for shear of sandwich structures, which includes foams (ASTM C273). Jarvis, *et al.* [41], used this method to test Ni-Cr foams brazed to Ti plates, however that tested the shear behaviour of the bulk of the foam rather than the foam-braze interface.

Figure 3-12 illustrates the shear test sample dimensions. From the sections of brazed material manufactured by Rolls Royce, samples 25 x 25 x 10mm were EDM cut. This meant that the sample size was above the recommended minimum geometry limit for shear testing, of 3 times the average pore diameter. Figure 3-13 illustrates the rig used for shear testing. It is designed to constrain the joint

loading to one degree of freedom during testing, in order to obtain a pure shear load on the braze-foam join. A clear wall, made from polycarbonate, was manufactured for the rig to allow observation of the shear deformation process during testing.

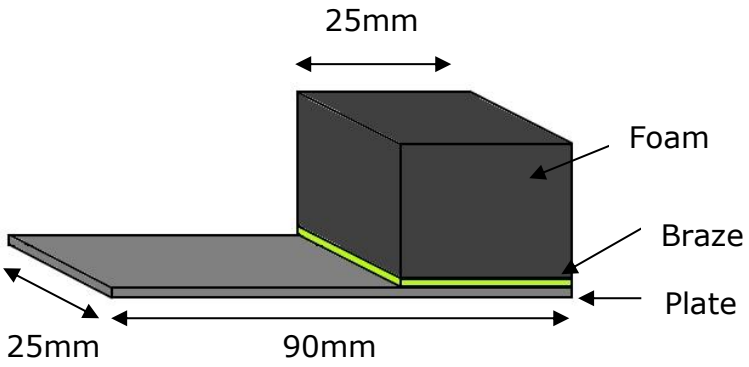


Figure 3-12. Shear testing sample dimensions.

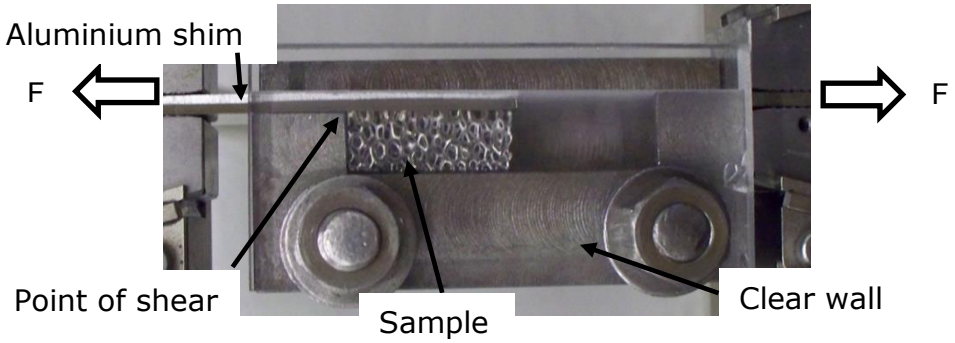


Figure 3-13. Image of the shear testing rig showing the direction of force, and the point of shear.

Figure 3-14(a) illustrates how the samples are sheared, with the point of shear along the braze bond plane. As the distance the incursion plane has travelled is known it is possible to calculate the reducing bond area, and therefore the shear stress throughout the testing. Figure 3-14 (b) illustrates the terminology used in this

calculation. As the incursion plane moves through the sample, the incursion length (L_i) is subtracted from the original length (L_1) and then multiplied by the second base length (L_2). This method assumes that the area in front of the incursion plane is bonded and that load is distributed evenly across it. The stress-incursion plots calculated using this method can be seen on the next page.

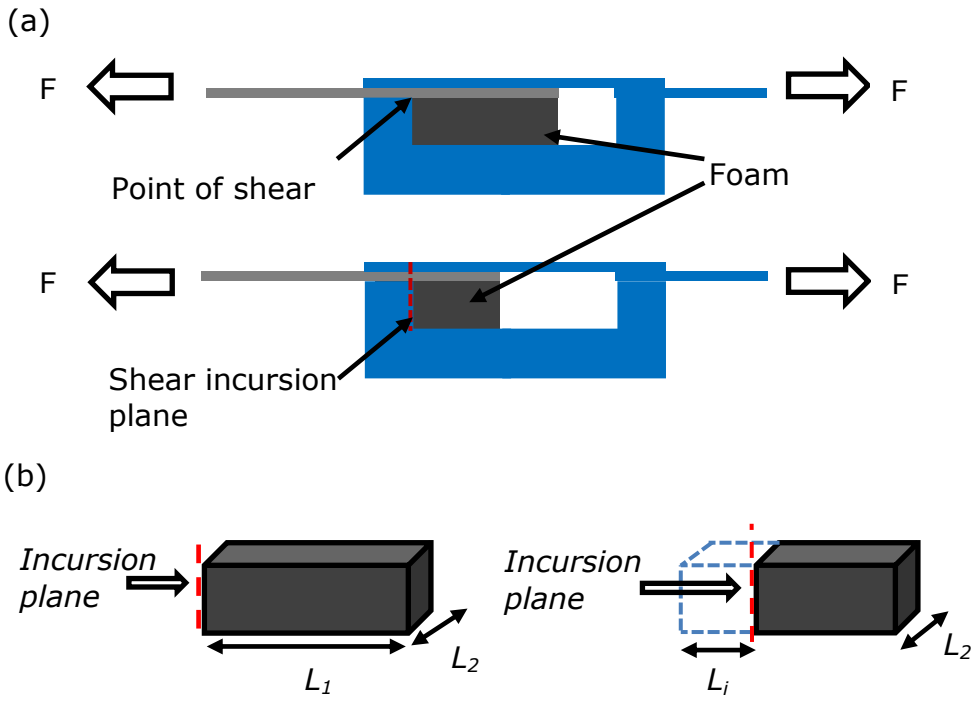


Figure 3-14. Illustrates how the shear rig works and the terminology used (a), and sample lengths used to calculate the reducing area (b).

As the Ni backing plate thickness was smaller than that for which the rig was designed, an Al plate was used to as a shim to fill the remaining thickness.

Similar to tensile testing, the parameters were matched with the compression testing speeds at 2mm/min.

3.4.4 Machinability Testing

In order to analyse the machinability of the foam, a simple machining operation was designed to create similar channel cuts to those made by Rolls Royce, which would allow for basic analysis and comparison between the varying machining parameters.

A milling machine was used at both high and low tool speeds, 200RPM and 80RPM respectively. At the two speeds channels were cut at both high and low depth in to the sample material, illustrated in Figure 3-15. The feed rate was kept constant for all cuts made to allow for comparison. Only 1116 foam material was machined as this was what the engine tiles were made from.

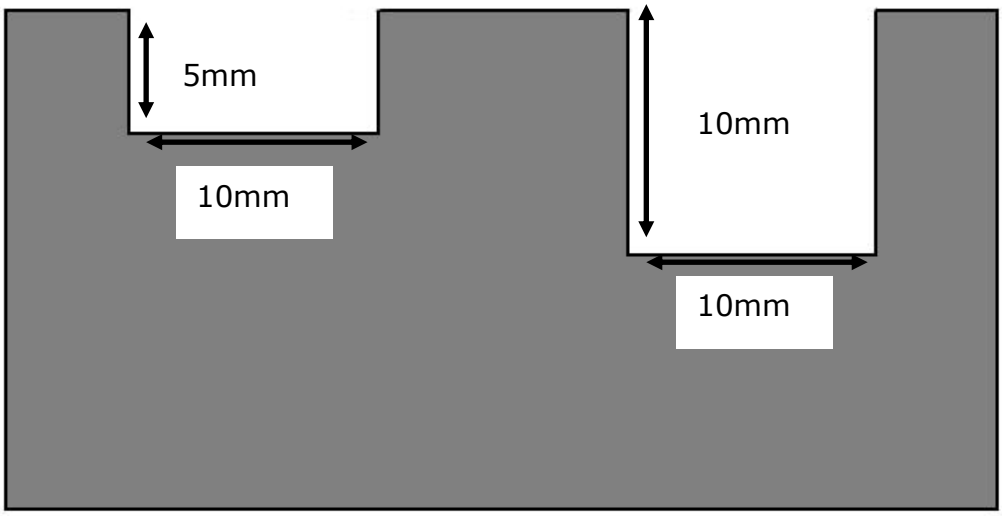


Figure 3-15. Illustration of the channel cuts milled for machinability analysis.

3.5 CHEMICAL ANALYSIS

Two chemical analysis techniques were employed to investigate the variation in chromium content both across the sheet and through the thickness of the material. A semi quantitative/qualitative approach was taken to the investigation as neither method can quantify to a high degree of accuracy automatically.

3.5.1 Energy Dispersive X-Ray Spectroscopy (EDX) Analysis

Energy dispersive X-ray spectroscopy (EDX) was performed on several samples during their investigation using the SEM. Analysis was performed on selected locations across the sample surface, as well as the surface of a cross-section, to investigate how the Cr content varied throughout the foam. Element mapping was also undertaken in order to image the varying chromium content. EDX works by detecting the characteristic X-rays produced by interactions between the electron beam and the sample atoms. The detector feeds this information into a multi-channel analyser. The intensity-energy spectra can be used to determine the elements by comparing the peaks against those of known samples. The resolution of the analysis is can be in the nm scale, but is dependent up on the beam spot size used (~1μm effective spot size as used). The analysis can be time consuming (even when using the automated quantification software) and so not all samples were analysed by this method. Errors in quantification by this method can be up to 25%.

3.5.2 Spark Atomic Emission Spectroscopy (AES)

Spark atomic emission spectroscopy (AES) has several advantages over other chemical analysis methods. It requires little or no preparation of the samples and is fast, with results obtained within a minute. For this reason it is ideal for the analysis of multiple samples. AES works by placing a metallic sample on a spark stand where it is flooded with Ar and a rapid series of high current sparks is produced. The spark heats the sample to a high temperature to excite the atoms within it. The excited atoms emit light at characteristic wavelengths that can be dispersed with a monochromator and detected. The spectra produced is then analysed and compared against recorded spectra of known elements in order to identify the alloy composition [66-67].

Due to the Ar gas being required for analysis, porous samples must be compressed in order to prevent Ar passage through the open framework. Therefore, samples that had been used in compression tests were used, with some further consolidation performed by rolling the samples. The samples were repeatedly folded and rolled until a thickness of ~1mm was achieved. Three points for analysis were used, spread over the surface of the sample to avoid the burn radius (<8mm) of the other point locations. In some locations adequate Ar shielding could not be reached and so the nearest position that allowed a reading to be taken was used.

3.6 CORROSION ANALYSIS

Analysis of the corrosion resistance of the foams was performed using the accelerated corrosion test of salt spray fog. Given that artificial corrosion tests of samples never give results that correlate with the performance in the application environment (due to varying conditions encountered effecting the chemistry of reactions), and that Choe, *et al.* [4], have already reported that oxidation behaviour of Ni-Cr foams is similar to Ni-Cr solids, it was decided that a simple qualitative analysis be performed to investigate whether there are large variations in corrosion resistance across the sheet [68].

The test was performed to BS EN ISO 9227:2006 standards by placing the samples, both brazed and non-brazed, in a spray cabinet at an angle of 15-30°. A fog environment was then produced by air atomisation of a 5wt.% sodium chloride solution, and the cabinet was maintained at a constant temperature of 35°C. The samples were then removed every 100 hours and visually analysed. Prior to testing the samples, they were cleaned by using a gas canister to blow dirt from the surface, followed by being washed with acetone and dried.

4 ANALYSIS OF AS SUPPLIED NON-BRAZED FOAM

The aims of the research in this chapter were; to analyse the mechanical properties of the metallic foam and the relationship of these properties to the sheets anisotropic nature. Analyse the machinability of the metal foam, and the optimum machining parameters.

4.1 SHEET PROPERTIES AND MACROSTRUCTURE ANALYSIS OF AS SUPPLIED FOAM

4.1.1 Optical and Scanning Electron Microscopy (SEM) Analysis

As has been previously stated, two foam sheets were studied. Figure 4-1(a) shows an image of the 1116 material, and (b) shows the 1723 material. The 1116 material is supplied in a thickness of 20mm and the 1723 in 10mm.

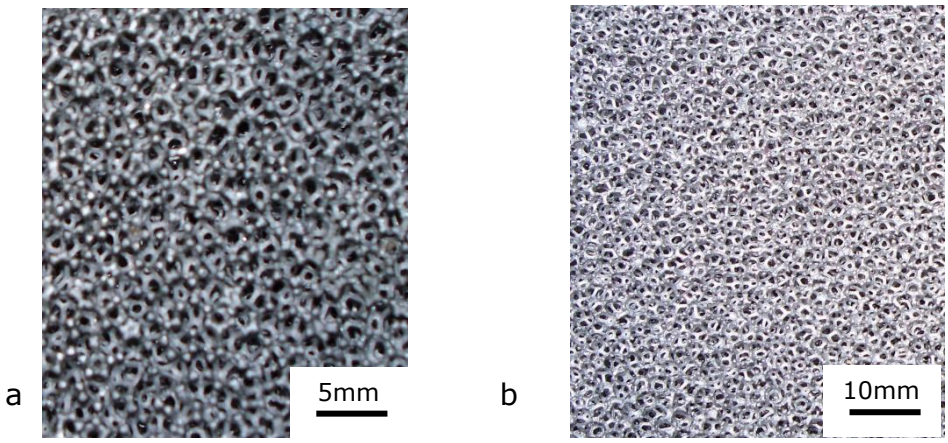


Figure 4-1. Images of 1116 sample (a) and 1723 sample (b) showing difference in pore size.

From initial observations of the foam by eye a 'dark band' was visible through the centre of the foam running through the longitudinal length. Figure 4-2 shows two images taken of a visible 'dark band' region in both the 1116 and 1723 samples.

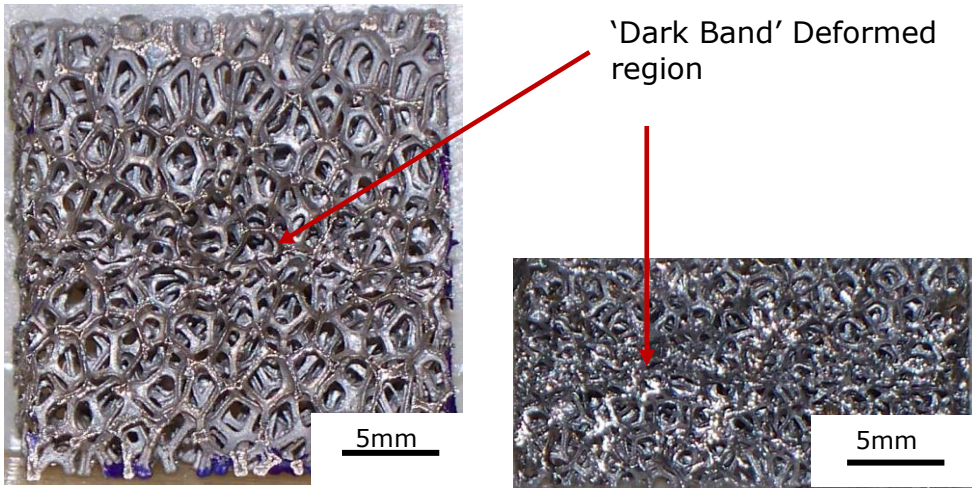


Figure 4-2. Images of 1116 sample (a) and 1723 sample (b) showing the 'dark band' deformed region.

Further analysis using SEM revealed that this 'dark band' was in fact an area of deformed and bent struts. Images taken (Figure 4-3) show that this area also shows signs of strut walls that have undergone 'unzipping'. The images in Figure 4-4 show the pores viewed above and below this deformed region. They don't show signs of strut deformation but they do illustrate the elongation of the pores in the short traverse direction.

Reports of a 'dark band' region within open-cell foams could not be found in the literature, including those which have performed studies with Recemat foam, such as Onck, *et al.* [3] and Khyargoli, *et al.* [69]. Recemat themselves make no mention of the 'dark band'

either. It is unknown why the deformity is not reported in the Recemat studies, but it may be that the less thick and finer pore samples tested showed no signs of it.

There are several possibilities for the method by which these defects could be created. The first is that during the sectioning of the metal foam (by the manufacturers) into sheets the saw used compresses the material. This way would only be possible if there is sectioning of the metal foam by the manufacturer prior to shipping, and that the sheets aren't sectioned in their polyurethane foam state.

The 'dark band' could be an inherited defect from the polyurethane substrate, whereby the 'dark band' was present during the electroplating process and the structure remained after the polyurethane removal. However it is uncertain how, or why, the polyurethane foam would be deformed in this region. For the 'dark band' to be present within the polyurethane foam it would have had to be compressed prior to electroplating, and there is no literature to support why that would be necessary.

There is a method of Ni foam production, which deposits the metal whilst the polymer substrate is under tension, to create high aspect ratios [37]. The IncoFoam's produced by this method are <5mm thick, therefore it may be that above this thickness (1723 is 10mm) the mid-section struts are too thin to support the weight of the deposited material. Therefore during the removal of the polyurethane substrate, the metal foam could compress under its own weight, bending the struts in the midsection.

A likely reason for the "dark band" is that for thickness control the sheet is passed through rollers, in order to compress the material to the required thickness. Onck, *et al.* [3], reported that the bending of struts can cause "unzipping" of thin strut walls, which would be produced near the centre of the material due to the deposition/throwing power of the Cr and Ni layers, and is likely why the "dark band" is seen in this area.

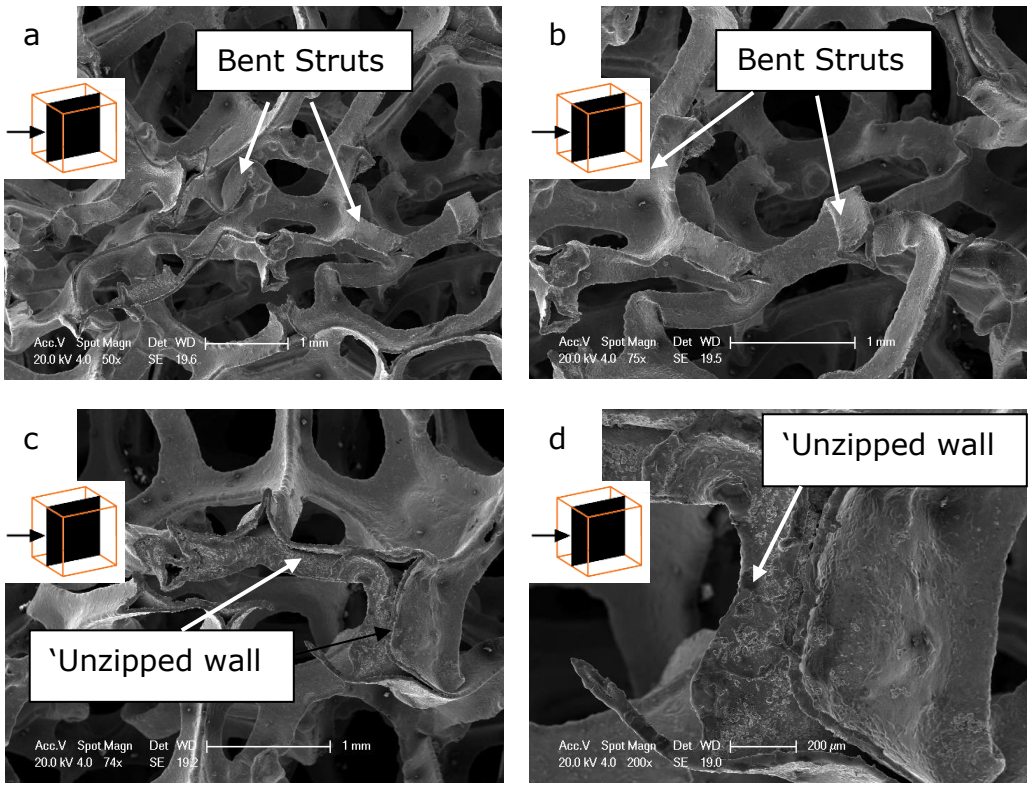


Figure 4-3. SEM images of the deformed region in a 1116 foam sample, showing bent struts in images (a-b) and unzipping in (c-d)

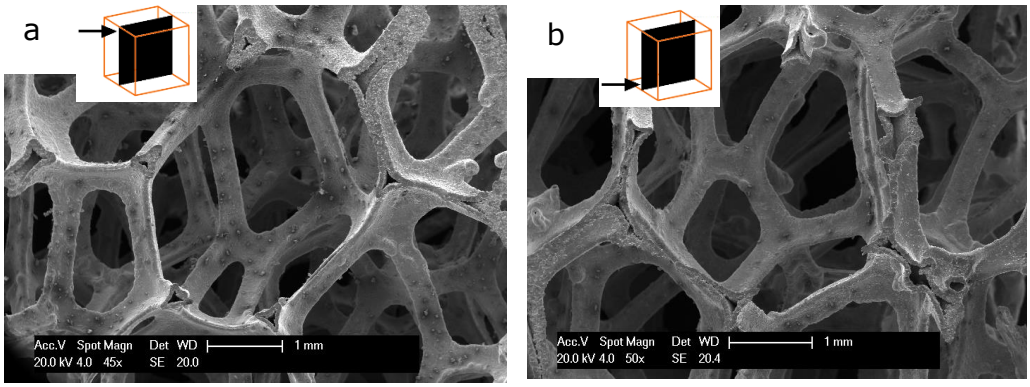


Figure 4-4. SEM images of pores above (a) and below (b) the deformed region

Examining the strut cross-sections (Figure 4-5) shows that the struts have thicker walls near the surface (~200µm) that gradually reduces the closer they are to the midsection (~50µm) in the ST direction. This is likely to lead the already deformed region to be sites for the initial deformation during compression and failure during tensile testing. Figure 4-6 shows the struts near the surface of the 1116 and 1723 samples. The 1116 struts were observed to be larger and have thicker walls than those of the 1723 (~200µm to ~100µm respectively). This illustrates the limitations of the electroplating process of Ni-Cr foams, in creating a uniform coating, which was reported in the literature. The coating thickness will vary through the ST of the sample, and the thicker samples will have thicker coatings nearer the surface.

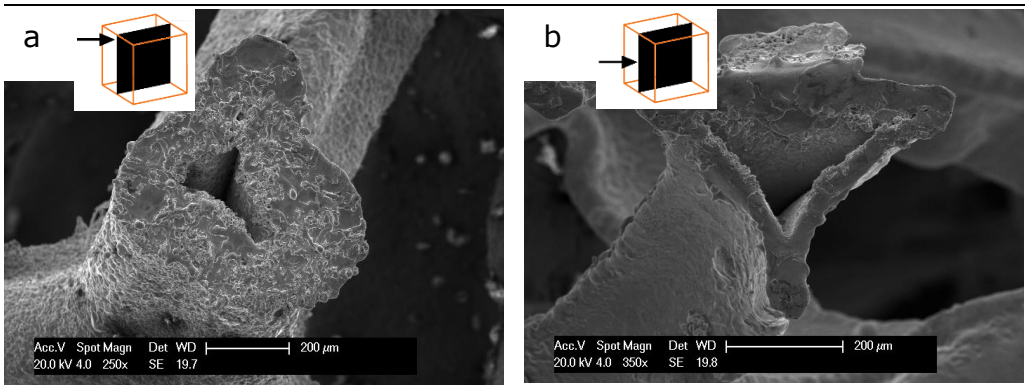


Figure 4-5. SEM images showing variation between thicknesses of strut walls near the surface (a) and at the mid-section (b).

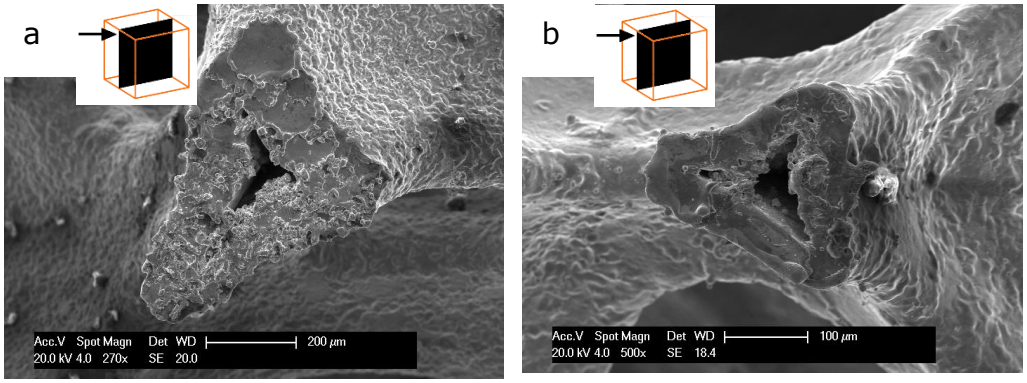


Figure 4-6. SEM images of illustrating the larger strut sizes of 1116 samples (a) compared to 1723 (b)

Further observations made during SEM analysis were of features such as 'exhaust' holes created during the burn out process stage (Figure 4-7), and of struts which had been impacted by debris (possibly during sectioning by bandsaw) which had caused some removal of material (Figure 4-8). These sites can not only act as weak points during deformation and crack initiation sites but can also act as corrosion initiation sites for pitting and crevice mechanisms.

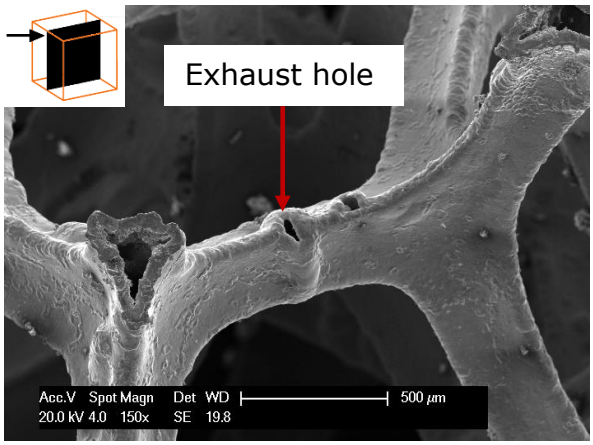


Figure 4-7. SEM image of 'exhaust' hole on a strut wall in a 1723 sample.

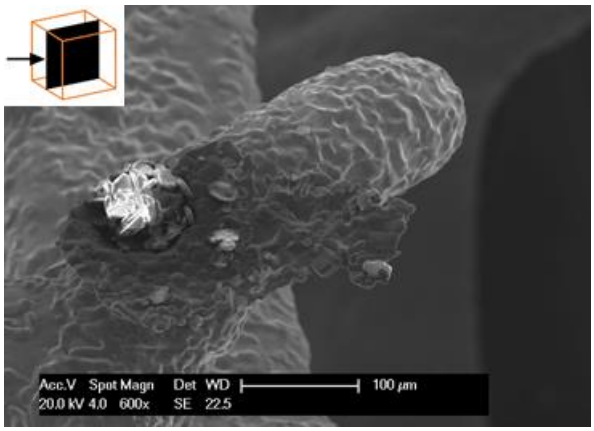


Figure 4-8. SEM image of debris impact on a 1723 sample strut causing peeling.

Analysis of the microstructure (un-polished and un-etched) shows a predominantly fine-grained microstructure, with a small amount of large grains interspersed randomly throughout the foam (Figure 4-9). These grains are the likely result of irregular nucleation grain growth, during electro-deposition, caused by the defects in the conductive layer applied to the polyurethane foam. As was mentioned in the literature, defects affect the current density of the

samples and can lead to larger deposits of material in a localised area.

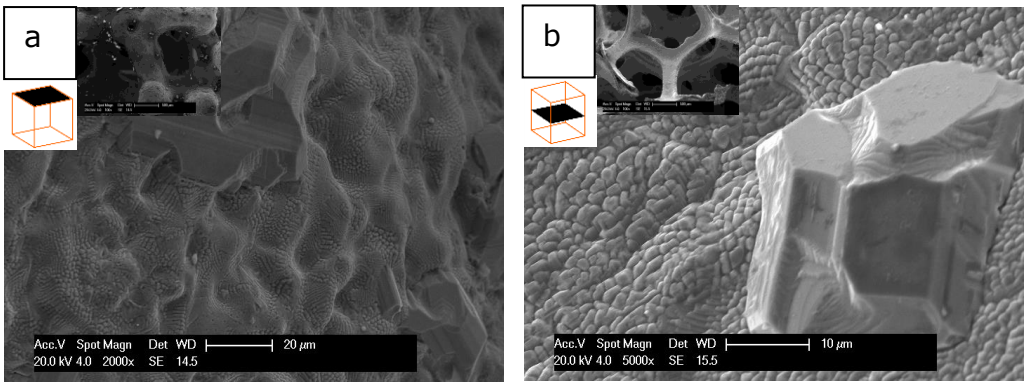


Figure 4-9. SEM images showing the microstructure of the Ni-Cr struts. (a) shows the predominantly fine-grained microstructure. (b) shows a large grain.

4.1.2 X-Ray Micro-Tomography (µCT) Analysis

A 1116 sample was scanned and a 3D model rendered for slicing (Figure 4-10). This allowed for cross-sections of the sample to be viewed without any structural changes being caused by machining. As can be seen in Figure 4-11 the dense mid-section 'dark band' is present throughout and is not a facet of the sectioning process used to section the sample. However it is hard to determine whether there are deformed struts as the resolution of the images (20µm) is not much smaller than the strut wall thickness (>50µm).

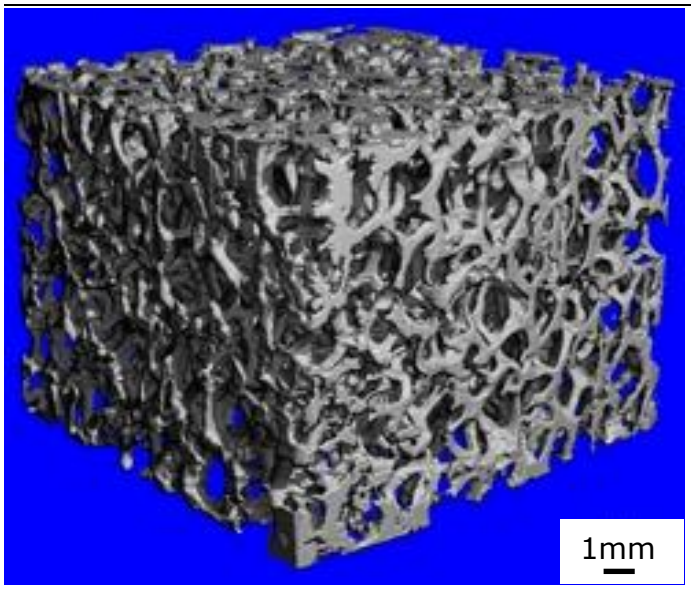


Figure 4-10. 3D rendered model of a 1116 sample using X-Ray Micro-Tomography.

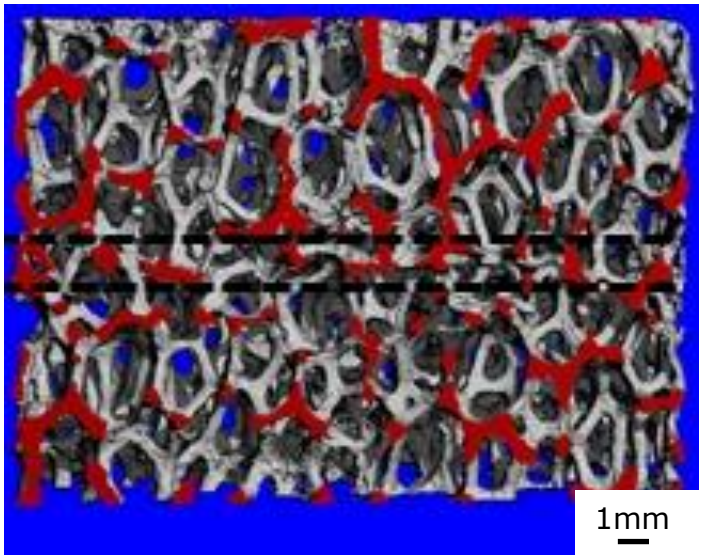


Figure 4-11. Slice made through the cross-section of the rendered 3D model, with the new face coloured red, and highlighting the deformed area.

Using the slices obtained from the scan the relative area, metal area (MA)/ total area (TA) (where the MA is the area of material and TA is the total area of the slice), was plotted against the depth. Figure 4-12 and Figure 4-13 show the plots of the relative area against depth for both 1723 and 1116 foams respectively. Both plots show a

high volume of material at the surfaces which decreases towards the midsection, and then increases again around the midsection area. The high relative area at the surface is due to the thicker struts walls, which is also why the relative area is larger for the 1116 samples compared to the 1723 samples. The large relative area in the midsection corresponds to the 'dark band' region, it is more pronounced in the 1723 foam, due in part to the reduced thickness of the material and the thicker struts of the 1116 foam. The large relative area of the midsection indicates that 'dark band' region is the result of both deformed struts and a larger volume of material being present. This could possibly be the result of densification of the foam during either its polyurethane or metal foam state.

Figure 4-14 illustrates the line and circular methods used to determine the pore size of the samples. Table 4-1 shows the average pore size calculated along with the variance percentage. As the pores aren't clearly defined there is the chance for error in the number of pores actually intersected. The inclusion, or missing, of a pore can cause an error of ±20μm in the ST axis, and ±45μm in the LL axis.

From the results it can be seen that the line method, as predicted, gave a slightly smaller pore size estimate. Comparison of the average results shows that there is a negligible variation in pore size between the 1723 samples. This indicates that any variation in density or strength is not as a result of pore size.

Sample	**Short Traverse Axis**		**Longitudinal Length Axis**	
1723	**Circle Method** Average Pore Size / mm (Variance / %)	**Line Method** Average Pore Size / mm (Variance / %)	**Circle Method** Average Pore Size / mm (Variance / %)	**Line Method** Average Pore Size / mm (Variance / %)
A17	1.31 (4)	1.24 (4)	1.35 (5)	1.33 (7)
D17	1.31 (5)	1.26 (6)	1.38 (4)	1.32 (4)
H17	1.30 (3)	1.24 (7)	1.39 (6)	1.26 (6)
1116				
2C	1.84 (3)	1.93 (5)	2.06 (5)	2.05 (7)

Table 4-1 Table showing estimated average pore sizes for 1723 and 1116 foam samples, along with the variance percentages.

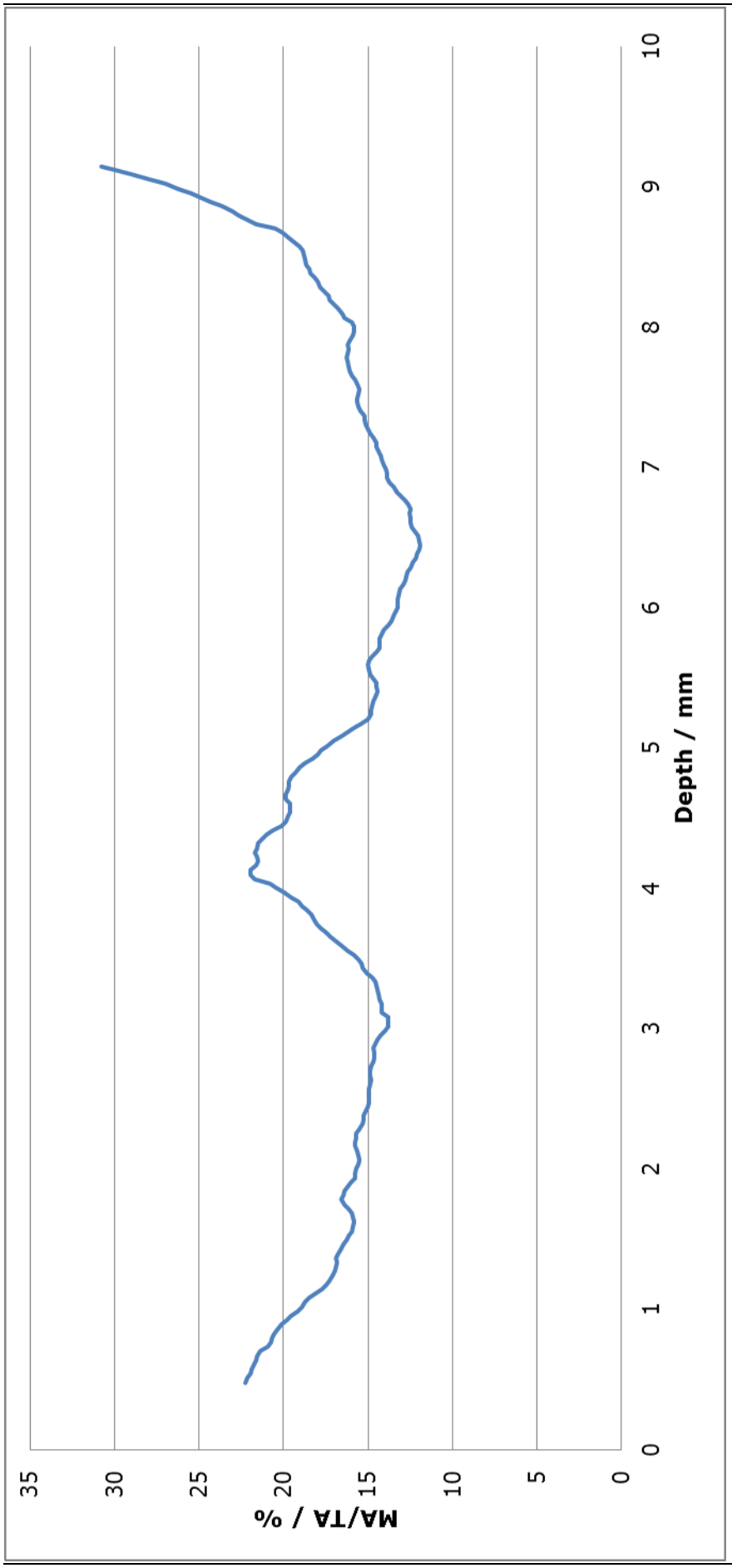


Figure 4-12. Plot of the relative area against depth of a 1723 foam sample.

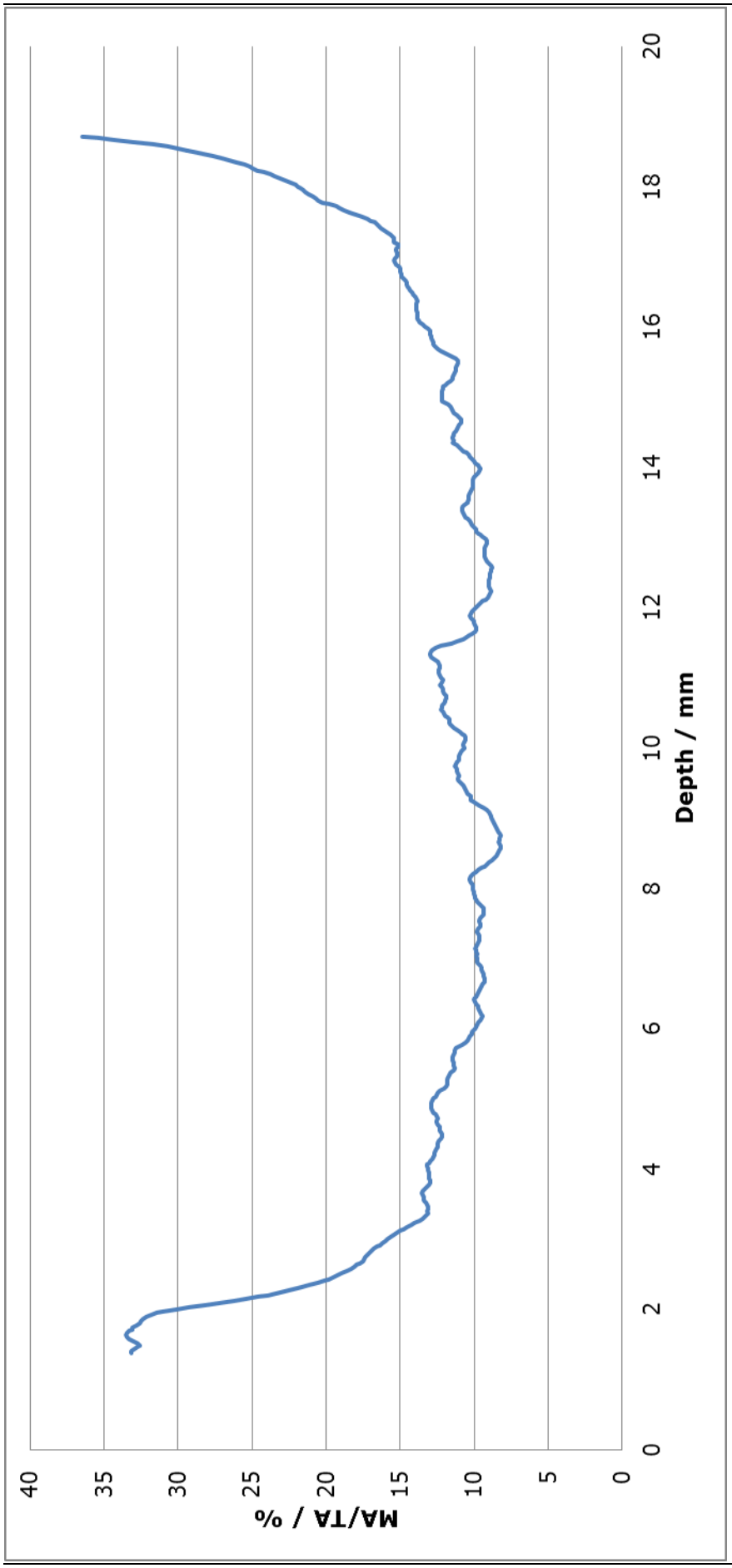


Figure 4-13. Plot of relative area against depth of a 1116 foam sample.

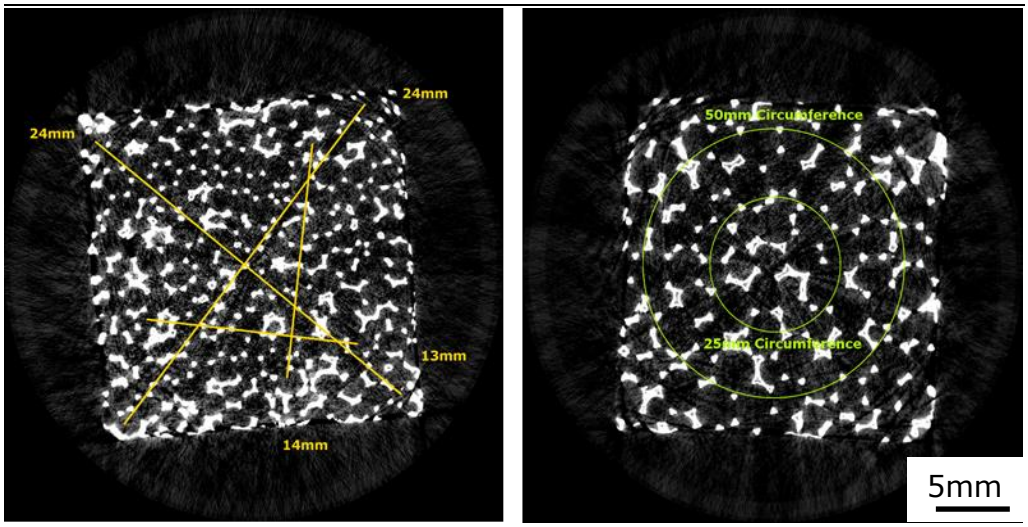


Figure 4-14. Line and circular methods for determining pore size.

4.1.3 Density

The bulk densities calculated for the 1116 and 1723 samples can be seen in Table 4-2. The 1723 samples showed a large variance in densities (a layout plot of which can be seen in Appendix 2) and so a small localised area was also tested to compare. It was found that the localised area and the 1116 foam samples had significantly less variance, but both had fewer samples tested and the exact location that the 1116 strip came from in the sheet is unknown. Therefore it is possible that had an entire sheet of the 1116 foam been analysed a similar variance in the results would have been observed.

As can be seen in the Figure 4-15 layout plot, the most highly dense areas are found towards the edge of the sheet and the density decreases towards the centre of the sheet.

1116	
Average ρ	0.57
Std Dev	0.02
Variance	2.91%

1723	
Average ρ	0.65
Std Dev	0.09
Variance	14.38%

Local Area	
Average ρ	0.59
Std Dev	0.01
Variance	1.19%

Table 4-2. Calculated average densities (g/cm3), for 1116 and 1723 samples as well as for a localised area of 1723 samples.

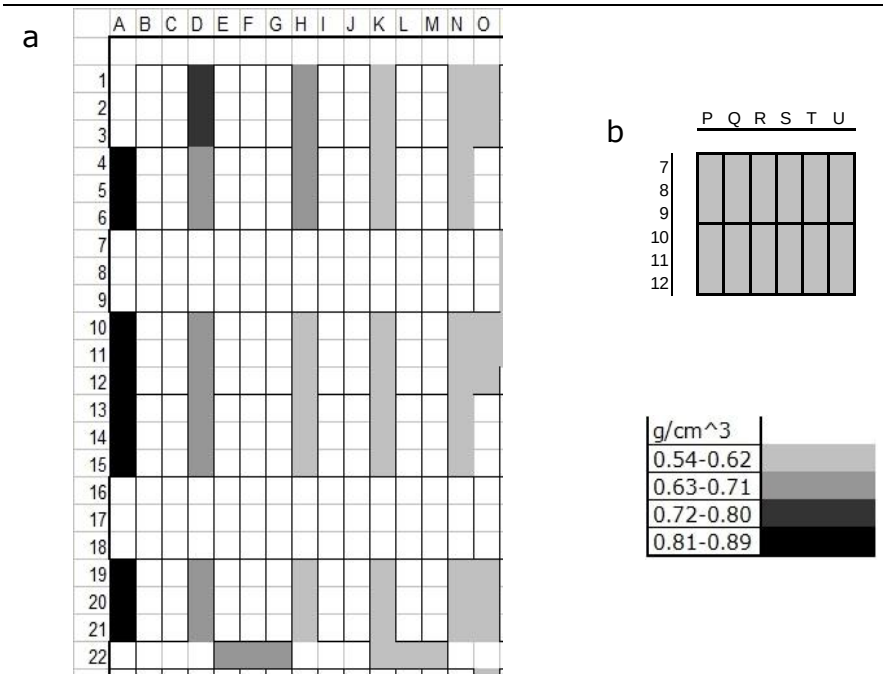


Figure 4-15. Density layout plot for (a) the 1723 samples showing higher density towards the edge of the sample, and (b) the localised area. (Edited version of full plot seen in Appendix 2)

Unfortunately due to the hollow nature of the struts, fully enclosed volumes cannot be measured and thus a truly accurate determination of the density of the samples, using Pycnometry, cannot be performed. If the thickness of the samples is relatively smaller, then the proportion of enclosed volume is higher, but this depends on the proportion of cut (open) ends. However on the assumption that a similar amount of trapped spaces exist, relative to the foam size, within all the samples then comparison can be made between them. During the X–ray Tomography work it was noted that relative volume of material to sample size was similar for the samples across the sheet. Ideally the volume fraction of the samples would have been calculated by that method, however the large strut thicknesses near the surfaces of the sample prevented

accurate resolution by the X-ray, and as the large surface thicknesses contained much of the mass of the samples the Pycnometry results may be more accurate.

The results from the testing (a table of results is available in Appendix 3) concluded that the 1723 and the 1116 foams are of similar density (Table 4-3), assuming that the 1116 foam samples represent an average of the sheet from which it came. The 1723 also exhibited a much higher volume in the A column samples than the rest of the sheet samples. The H column samples were also of a higher volume than the O column (Table 4-4).

	Volume / cm^3	**Density / g/cm^3**
1116	0.16	7.76
1723	0.17	7.76

Table 4-3. Average volume and density for 1116 and 1723 samples

Column	**Volume / cm^3**
A	0.21
H	0.16
O	0.14

Table 4-4. Average volume of samples taken from columns in the 1723 material

The bulk density assumed the volumes were uniform throughout the sheet, and therefore the higher mass measurements recorded at the edges of the sheet produced a higher calculated density. The Pycnometry results show that the volume is not uniform, and that the there is a higher volume of material present at the edges of the sheet.

4.1.4 Atomic Emission Spectroscopy (AES) Chemical Analysis

It was not possible to use this technique to analyse the 1116 samples, as even after further compression (after the compression tests) had been applied the porosity of the sample was too high for adequate Ar shielding.

Some of the Cr results recorded were higher than the machine could analyse and so only the maximum value of 33% was returned. However when tests were performed on the reverse side of the samples, none achieved out of range results. An average of these two sets of results was therefore used. The central point on the sample where the arc forms was found to burn to a depth of up to 0.4mm. With the folding of the sample, and the analysis being performed in a total of six locations to a depth close to half the full thickness, it was believed that the results would give a true average chemical composition result for each sample.

The results of the 1723 samples, which were able to be analysed, can be seen in Table 4-5. The Cr content was on average ~29%, but varied from a minimum of ~25% to a maximum of 32%. This was within the 20-32% range stated by the manufacturer.

	%Ni	%Cr
AVERAGE	70.05	28.89
STD DEV	2.01	1.74
VARIANCE	2.9%	6.0%

Table 4-5. Chemical composition estimation derived from AES results.

There was no clearly defined distribution pattern of Cr content (Figure 4-16); although a slight trend towards larger Cr content in the centre of the sheet was seen. This was not expected, as it had been assumed that the edges of the sheet would have a higher Cr content. This assumption was due to the throwing power limitations, associated with the electroplating production method, not being a problem on the edge surface which would allow a thicker Cr coating through the thickness of the foam in this area.

The higher Cr content measured towards the centre could be the result of how the measurements were read. After the foam had been compressed and rolled to allow an adequate Ar shielding to be made, the surface of the "new" sample was a combination of the top and midsections of the "original" sample. It was not known exactly from where in the "original" sample the "new" surface measurements were taken. Therefore different samples from across the sheet may have been measured in areas from different depths within the thickness. Further to this, as was discussed in the literature review, variations in the current density over the sheet during electroplating can vary the thickness of material deposition. It is possible therefore that more Cr was deposited near the centre for this reason.

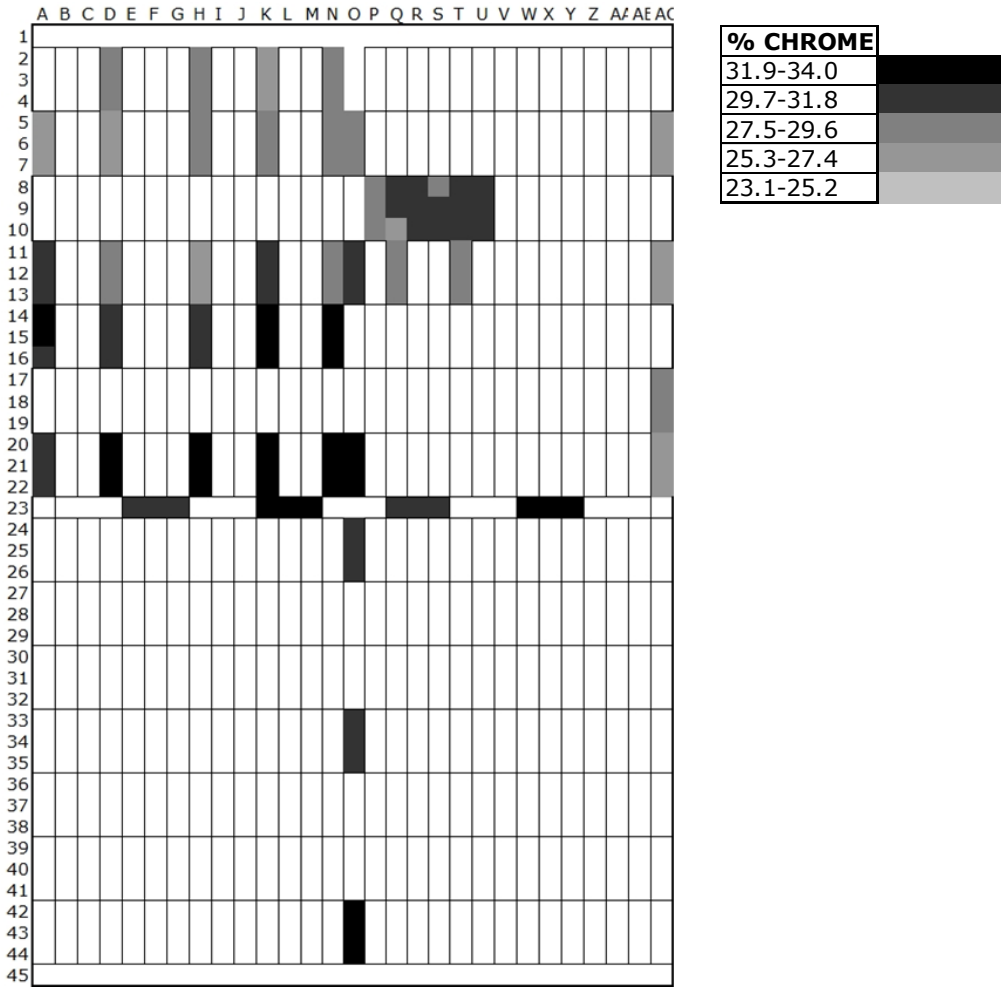


Figure 4-16. Chemical composition layout plot as measured by AES.

4.2 MICROSTRUCTURE ANALYSIS OF AS SUPPLIED FOAM

4.2.1 Optical and Scanning Electron Microscopy (SEM) of the Microstructure

Etched 1723 samples showed that whilst struts close to the surface contained a visible grain structure those in the middle did not (Figure 4-17(a)). However the middle struts did contain a second phase which can be seen in Figure 4-17(b). Although visible in areas throughout the strut walls it was most abundant at the corners. The etched 1116 samples showed similar differences between the struts at the top and middle sections, as well as a visible Cr-rich layer

(~10μm) upon the surface of struts near both the top and bottom of the sample (Figure 4-18 (a)). Figure 4-18 (b) not only shows a similar secondary phase seen in 1723 samples but also shows evidence of wall defects (also found in 1723 samples as well).

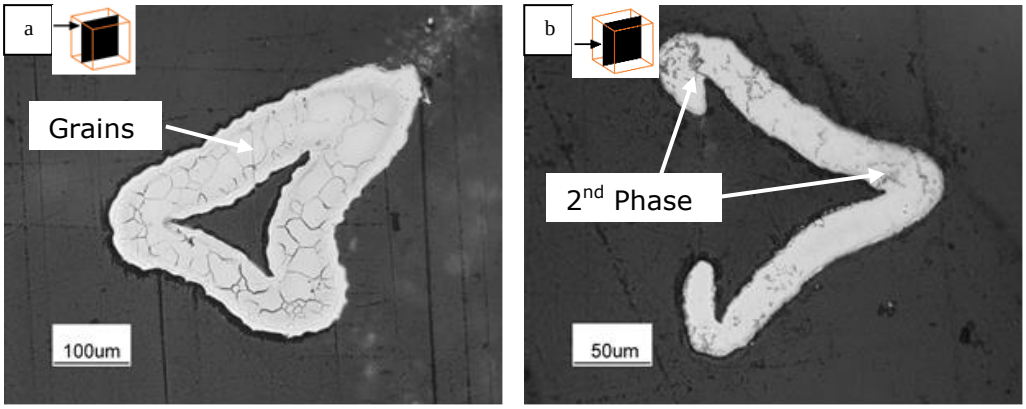


Figure 4-17. Etched samples of 1723 material, showing a strut from the top of the sample with grains (a), and from the middle section showing 2-phases (b).

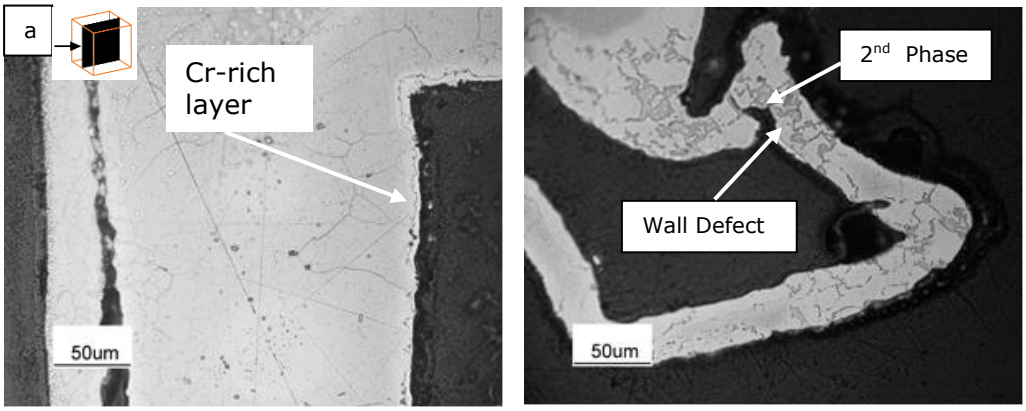


Figure 4-18. Etched images from an 1116 sample. Image (a) shows a strut from the top, with Cr along the edges. Image (b) is from a strut in the middle of the sample, showing the second phase present, as well as a wall defect.

4.2.2 EDX Chemical Analysis Of Supplied Foam Microstructure

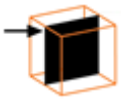
The analysis was performed by applying area scans over the struts at three locations within the samples, near the surface (~0-2mm), further below the surface (~2-3mm for the 1723 foam samples and ~3-6mm for the 1116 foam samples) and near the midsection of the foams. Table 4-6 and Table 4-7 show the estimated composition for 1723 and 1116 samples, respectively, at a location near their surfaces. The 1116 samples show much less Cr within the strut walls compared to the 1723 foam. Table 4-8 and Table 4-9 show the results from locations further below the surface, and at the midsection, respectively, for the same 1116 sample. They show that the percentage of Cr increases towards the centre of the sample.

Figure 4-19 shows a chemical line scan performed through the wall thickness of an 1116 sample taken near the top surface of the foam. As can be seen the wall is predominantly Ni in composition until reaching the edges of the strut walls in which the Cr increases. This type of scan is representative of the strut near the surfaces of 1116 samples. Figure 4-20 is a line scan for a 1723 sample, taken at the top surface. Like the 1116 samples it is predominantly Ni in composition, which decreases close to edge when the Cr level increases. Figure 4-21 shows a line scan from a strut near the mid-section of an 1116 sample. Although there is still a high Cr content near the edges of the strut it is also found within the bulk of the section as well. Figure 4-22 shows the line scan from a strut near the

mid-section of a 1723 sample. It shows a similar profile to that of the 1116 sample, with Cr being found throughout the thickness of the strut.

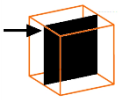
It is concluded, therefore, that Cr coating deposited onto the surface of the strut walls has diffused into them. In the mid-section, where the strut walls are thin, the Cr has been able to diffuse through the thickness of the wall. Near the surface of the samples, the strut walls are thicker and the Cr has not diffused throughout. Along with the increased Cr likely to have been deposited at the surface (due to the throwing power), a higher Cr content is found on the surface of these struts (similar to that which was reported by Onck, *et al.* [4]). As the Cr content was measured around the middle of the strut wall (missing the edges of the strut), the thinner struts with their increased Cr diffusion would return higher Cr content measurements. This explains why the Cr content was measured as increasing towards the midsection, despite larger deposits having probably been made on the surface of the samples.

Figure 4-23 shows an image of a strut near the mid-section of an 1116 sample with a secondary phase visible. Point analysis revealed the phase to be highly Cr-rich; with Ni and trace amounts of Si (Further examples are available in Appendix 4).



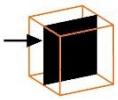
	Element wt%	Atomic wt%
Cr K	39.27	42.20
Ni K	60.73	57.80

Table 4-6. 1723 top surface strut EDX chemical analysis.



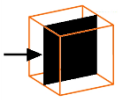
	Element wt %	Atomic wt %
Cr K	29.55	31.88
Ni K	66.27	63.33

Table 4-7. 1116 top surface strut EDX chemical analysis.



	Element wt %	Atomic wt %
Cr K	36.94	39.58
Ni K	58.69	55.71

Table 4-8. 1116 below surface strut EDX chemical analysis.



	Element wt %	Atomic wt %
Cr K	43.05	46.02
Ni K	55.60	52.64

Table 4-9. 1116 mid-section strut EDX chemical analysis.

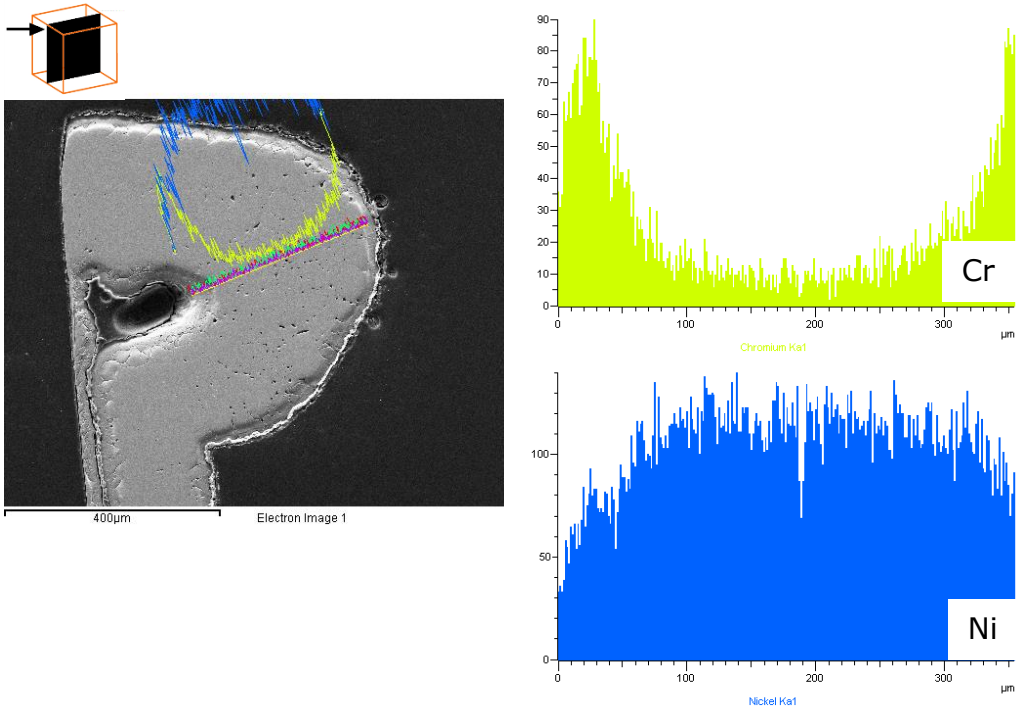


Figure 4-19. 1116 top surface strut EDX line scan with Cr and Ni profiles.

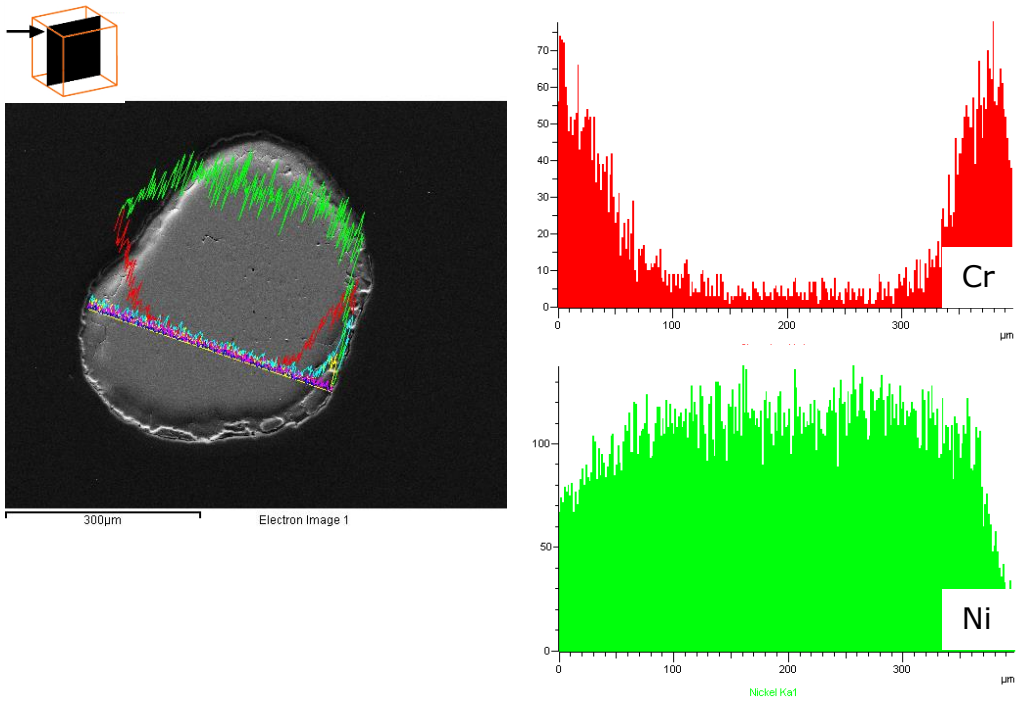


Figure 4-20. 1723 top surface strut EDX line scan with Cr and Ni profiles.

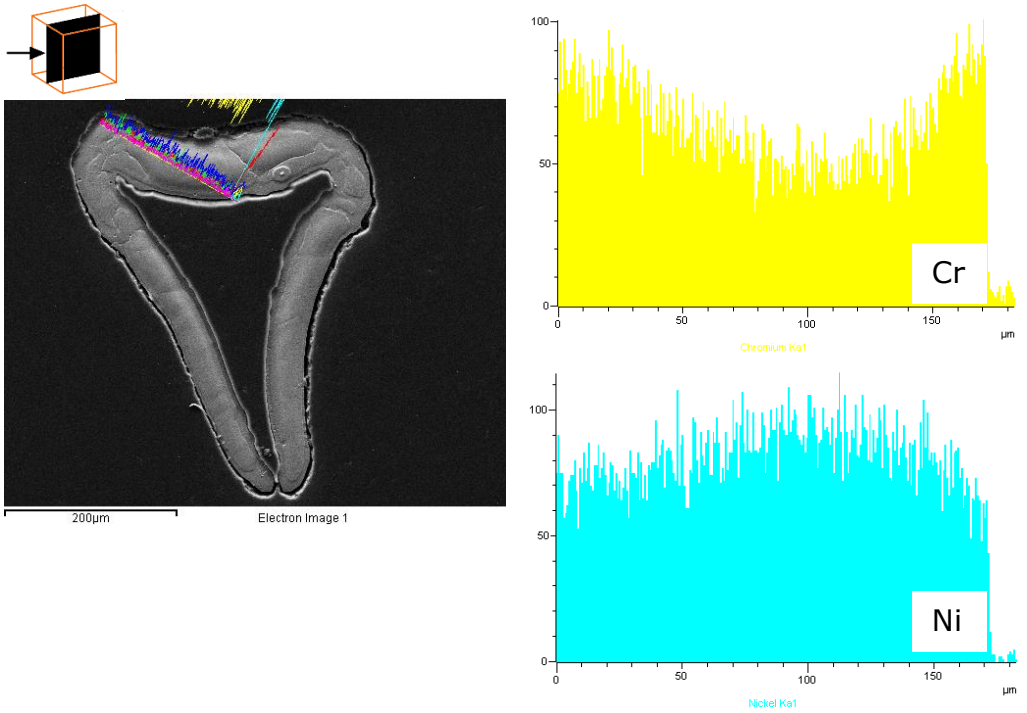


Figure 4-21. 1116 Mid-section strut EDX line scan with Cr and Ni profiles.

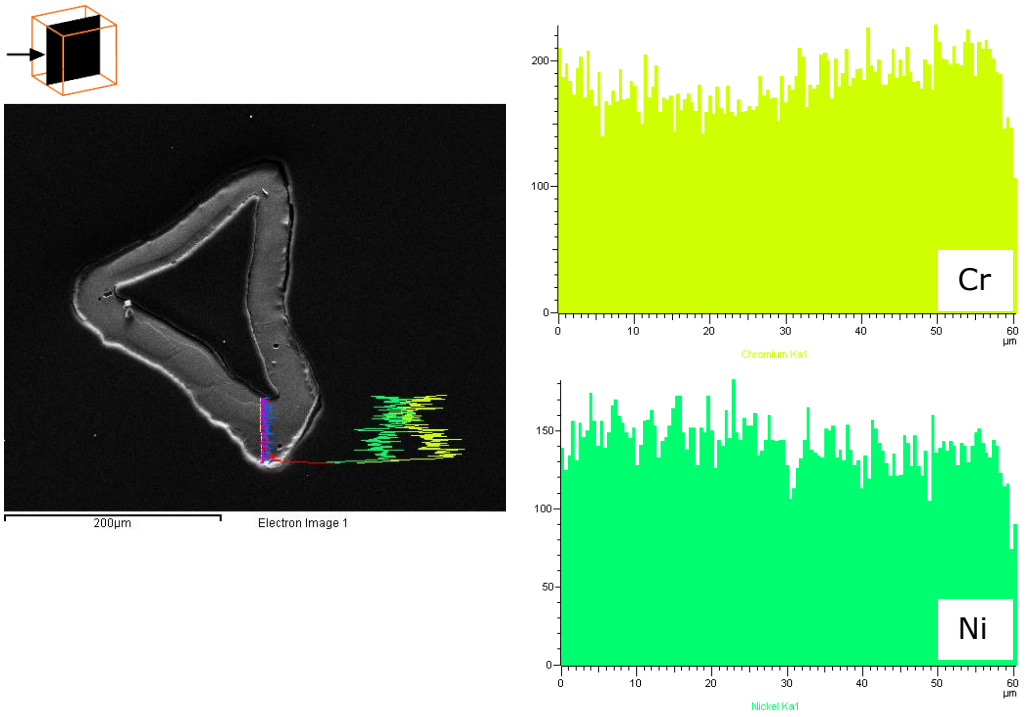
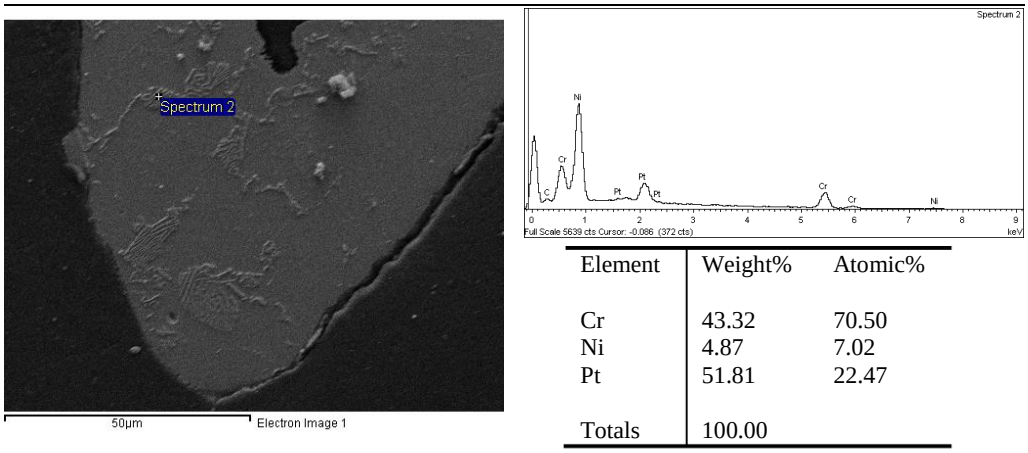


Figure 4-22. 1723 mid-section strut EDX line scan with Cr and Ni profiles.



Element	Weight%	Atomic%
Cr	43.32	70.50
Ni	4.87	7.02
Pt	51.81	22.47
Totals	100.00	

Figure 4-23. SEM image of the secondary phase present in the strut walls. Showing the location and results of an EDX analysis (a Pt coating had been applied).

4.3 MECHANICAL TESTING OF THE AS-SUPPLIED FOAMS

4.3.1 Compression Testing

4.3.1.1 1723 Foam Samples

The results of the compression tests on 1723 samples produced compressive stress-strain plots similar to those discussed in the literature review, with an initial increase in stress up to the yield, followed by a plateau region, and finally an increase in stress during densification (Figure 4-24). The average compressive stress (across the whole sheet) at proof strain was 3.48 MPa, at 25% strain was 6.48 MPa and at 60% strain was 17.40 MPa. As can be seen in Figure 4-24 with increasing strain there is a larger degree of scatter. This is reflected in the standard deviation and variance calculated for the three sets of strain values in Table 4-10. It was also found that higher strength corresponded to samples from areas at the sheet edge, with samples getting progressively weaker towards the centre of the sheet (a layout plot can be seen in Appendix 5). The

maximum compressive stress recorded, at 60% strain, was for an edge sample at ~27 MPa, whereas the lowest was from near the centre of the sheet at ~13 MPa.

A comparison against the results obtained from a localised area (Table 4-11) shows how the large property variations observed may not have been reported previously due to there being little variation when samples are obtained from one small area. The variance at 60% strain being 21% for the entire sheet but only 3% for the localised area

Proof Strain		**25% Strain**		**60% Strain**	
Mean	3.48	Mean	6.48	Mean	17.40
Standard Dev	0.38	Standard Dev	0.76	Standard Dev	3.69
Variance	10.8%	Variance	11.7%	Variance	21.2%

Table 4-10. Average compressive stresses (MPa), over the entire sheet area, for the three strains.

Proof Strain		**25% Strain**		**60% Strain**	
Mean	3.17	Mean	6.08	Mean	14.94
Standard Dev	0.25	Standard Dev	0.35	Standard Dev	0.42
Variance	7.8%	Variance	5.7%	Variance	2.8%

Table 4-11. Average compressive stresses (MPa) for the three strain areas. All samples are from a localised area.

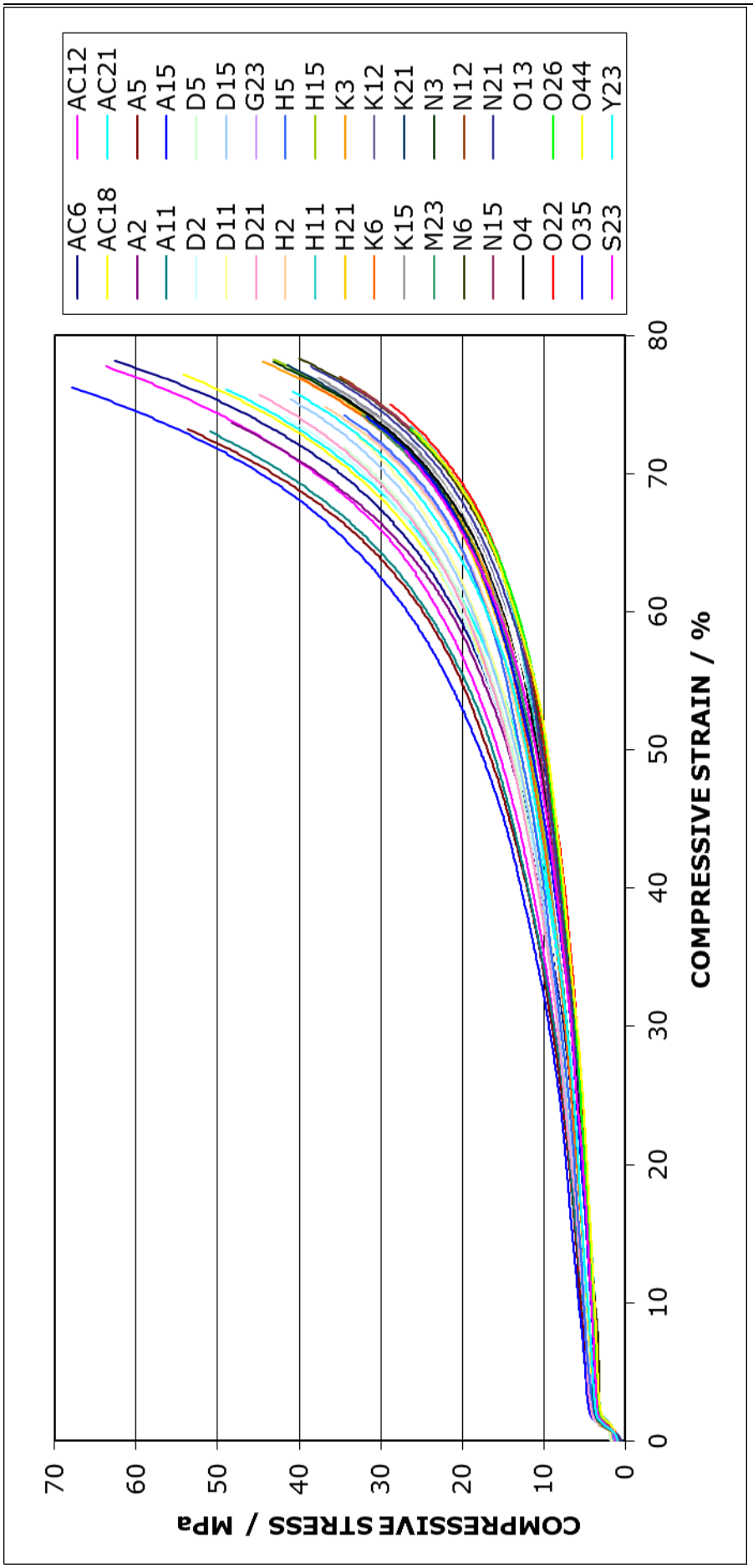


Figure 4-24. Compressive stress-strain plots for 1723 samples, showing variation between samples across the whole sheet area.

4.3.1.2 1116 Foam Samples

The 1116 sample results in both the short traverse (Table 4-12) and the longitudinal length (Table 4-13) directions showed good uniformity with little variation across the strip in comparison with the 1723 samples (a layout plot can be seen in Appendix 6 and stress-strain plots for both the ST and longitudinal directions can be seen in Appendices 7 and 8 respectively). Figure 4-25 shows a plot of the average results of tests performed in the ST and longitudinal directions. It can be seen that the longitudinal samples have a higher initial maximum stress before experiencing a flatter (less inclined) plateau region, which indicates a more homogenous structure. The differences in plots can be attributed to the way in which the samples collapse. It was observed that in the ST tests, the collapse was initiated at the deformed 'dark band' region (Figure 4-26). In the longitudinal directional test, samples underwent collapse in a more uniform manner across the sample (Figure 4-27).

Proof Stress		**25% Strain**		**60% Strain**	
Mean	1.30	Mean	2.92	Mean	11.66
Standard Dev	0.19	Standard Dev	0.24	Standard Dev	0.44
Variance	14.4%	Variance	8.4%	Variance	3.8%

Table 4-12. Compression stresses (MPa) for 1116 samples in the ST axis.

Proof Stress		**25% Strain**		**60% Strain**	
Mean	2.06	Mean	3.77	Mean	10.42
Standard Dev	0.15	Standard Dev	0.22	Standard Dev	0.82
Variance	7.4%	Variance	5.8%	Variance	7.9%

Table 4-13. Compression stresses (MPa) for 1116 samples in the longitudinal axis

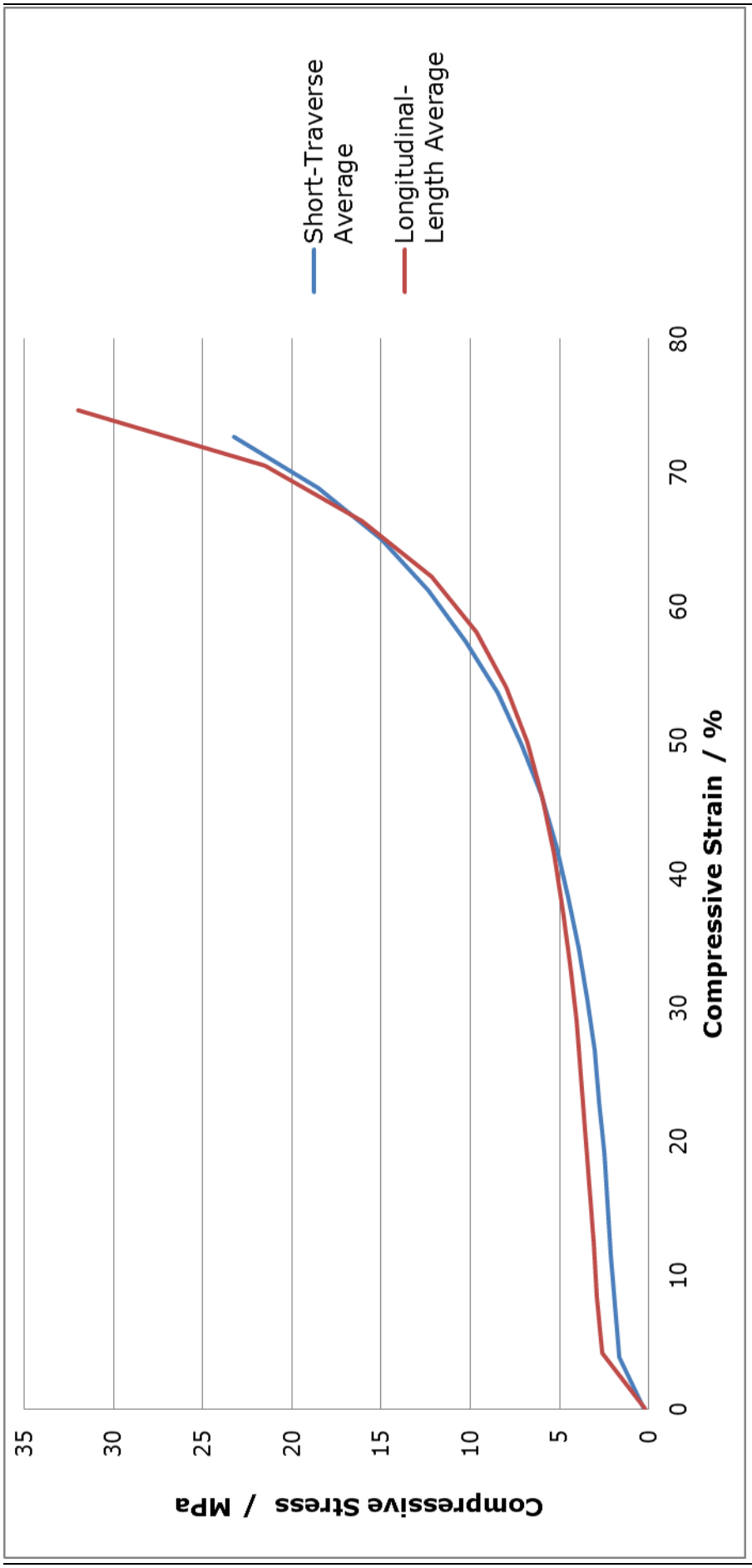


Figure 4-25. Compressive stress-strain plots comparing the short-traverse and longitudinal-length axis for the 1116 foam samples.

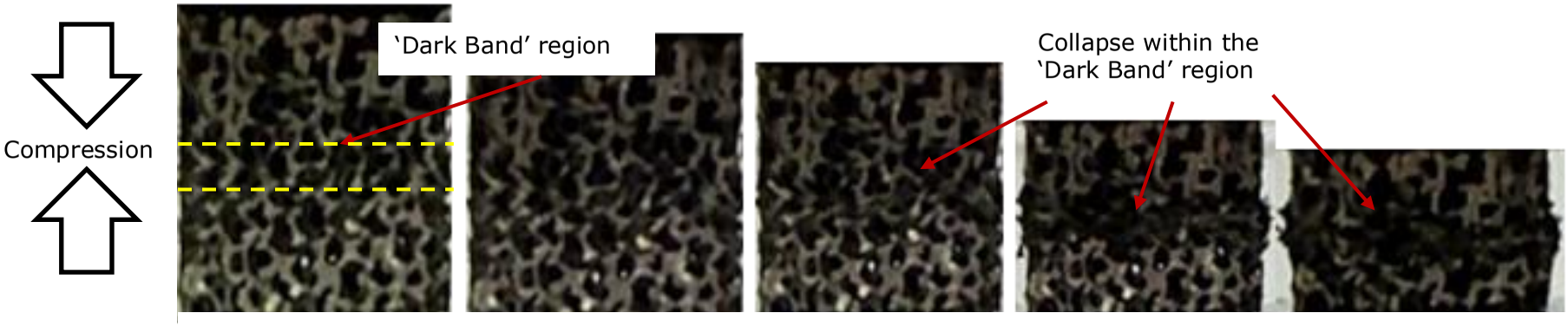


Figure 4-26. Images taken of a 1116 sample during compression testing in the ST axis, showing the deformation occurring initially in the 'dark-band' region.

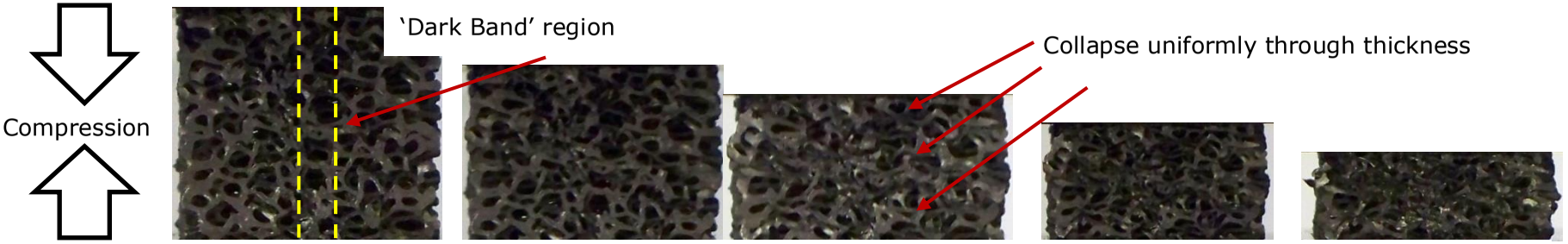


Figure 4-27. Images taken of a 1116 sample during compression testing in the longitudinal axis, showing the deformation occurring more uniformly throughout.

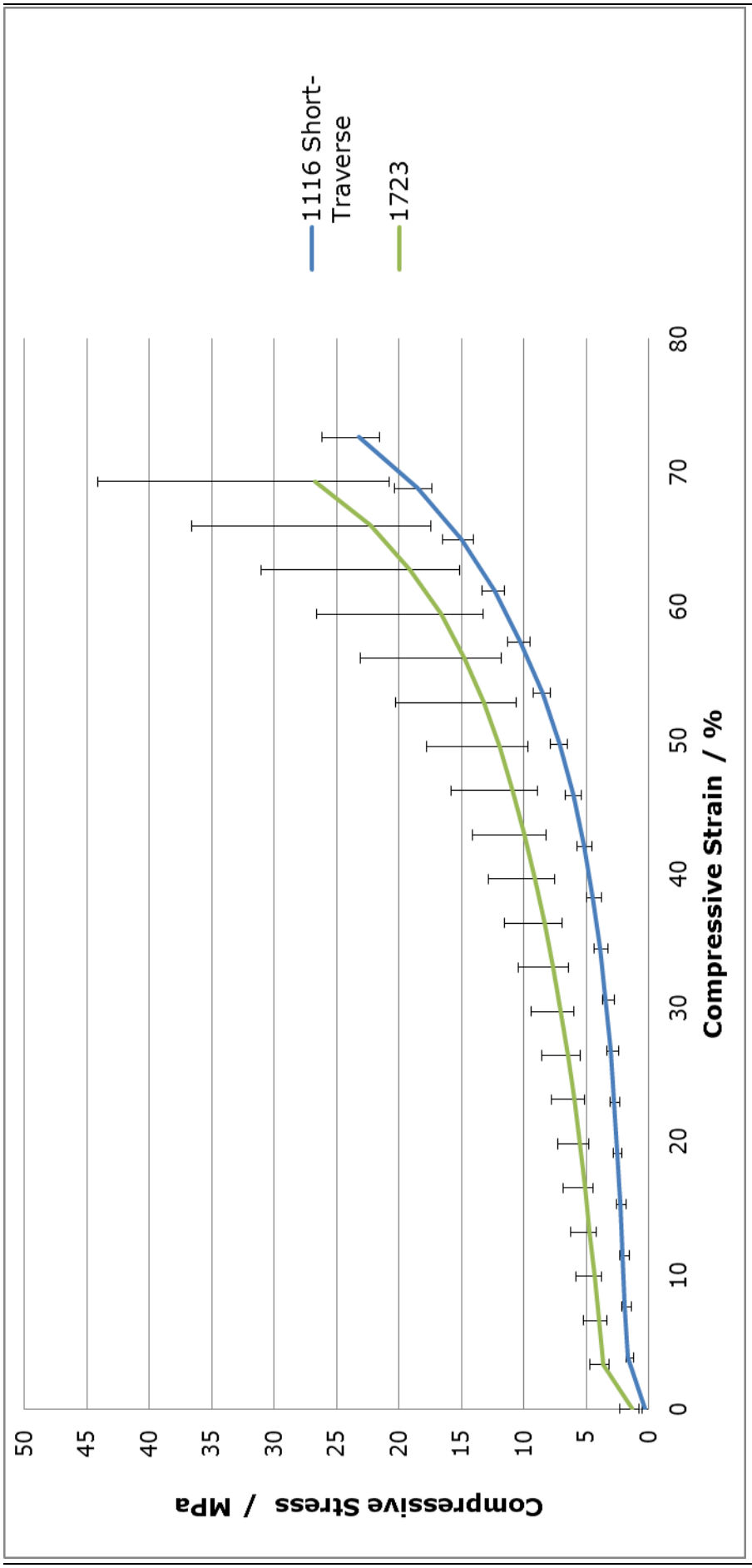


Figure 4-28. Average compressive stress-strain plots comparing the 1723 and 1116 samples, showing their maximum and minimum values.

4.3.1.3 1116 vs 1723 Compressive Stress-Strain

As can be seen in Figure 4-28, the 1723 samples exhibit higher compressive stress at comparative strain, when compared to the 1116 samples. It can also be seen that there is a larger variation in the 1723 samples, shown by the bars which represent the maximum and minimum stresses recorded at the given strain. However it is assumed that the 1116 samples would exhibit a similar variation if tests could have been performed on samples from an entire sheet.

4.3.1.4 Pore Size vs Compressive Stress

In order to analyse the effect of the pore/cell size on the strength of the foam, a plot of the two was compiled. Unfortunately samples used for X-ray CT analysis were not used for any mechanical testing. This was due to the X-ray CT machine having a maximum sample size that was smaller than the size used for mechanical testing. Therefore the pore sizes averaged over each column of the sheet are plotted against the compressive stresses averaged over the same columns. Figure 4-29 shows the plot produced which indicates the trend of the larger pore size reducing the compressive stress. This correlation is to be expected, as if the model for the cell is illustrated as a cube, such as the one discussed in the literature review, then a longer beam (wider cell) will buckle under lower force.

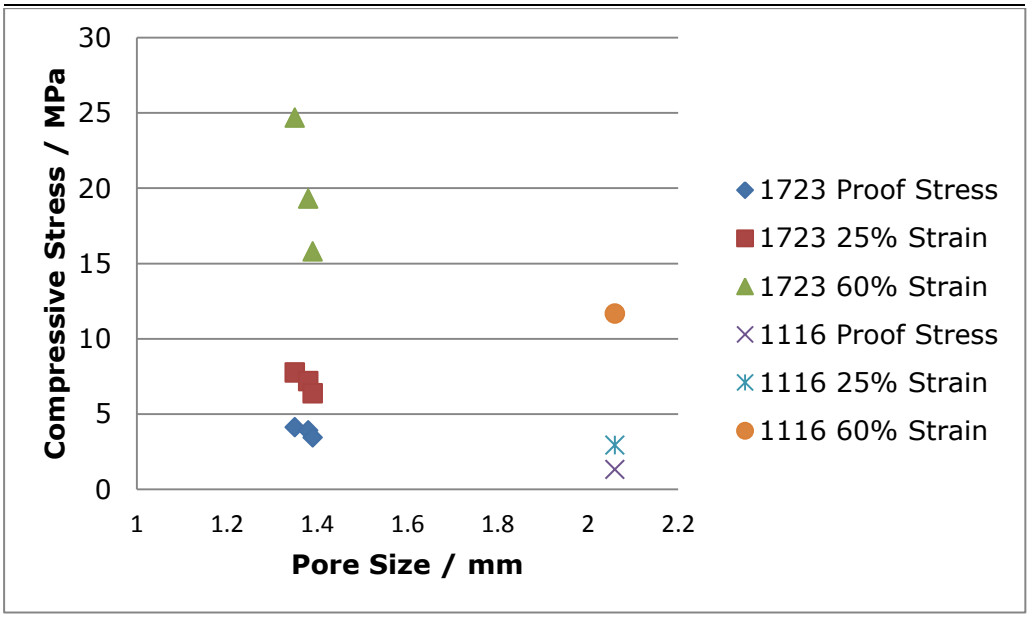


Figure 4-29 Average proof stress and compressive stress at 25% and 60% strain (in the ST orientation), plotted against the average pore size of the samples

4.3.1.5 Chemical Composition vs Compressive Stress

To determine the effect of the chemical composition on the compressive stress of the foam, a plot of the two data sets was made (Figure 4-30). As previously stated it was not possible to measure the chemical composition of the 1116 foam samples, therefore only the 1723 samples are plotted, with their respective proof stress, and stresses at 25% and 60% strain. It can be seen from the plot that there is little correlation between the Cr content of the foam and the compressive stress. Although a slight trend of higher Cr content reducing the 25% strain compressive stress is seen, the proof stress and densification stress (60% strain) show no correlation at all. A higher Cr content should produce higher mass, higher density and higher strength, through both the added density but also solid solution strengthening, however its lack of correlation

indicates that this may not the driving factor in determining the compressive strength of the foam. As was observed in the microscopy and chemical analysis many of the larger struts contained large Cr layers on the surface which had not diffused into the bulk of the strut material. Areas of the foam sheet containing high compositions of Cr may not therefore have the "additional" strength offered by solid solution strengthening.

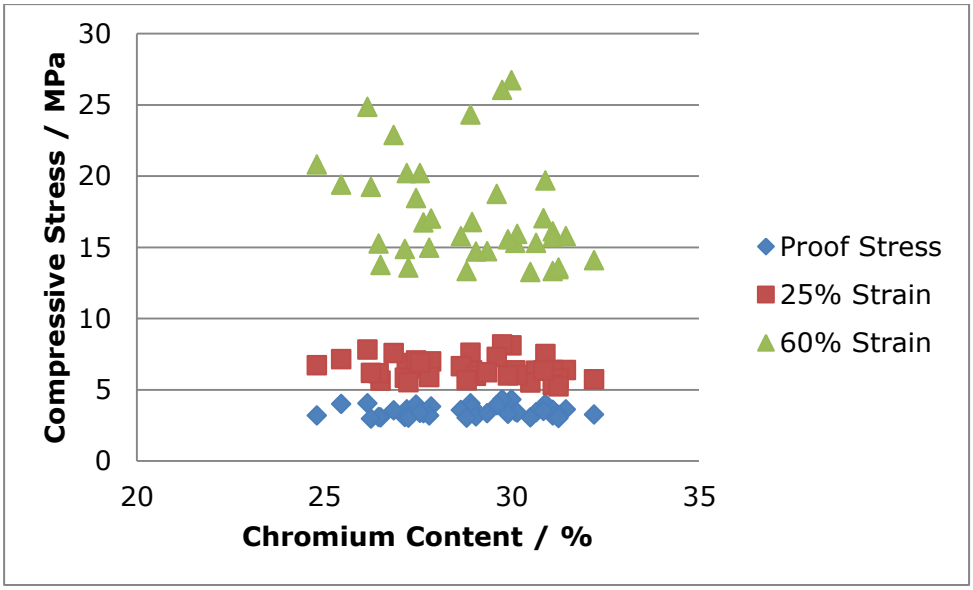


Figure 4-30 Compressive stress plotted against the chromium content for the 1723 foam

4.3.1.6 Density vs Compressive Stress

The effect of the density on the compressive stress of the samples was investigated by plotting the bulk densities calculated for each 1723 foam sample against the proof stress and the compressive stresses at 25% and 60% strain (Figure 4-31). From the plot it can be seen that there is a strong correlation, with the increase in density resulting in an increase in compressive stress.

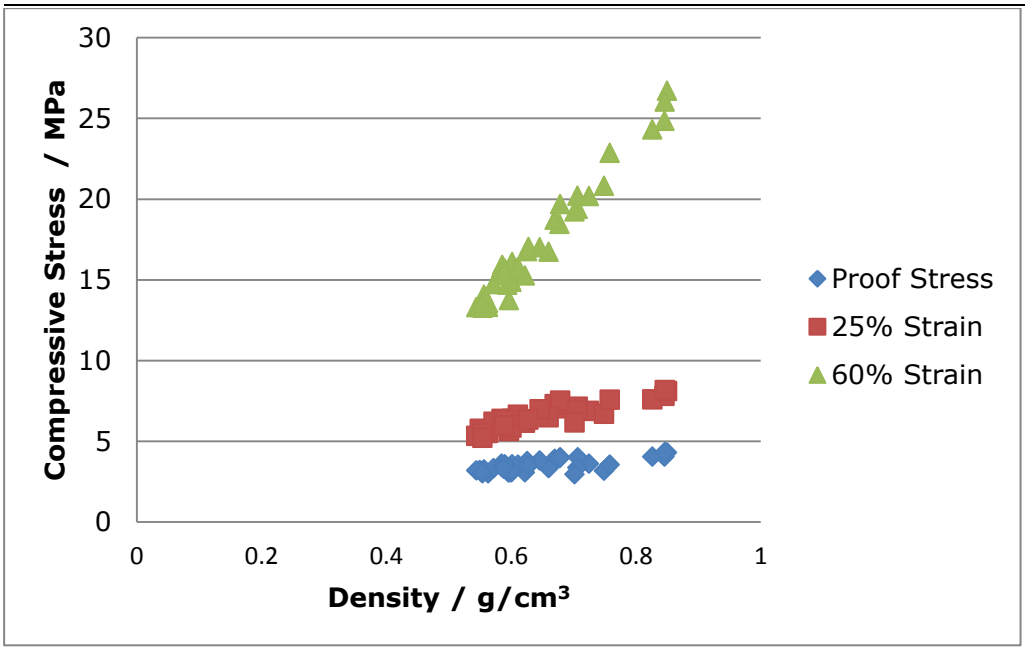


Figure 4-31 Plots of the compressive stresses against density for the 1723 foam samples

Further analysis of the effect of the density was performed by plotting the relative yield against relative density to better compare the two foams. Figure 4-32 shows the plot of the relative yields and densities for the 1723 samples and the 1116 samples in both the ST and LL orientation. Each plotted point represents the average for the column in the sheet (1116 samples are all from the single strip) with the bars representing the variation in properties in the column. It can be seen that the majority of the 1723 samples and the 1116 ST samples show a strong correlation with the model relationship defined in Eqn 2-1, with a constant C of 0.3.

The 1116 LL samples were shown to have a higher relative yield stress than the 1116 ST samples. This would be expected as the "dark band" does not reduce the yield strength in this orientation, and the cell orientation is different. From the plot it was calculated

that the 1116 LL orientation samples correlate with a constant C = 0.5. A more thorough determination of the constant value would require samples to be tested over an entire sheet similar to the 1723 samples.

Two points of the 1723 sample did not correlate as well with the model as the rest of the sheet samples. Both columns A and AC which were located at the edges of the sheets, display a similar gradient on the plot but fall below the model line. From the positioning of the points on the plot it would indicate that the values calculated for the relative density are wrong. Previous investigations had shown that the Cr content was not relatively high in these locations, and the pycnometry results showed that the volume of material present at the edges was higher, which is not accounted for in the bulk calculations. If the volume of material is actually higher, then the calculated density will be reduced, and as less Cr diffused into the thicker struts the bulk material density value should likely be higher as well. The change in these values would reduce the relative density shifting the points towards the model line on the plot.

Altering the density for the edge sample points of the 1723 foam sheet would also correct what appears to be a contradiction between the Compressive Stress – Density plot and the Relative Yield – Relative Density plot, which both show a straight linear trend despite the relative plot being on a logarithmic scale. The shifting of the edge sample points along the density axis of the Compressive

Stress-Density plot would begin to create a curved trend line, where-as the shift on the Relative Yield – Relative Density plot would put the points closer to the straight trend line.

As can be seen in the Relative Yield - Relative Density plot the 1723 samples of the same relative density have a higher relative yield than the 1116 samples. Although there may be some shifting in the relative density axis for the 1116 plot point, due to the way in which the density was calculated (similar for the 1723 edge samples), the pycnometry results did show that the 1116 and 1723 samples were of the same relative density. This would likely have been proven had a wider selection of 1116 samples been available.

The variation in strength is not therefore due to the density, and it was previously shown that the pore size difference, although showing a slight trend, did not correlate either. The plot of the Chemical Composition – Compressive Stress showed that variation in the Cr content had minimal effect on the strength for the 1723 sample, and although chemical analysis was not performed on the 1116 samples Recemat states that the 1116 material should have a composition within the same range as the 1723. The main difference between the two types of sample that has been observed is that of the diffusion of Cr. The SEM and EDX work undertaken showed that in the case of thick walled struts, like those of the 1116 samples, there was a Cr layer with, where-as the relatively thinner struts of the 1723 had more Cr diffused within. The bulk yield values used to calculate the relative yield were based off of material with diffused

Cr content. As the 1116 sample does not have fully diffused Cr (similar to the 1723 edge samples) the position on the plot may not be in error, and a more representative bulk yield value would correct this. The origin of the variation in strength in the foam samples therefore is linked to the amount of Cr that has diffused into the struts to assist through solid solution strengthening.

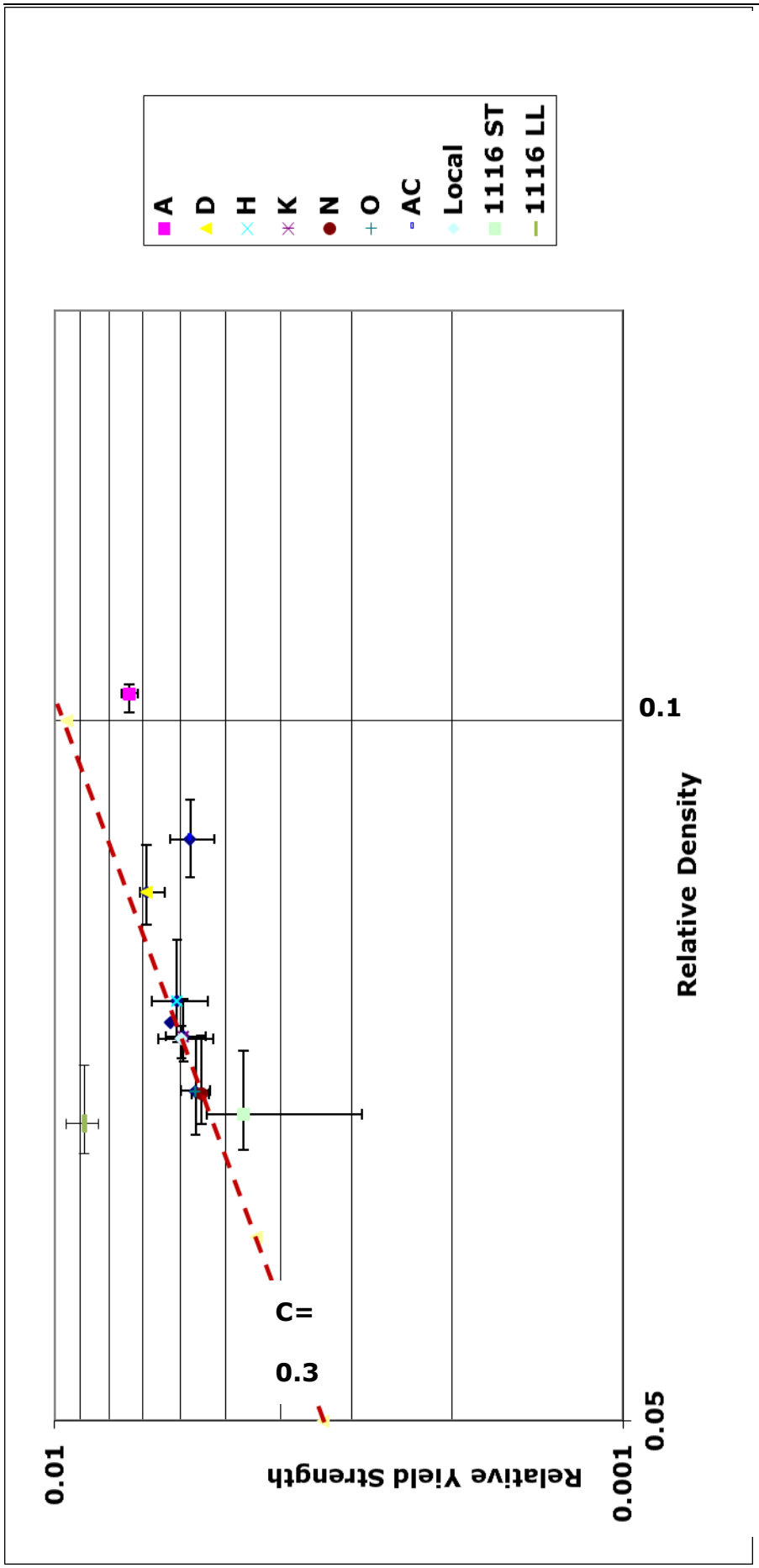


Figure 4-32 Plot of the relative yield strength against relative density for the 1116 and 1723 foam samples, with the theoretical model line plotted as well

A new plot of the relative yield strength vs the relative density was created with the addition of the results from the study of Ni-Cr foams produced by Choe *et al*. (Figure 4-33). From the plot it can be seen that the Recemat foams exhibit both higher relative densities and higher relative yield strengths. It can also be seen that the Recemat foam samples correlate well with the theoretical model whilst the other foam samples diverge more. Choe, *et al*. quoted a gradient of 2.5 for their samples, whilst the Recemat samples conform to the 1.5 gradient.

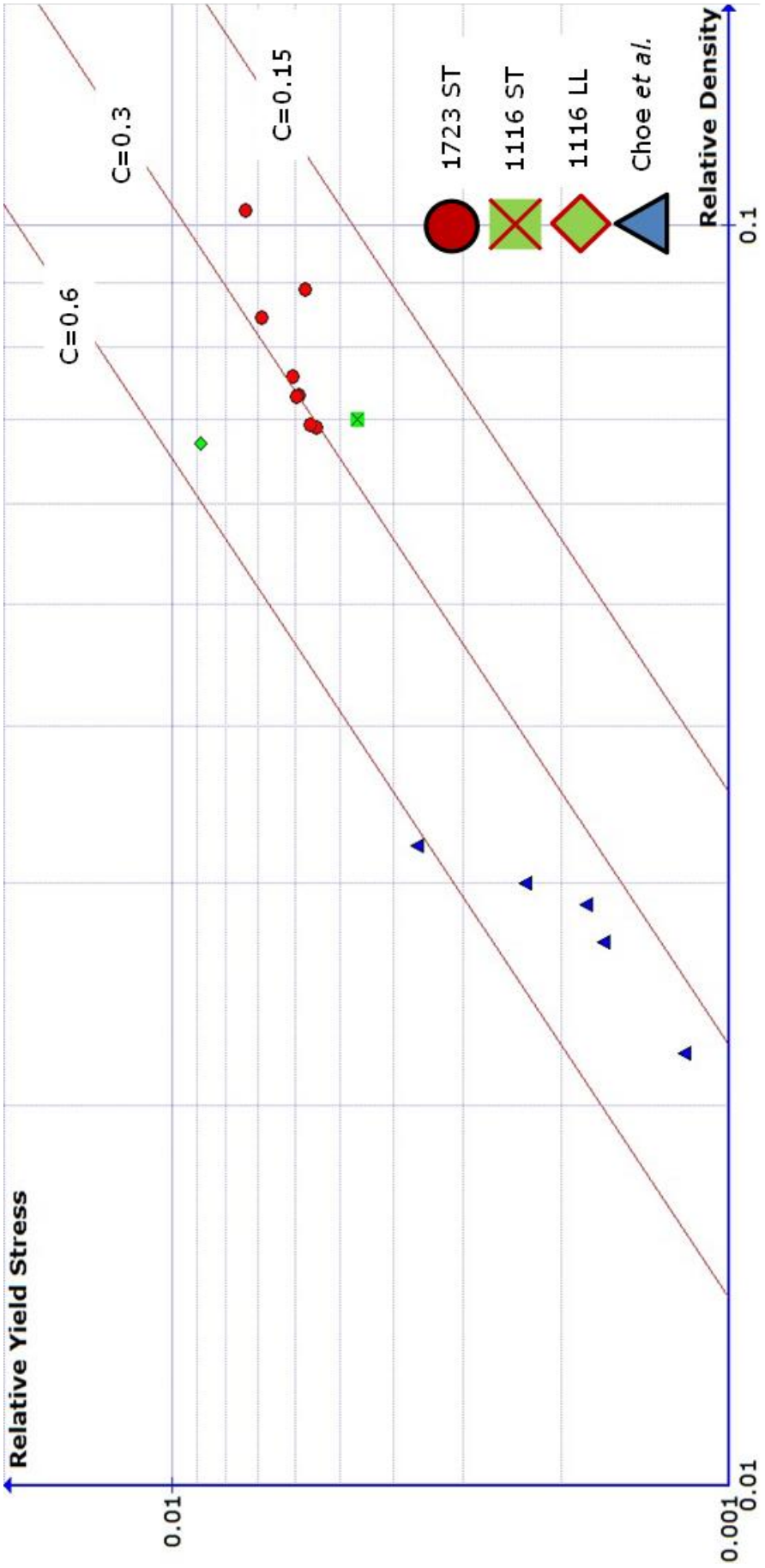


Figure 4-33 Plot of the relative yield strength against relative density for the 1116 and 1723 foam samples, as well as the plots of the Choe, *et al*. samples.

4.3.2 Tensile Testing

1723 Foam Samples

The results of the tensile testing of the 1723 samples showed a much lesser degree of scatter across the sheet than had been observed in the compression test results (Table 4-14). Figure 4-34 shows the stress-strain plot for the 1723 samples. It can be seen that the AC3 sample fails at a much lower stress than the others and doesn't follow the same stress-strain profile that the other samples did. Although the sample appeared to be of sound quality it did come from a corner of the sheet that had some damage and is probably the reason for the discrepancies. By removing the AC3 data the results achieve an even smaller degree of scatter (Table 4-15).

	Proof Stress	**UTS**
Mean Stress (MPa)	1.83	4.50
Standard Deviation	0.17	0.47
Variance %	9%	10%

Table 4-14. Tensile test results for 1723 samples.

	Proof Stress	**UTS**
Mean Stress (MPa)	1.79	4.63
Standard Deviation	0.09	0.23
Variance %	5%	5%

Table 4-15. Tensile test results for 1723 samples, with the removal of AC3 data.

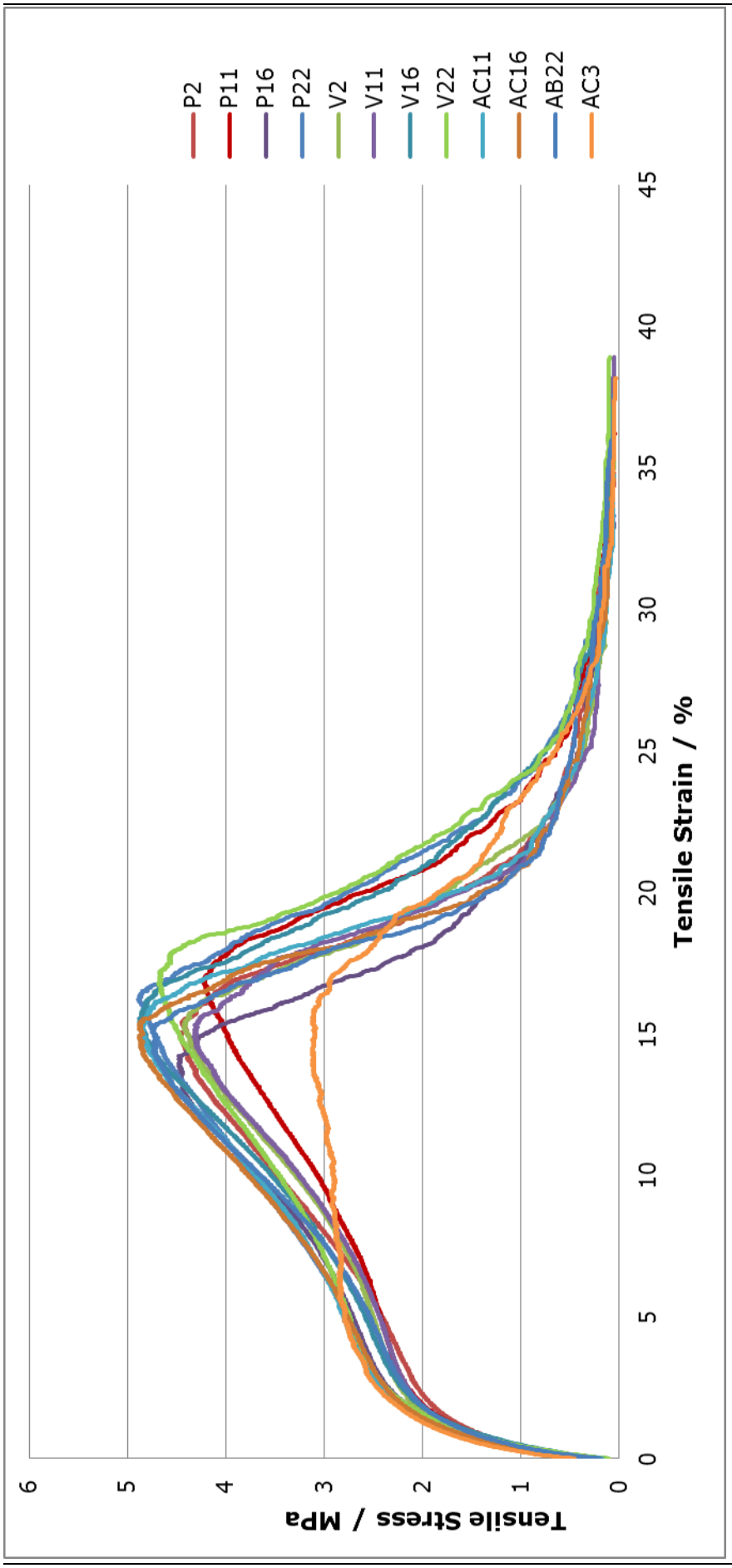


Figure 4-34. Tensile stress-strain plots for 1723 foam samples.

4.3.2.1 1116 Foam Samples

The 1116 sample results, in both the ST (Table 4-16) and LL (Table 4-17) orientations, showed good uniformity with little variation, similar to the 1723 samples. Figure 4-35 shows the stress-strain plots for the average ST and LL orientated samples. The LL orientation exhibits a conventional tensile failure plot, with a linear elastic region, followed by a linear hardening region, and then failure. The ST orientation exhibits the same plot features as the 1723 samples, with a plateau region following the linear elastic region. The LL orientation also achieves a greater proof stress and UTS than the ST orientation.

The way in which the samples failed depended upon their orientation. Figure 4-36 illustrates how the ST orientated samples begin to align the struts, within the deformed 'dark band' region, with the direction of the tensile stress. This causes the overall shape of the foam to neck within the centre. Once the struts have aligned within the deformed region, struts outside this region begin to align. Failures begin to occur in the struts, predominantly within the deformed region, until it the foam has completely failed.

Figure 4-37 illustrates how the LL orientated samples align the struts with the tensile load direction. Unlike the ST orientated sample, struts throughout the thickness of the foam begin to align. As the load is increased, the foam begins to neck and struts fail, the location of the initial failure is likely to be the weakest area within the foam. Struts continue to fail from the initial site throughout the

foam until complete failure. Figure 4-38 shows the various failure paths through the foam samples in the LL orientation.

	Proof Stress	**UTS**
Mean	1.29	3.97
Standard Deviation	0.01	0.29
Coefficient of Variance	1%	7%

Table 4-16. Tensile test results for 1116 samples in the ST axis.

	Proof Stress	**UTS**
Mean	2.31	5.12
Standard Deviation	0.08	0.07
Coefficient of Variance	4%	1%

Table 4-17. Tensile test results for 1116 samples in the LL axis.

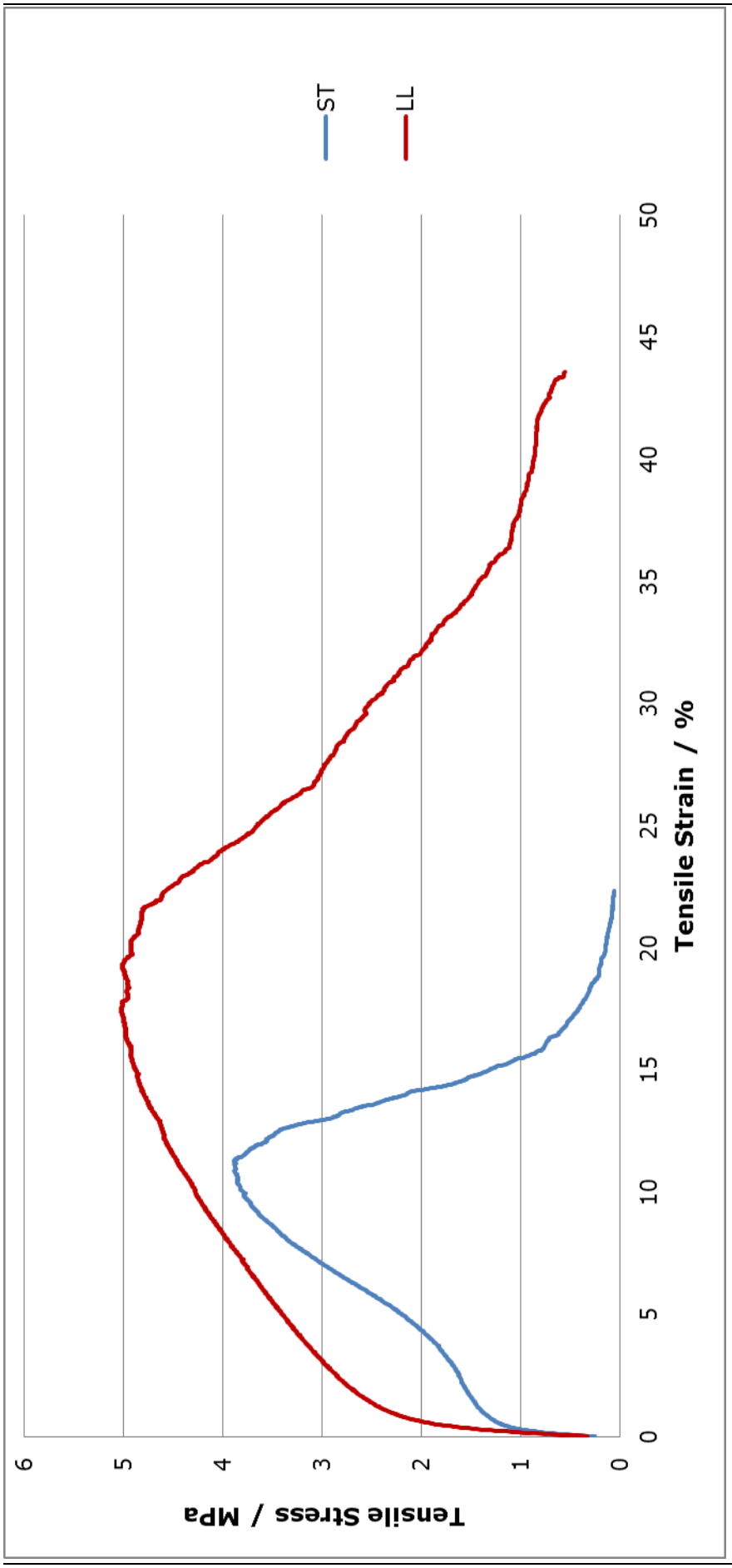


Figure 4-35. Tensile stress-strain plot comparing the ST and LL orientations for 1116 foam samples.

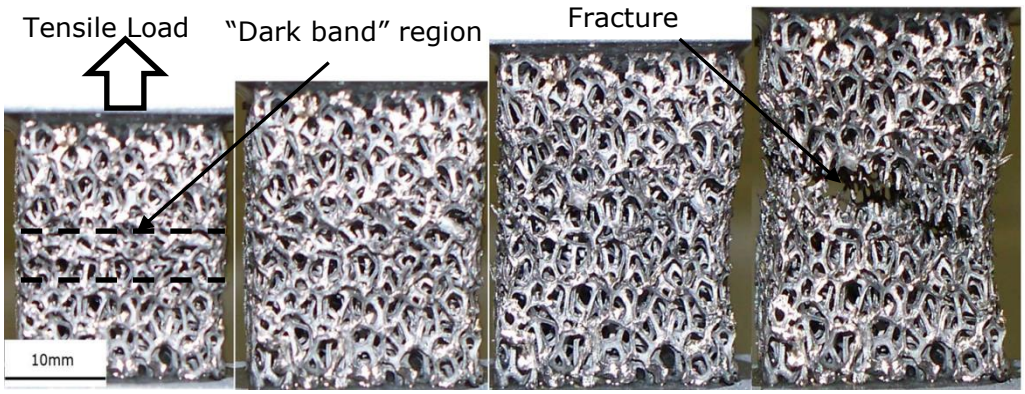


Figure 4-36. Images taken of 1116 sample during tensile testing in the ST axis, showing the deformation occuring initially in the 'dark band' region.

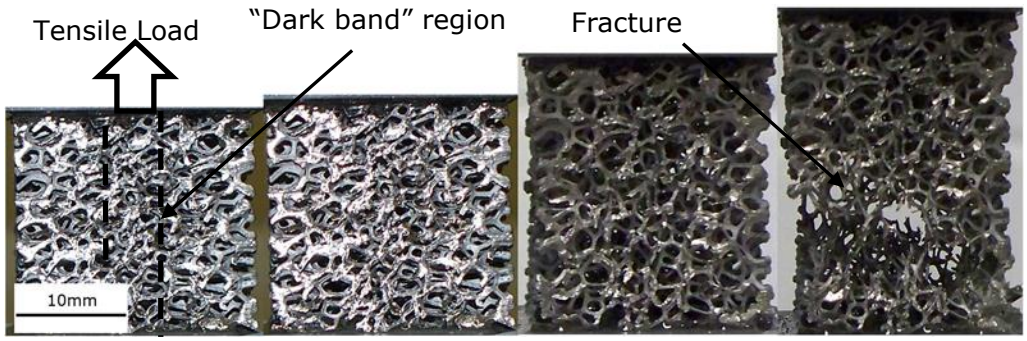


Figure 4-37. Images taken of a 1116 sample during tensile testing in the LL axis, showing the deformation occuring more uniformly throughout.

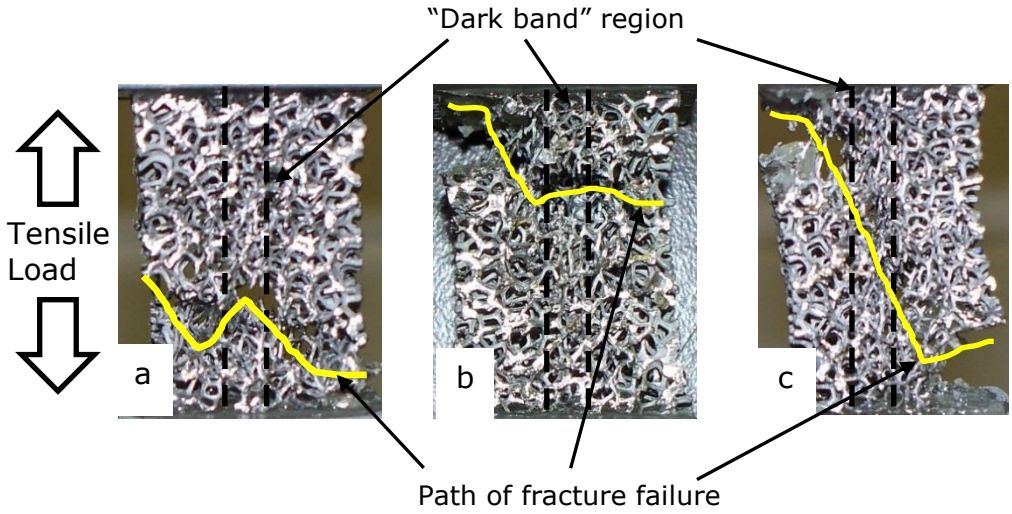


Figure 4-38. Images of the failed tensile test 1116 LL axis foam samples, (a) 1F, (b) 4F and (c) 7F, showing the path of fracture failure.

4.3.2.2 Analysis of foam struts after tensile testing

The majority of strut failures were found to be ductile and failure was initiated by necking in the strut wall. Figure 4-39 shows several SEM images from various samples that have undergone tensile testing. Figure 4-39(a) and (b) show areas where struts have been bent causing tears in the strut walls. Figure 4-39(a) appears to have had a part removed as well. Figure 4-39(b) shows the failure line through the strut as well as signs of ductile failure in the wall. Figure 4-39 (c) and (d) show the necking of the struts in 1116 and 1723 samples respectively.

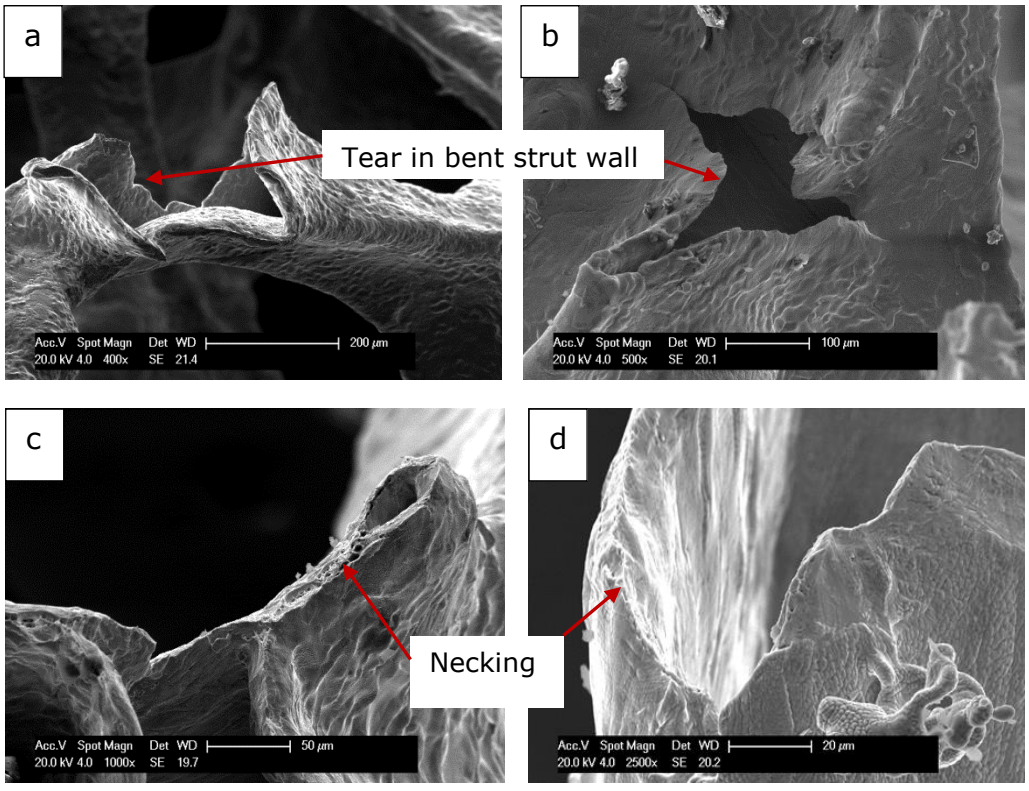


Figure 4-39. SEM images of failure sites formed during tensile testing. Images (a-b) show areas where bent struts have torn apart. Images (c-d) show struts where necking has occurred.

Figure 4-40 shows two etched struts from samples after undergoing tensile testing. Figure 4-40(a) shows a strut wall that has undergone necking, with the second phase in the necked area. Figure 4-40(b) shows a crack that has all but passed through the strut wall, indicating some brittle failures do occur. In this case however there is no second phase present. An embrittling phase was not observed by Choe *et al.* [3] in their investigation, indicating that the heat treatment that their foam samples underwent prior to testing had removed the phase.

Whilst the second phase in the microstructure is observed in the deformed 'dark band' region, the areas with the highest concentration didn't always correspond to the failure sites. This indicates that it is more likely that the crack initiation sites were defects on the surfaces of the strut walls caused by the manufacturing of the foam, as discussed in the literature review.

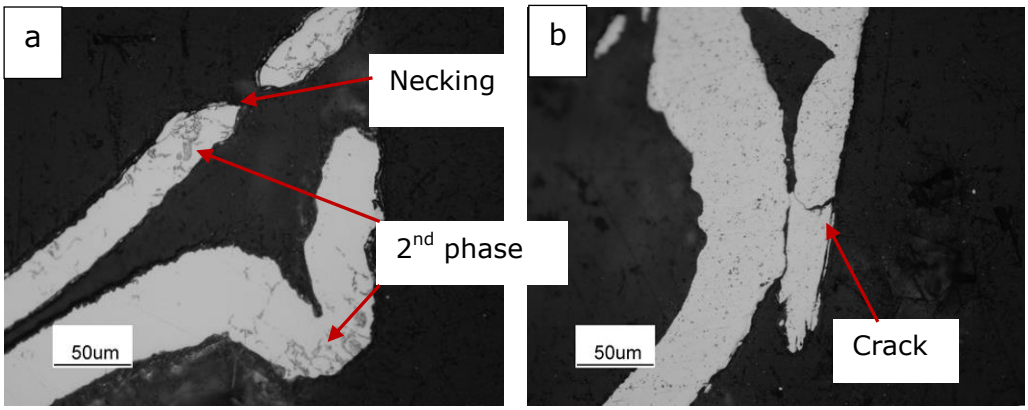


Figure 4-40. Etched images of struts from samples that have undergone tensile testing. Image (a) show the cross-section of necked strut with a second phase present. Image (b) shows a strut through which a crack has past.

4.3.2.3 Pore Size vs Tensile Stress

In order to analyse the effect of the pore/cell size on the tensile strength of the foam, a plot of the two was compiled. Unfortunately, similar to the compression test, samples used for X-ray CT analysis were not used for any mechanical testing, due to the X-ray CT machine having a maximum sample size that was smaller than the size used for mechanical testing. Therefore the pore sizes which were averaged over each column of the sheet are plotted against the tensile stresses averaged over the same columns. Figure 1 29 shows the plot produced which indicates the trend of the larger pore size reducing the tensile stress. This correlation is to be expected, as if the model for the cell is illustrated as a cube, such as the one discussed in the literature review, then a longer beam (wider cell) will require less force to produce the bending moment required for elongation of the sample.

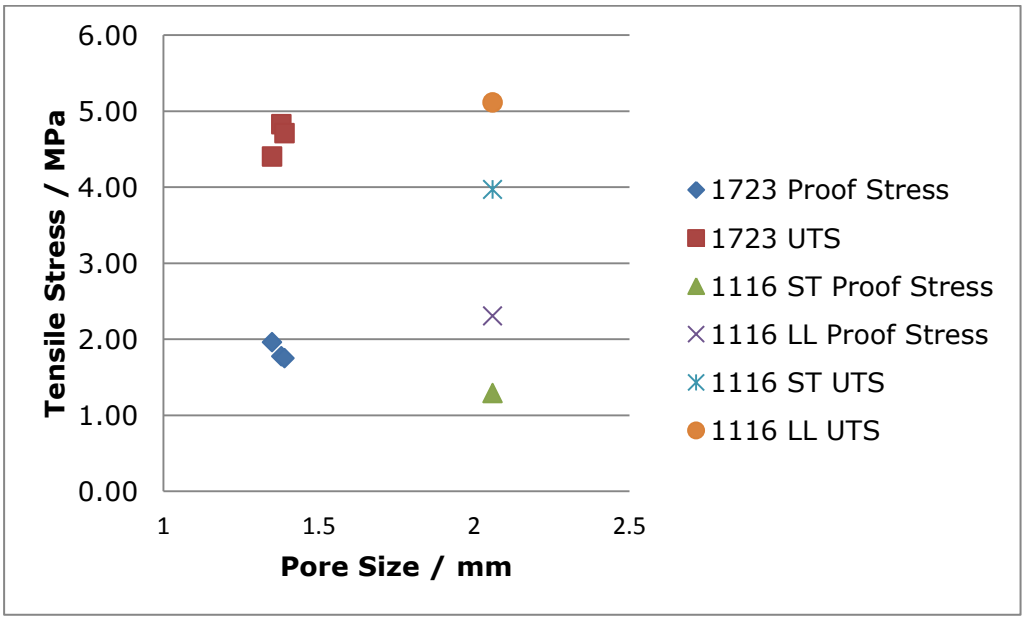


Figure 4-41 Average proof stress and UTS, plotted against the average pore size of the 1723 and 1116 samples

4.3.2.4 Chemical Composition vs Tensile Stress

To determine the effect of the chemical composition on the tensile stress of the foam, a plot of the two data sets was made (Figure 1 30). As previously stated it was not possible to measure the chemical composition of the 1116 foam samples, therefore only the 1723 samples are plotted, with their respective proof stress and UTS. No clear trend is visible in the plot. Although the UTS plot does indicate increased UTS with increased Cr content, without the addition of the AC3 sample (which failed early), the trend line does not correlate as strongly.

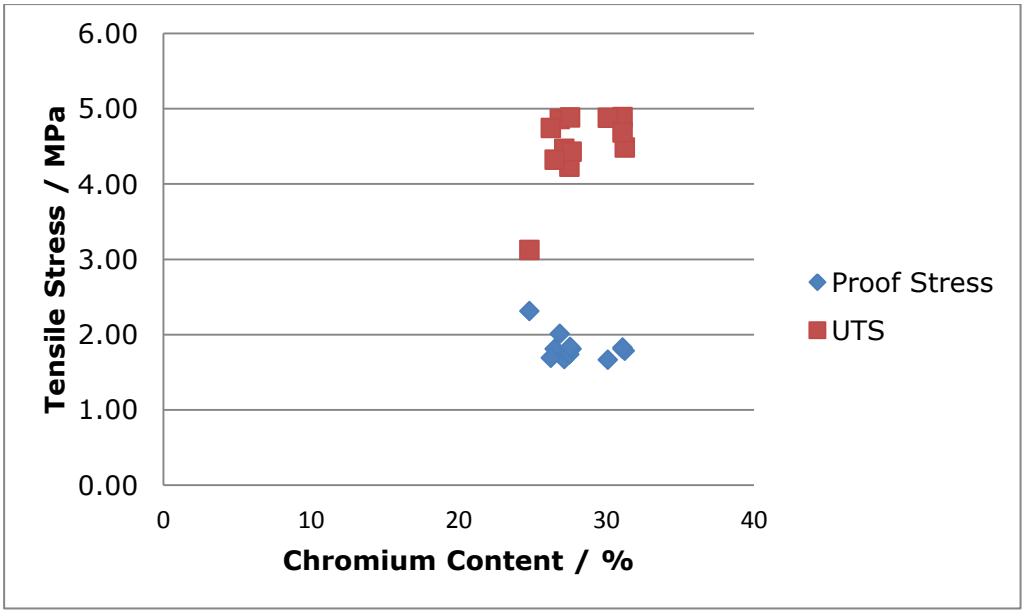


Figure 4-42 Tensile stress plotted against the chromium content for the 1723 foam

4.3.2.5 Density vs Tensile Stress

The effect of the density on the compressive stress of the samples was investigated by plotting the bulk densities calculated for each 1723 foam sample against the proof stress and the UTS (Figure

4-43). From the plot it can be seen that there is a correlation, with the increase in density resulting in an increase in the UTS. However, similar to the chemical composition plot, the removal of the early failure sample (AC3) removes the strength of the correlation.

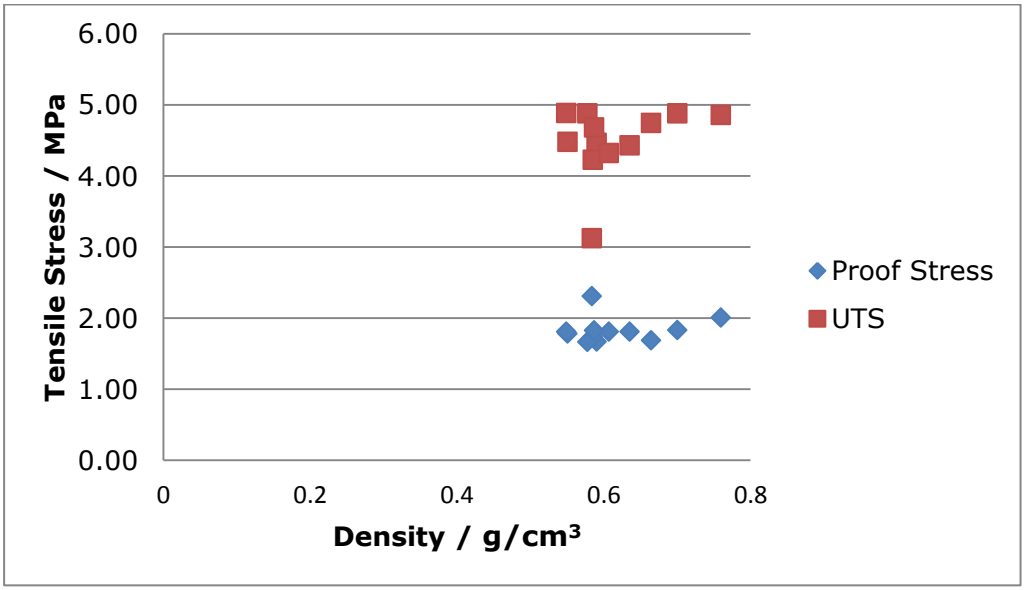


Figure 4-43 Plots of the tensile stresses against density for the 1723 foam samples

4.3.2.6 1116 vs. 1723

Figure 4-44 shows the average stress-strain plots for the 1116 and 1723 samples tested in the ST axis. It can be seen that they follow a similar profile, but the 1723 samples have a higher proof stress and UTS.

Although a trend towards higher tensile strength from increased density and Cr content the most significant factor that affects the failure of the samples are the defects present within the struts.

Failure in the ST orientated samples occurs in the deformed 'dark band' region, where the struts have the thinnest walls but also where there are the most defects, such as unzipped walls.

As the thickness of the strut walls, in the LL orientation, is similar throughout the direction of the applied force, there is no localised point for failure to occur. Failure occurs at various locations throughout the different samples, and the direction in which the struts fail is dependent on the 'weakest line'. This is the path which has the highest number of defects and thinnest strut walls.

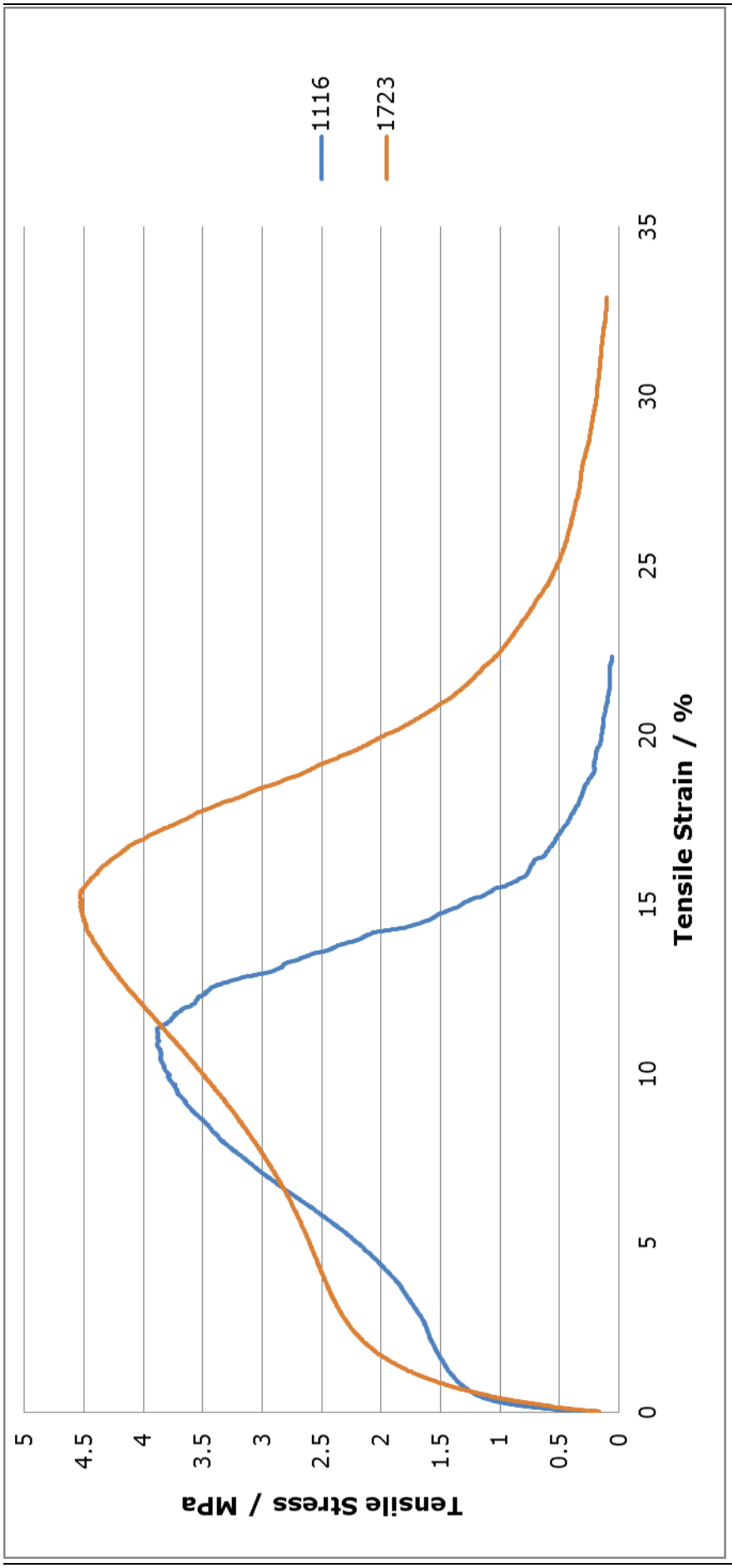


Figure 4-44. Tensile stress-strain plot comparing the 1723 and 1116 foam samples in the ST axis.

4.3.3 Comparison of Compression and Tensile Strengths

Figure 4-45 shows stress-strain plots of the average results of the 1723 and 1116 samples (in both orientations), tested with compressive and tensile loads. It can be seen that the compressive stress-strain plots for the samples have much larger variation between the tensile plots. However the tensile plots do vary in shape between the ST and LL orientations. In both cases the presence of the deformed area in the centre of the foam samples affects the results (especially in the ST orientation). A wider variance might have been observed if samples from the 1116 were tested from more areas of a sheet. Something that was not possible with the limited material available to the author.

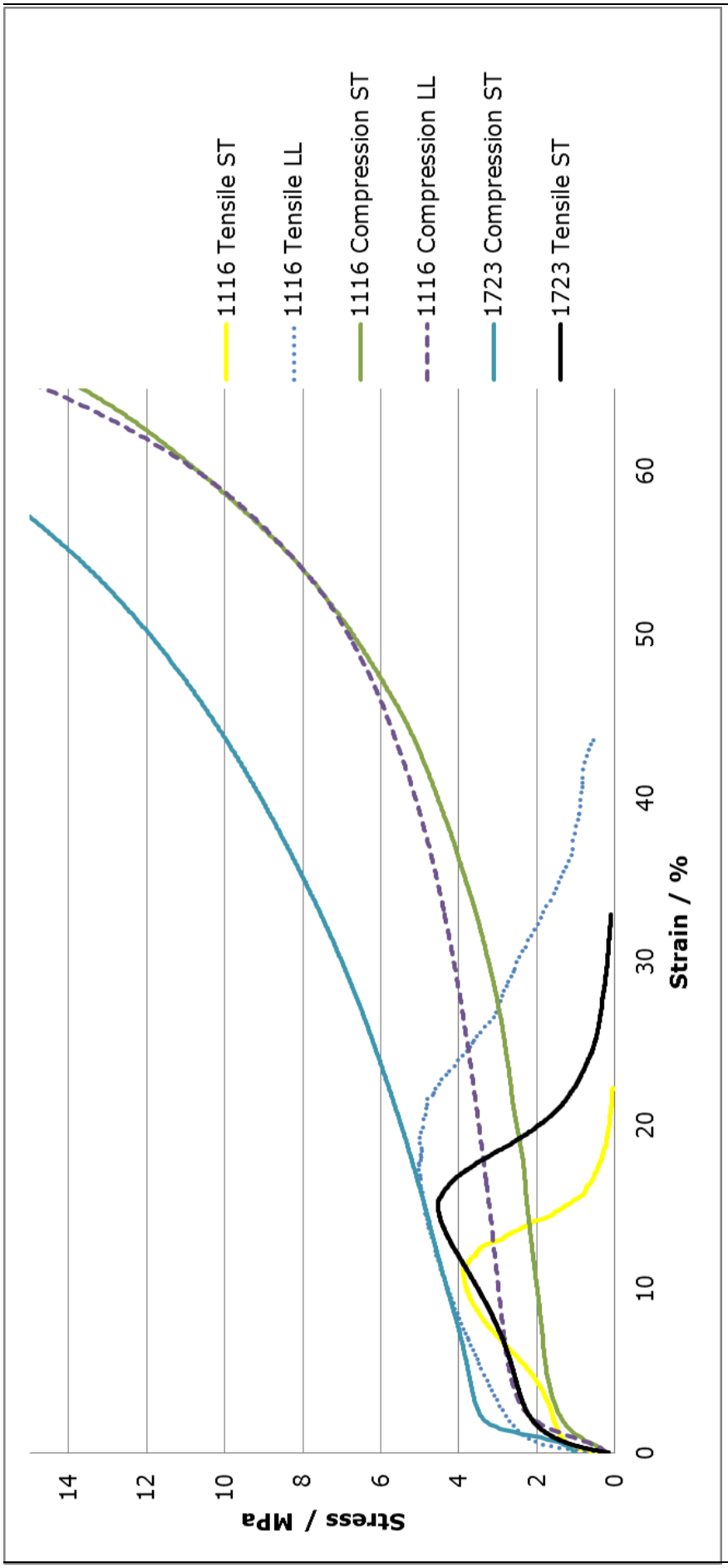


Figure 4-45. Average stress-strain plots for the 1723 ans 1116 foam samples, from both compressive and tensile loading, and in both the ST and LL orientations.

4.3.4 Machinability

Figure 4-46 shows images taken of the machined surfaces, with the tool trail direction from the bottom of the images to the top. It can be seen that in both instances the high cut depth produced the largest amount of flash, pushed out from the material by the tool bit during cutting. It can also be seen how the low depth cuts only produce flash when machined with a low tool RPM. Inspection of the cut surfaces did not show signs of smearing in the material, with the irregular strut shapes seen at the larger cut depths due to them being in the deformed 'dark band' region of the sample to begin with and not the result of the tool causing plastic deformation.

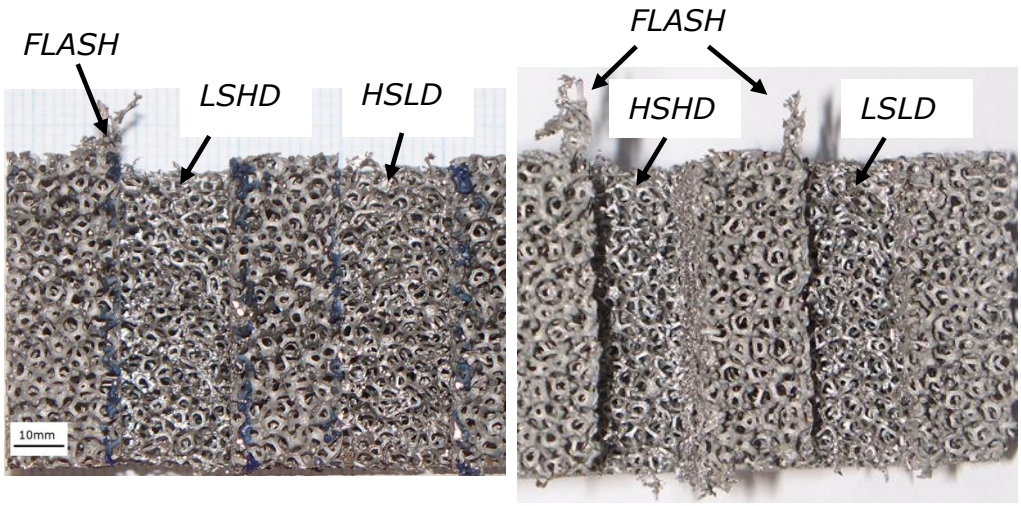


Figure 4-46. Images of the resulting finishes from cuts made at, low tool speed high cut depth (LSHD), high tool speed low cut depth (HSLD), high tool speed high cut depth (HSHD) and low tool speed low cut depth (LSLD). The flash produced by the cuts are also highlighted.

Figure 4-47 shows etched cross-sections of the high speed cut finishes. It can be seen that the struts at the sides of the channel are cut "cleanly", with no visible deformation from their initial

positions, at both low cut depth (a) and high cut depth (b). At the higher cut depth some deformed struts were visible (c), although whether this was due to the cutting process or due to being in the deformed 'dark band' region is unclear. Figure 4-47 (d) is an image of a strut of the base of the cut channel, as can be seen the cut has taken place without the bending deformation of the strut walls.

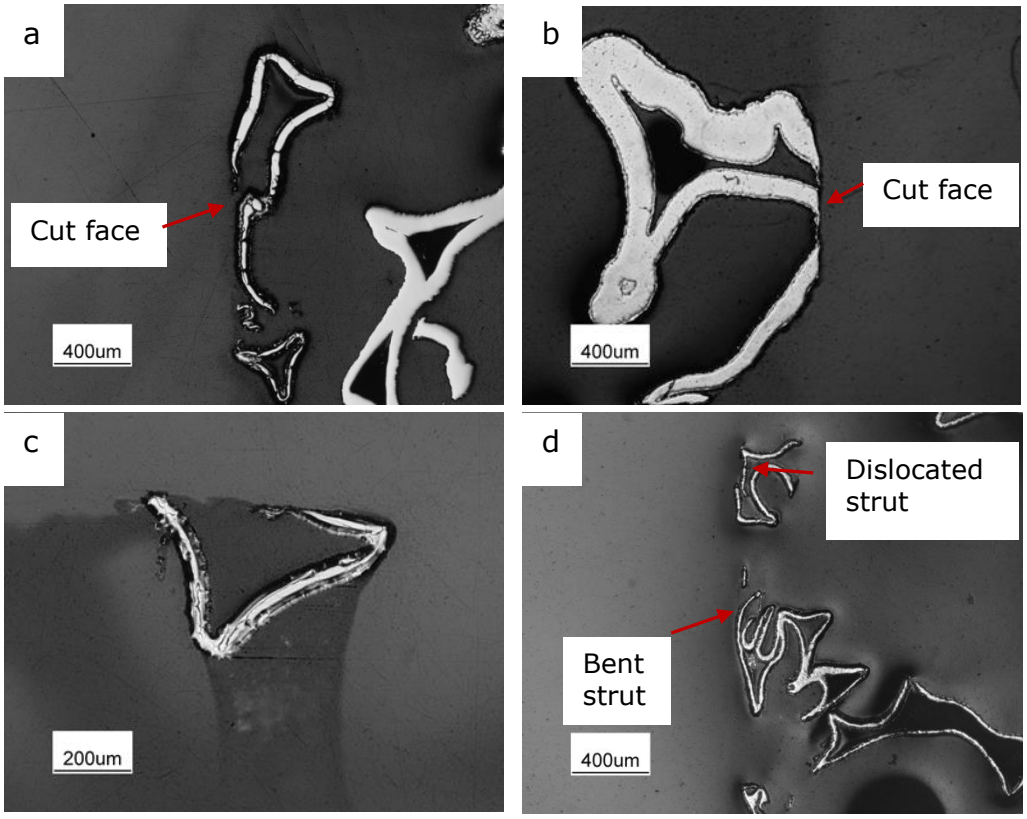


Figure 4-47. Cross-section images taken of the cut faces of the channel walls, machined at high speed. Images (a-b) are cut struts from the side walls of the material cut at low depth, and high depth, respectively. Image (c) is a cut strut from the base of the base of the high depth cut. Image (d) shows cut and deformed struts from a high depth.

Figure 4-48 shows etched cross-sections of the low speed cut finishes. Figure 4-48 (a-b) are struts in the walls of the channel from a low depth and high depth respectively. Figure 4-48 (a) shows a strut which has been cut but has also deformed during the process.

Figure 4-48(b) shows struts that have not been cut, but are at the surface where the cut face is, indicating movement away from the cut plane before the tool arrived at its location. Figure 4-48 (c) is an image from the base of the channel with the cut plane marked. It can be seen that the strut on the right of the image has not been cut or deformed, whereas the strut on the left has. Again this indicates movement of the struts prior to the tool reaching the location. Figure 4-48 (d) is further proof of strut movement. Within the image it can be seen that the two cut faces don't align, with the bottom strut pushed into the channel, indicating movement after cutting.

Comparing the deformations created by machining, it can be seen that shallow depths of cut at high tool RPM produced the best results, as had been reported in the literature. The high RPM of the tool caused cuts to the struts, which failed in a brittle way. This produces a better finish than the high depth and low tool speed cuts. At the low RPM some struts deformed plastically, bending out away from the cut surface rather than being cut. Some struts after being forced back away from the cut path by the incursion of the tool, rest back close to their original position. This of course creates imperfect geometry. Optimal machining parameters would therefore be suggested to be high tool RPM at low depth of cut.

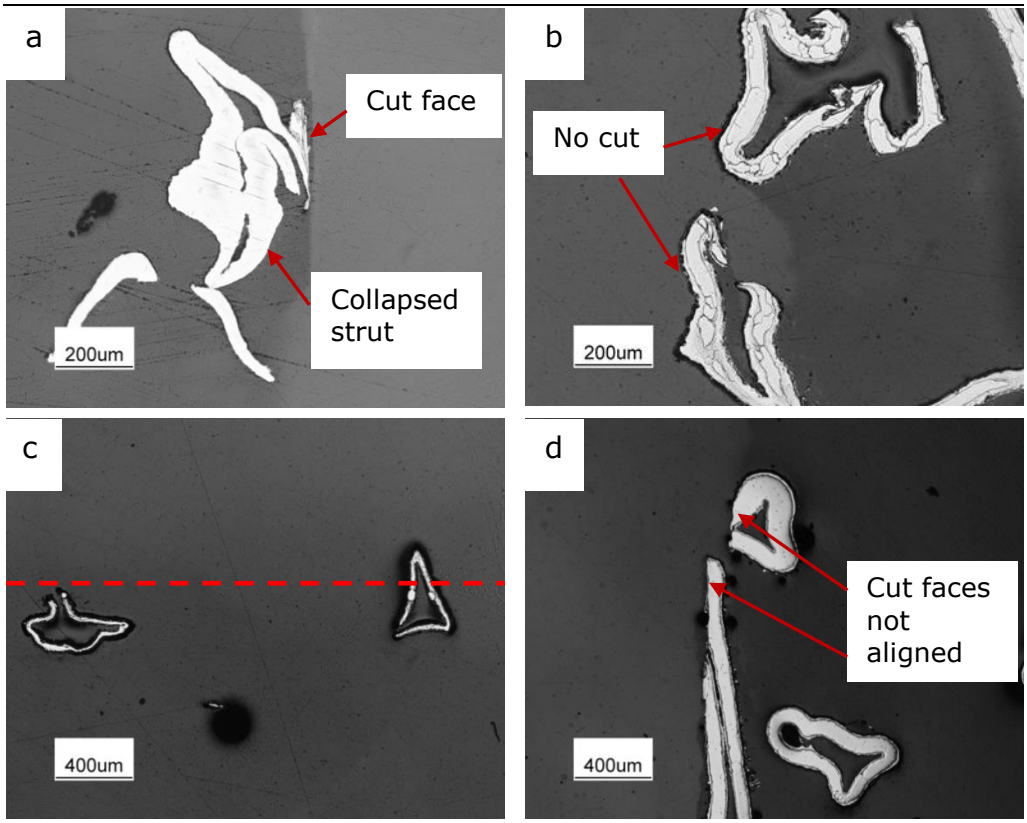


Figure 4-48. Cross section images of the channel after machining at low speed, at both high and low depths. Images (a-b) show struts from the side walls of the channel at low depth and high depth, respectively. Image (c) is an image from the base of the channel, with the cut plane highlighted. Image (d) is an image from the side wall at high depth showing misalignment.

4.4 CONCLUSIONS

The aims of the research in this chapter were; to analyse the mechanical properties of the metallic foam and the relationship of these properties to the sheets anisotropic nature. Analyse the machinability of the metal foam, and the optimum machining parameters.

Microscopy analysis of the un-brazed foam material revealed that the samples have a 'dark band' deformed region running through the longitudinal length of the samples. The struts of the samples

also have thicker walls nearer the surface, which have a grain structure and thinner walls in the middle with a secondary phase present. The distribution of strut size, as well as the deformed region, leads to the already deformed region being the initial deformation site. The 'dark band' could be caused in several ways; it could be an inherited defect from the original polyurethane, caused during the manufacture or cutting process, or it could be caused during cutting of the metal foam sheet by the manufacturer. It is most likely however to be a result of the thickness control by the manufacturer, whereby the sheet is fed through rollers with a gap of specific thickness.

Compression testing revealed that the 1723 material was found to be of higher strength than the 1116 material. High compressive strength regions were found at the edges of the 1723 sheet, with lower strength regions towards the centre of the sheet (as 1116 sample was only a strip it is assumed that it will also have these variations across its entire sheet). There is a good correlation between the strength plots and the density plots. However there isn't between the Cr content and the density. The Cr content distribution is not well defined with high content areas at both the edge and the centre of the sheet. Analysis between the chemical composition and the strength, as well as the relative yield and relative density, suggests that the lack of Cr diffusion into the thicker struts reduces the strength of the foam samples, which is why the 1723 foam material is relatively stronger than the 1116 material.

Tensile testing revealed that failure was dependent upon the defects within the foam, rather than the density variations throughout the sheet material. LL orientated samples had a higher tensile strength than those of the short traverse orientation, predominantly due to the deformed 'dark band' region having a low tensile strength. This region was also found to cause a plateau region to occur in stress-strain plots of the ST orientated samples.

The relative yield strength against relative density for the ST orientated samples was observed to have a strong correlation with the theoretical model with the constant of C=0.3. Two set of samples that did not correlate with the theoretical model where from the edges of the sheet. It is believed that a better correlation would be achieved if the relative density was calculated using a larger volume that better represented the sample. The pycnometry results indicated that a larger volume of material (strut wall) was found in the edge samples when compared to the main bulk of the sheet. Further improvement to the correlation would result from the use of a lower solid yield stress when calculating the relative stress. Although high Cr content was recorded for the edge samples, the EDX analysis showed that thicker strut samples had not diffused the Cr. The struts would therefore not correspond to the solid material stress of the same Cr content.

The LL orientated 1116 sample had a larger relative compressive strength and it was found to correlate more with a constant C=0.5.

Analysis of the machinability of the foams revealed that fast tool speed, at low depth of cuts produced the best results. Lower speed and higher depths of cut produced bending of the struts rather than cutting. In some cases this caused some struts to be moved out of the cutting path, only to return to their original positions after the tool had passed. The effect could be problematic, when filled for sealing, on the geometry and could introduce stresses to the parts.

5 ANALYSIS OF BRAZED FOAM MATERIAL

5.1 OPTICAL AND SCANNING ELECTRON MICROSCOPY OF BRAZED FOAM

From initial observations, by eye, of a Ni plate sample (with a layer of braze and without any foam attached), indentations were visible across the surface. In Figure 5-1 several large indentations are visible, along with the markings of were cuts were to be made for further analysis. Whilst a braze layer is not expected to be of perfect uniform thickness, these indentations were remarkable in that they were of a depth that reached the plate surface.

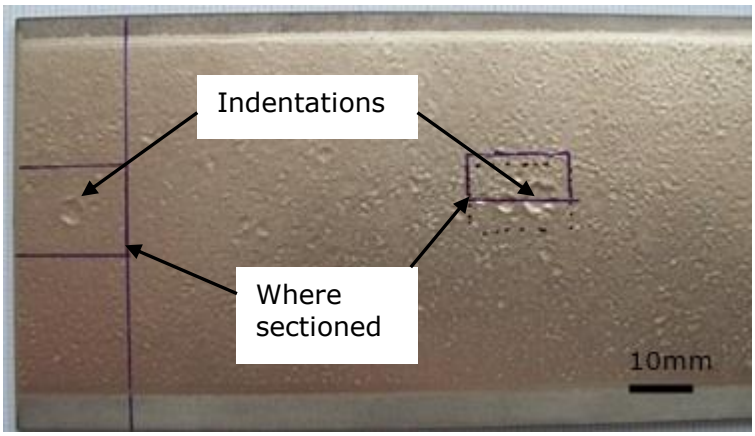
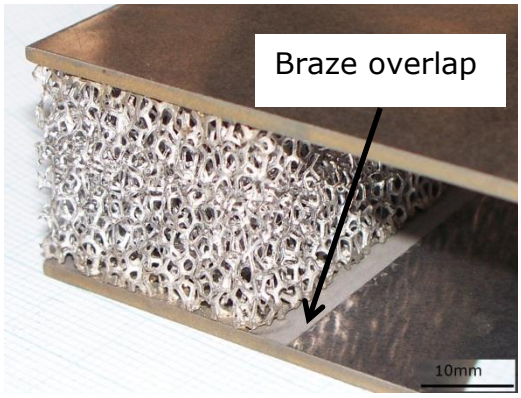


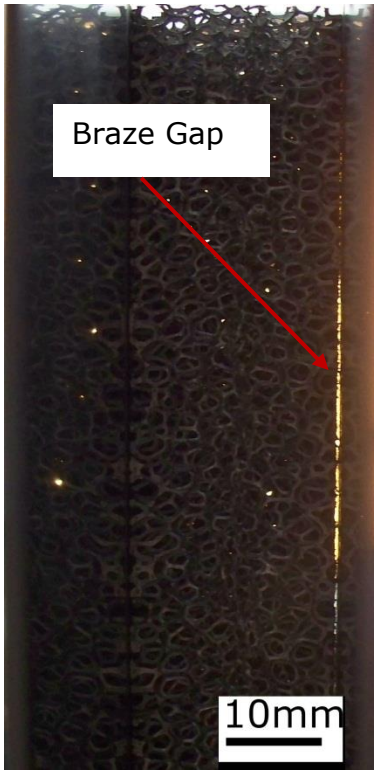
Figure 5-1. Ni plate with braze layer showing several large indentations in the braze layer.

Figure 5-2 (a) is an image of a sample manufactured for shear testing, where the overlap of the braze tape is visible. Figure 5-2(b) is an image of the same sample held towards the light, where it is clearly visible that there is a gap in the bond between the Ni plate and the foam. Once the sample had been sectioned by EDM the poor

bond region could be examined. Figure 5-3 (a) shows the foam surface with braze material coating the struts, indicating that the braze and foam were in contact during the manufacturing process. Figure 5-3 (b) shows the braze surface of the Ni plate that corresponds to Figure 5-3 (a). It can be seen that there is a "dull" area which covers the majority of the surface, and a "shiny" area which covers a thin strip on the inner edge. Figure 5-4 is an image of another sectioned sample with which the foam and Ni plate have come apart. Again there is braze material on the foam struts, and areas which are "dull" and "shiny" on the Ni plate, although on this sample it is roughly a 50/50 divide.



a



b

Figure 5-2. Images of samples manufactured for shear testing. Image (a) shows the overlap of the braze layer. Image (b) shows the gap in the bond between the foam and Ni plate.

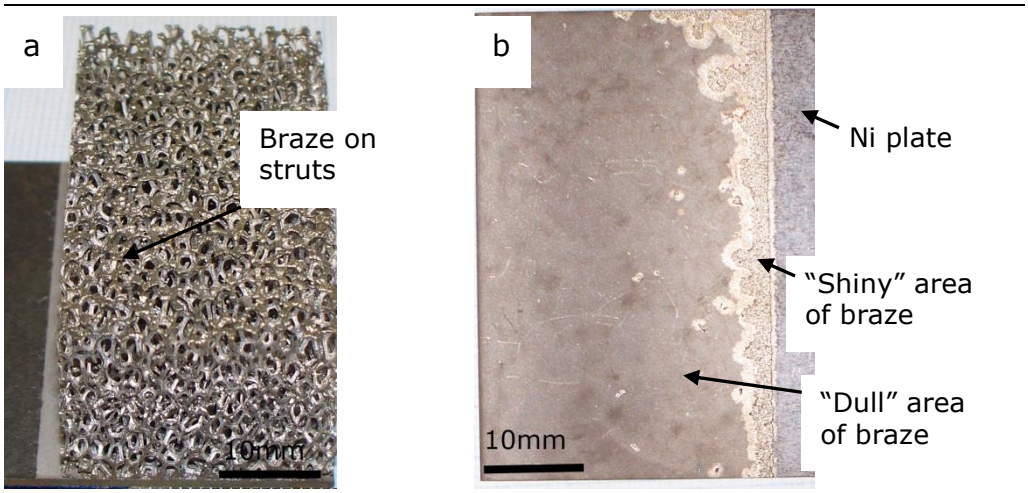


Figure 5-3. Images of foam and plate section region of no bond in Figure 5-2. Showing the braze on the struts (a), and the predominantly "dull" area seen, along with a small strip of "shiny" along the edge of the Ni plate (b).

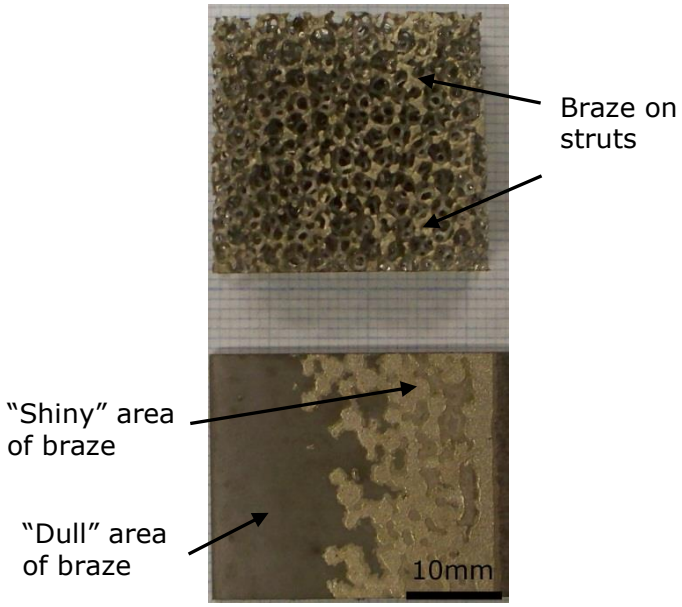


Figure 5-4. Image foam and Ni plate from sample with a poor bond. It has a "dull" and a "shiny area" on the plate ~ 50/50 split.

Analysis of the etched brazed Ni plate showed that there was several phases present throughout both the plate and braze. Figure 5-5 (a) shows the braze layer, which has a darkened region below, which is above the fine grained Ni plate. Figure 5-5 (b) is a magnified

image and shows that there is a secondary phase within the braze layer, and that the darkened region is a series of needle-like and blocky phase structures similar to those reported by Pouranvari, *et al.* [52].

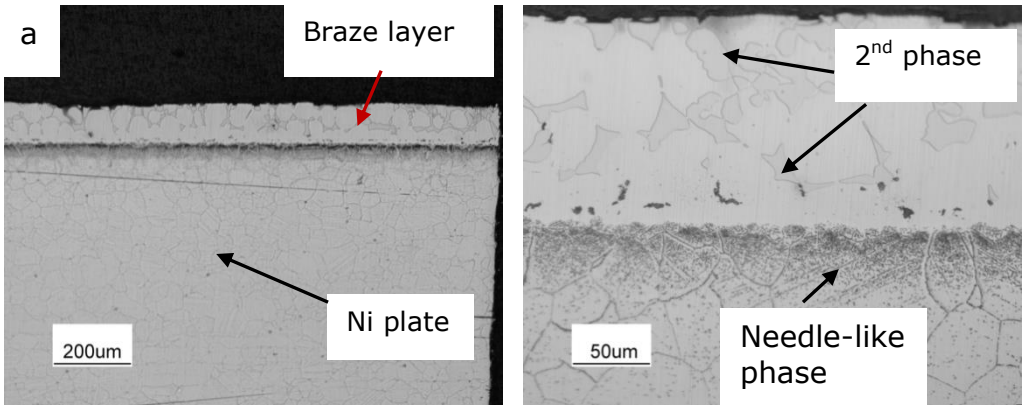


Figure 5-5. Etched images of the braze layer on the Ni plate with a fine grain structure (a). A secondary phase is seen within the braze layer as well as a needle-like phase below the braze (b).

Figure 5-6 shows an SEM surface image of the indentation area edge. It can be seen that the lower area (within the indentation) has a smaller grain size than that of the top area. Figure 5-6 shows an etched cross-section view of the indentation edge. The secondary phase within the braze layer has become more concentrated, which is the reason the grain structure on the lower area appears to have a finer grain structure. Figure 5-8 shows the area where the braze ceases to cover the Ni plate. The needle-like phase does not appear within this region, unlike the areas where braze is present. Figure 5-9(a) and Figure 5-9(b) show high magnification images of the no-braze area, and the edge of the braze area respectively. It can be seen that in the area of no-braze there are no secondary phases

present unlike the braze edge area. Although the braze edge area does contain a secondary phase it is much less than that found in that areas of braze outside the indentation area.

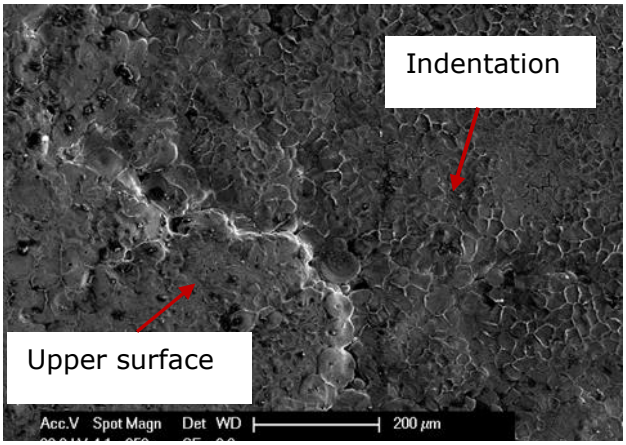


Figure 5-6. SEM image of the indentation edge, with larger grains visible on the upper most surface.

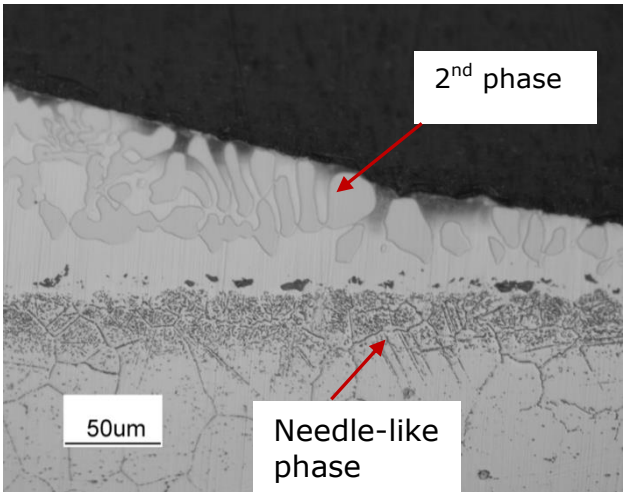


Figure 5-7. Image the etched braze layer close to the edge of the indentation area, showing the secondary phase crowding the braze layer.

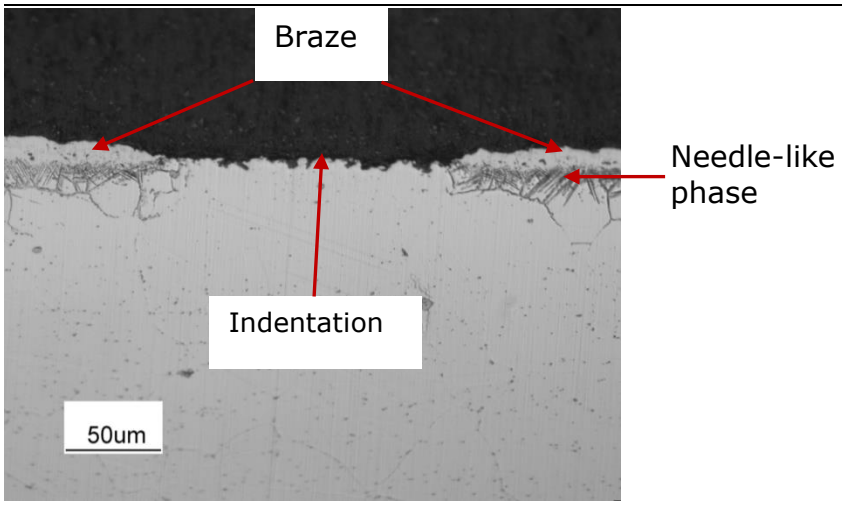


Figure 5-8. Etched image of the centre of the indentation. There is no braze and unlike the braze layer either side there is no needle-like phase either

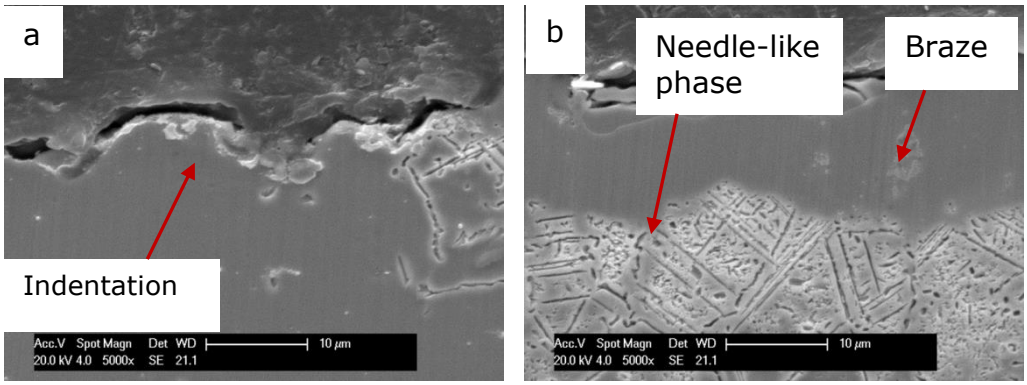


Figure 5-9. SEM images of the indentation area. (a) shows the area of no braze which shows no secondary phase. (b) shows the area of braze just before the no braze area with several phases visible.

Figure 5-10 is an image of the etched Ni plate of a sample which has had foam brazed to it. In comparison with the brazed Ni plate (Figure 5-5(a)) it can be seen that the grain size is larger throughout. Figure 5-11 shows a strut which has been brazed to the Ni plate. The secondary phase present in the braze layer is like that which is seen without the foam, however the needle-like phase is

not present. Within the foam strut walls another phase is visible similar to that seen predominantly in the struts in the middle of foam samples. Along the edges of the strut can be seen the Cr phase layer with braze material which has wicked up the sides. In the centre of the strut, in an area usually void, there is material with phases similar to that of the braze layer. Elsewhere in the foam sample similar fillings were seen. Figure 5-12 (a) is a strut from a non-brazed foam sample, and Figure 5-12 (b) is a strut from a brazed sample. It can be seen that although strut (b) is similar distance from the surface of the foam as strut (a), and should therefore have a void at its centre, it does not. The filler material is therefore likely to be the braze material that has been wicked through, or around, the struts.

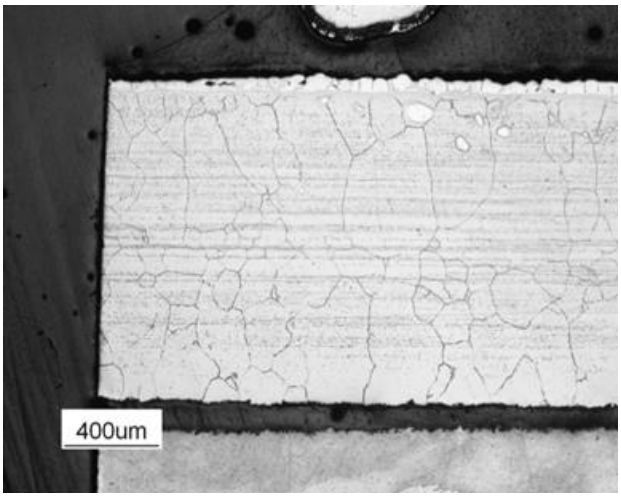


Figure 5-10. Image of an etched Ni plate from a brazed foam sample, showing a large grain structure.

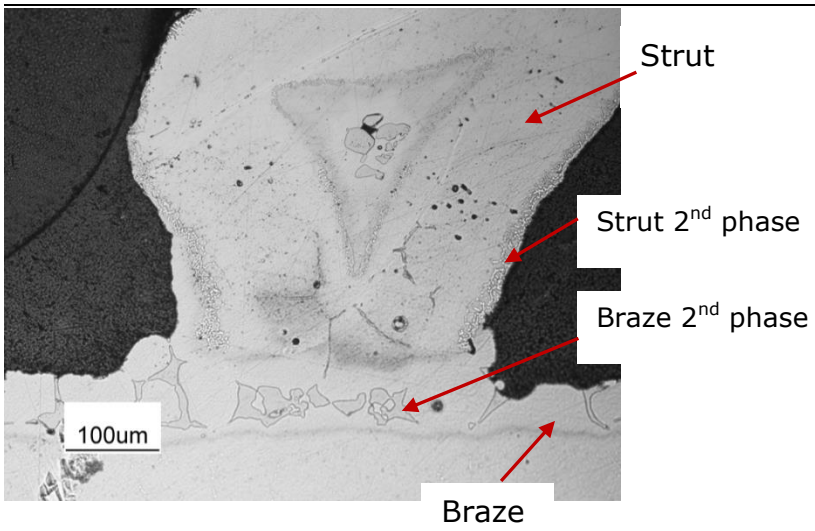


Figure 5-11. Image of a strut that has bonded well to the Ni plate with the braze. Several phases are visible but no needle-like phase below the braze layer.

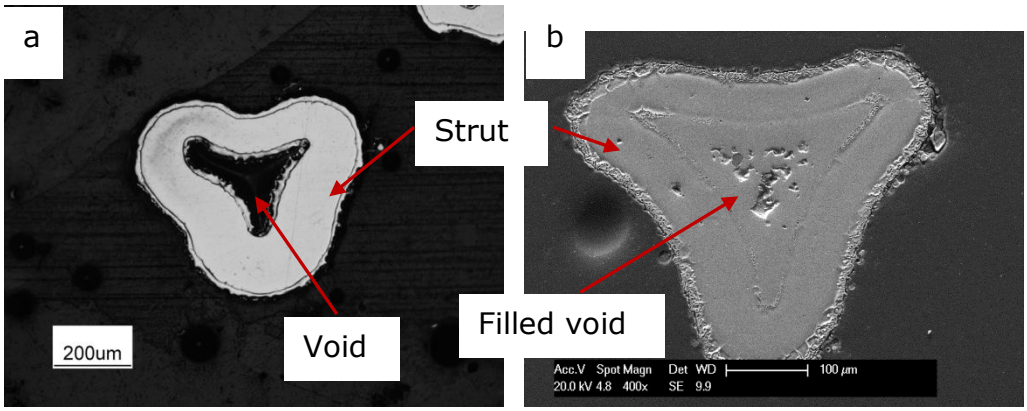


Figure 5-12. Images of two struts from roughly 2mm away from the foam surface; (a) is from a sample not brazed and (b) is from a sample that is, and contains material within its void.

Figure 5-13 is an image of a brazed foam plate. It can be seen that the strut is surrounded by braze, however there are patches within the plate where there is no braze, a "dull" area similar to that seen by an un-bonded sample. The cross-section image in Figure 5-14 shows a gap in the braze layer close to a strut that has bonded well.

The gap appears even though there are no signs of any difference between it and the areas of braze layer. A similar thing is seen in Figure 5-15 where there is a gap in the braze layer right next to where the strut has bonded.

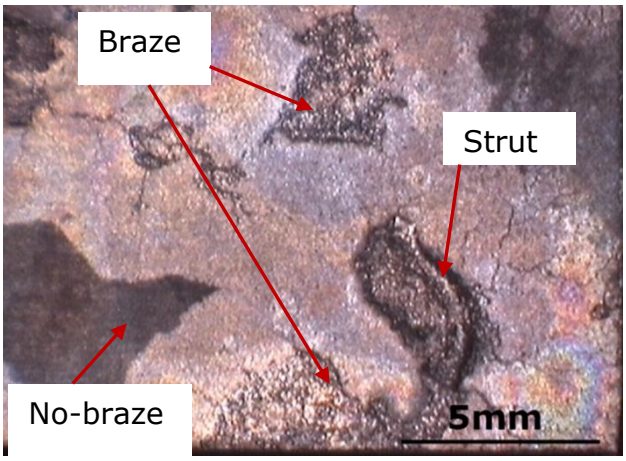


Figure 5-13. Surface of a brazed foam sample that has been sectioned, showing braze concentrated around a strut along with a "dull" area of no braze close by.

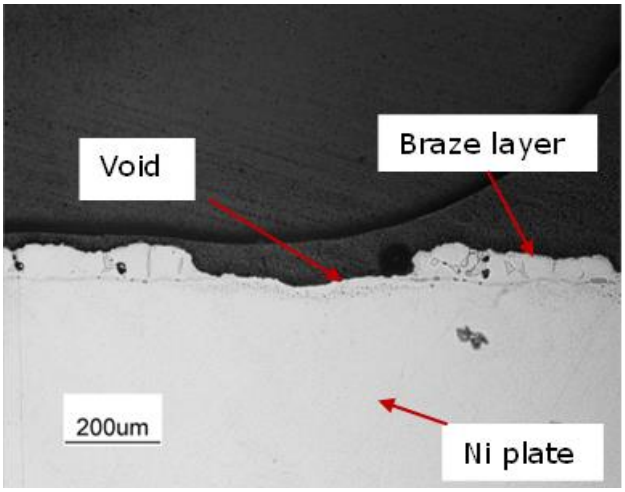


Figure 5-14. An image of a brazed foam sample showing a void within the braze layer.

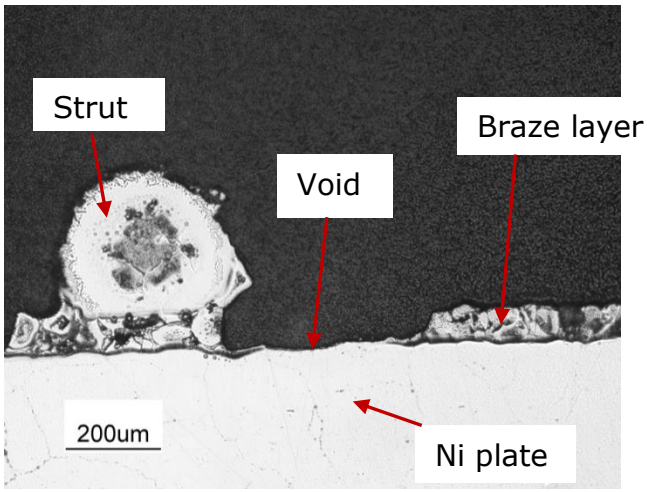


Figure 5-15. Image of a brazed foam strut, which has a void within the braze layer next to the strut.

Figure 5-16 schematically represents what is thought to be taking place, from the analysis of the various struts on the bond surfaces and the braze layer on the Ni plate. Initially set up with the braze between the plate and the strut (Figure 5-16 (a)), when the brazing heat treatment begins the braze wicks up the centre of the strut and in some cases up the sides of the hollow strut (Figure 5-16 (b)). Several variations of wicking behaviour can occur: (Figure 5-16 (c)) illustrates how if there is a gap between the braze and strut, then the capillary action won't take affect and there will be no wicking of the braze. (Figure 5-16 (d)) illustrates how in some cases only a small amount of braze is wicked up. (Figure 5-16 €) illustrates the opposite case, in which a large amount of braze material is wicked up the strut, depleting the amount of braze material surrounding the strut (and bonded to the Ni plate). Too much wicking can cause depletion of braze material from other struts with in the localised area of the foam (Figure 5-16 (f))

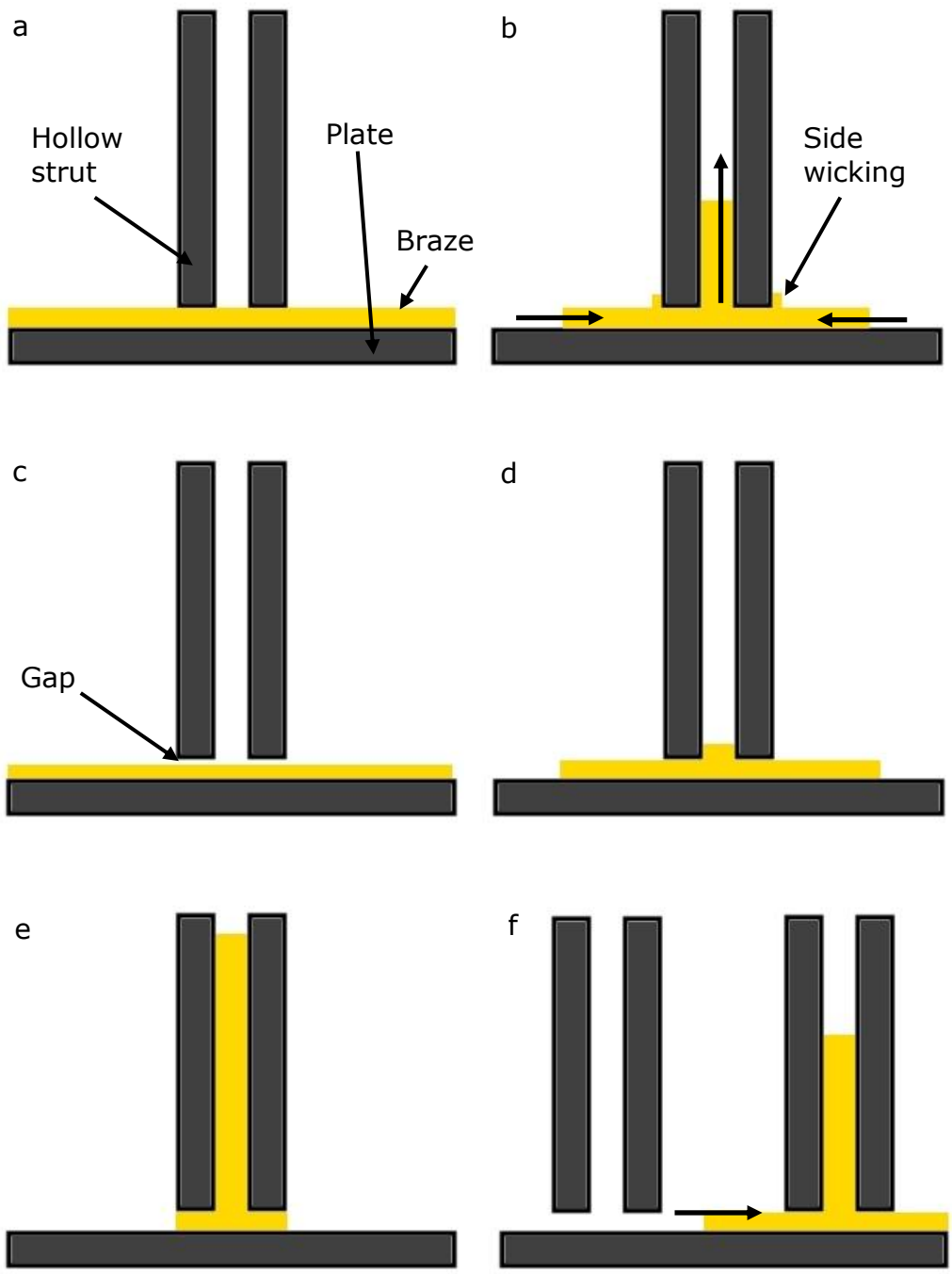


Figure 5-16. Illustrations of the wicking behaviour of the braze material (a-b), and the various bonds created such as; no wicking (c), a little wicking (d), a large amount of wicking (e), and wicking depleting material from other struts (f).

Figure 5-17 shows an image from a brazed foam Ni plate sample from which the plate had not bonded well (it came loose during EDM cutting). Like the Ni plate with braze sample it too has needle-like

phases in areas where the braze layer is. It can also be seen that the grain boundaries close to the braze layer have a darker contrast than the grain boundaries that surround it.

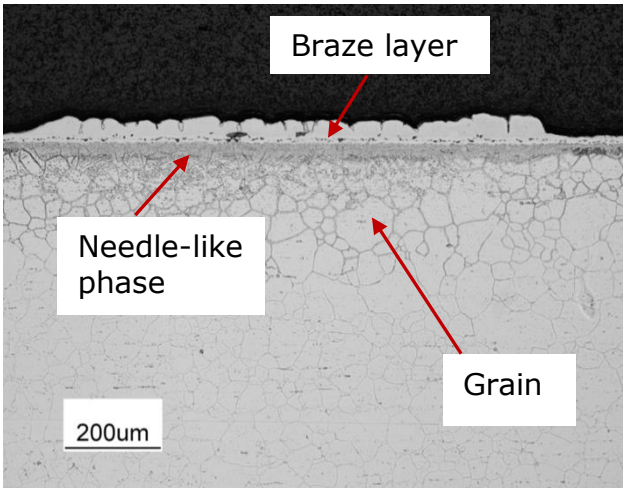


Figure 5-17. Image of a brazed layer from a brazed foam sample that had not bonded well. The needle-like phase is present below the braze layer as well as a darkening of the contrast in the immediate grain boundary vicinity.

Figure 5-18 shows an image of an etched strut from the middle of a foam sample that has been brazed. Unlike similar areas in the non-brazed foam samples, a secondary phase was not visible in any of the brazed foam struts. It is likely therefore that these phases are $CrNi_3$ which forms in 70%Ni-30%Cr at around 580°C (Figure 2-16), as the brazed samples go through a heat treatment process which would remove the phase.

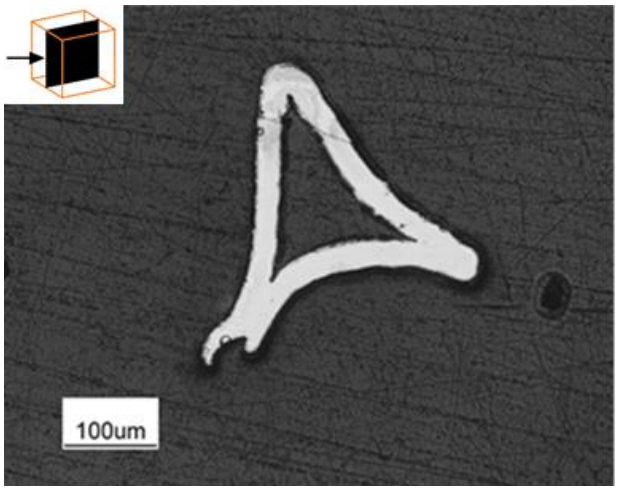
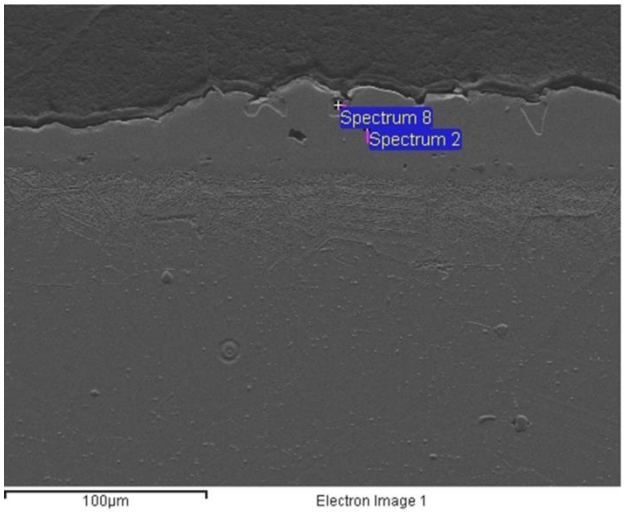


Figure 5-18. Image of an etched strut in the middle of a brazed foam sample.

5.2 EDX CHEMICAL ANALYSIS OF BRAZED FOAM

Figure 5-19. shows two EDX chemical spot analyses for both phases present in the braze layer (further examples are shown in Appendix 4). It was observed that the two phases were Ni rich and conformed to the literature on the chemical analysis of similar brazed material (Poranvari, *et al.* [52]), whereby the lower Si content corresponded to the Ni-B phase, and the higher Si content corresponded to the γ-Ni eutectic solid solution. Other elements such as Co, Cr, Ti and Al also appeared within the braze layer, all of which are elements found within the Ni-plate material. The etchant used was sacrificial of the Cr phases, and the addition of a Cr-B phase meant that this was the most eroded phase. Therefore the conclusion was made that the needle-like structures were Cr-B.



Element	Weight%	Atomic%
Si K	3.29	8.05
Cr K	1.28	1.69
Co K	0.55	0.65
Ni K	68.76	80.50
Au M	26.12	9.12
Totals	100.00	

Spectrum 2

Element	Weight%	Atomic%
Cr K	0.47	0.68
Ni K	69.44	87.53
Au M	28.85	10.84
Totals	100.00	

Spectrum 8

Figure 5-19. SEM image of the phases present in and around the braze layer, showing the locations and results of two of the EDX analyses.

Figure 5-20 is a line scan through the braze layer into both the plate and the foam strut. It can be seen that Cr content varies from being present within the Ni plate, to being absent within the braze layer and the bottom of the strut, to increasing in content towards what was the inner wall of the strut. The assumption is therefore that the Cr has diffused away from the braze layer into the Ni plate, forming a phase with one of the other elements from within the braze tape. The literature on this diffusing process would suggest that the phases are likely to be a Cr-C or a Cr-B.

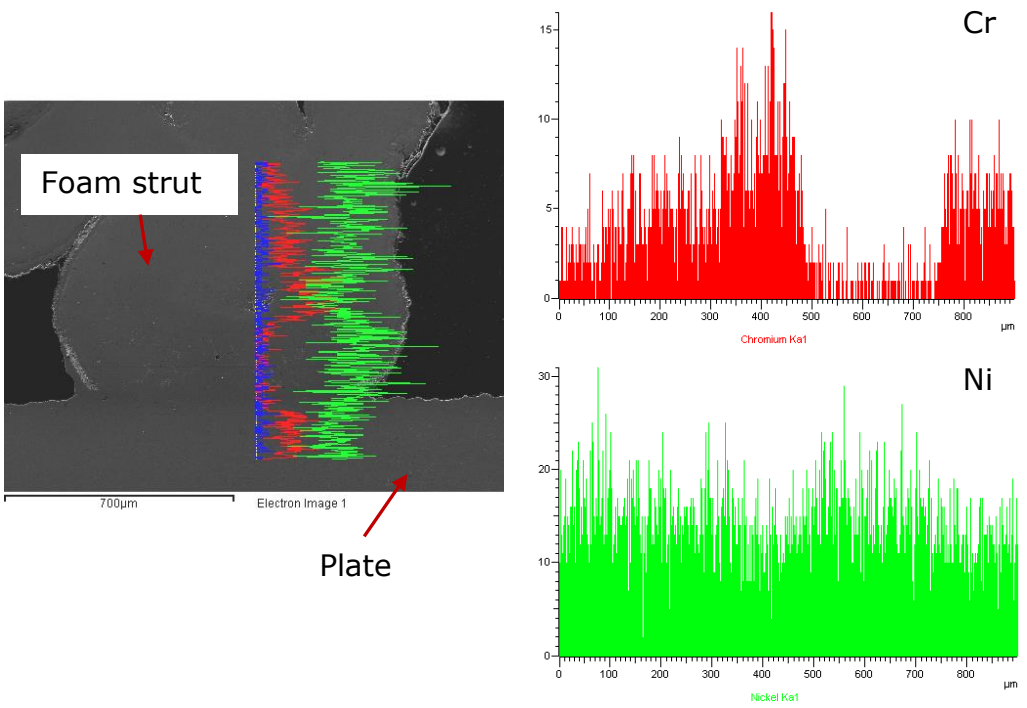


Figure 5-20 An EDX line scan with Cr and Ni profiles of a brazed foam sample. The line intersects through the strut, braze layer and Ni plate.

Figure 5-21 shows a strut roughly 1mm away from the braze layer which has its void filled. The line scan through the strut reveals that the filled material contains Si, and low Cr content away from the strut wall. These properties are similar to that of the braze layer, and as such it assumed that filler material is the braze material, which has wicked up through the strut (out of plane).

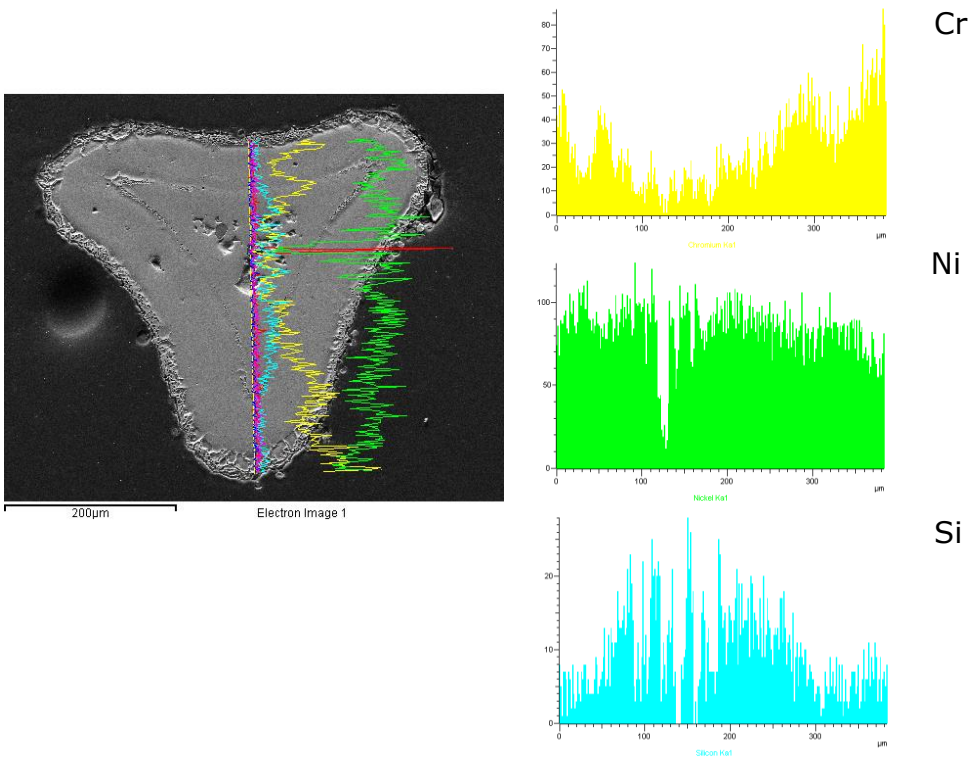


Figure 5-21. An EDX line scan with Cr, Ni and Si profiles of a brazed foam sample with a wicked braze centre.

5.3 BRAZE NDE ANALYSIS

Prior to brazed foams being shear and tensile tested, the samples were NDE scanned to analyse the quality of the braze. Figure 5-22 illustrates the analysis process for a sample, the full scan data and images for all the samples can be found in Appendix 9. First the scan data is converted into a C-scan image and a threshold is set (a). This process was done, and the threshold set, by a Rolls Royce technician and was performed in the same way they had previously done for the test engine samples. The image was then colour split using Image J and the "green" image was selected (b). Finally the image was converted to a black and white image using the Binary

Process function in Image J (c). In this final image the black areas represent areas of "good" bonding between the plate and foam, and white areas representing "poor" and no bonding. These areas are deemed representative of the true bond area of the samples, and and are used for subsequent analysis by defining the areas as a percentage of the total sample area. Table 5-1 and Table 5-2 show the areas measured for the tensile and shear test samples respectively. The samples are arranged in the order of the largest area to the smallest area with the largest area sample assumed to be the best. As the tensile tests have two braze areas (top surface and bottom) the value used is the smaller of the two.

The NDE analysis of the samples showed that there was a large variance in the braze quality. The tensile test sample varied from as little as 7% to 52% of "good" bonded area. Although <50% bond seems low, the contact area of a sectioned foam sample is only ~11% (calculated from 2D slice images of a 3D rendered microCT model). Samples were expected to have a higher percentage area than just the foam contact, as wicking of the braze around the struts would cause localised thicker regions, which would cause higher intensity peaks in the detector. However percentage areas less than foam contact area was not expected, as it was assumed the minimum amount of contact would be with the foam struts. This lack of "good" bond area could be the result of either not all the struts bonding or the majority of struts not being fully in contact with the plate.

From analysis of the area alone, it would appear from the initial scans that all but the BA4 and BA7 samples would have at least struts bonded (all but 4B2 in the shear test samples). However this is assuming the braze is distributed evenly in the other samples.

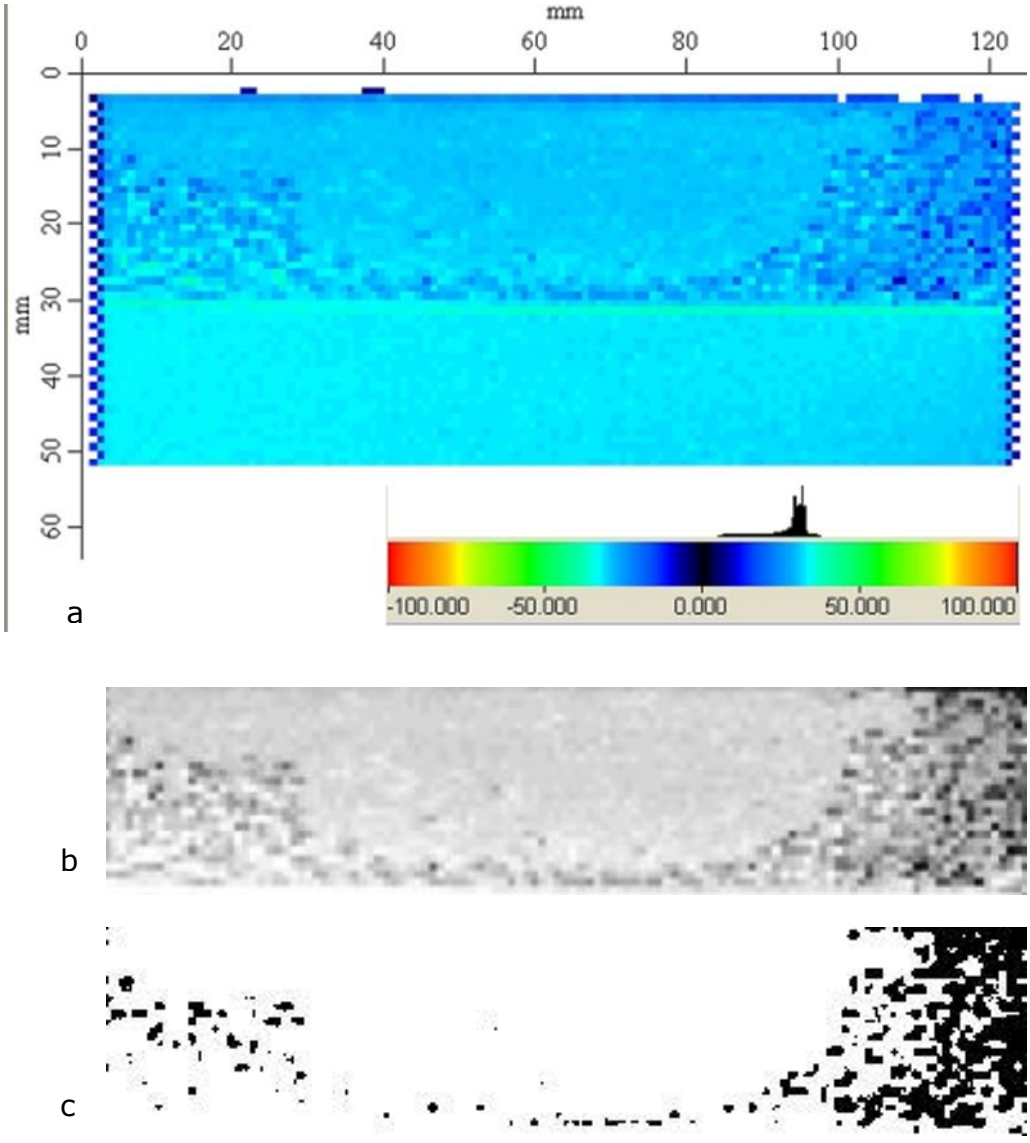


Figure 5-22. Process for quantifying the good braze area. (a) is the NDE C-scan image along with the percentage intensity threshold. (b) is the "green" colour split of the image. (c) is the binary image created from the "green" image.

Sample	% Area
AA4	56%
AA1	52%
AA3	51%
AA2	46%
BA3	32%
BA1	29%
BA5	12%
BA4	10%
BA7	7%
Mean	33%
St Dev	18%
Variance	56%

Table 5-1. Estimated areas of "good" braze quality for the tensile test samples.

Sample	% Area
A	40%
4A2	51%
C	38%
B	33%
4B1	30%
4A1	29%
4B2	8%
Mean	33%
St Dev	12%
Variance	37%

Table 5-2 Estimated areas of "good" braze quality for shear test samples.

5.4 X-RAY MICRO-TOMOGRAPHY (MCT) ANALYSIS OF BRAZE FOAM

It was possible to image, reasonably well, the outer areas of bonded samples. Figure 5-23 shows a 3D reconstruction (a) of the base of sample (b) which has been scanned. It is possible to identify the edge where the foam has come away from the plate. However the resolutions at which this can be used to identify poor braze quality is limited to roughly that which can be seen by the eye.

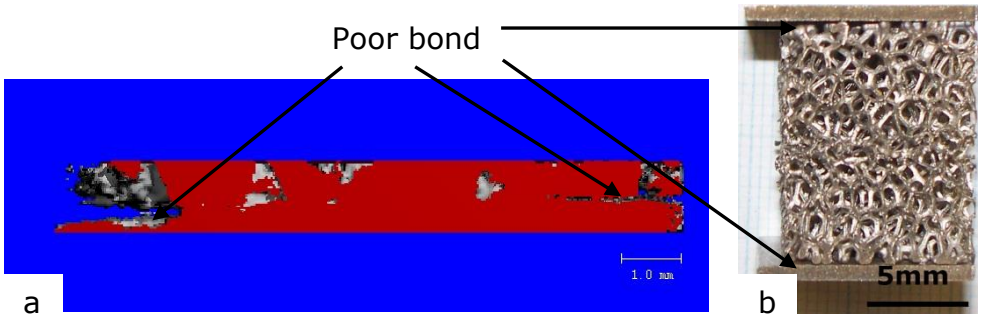


Figure 5-23. MicroCT image slice through the 3D rendered model of the sample in (b). Areas of poor bond are visible at the edges of the sample.

Figure 5-24 shows a NDE scan of one of the samples which showed an area of poor braze in a relatively large area. When looking at the sample it was possible to make out that the foam was not bonded to the plate, and clearance existed between them, by a similar amount to that in Figure 5-23. Figure 5-25 shows several image slices of the 3D rendered model created of the poor braze area. It is possible to see the area within sample where there is poor bonding, however due to the threshold parameters required to render the model, the resolution is reduced and so no significant detail is obtained.

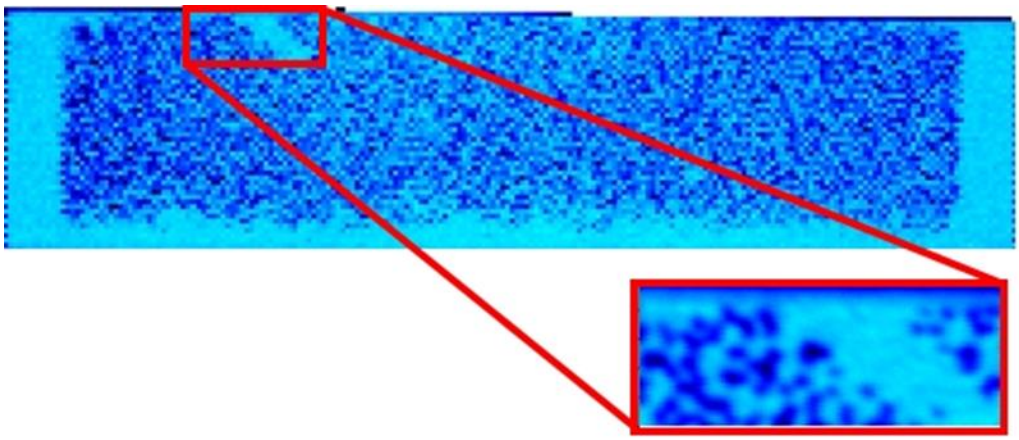


Figure 5-24. Relatively large area of no braze bond found in the NDE C-scan image.

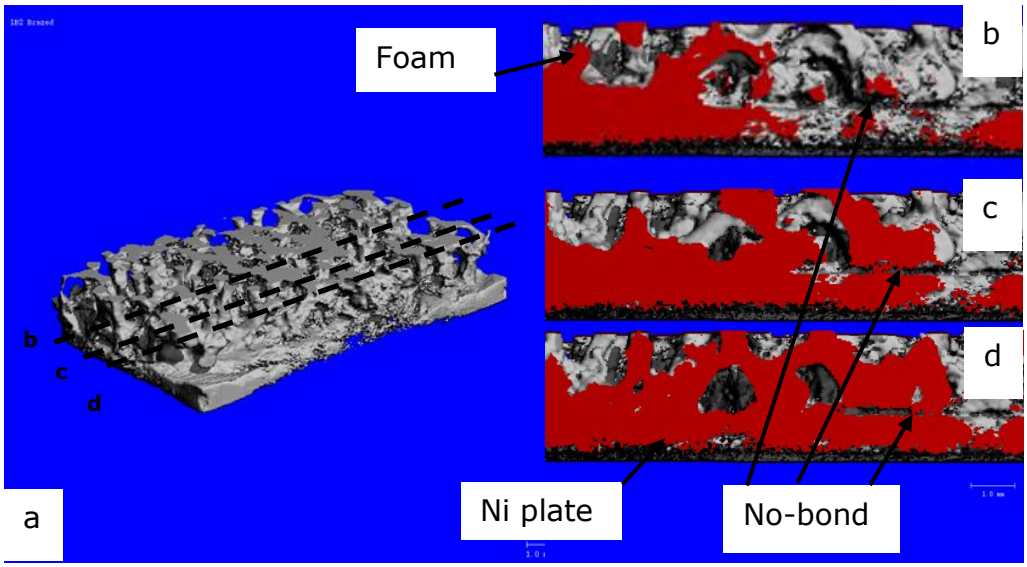


Figure 5-25. MicroCT 3D rendered image of the area of no bonding seen in Figure 5-24 (a). Images (b)-(d) are slices taken through the image increasingly further back from the front face, and show the area of no bonding from within the sample.

5.5 MECHANICAL TESTING OF BRAZED FOAM

5.5.1 Compression Testing of Brazed Foam

As can be seen in Figure 5-26 the brazed foam failed in a similar way to the non-brazed 1116 foam, with collapsing occurring in the deformed mid-section 'dark band' region. The yield strengths, as well as the stress-strain curves (Figure 5-27), were found to correlate with the non-brazed 1116 foam samples.

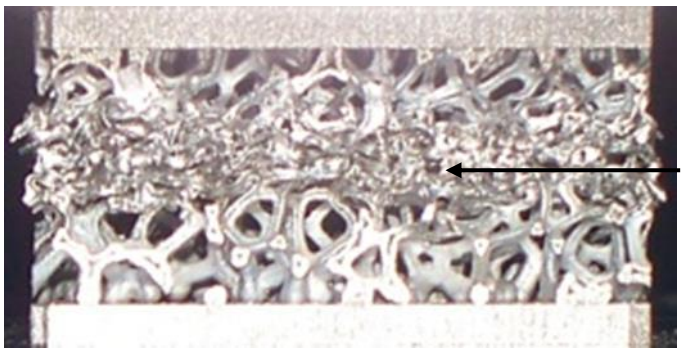


Figure 5-26. Image of a brazed foam sample undergoing compression testing, with the collapse in the deformed mid-section visible.

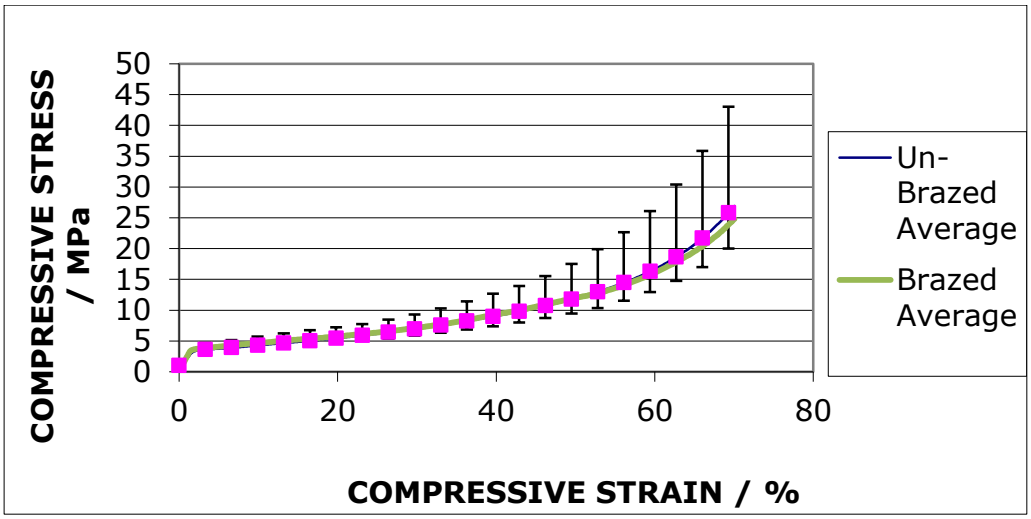


Figure 5-27 Plot of the compressive stress against compressive strain for the average brazed and un-brazed 1116 ST foam sample

Figure 5-28 shows the bond area of a strut after compression testing. As can be seen there are no signs of cracks or voids forming in the braze from the stress caused by the struts static nature compared to the outward expansion of the bulk foam material during collapse.

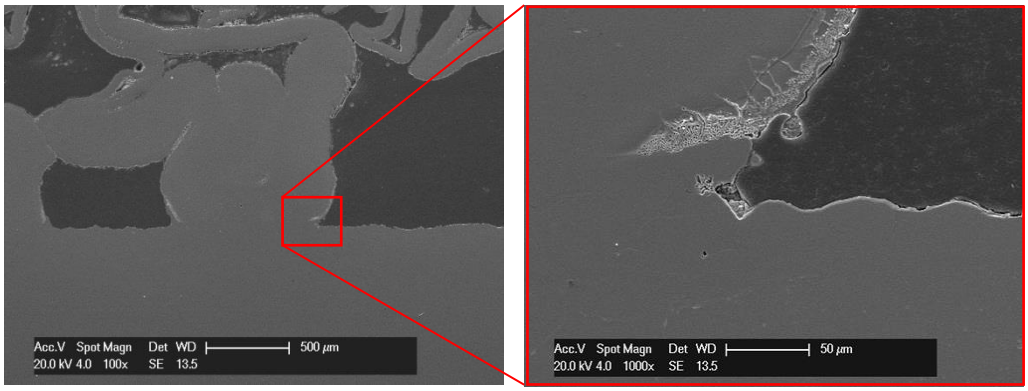


Figure 5-28. SEM image of the braze bond layer of a foam strut after compression testing, showing no signs of damage to the braze layer

5.5.2 Tensile Testing of Brazed Foam

Using the NDE ultrasound scans of the brazed foam material, several samples were chosen with bond areas ranging large to small (determined by the calculated area percentage above the threshold in C-scan images), a complete breakdown from where the samples were cut and their NDE scans can be found in Appendix 9.

Due to the samples not being perfectly true and level, the clamps could not fasten the plate to the tensile rig T-section flush, and instead had to be positioned so that the foam was aligned as best possible with the tensile direction. This caused the plate to bend during the testing, as can be seen in Figure 5-29.

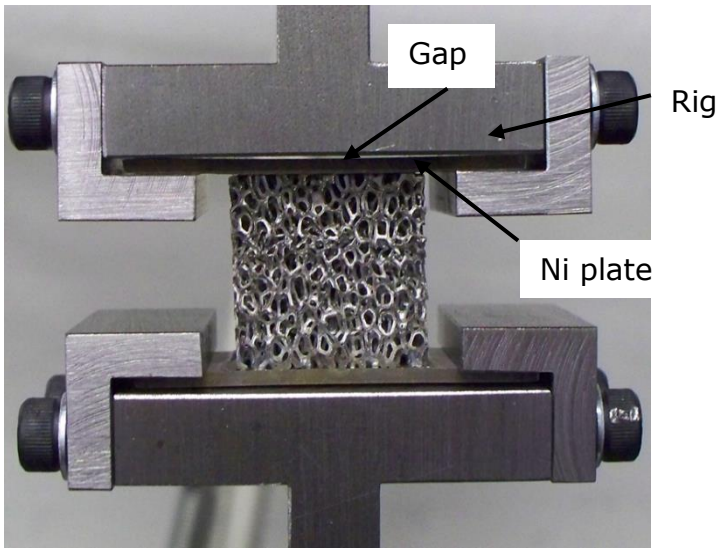


Figure 5-29. Image of a tensile test sample clamped to the rig, with the foam sample aligned as best possible. Showing bending of the plate during testing.

The results of tensile testing can be seen in Table 5-3. Contained within it, for each sample, are the NDE bond percentage areas, the maximum load reached, and the 0.2% proof and UTS calculated by using both the area defined by the sample cross-section (20x20mm) and the areas derived for the NDE bond areas. The NDE derived area was the smaller area of the two bonded faces, as it was assumed that the failure would occur where there was the least bonding.

Sample	NDE Area	Max Load (N)	Foam X-Sec Area 0.2% Proof Stress (MPa)	Foam X-Sec Area UTS (MPa)	NDE Derived Area 0.2% Proof Stress (MPa)	NDE Derived Area UTS (MPa)
AA1	52%	1115.45	2.07	2.79	3.98	5.35
AA2	46%	1400.32	2.32	3.50	5.04	7.59
AA3	51%	1319.95	1.78	3.30	3.50	6.50
AA4	56%	1299.27	2.01	3.25	3.57	5.78
BA1	29%	875.58	1.64	2.79	5.67	5.35
BA3	32%	979.76	1.98	2.45	6.21	7.70
BA4	10%	982.51	2.23	2.46	21.21	23.40
BA5	12%	950.57	1.76	2.38	14.62	19.73
BA7	7%	1404.50	1.90	3.51	26.30	48.65
Mean	33%	1147.55	1.96	2.94	10.01	14.45
St Dev	18%	197.72	0.21	0.44	8.10	13.64
Variance	56%	17%	11%	15%	81%	94%

Table 5-3. Tensile results for brazed foam samples, with the proof stress and UTS calculated using both the foam sample cross-sectional area and the NDE derived area.

BA3, BA4 and BA5 failed within the braze-foam bond, whereas the remaining samples failed within the foam centre with some degree of peeling, but not complete, of the foam away from the braze bond. Figure 5-30 shows several images of the failures. Figure 5-30(a) is an image of sample AA2 which has undergone some peeling away of the foam from the braze layer at the corners of the foam. Figure 5-30(b) is an image of sample BA7 showing a smaller amount of peeling than AA2. Figure 5-30(c) is an image of sample BA4 and shows the plate pulled from the foam which has been slightly deformed during the extension. Figure 5-30(d) shows images from both the front and back of sample AA1. This sample was of note as the peeling of the foam from the braze layer occurred not only at the side edges but at the rear as well, leaving only a quarter left bonded.

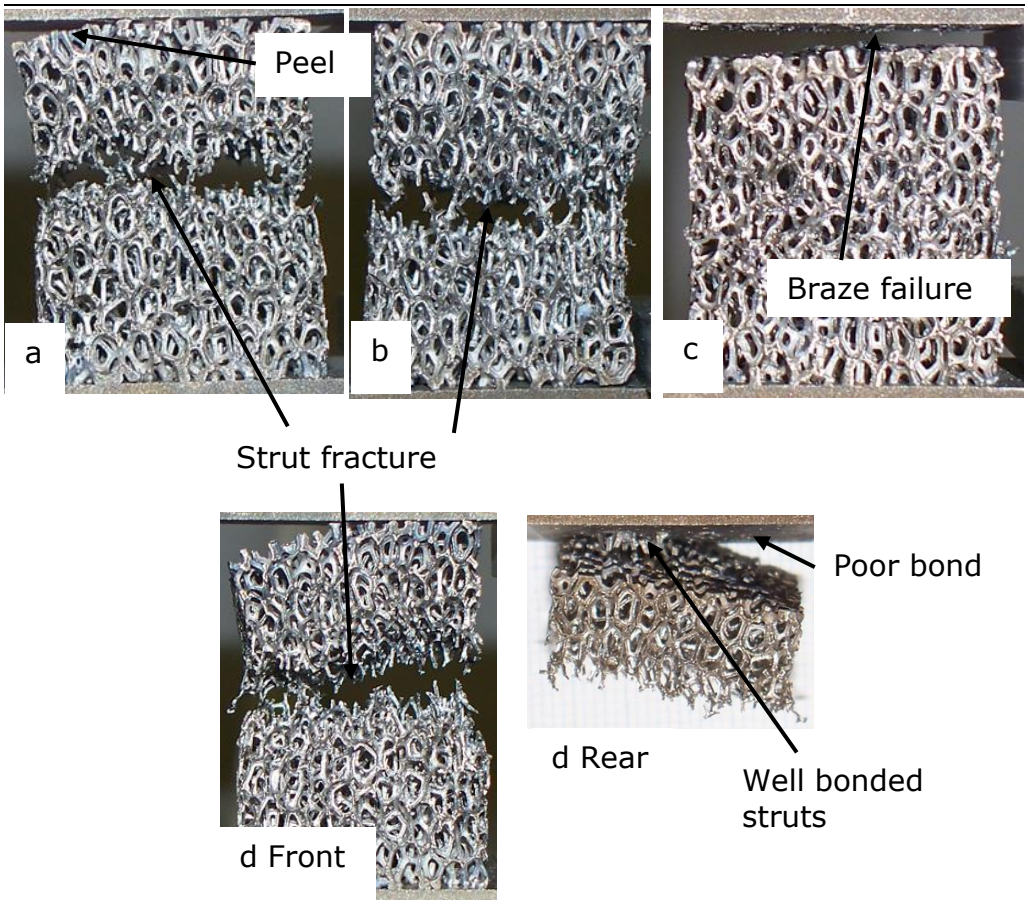


Figure 5-30. Images of the tensile failures for brazed samples AA2 (a), BA7 (b), BA4 (c) and the front and rear of AA1 (d).

The tensile stress-strain plots for the samples showed large scatter compared to the plots for just the foam. Figure 5-31 illustrates this with a stress-strain plot of the average tensile stress (along with markers for the upper and lower sample boundaries) up to 10% strain. It was calculated (see Table 5-3) that there was 11% variance. This additional variance (compared to the previously tested foams) must therefore be the result of initial bending in the backing plate as well as poorly bonded struts allowing reduced forces to achieve greater extensions of the sample.

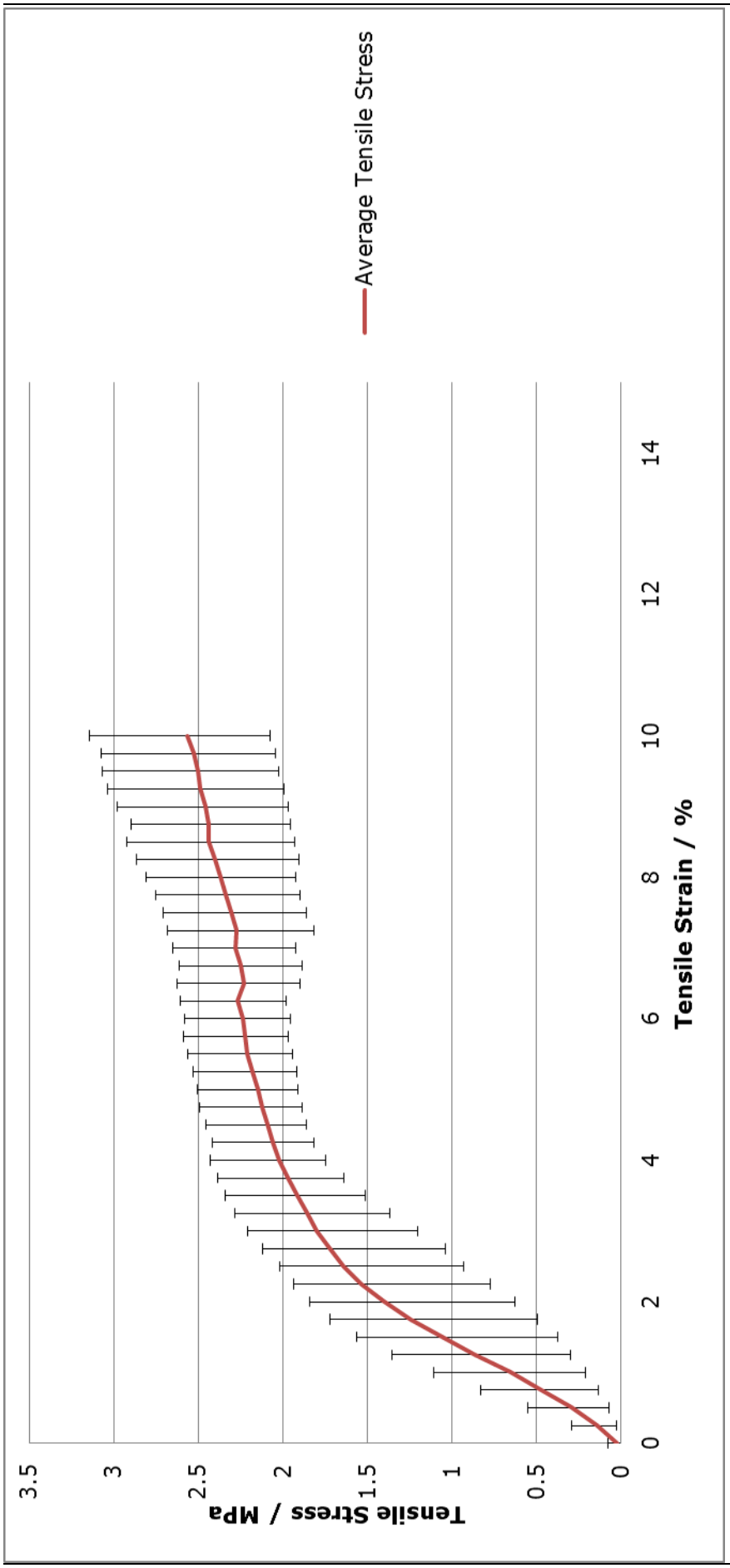


Figure 5-31. Average tensile stress-strain plot for the brazed foam samples, showing the variance between the maximum and minimum sample plots.

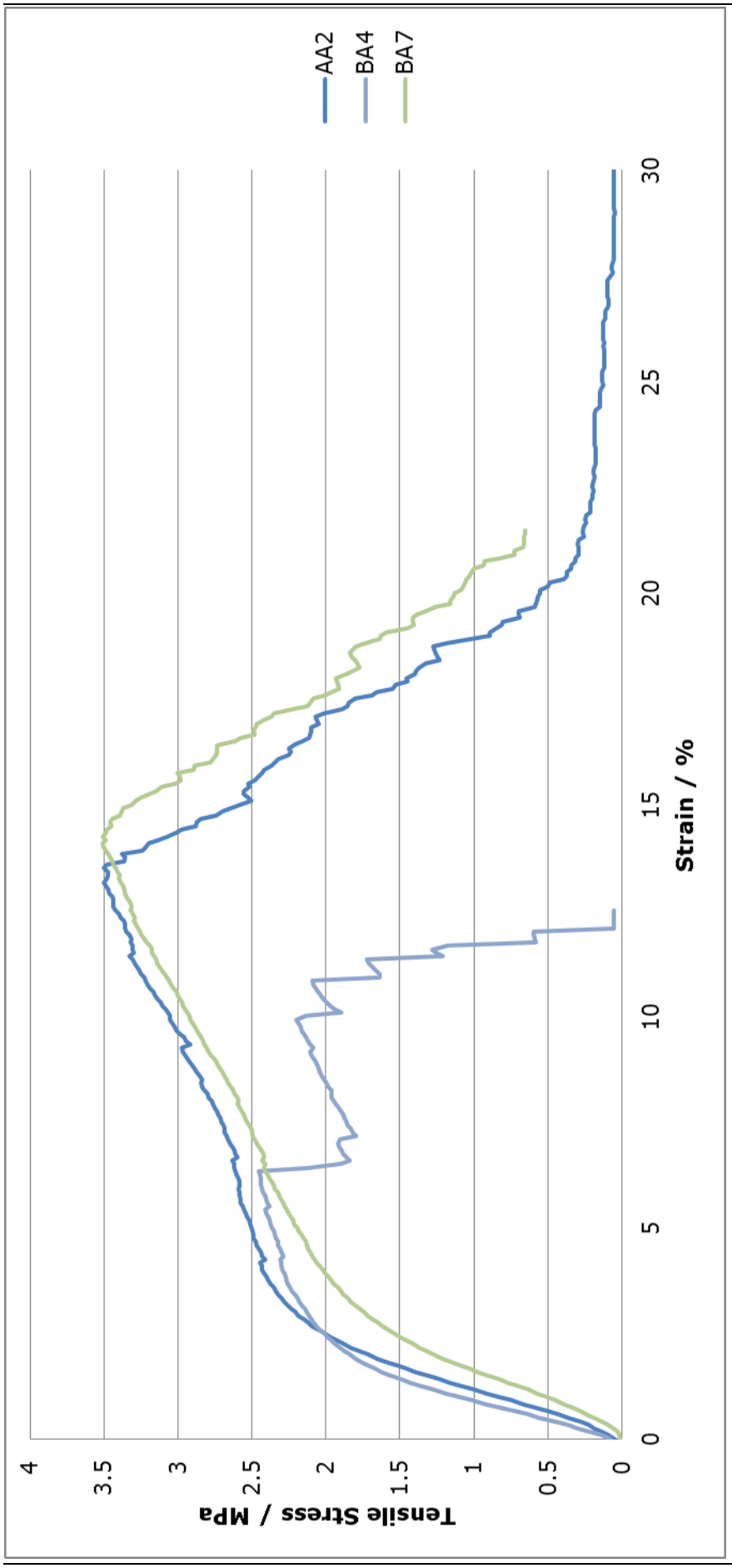


Figure 5-32. Tensile stress-strain plots for samples AA2, BA4 and BA7.

Figure 5-32 shows plots for three of the samples AA2, BA4 and BA7 (the plots for all samples can be seen in Appendix 10) and shows the characteristics of the two types of failure foam (AA2) and the bond (BA4). Of note was sample BA7, which although had the smallest NDE derived area, achieved the highest UTS.

Figure 5-33 shows a plot of the maximum load achieved by the sample against the NDE derived area. From this plot it is not possible to see a clear trend, there is a not well defined trend of an increase in braze area corresponding with an increase in max load.

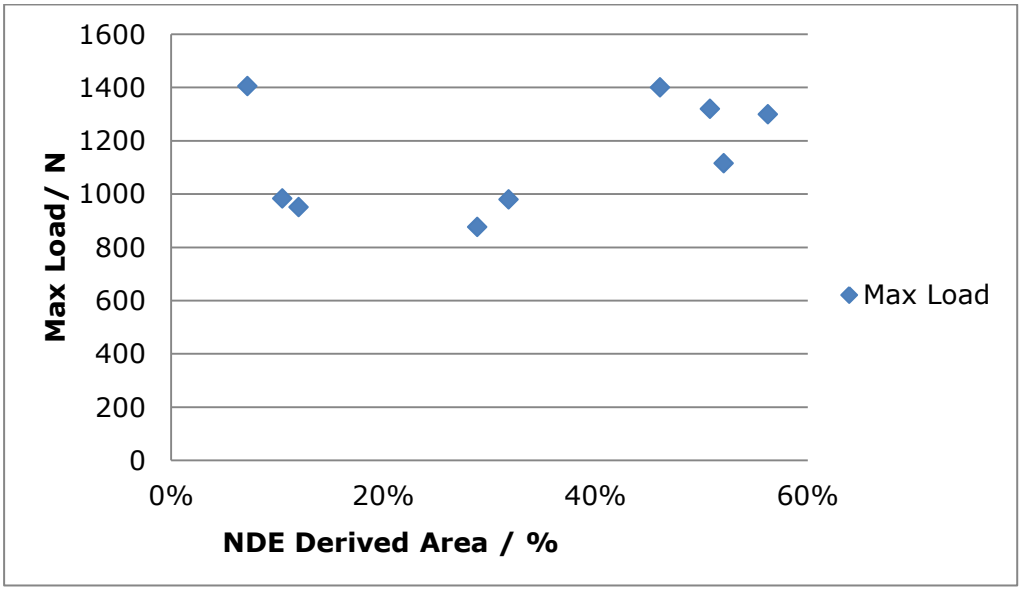


Figure 5-33 Plot of the maximum load against the NDE derived area for the brazed tensile samples

Figure 5-34 shows the plots of the UTS against the NDE derived area for the samples, with the stresses calculated using either the foam sample cross-section or the NDE derived area. The plots show that there is no trend between the NDE derived area and the UTS calculated using the foam cross-sectional area. However the plot

does show a trend for the UTS calculated from the NDE area, although it counter-intuitively trends with an increased area corresponding with a decreased UTS. It could be inferred from this that the lower area was due to the wicking of the braze, creating thicker strut walls and larger strut surface area coverage, and that the resulting struts which were heavily wicked were stronger for it.

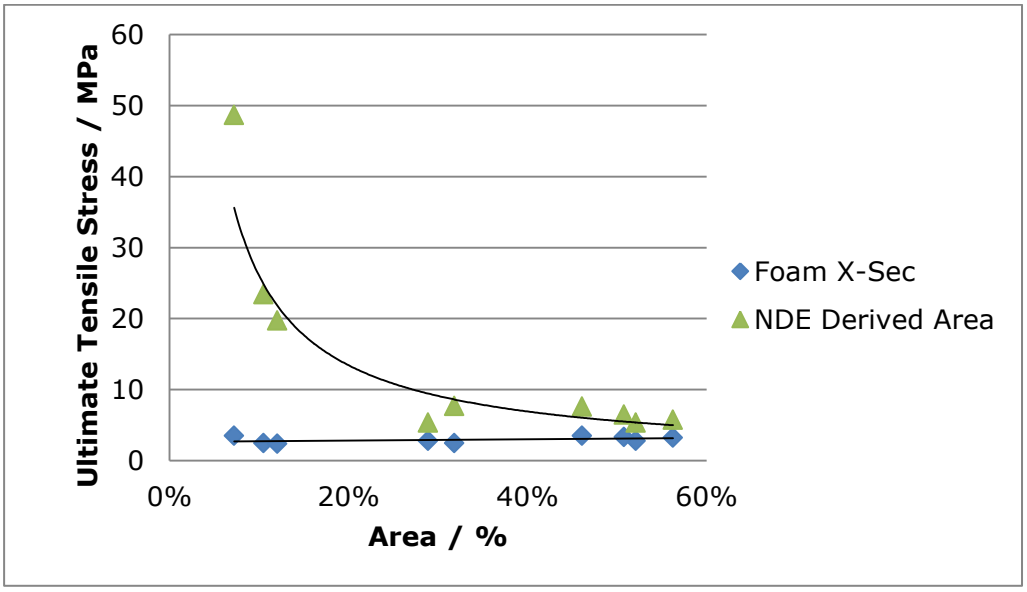


Figure 5-34 Plots of the UTS against NDE derived area, with the UTS calculated using the foam cross-section and the NDE derived area

Figure 5-35 shows images of etched struts from a tensile test. It can be seen in both (a) and (b) how there is no damage to the braze layer at the strut-braze-plate area. This was typical of the struts viewed, which had bonded well. Figure 5-36 is an image from the edge of a sample showing a strut that is elevated above the braze layer. This strut did not appear to have been brazed to the Ni plate as it does not have any braze material on the bottom. During testing when the foam peeled away at the corners this could have been

because the edge struts were not bonded, or had very weak bonding.

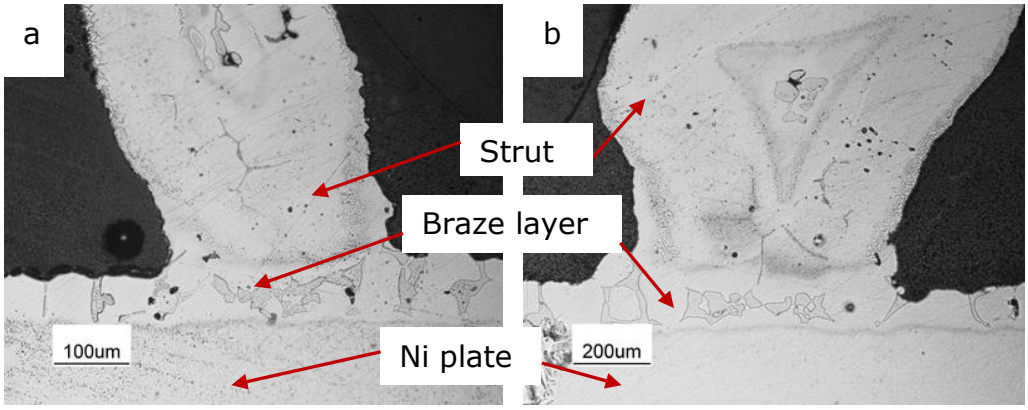


Figure 5-35. Images of two struts that have bonded well, showing no signs of damage to the braze bond layer after tensile testing.

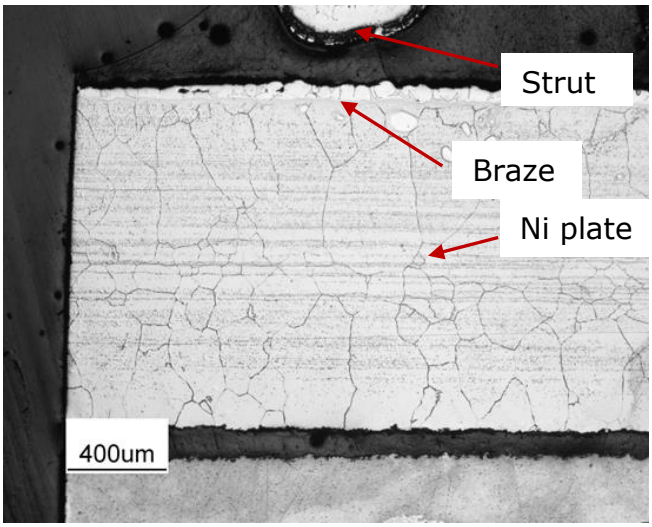


Figure 5-36. Image from the edge of a sample showing a strut above the braze layer.

Figure 5-37 shows SEM images taken from a well bonded area of a sample from which the Ni plate ultimately was pulled off. Figure 5-37(a) shows several struts with braze material coating the

bottoms and filling the void between them. Figure 5-37(b) is a close up image of one of the struts which has two "layers" of braze. The top surface is smooth whereas the bottom is rough which can be seen clearly in Figure 5-37(c). It can be assumed, from the variation in roughness that the smooth surface was in contact with the surface of the Ni plate and the rough surface is from the fracture within either the braze layer or the strut itself. This type of fracture surface could be seen in many of the struts, such as can be seen in Figure 5-37(d). Also seen in Figure 5-37(d) is fracture through the thickness of the braze layer. It is not known whether the fracture is between the two layers of braze tape that were applied, as they have similar composition, but it is a possibility.

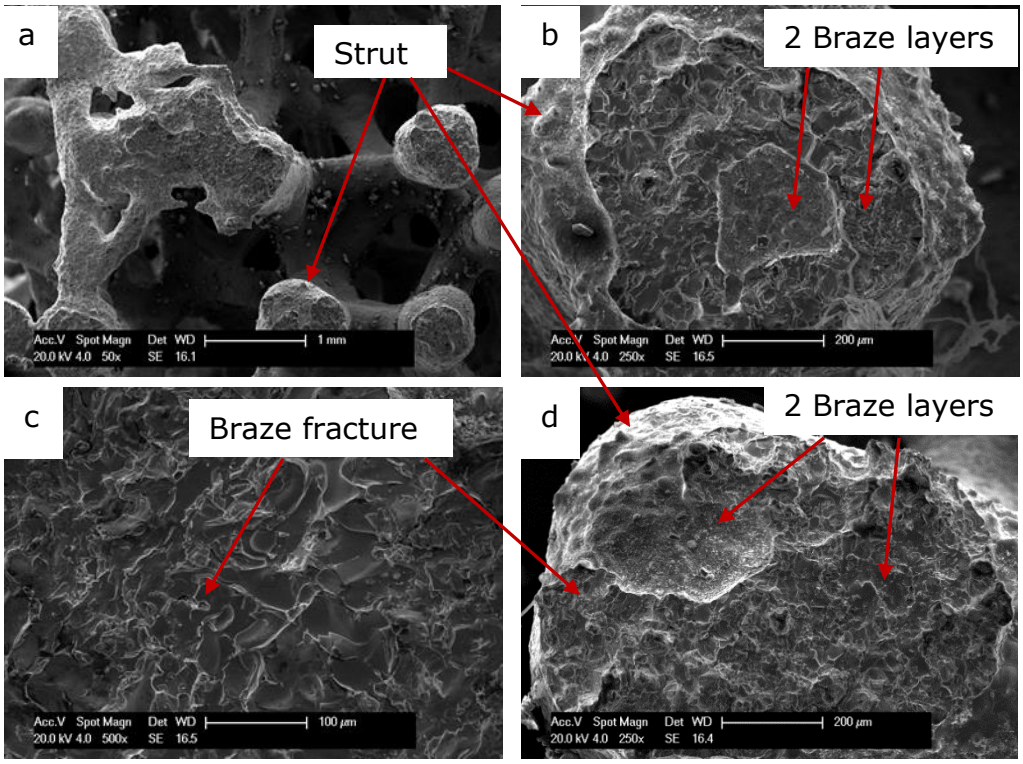


Figure 5-37. SEM images from an area of good bonding in a tensile brazed foam sample. Image (a) shows struts coated in braze material. Image (b) shows the bottom of a strut with braze material at two different depths. Image (c) shows the fracture surface on the braze layer. Image (d) shows a strut with a braze layer that has fractured through the thickness.

Figure 5-38 shows SEM images taken from a poorly bonded sample area from which the Ni plate was ultimately pulled off. Figure 5-38(a) shows several struts that have very little braze material bonded to them. On the right side of the image it can be seen that some of the struts have no braze material at all. Figure 5-38(b) is an image of a strut with a small amount of braze on the tip, which shows signs of braze fracture through the centre. Figure 5-38(c) Is an image of a strut that has braze material on the tip that has fractures through the thickness. The top surface is relatively smooth indicating contact with the Ni plate. Figure 5-38(d) is an image of a strut with a smooth surface and no braze. This appears to be a strut that has been ground during preparation for joining, but which no braze has bonded too.

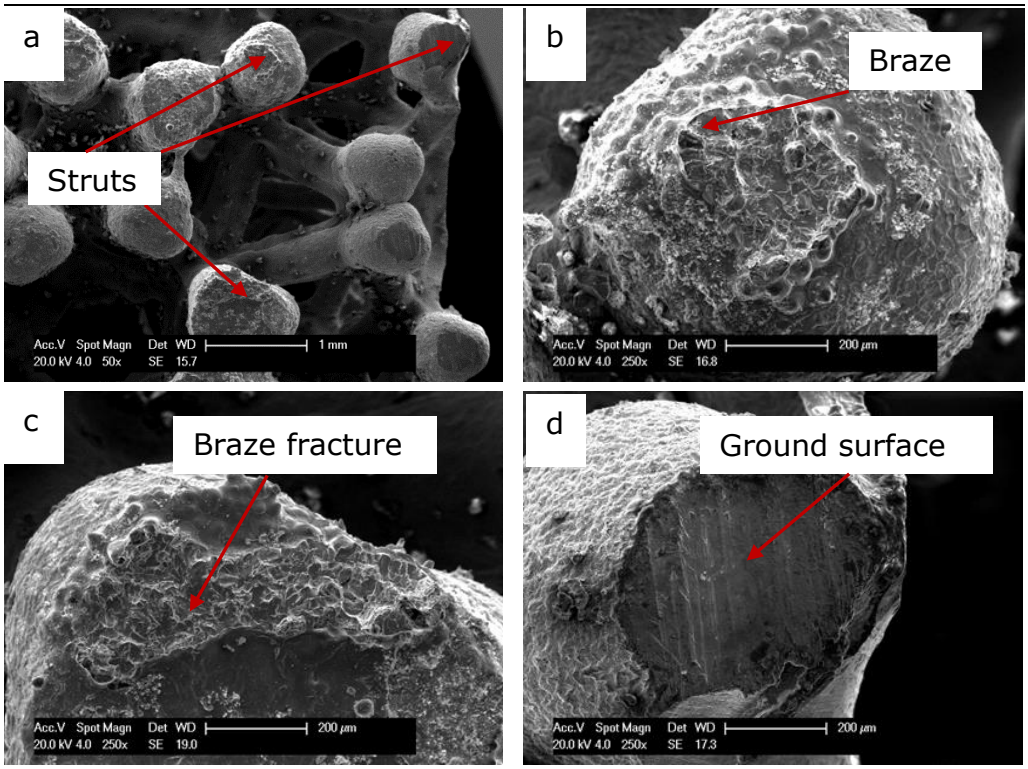


Figure 5-38. SEM images from an area of poor bonding in a tensile brazed foam sample. Image (a) shows struts with little, and on some no, braze material. Image (b) shows the bottom of a strut with a small amount of braze on the tip, which has fractured. Image (c) shows the braze layer on the bottom of a strut which has fractured through its thickness. Image (d) shows a strut with no braze material, which has previously been ground flat during manufacture.

Figure 5-39 Figure 5-39 shows SEM images taken of the Ni plate that was pulled of the brazed foam tensile test sample. Figure 5-39(a) shows an area where the base of a strut bonded well, whilst the surrounding area has little braze material. The strut bond was good enough that failure occurred within the strut Figure 5-39(b). The fracture surface doesn't display necking in the walls that was seen in the tensile testing of the just material. Here pores from pull-out are visible instead.

Figure 5-39 (c) shows an area where the base of struts bonded, with Figure 5-39 (d) being a magnified view of an area within it. It is

possible to observe the fracture surface in what appears to be the braze layer of the bond, as well as an area where the braze rises from the plate surface. The elevation was most likely caused by wicking of the braze material up the sides of the strut, then being left when the strut is pulled out. This feature is seen in other areas such as Figure 5-39(e). Figure 5-39(f) shows an area where there is a gap in the braze layer. There is not any fracture or pull out and it appears to be a void similar to that seen in just the brazed Ni plate analysis.

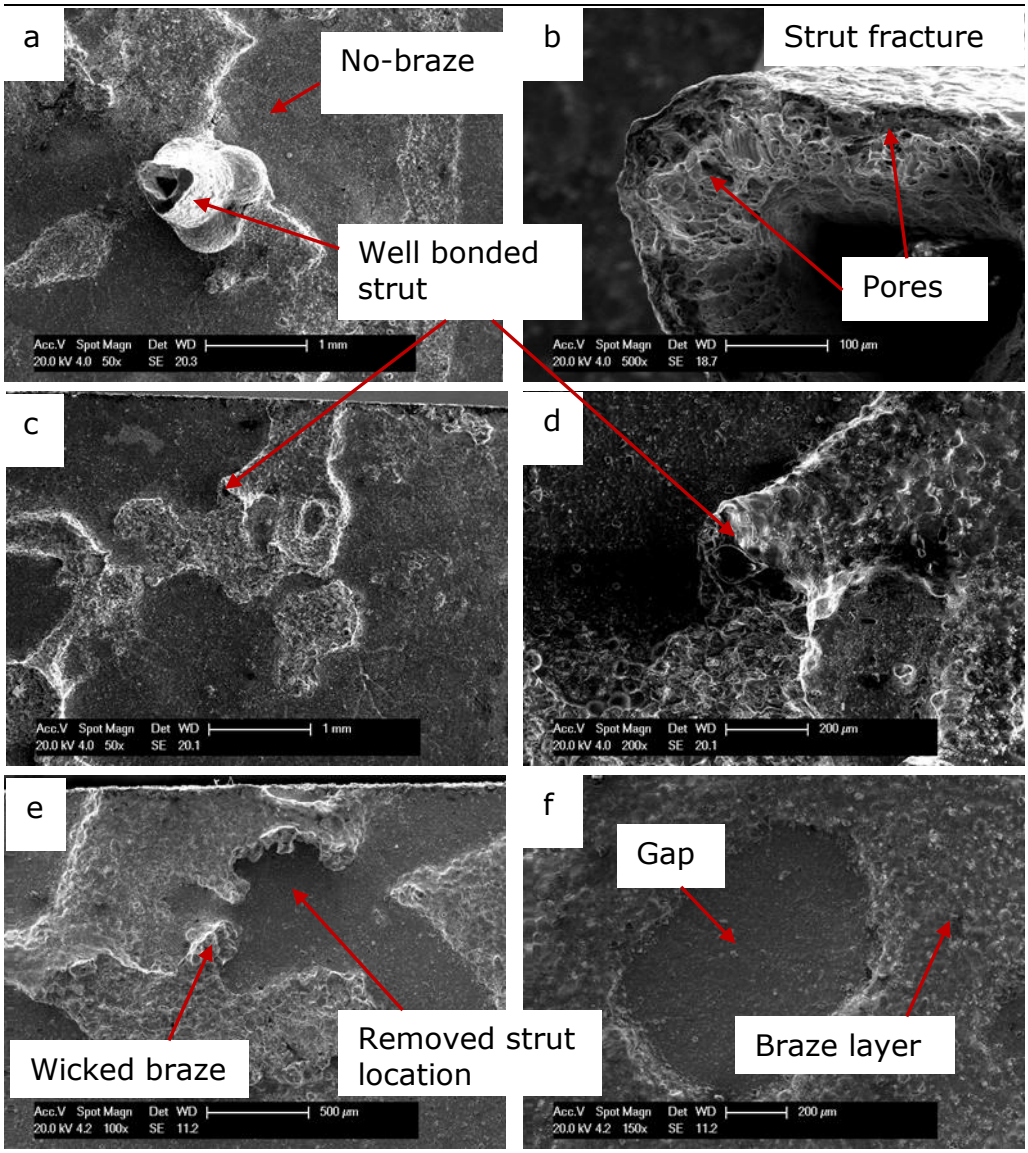


Figure 5-39. SEM images from a Ni plate pulled from a brazed foam sample during tensile testing showing; a well bonded strut (a-b); an area previous strut bond which has undergone fracture (c-d); areas of wicked braze which has not bonded well (d-e); areas of gaps in the braze layer (f).

The fracture of the braze layer was brittle, with crack propagation being most likely initiated in the voids caused by the diffusion of B out of the layer. Many of the struts showed signs of wicking both within and around their walls, with some struts above the braze surface having braze within them as well. It appears that this is why some areas of the plate had "dull" areas visible, in that the braze

had wicked away leaving the Ni plate visible behind. Having braze wicked through the strut would clearly strengthen the bond, as the surface area would increase, and due to the shapes of the struts a mechanical lock could be formed. This type of strongly bonded strut corresponds with the type of strut from the small NDE derived areas that were able to produce high UTS. However with too much wicking, the braze layer attached to the Ni plate is reduced, which will reduce the overall strength of the bond.

5.5.3 Shear Testing of Brazed Foam

Foam samples that were brazed to Ni plate underwent shear testing. The samples were taken from areas of good and bad braze quality determined by the NDE analysis (Images of the locations and braze can be found in Appendix 9), whereby bad braze refers to areas less than 10%, medium quality braze refers to areas less than 40% and good quality refers to areas above 40% . Areas of the as supplied material were so poorly bonded that the Ni plate came loose from the foam during sectioning which left fewer samples than initially had been intended to be tested.

Table 5-4 shows the results of the shear tested samples. Listed are the max shear stresses for each sample calculated using areas defined by; the cross-section of the foam sample and the NDE defined area. Figure 5-40 and Figure 5-41 are the shear stress-incursion plots of the samples with stress also calculated using the cross-section of the foam and the NDE derived analysis respectively.

It can be seen how samples B and 4B2 failed much earlier than the other samples, which accounts for the large variance in the results. By removing them from the results and comparing the other samples, a variance of 11% and 20% can be achieved by the cross-section and NDE derived area results respectively.

		Max Shear Stress (MPa)		
Sample	**NDE Derived Area (%)**	**Foam X-Section**	**NDE Area**	**Reducing Area**
A	40%	5.64	14.11	6.84
B	33%	1.40	4.30	1.50
C	38%	4.14	10.91	5.56
4A1	29%	5.03	17.13	8.37
4A2	51%	5.68	11.11	8.47
4B1	30%	5.15	17.35	6.01
4B2	8%	0.50	6.11	0.51
Mean	33%	3.94	11.58	5.32
St Dev	12%	1.96	4.69	2.92
Variance	37%	50%	41%	55%

Table 5-4. Shear test results for the brazed foam samples

Three types of failure sequences occurred during tensile testing. Figure 5-42 shows a sequence of images taken from the 4B1 sample test, which performed well. During shear the foam begins to collapse and the struts compact together at the end where the Ni plate is being pulled. Although the foam cell closest to the incursion point collapses, the remainder of the foam cells are unaffected. As incursion continues the process is repeated, with the closest cells deforming whilst the rest of the foam is unaffected. Once 50% of the foam has been sheared, the cells closest to the point of incursion continue to collapse but those further away including those

in the same plane deform only slightly, causing the foam to "curl up". The foam continues to deform whilst the struts bonded to the Ni plate pack closer and closer together, until the final bond is sheared.

Figure 5-43 shows a sequence of images taken from the sample C test, which had a medium quality performance. It started similar to that of sample 4B1 with foam cells collapsing closest to the incursion point, but the rest of the foam being unaffected. However, failure in the bond occurred before full densification of the foam.

Figure 5-44 shows two images of the 4B2 sample. The first is before the test ran and the second is taken at the point of failure. As can be seen almost no deformation has taken place.

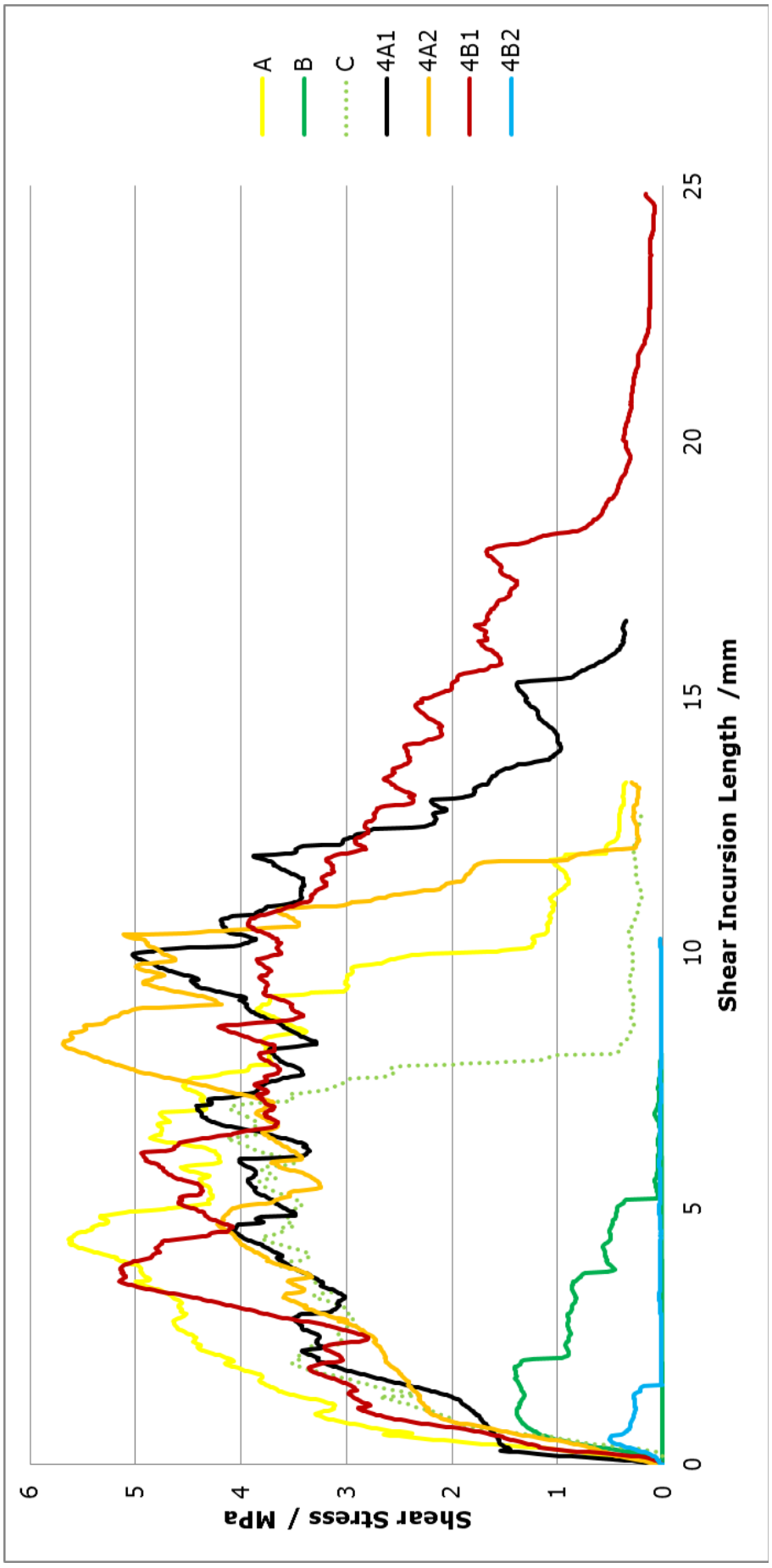


Figure 5-40. Shear stress-incursion plots for the areas derived from the cross-section of the foam samples.

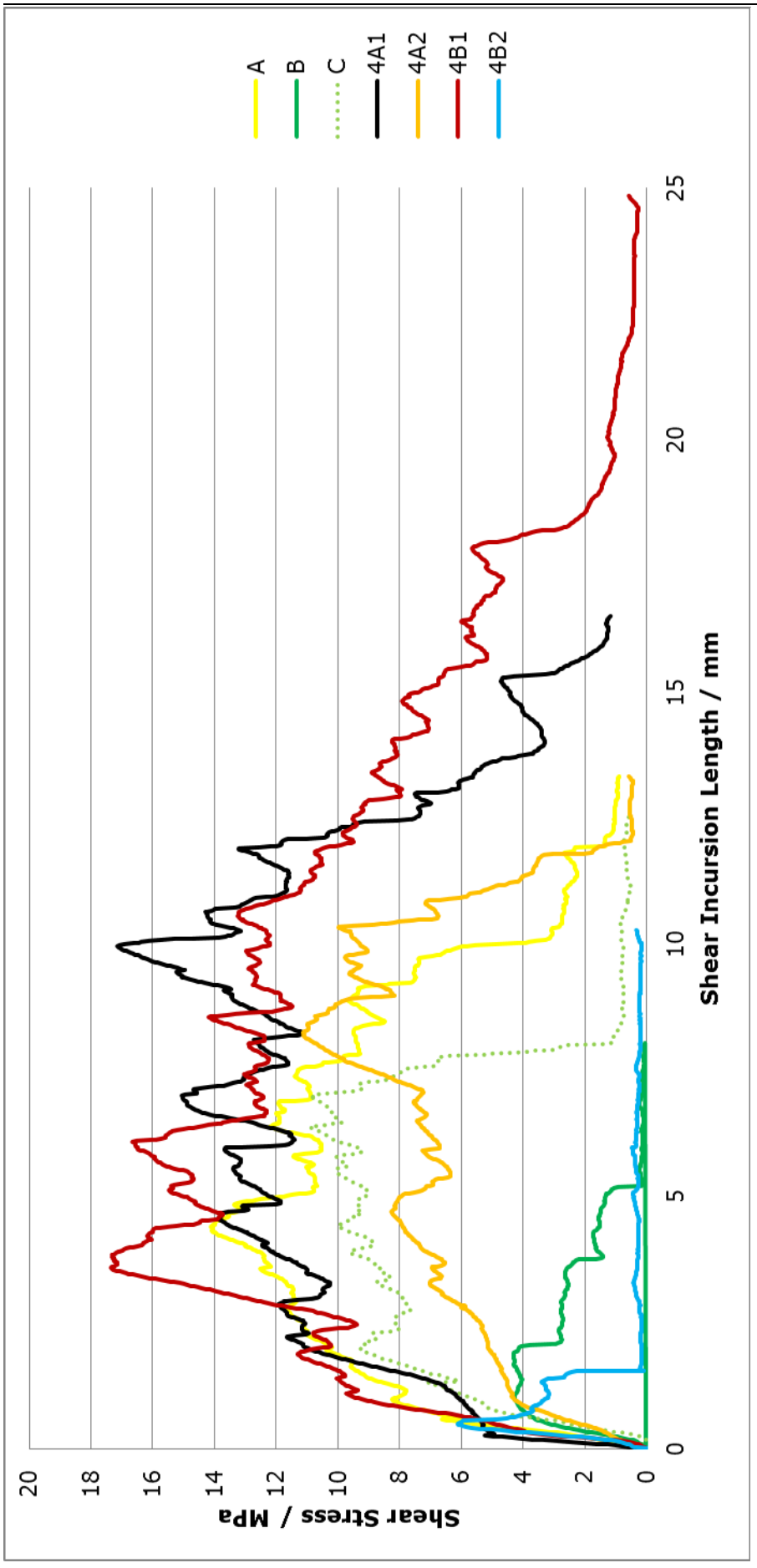


Figure 5-41. Shear stress-incursion plots for the areas derived from the NDE area%.

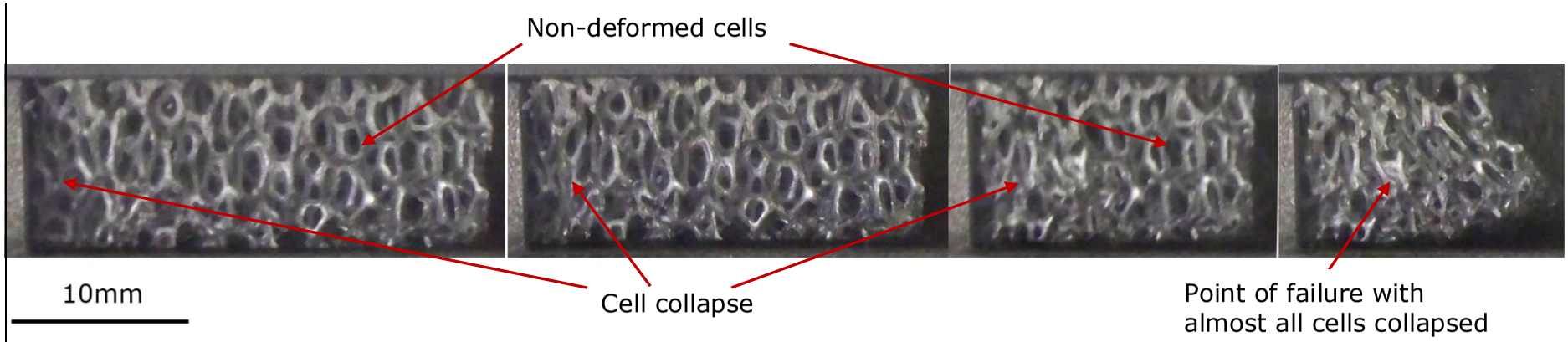


Figure 5-42. Sequence of images taken from the 4B1 sample shear test showing the deformation of the foam when there is a good bond.

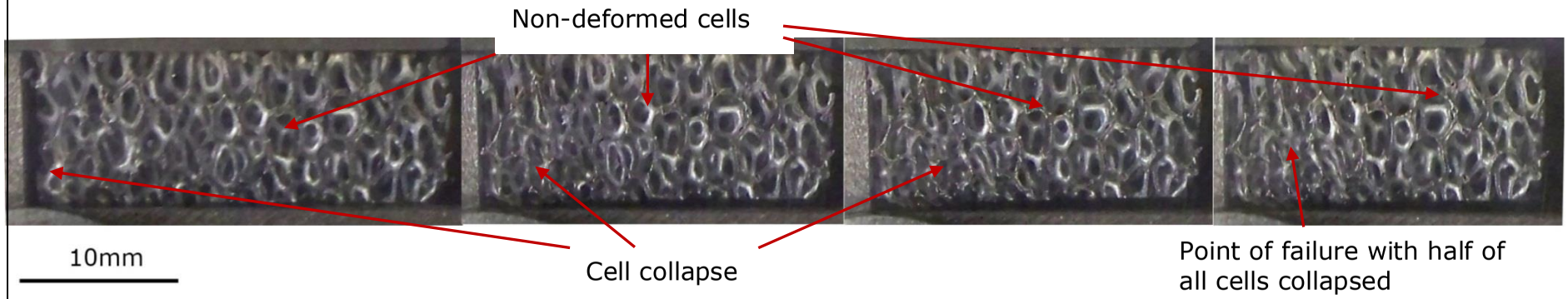


Figure 5-43. Sequence of images taken from the C sample shear test showing the deformation of the foam when there is a medium quality bond.

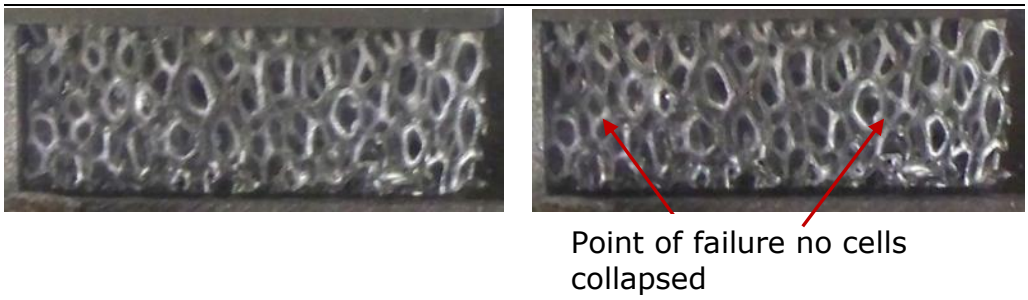


Figure 5-44. Two images of the 4B2 sample taken during shear testing. Image (a) is from the begining of the test and (b) is from the point of failure.

Figure 5-45 shows images of several samples having undergone shear testing. Each image displays the Ni plate and the foam sample with the braze side showing, and the shear direction being up. Figure 5-45(a) is an image of 4A2, which bonded well, and shows how the foam collapsed and compressed evenly. Figure 5-45(b) shows an image of sample 4B2 which failed early. The corresponding plate image shows how there was very little braze, and that it is all concentrated at the front edge in relation to where the shear incursion came from. Figure 5-45(c) shows an image of sample 4B1 which performed well. It can be seen how the sample has not deformed uniformly, with one side collapsing and the other relatively unaffected. Figure 5-45(d) shows an image of sample B which performed badly. It can be seen it has not deformed uniformly and is similar to the 4B1 sample with overall less deformation. Of note is that the image of the Ni plate shows large coverage of braze.

Figure 5-46 show several slices of a 3D microCT rendered model of the 4B1 sample. The first slice image is of the top surface (farthest away from the braze layer) of the sample, with the next images

increasingly into the sample until reaching the last slice which is at the base (close to the bond area). The top slice shows how during collapse the struts compact themselves with voids being filled as best the strut shape can fit. The closer the struts are to the bond area the more compact the struts have become, with the bottom slice having struts so compacted together they can’t be resolved.

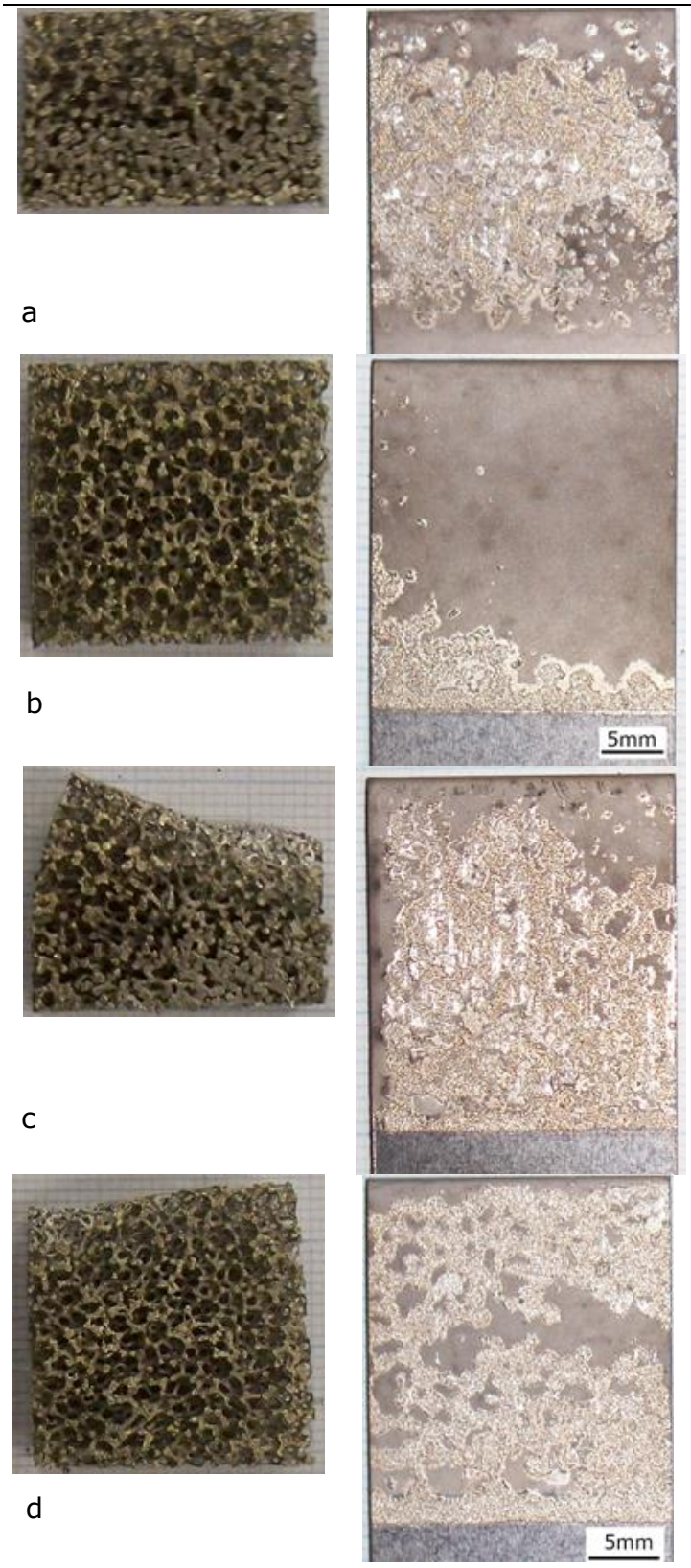


Figure 5-45. Images of foam samples and there corresponding Ni plates, after shear testing. With the braze sides showing and the direction of shear upwards.

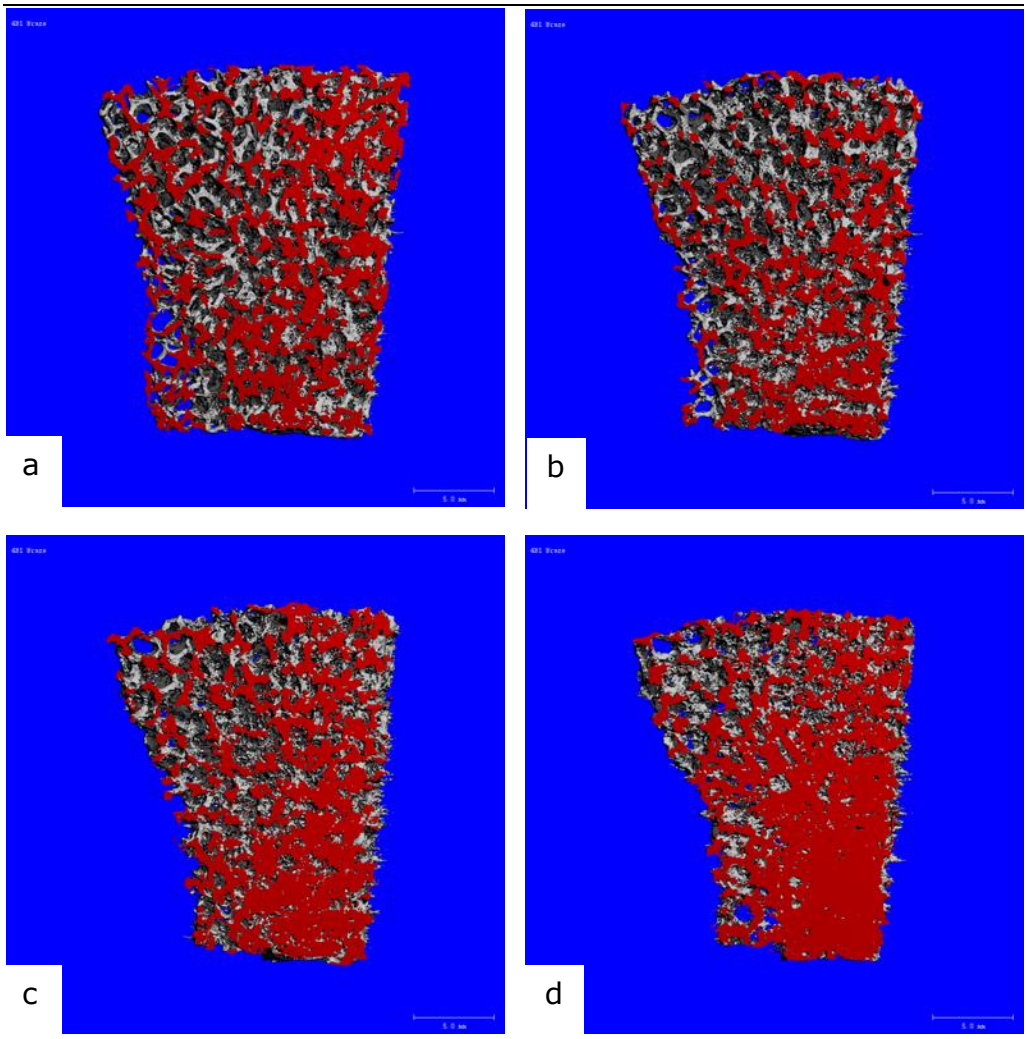


Figure 5-46. 2D slices of a 3D rendered microCT model of sample 4B1. Top slice (a) is at the top surface of the sample with each slice from deeper within until reaching close to bond area (d).

As the load is distributed among all the struts that are bonded, the combined bond strength must be greater than the load required for the foam cells to begin to collapse. As the foam material undergoing shear testing was aligned with the force being applied through the LL axis, and the method for cell failure was collapse and densification, the minimum bond strength required can be assumed to be the same as that required to achieve similar in compression testing. The 1116 samples that underwent compression testing in

the LL orientation had, at 25% strain, a stress of ~3.5MPa. By reviewing the shear stress-incursion plots in Figure 5-40 it can be seen that most of the samples are able to achieve this stress, however samples 4B2 and B were not. Sample 4B2 failed almost instantaneously, and sample B deformed only a small amount before failing. If these samples are plotted with the stresses calculated using the NDE derived areas, as can be seen in Figure 5-41, then both samples are able to achieve an initial maximum stress above 3.5MPa which would allow for initial cell collapse.

As the Ni plate is pulled during testing, and the incursion plane moves through the sample, there are fewer struts bonded to the plate. With a reduced area the stress within the sample will therefore change. Figure 5-47 shows two stress-incursion plots for sample 4B1 (used as it was one of the best bonded samples, the plot for all samples can be seen in Appendix 11, and the calculated maximum shear stresses in Table 5-4), one calculated using the foam cross-section of the foam sample (25x25mm) as the area, the other by reducing the area by the given incursion amount at each point. By doing this the plot changes shape and a plateau region is visible. This shows that collapse of the cells within the foam is uniform. The peaks and troughs of the plot also indicate the resistance of the struts to the shear, with higher peak corresponding to either stronger bonds or stronger struts.

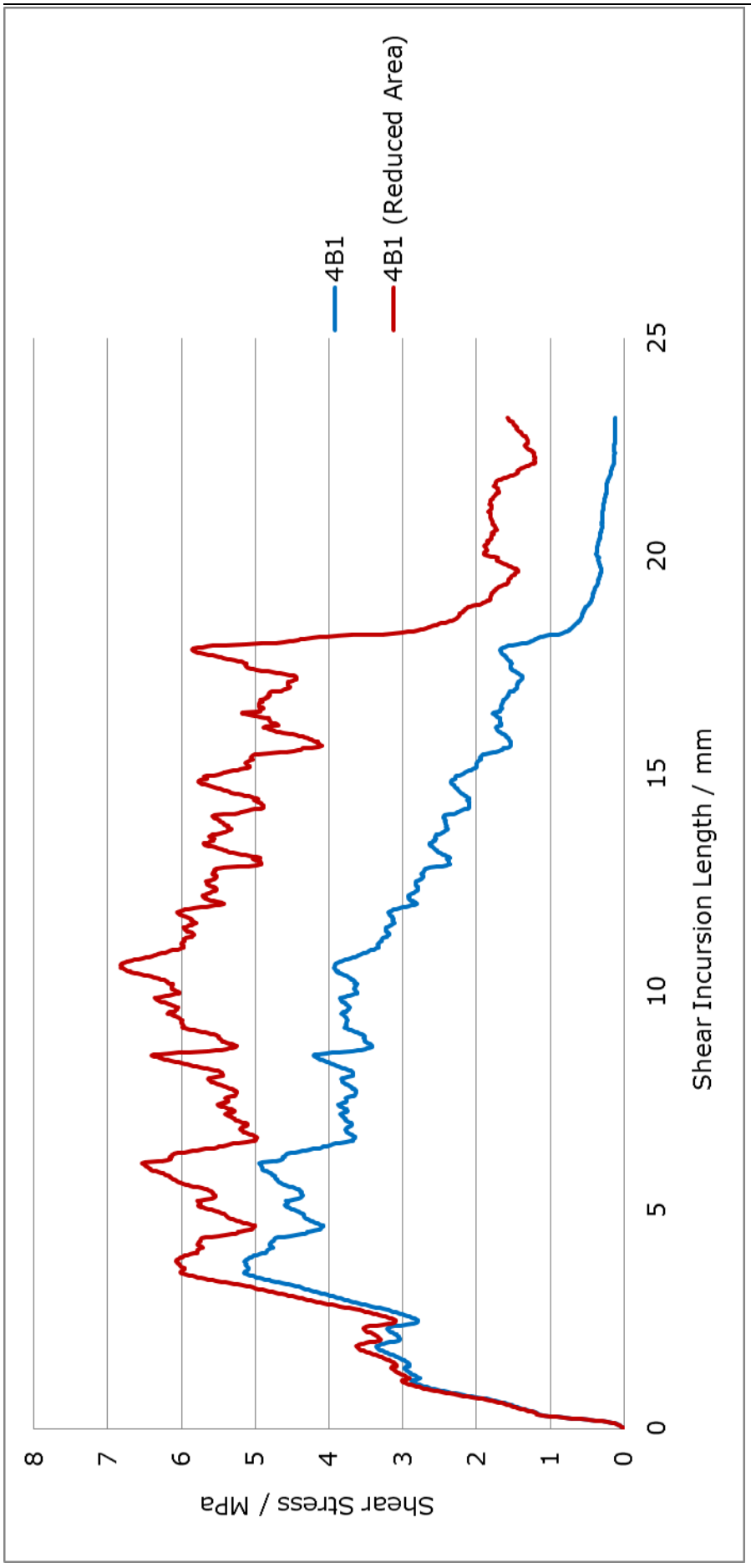


Figure 5-47. Shear stress-incursion plots for 4B1 sample, where the stress is calculated using the cross-section of the foam sample, and by an area reduced by the incursion amount.

Figure 5-48 shows the plot of the maximum shear test against NDE derived area, where the shear stress is calculated from areas defined by; the cross-section of the foam sample, the NDE analysis and a reducing area as the incursion plane moves through the sample. As can be seen there is a trend, for all calculated plots, for an increase in NDE derived area to correspond with an increase in max shear stress. Unlike during the tensile test, where, if the sample had only a few strong bonds, in a localised braze area, the foam would still fail before the braze. The shear also requires the struts to be bonded well throughout the sample, not just localised, as was seen with sample 4B2 which failed early, due to only being bonded in the area just in front of the initial incursion plane.

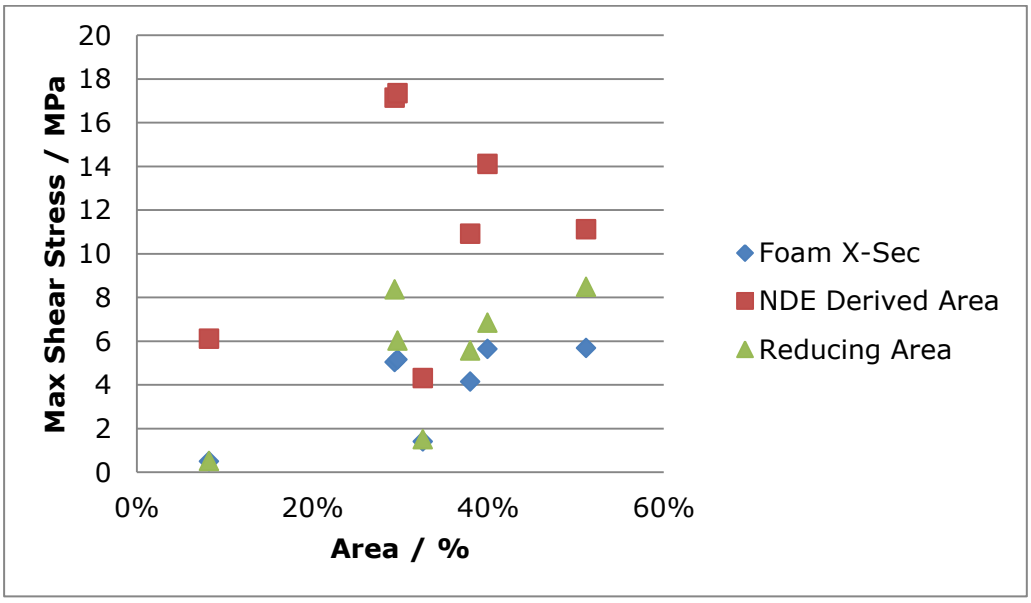


Figure 5-48 Plots of the maximum shear stress against NDE derived area, where the shear stress is calculated using the foam cross-section, the NDE derived area, and the reducing area

Samples 4A1 and B both had NDE derived bonded areas of ~30%, but performed completely differently with the B sample failing much earlier than expected and sample 4A1 performing very well. Figure 5-49 shows the Ni plates after shear testing of the samples. As can be seen, both samples have a wide distribution of braze through the sample, but the 4A1 sample (a) has much less braze visible on the surface than sample B (b). Very few strut remnants are left in the bond layer of the B sample, but almost the entirety of the remaining material on the plate is that of strut remnants with braze surrounding. It can therefore be inferred that the braze material wicked into the 4A1 struts and remained bonded to the plate creating the strongest possible bond, whereas the braze in sample B did not wick as much leaving the struts weakly bonded to the plate and, despite large coverage, failed early.

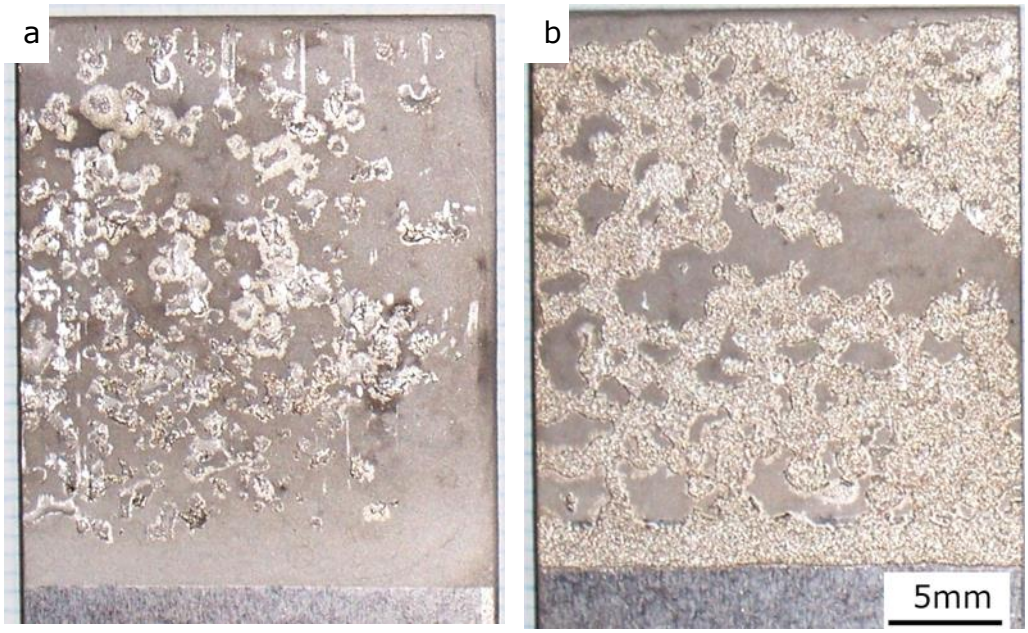


Figure 5-49. Images of the Ni plates braze layer for samples 4A1 (a) and sample B (b).

Failure of the bond was found to be either by fracturing of the strut, fracturing of the braze layer, or there being no bond to fail.

Figure 5-50 shows several images obtained by SEM of the bond surface of the foam sample after shear testing. Figure 5-50(a) shows the compacting of the struts near to the initial incursion point. It can be seen how some struts have failed by fracture within themselves and others by fracture within the braze layer. Figure 5-50(b) shows a strut that has undergone failure by both fracture within itself and with the braze layer. Figure 5-50(c) is an image of the fracture surface that had occurred in the braze layer. Figure 5-50(d) is an image showing a strut that has bent during the shear testing, which has caused cracks to appear in the wall.

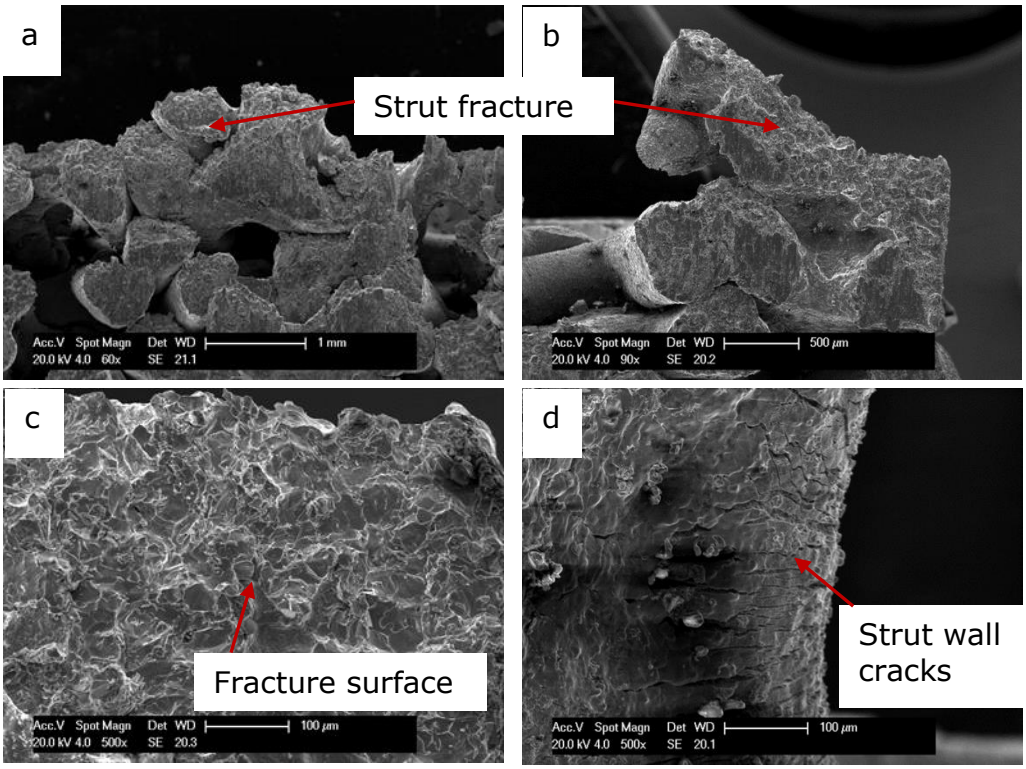


Figure 5-50. SEM images the foam sample after shear testing. All images are from the previously bonded surface. Images (a-b) show the fracture struts, (c) shows a braze fractured surface, and (d) shows cracking in a strut wall.

Figure 5-51 shows etched cross-sections for a foam sample that had undergone shear testing. Figure 5-51 (a) shows an image of struts that were bonded to the Ni plate (the plate ran across the top of the images, being pulled to the left of the images). It can be seen how during compaction of the struts, the middle triangular strut had been forced over the bottom of the strut to the left. As the triangular strut has a wicked braze centre, it is stronger, and the force needed to compress it is more than that required for it to realign. Figure 5-51 (b) shows an image from the rear end of the shear sample foam. Here the right hand strut has been deformed around the centre strut. The same strut also tails off at an angle, which corresponds to, as stated before, the bond surface compacting whilst the far surface remains relatively non-deformed. Figure 5-51 (c) is a magnified image of the centre strut, and shows the tearing away of the braze layer, with a large void in the strut wall visible, indicating a partial strut/partial braze failure. Figure 5-51 (d) is a magnified image of the bond surface of the right hand strut in image Figure 5-51 (b), it shows the secondary phase that was present in the braze layer, indicating that this is the braze layer.

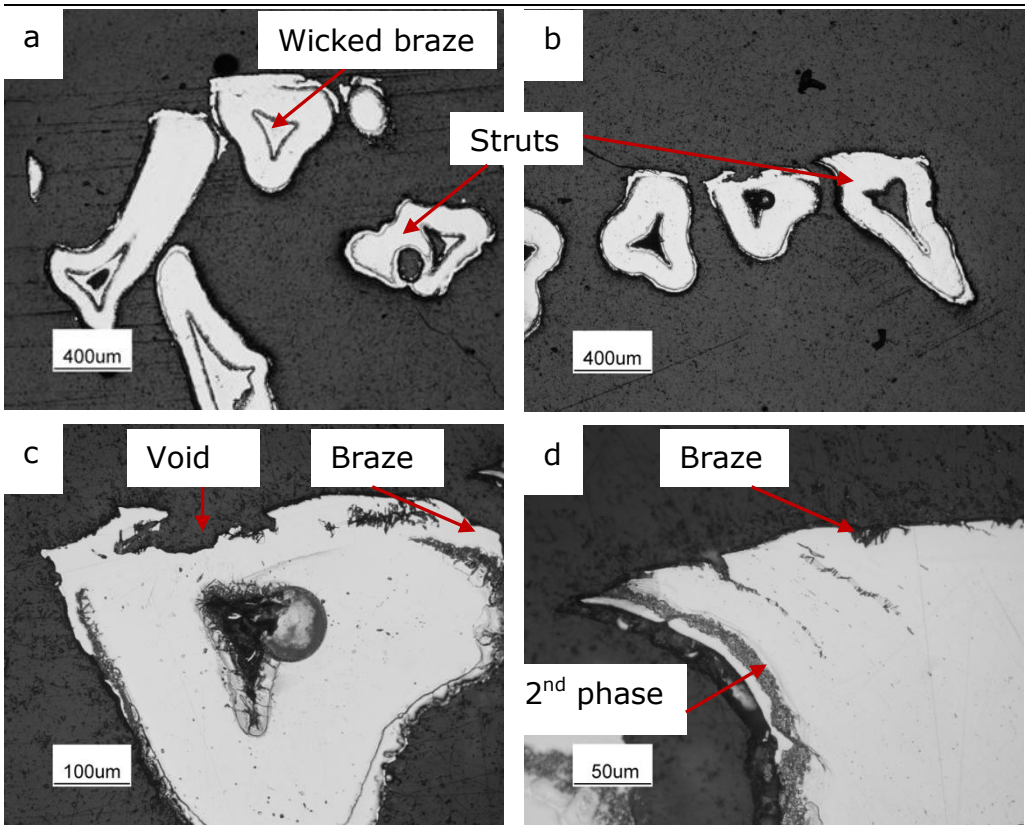


Figure 5-51. Images of etched foam samples after undergoing shear tests. Images (a-b) show the compacting of the struts which were closest to the bond area. Images (c-d) show magnified images of the struts and the failed brazed layer.

Figure 5-52 shows SEM images taken of the Ni plate braze layers after samples had undergone shear testing. Figure 5-52(a) shows an image of strut still bonded to the Ni plate. It has fractured, but as can be seen in Figure 5-52(b) the braze layer is still intact. Also shown in Figure 5-52(b) is the thick layer of braze material that is around the strut. Figure 5-52(c) is an image of another strut that has remained bonded, although it has fractured at the base with the braze layer, and can be seen more clearly in Figure 5-52(d). Figure 5-52(d) also shows how the facture lines in the braze are along the grain boundaries. In contrast to the previous struts, Figure 5-52(e)

shows the remains of a strut, which had remained bonded despite having little braze material in the surrounding area. This shows that large braze deposits around the strut aren't necessarily needed for a strong bond. Figure 5-52(f) is an image from the site of a removed strut, that outline of which is visible by the fractured surface. EDX analysis of the surface revealed it was in the braze layer. Figure 5-52(g) is an image of a sheared strut that has been rubbed relatively smooth during testing. It is similar in size to the strut removed in Figure 5-52(f), with a similar amount of braze material surrounding it, however despite this one failed in the strut and the other in the braze. It is assumed, therefore, that the fractures of the samples are determined by the weakest path that a crack can propagate through.

Figure 5-53 shows two images from the Ni plate braze layer of the 4B2 sample that failed almost instantaneously. Figure 5-53(a) shows the needle-like phase beneath the braze layer as well as darker contrast grain boundaries, both likely due to the B diffusion. Figure 5-53(b) is an image of another area of the braze layer which shows voids within the braze. It was not possible to determine whether or not the struts had bonded along the plate as gaps in the braze layer could be similar to those seen in the just brazed Ni plate, rather than strut removal, or possibly not even be within the cross-sectioned plane that was cut. The voids left by the diffusion of the B, are likely to act as the crack initiation sites.

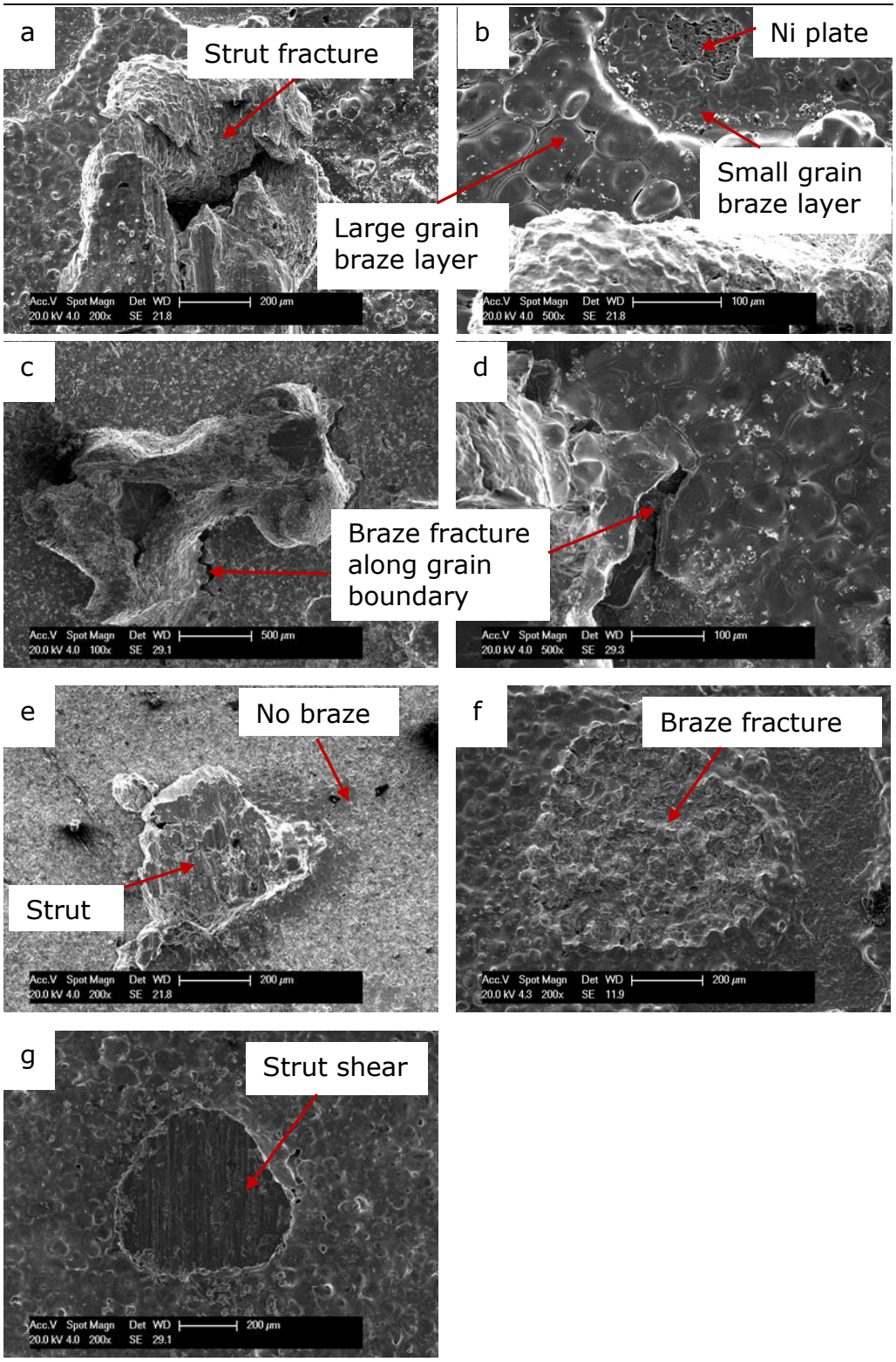


Figure 5-52. SEM images of the Ni plate braze layer following shear testing, showing sites of struts that have remained bonded (a-e), sites where the strut/bond has failed (f-g).

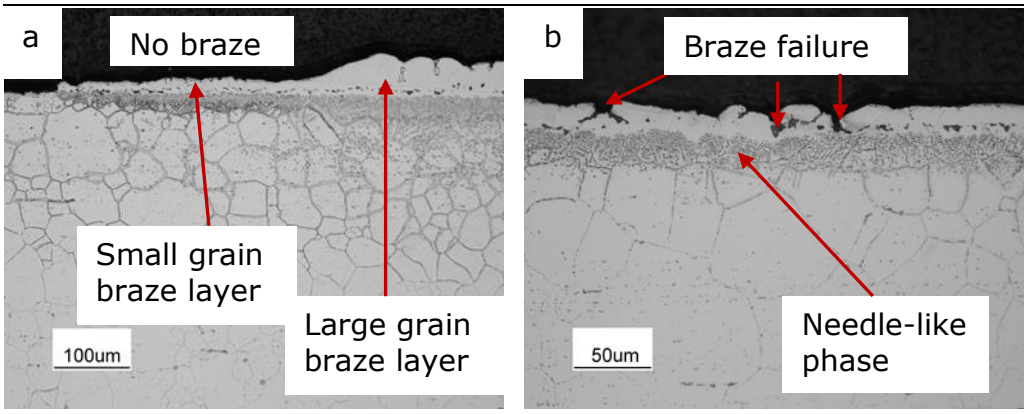


Figure 5-53. Etched cross-section images of the Ni plate braze layer, of the 4B2 sample following shear testing.

5.6 NDE BRAZE ANALYSIS

As has been reported in the previous section, the NDE analysis produced predictions for the bond areas of the samples, and was reasonably accurate in determining how the sample would perform. However the performance of the braze layer bond has less to do with the amount of braze but more to do with the quality of the bond, which is increased with the right amount of wicking to bond to the strut, but not too much that would cause the area bonded to the Ni plate to diminish.

Figure 5-54 shows the Ni plates after shear testing and the corresponding NDE C-scan image. Sample A (a) shows the large area void of braze material, and sample B (b) shows the good distribution of braze. From visual and area estimation (compared to other samples) it could be assumed that both samples were of reasonable quality (both over 30% braze coverage). However sample B failed early, and despite having the second largest braze

area it did not have the second largest shear strength. As was seen in the previous section, sample 4A1 performed very well, but had it been decided using the current method employed by Rolls Royce, whereby the largest bond areas are chosen, then it would have been discarded.

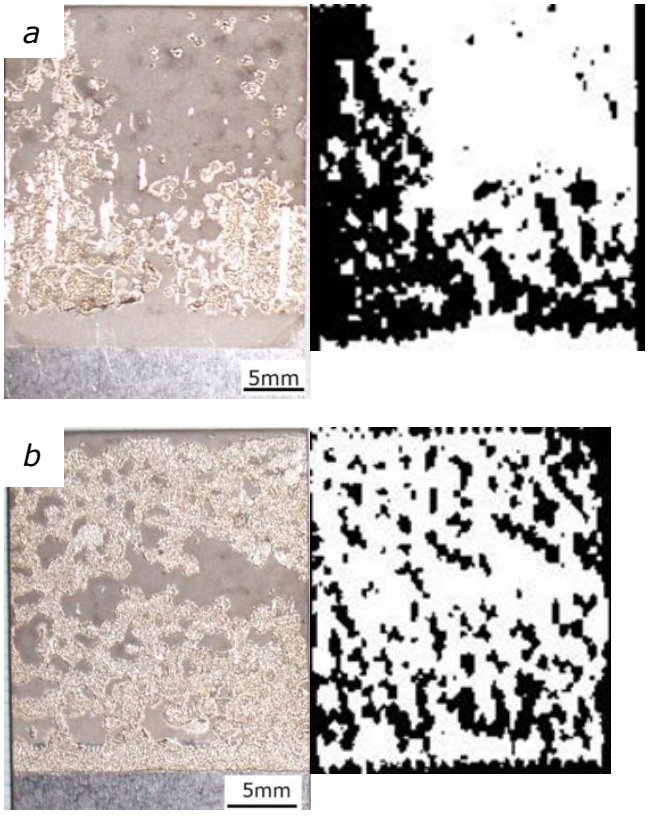


Figure 5-54. Comparison of real and NDE scan images of the brazed plate for samples A (a) and B (b).

The problem is that the NDE analysis can only resolve the variation in density in contact with the other side of the Ni plate. How much braze has wicked, and bonded well is not known. Attempts were made to locate the wicked braze using the X-ray micro-ct. As previously mentioned the Ni plate caused too much interference for accurate imaging close to the braze layer, therefore foam samples

that had separated from the Ni plate, after testing, were scanned. Figure 5-55 shows x-ray micro-ct images of the scans performed on a non-brazed 1116 sample (a), and an 1116 shear sample that separated from the Ni plate. The images are aligned so that the shear sample is in line with were it would be in the non-brazed sample, as grinding had been performed on it. It can be seen how the scans show relatively thicker struts in the shear sample further from the bottom of the sample. Whilst this could be a sign of the wicking of the braze material, it is not conclusive, as the strut thickness varies from sample to sample. Due to the limitations of the sample size that was possible to be scanned using the x-ray microCT, it was not possible to scan samples before and after the brazing process to truly analyse the wicking behaviour.

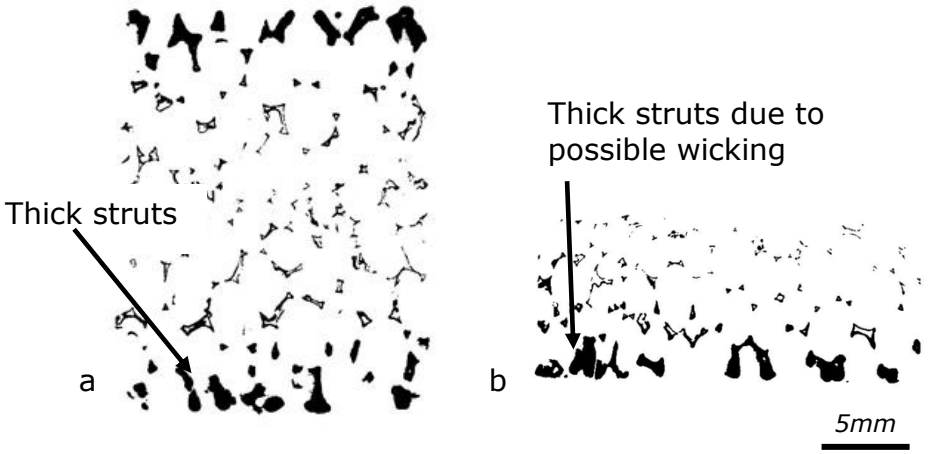


Figure 5-55. Comparison of microCT scans of non-brazed (a) and brazed (b) foam material, with the thickness of the struts in the brazed sample possibly due to wicking.

5.7 CONCLUSION

The aims of the research undertaken for in this chapter were; to analyse the braze bond of the foam material, and evaluate the effectiveness of the NDE process.

Microscopy analysis of the brazed foam material revealed that there were many areas of the samples that had a poor, even no, amount of braze material coverage, which was most likely due to the wicking of the braze material by the struts. The boron, present in the braze layer, had diffused out forming Cr-B phases in the struts and the plate, as well as Ni-B phase within the braze. The diffusion of the B had left voids within the braze that weakened the braze bond. The previously seen Cr-Ni secondary phase seen in the un-brazed material was no longer visible, due to the brazing process heat treatment removing it.

The shear failure of the foam was characterised by the collapse and subsequent densification of the cells at the point closest to the shear incursion face. The cells deformed in rows, with the next row of cells remaining intact until the previous row had been sheared at its struts bond.

As the Ni plate is pulled during shear testing, the bonded area is reduced and the stress within the sample therefore changes. By accounting for the reducing bond area the stress-strain plot reveals a plateau, indicating that the shear forces act at a constant to deform the cells. This also showed that the cells have a relatively uniform strength throughout the samples in the LL.

Ultrasound NDE analysis estimation of the braze coverage of the samples, were reasonably accurate. The largest areas determined by the NDE method, corresponded with the stronger samples. However it was observed that the performance of the braze layer bond has less to do with the amount of braze but more to do with the quality of the bond, with the quality increased with the right amount of wicking to bond the strut, but not too much that would cause the area bonded to the Ni plate to diminish.

6 DIGITAL IMAGE CORRELATION

6.1 INITIAL TRIALS

The Digital Image Correlation (DIC) method for analysis of compressive and tensile failure of the foams was to be used for all mechanical testing samples. However initial trials of the DIC produced incomprehensible results. Figure 6-1 (a) shows the small area that the system was able to identify, and Figure 6-1(b) shows the reconstructed model of the sample. Several variations of the setup parameters were trialled but all resulted in similar results. Contact with the system support produced no solutions, and it was the technician's opinion that the large pore size was allowing imaging from behind the front plane of the sample, creating a conflict in the modelling software. Attempts to limit visibility of these struts proved unsuccessful as well. As use of the DIC was deemed unsuitable it was decided to continue the investigation of the materials using conventional methods.

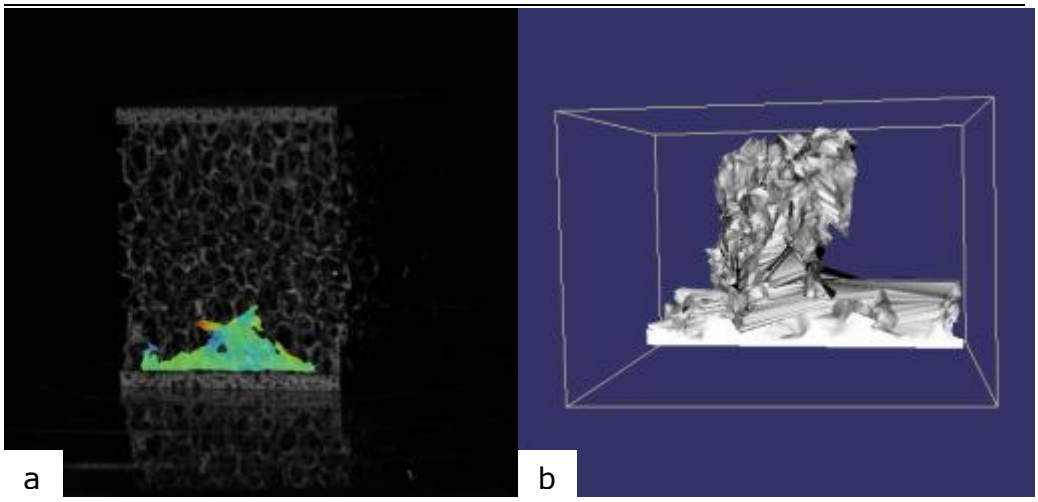


Figure 6-1 Images from the initial trials of the DIC method showing the small area that the system could recognise (a), and the incomprehensible reconstruction (b)

6.2 SECONDARY TRIALS

Upon completion of the experimental work a possible solution to the DIC problem was suggested. The previous trial work had used a two camera approach for a 3D analysis. However a single camera 2D analysis test would allow for an easier reconstruction. Unfortunately due to the conventional tests having been run there were few samples to test with this new method. The following sections describe the results from the few samples that remained and were able to be tested with the new method. Although not an exhaustive sample range the data does highlight and complement several of the claims made in the analysis of the conventionally tested sections.

6.2.1 Compression Testing 1723 Foam

As in the conventional testing, the 1723 foam sample was compression tested in the ST orientation with the testing parameters. Figure 6-2 shows images of sample D14 during testing

with the measured displacement (mm) plotted for the Y-axis (b) and X-axis (c).

As the compression of the sample progressed, an increased amount of sample moved sufficiently out of the plane that the camera was focussed on, that measurements were no longer recorded. In 3D analysis this would be corrected for, but as only 2D analysis could be performed, the data of the struts nearing the densified region of the sample was lost, and the amount of displacement of each strut as "fit in" to the densified region could not be measured fully.

It can be seen in the Y-axis sequence of images (b) that the majority of the densification of the sample takes place in the central "dark band" region, with both the top and bottom of the sample showing little variation in displacement. As the sample is compressed the central densified area increases and more material is moved out of plane causing loss of data.

Analysis of the X-axis sequence of images (c), shows that there are areas of localised displacement during compression. These areas correspond with struts that are bending to "fit" within gaps of the densified region, and eventually move out of plane.

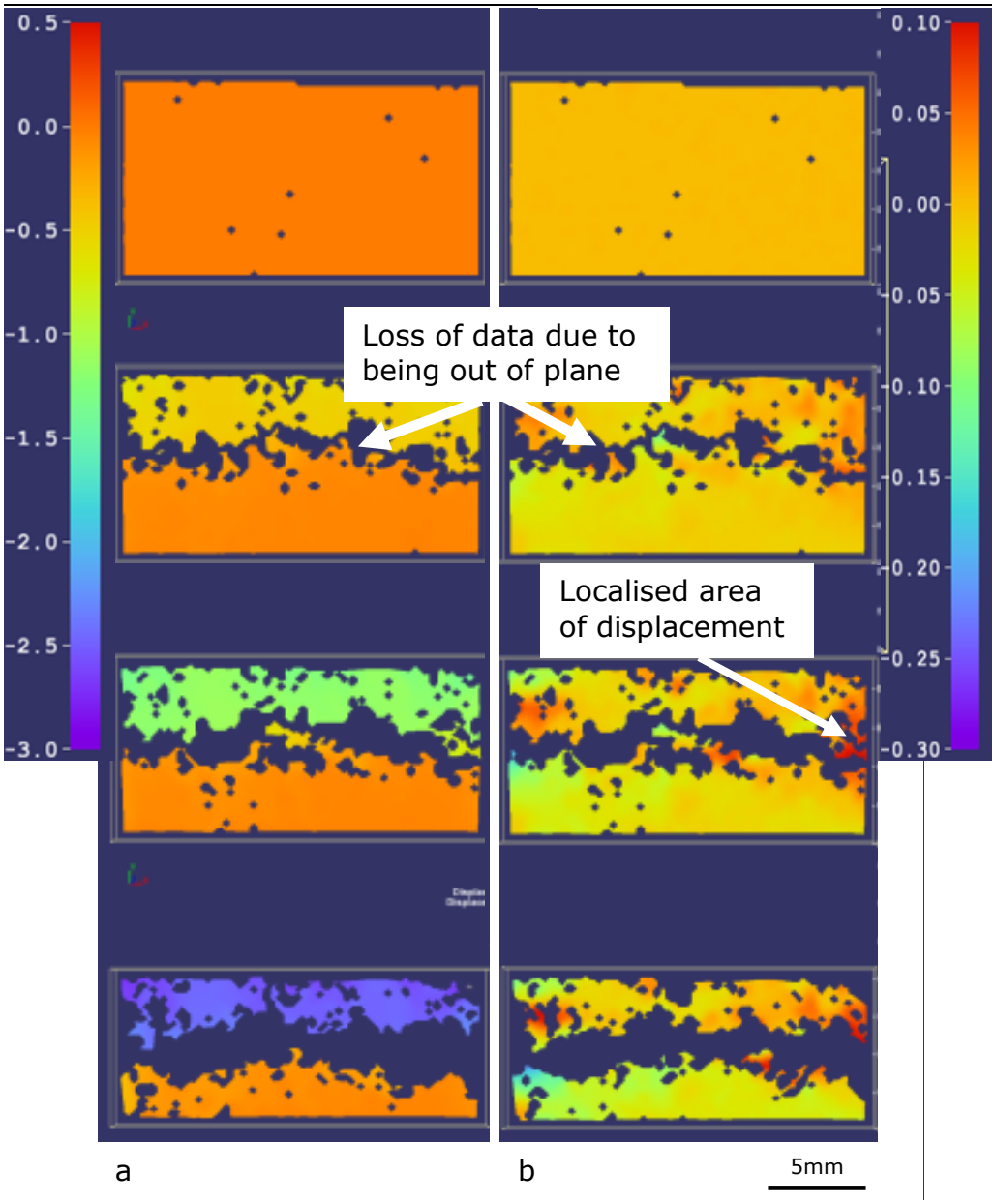


Figure 6-2 Images of the DIC analysis of the 1723 foam sample, ST orientation compression test, with displacement plots (mm) of the Y-axis (a) and X-axis (b).

6.2.2 Compression Testing 1116 Foam

Similarly to the 1723 foam the 1116 foam was tested with same parameters as the conventional tests. Two tests were performed one in the ST orientation and one in the LL orientation.

Figure 6-3 shows images of sample A15 with the measured displacement in the Y-axis (a) and X-axis (b) plotted. The sample was tested in the ST orientation and displays similar results to the 1723 sample also tested in the ST orientation, with the majority of the densification of the sample taking place in the central "dark band" region, with both the top and bottom of the sample showing little variation in displacement (b). In contrast to the 1723 sample, the A15 sample exhibited fewer areas of localised displacement. This is likely due to the larger amount of space for the struts to "fit" into during densification.

Figure 6-4 shows images of sample 6E during LL compression testing, with the measured displacement in the Y-axis (a) and X-axis (b) plotted. When compared to the ST orientation tests it can be seen that there is much more displacement of the struts in both the X and Y-axis. Two intersecting lines of densification are observed, in comparison to the single line created in the "dark band" region seen in the ST orientation tests. Without the "dark band" region acting as an initiation site for collapse, the struts collapse along the weakest sections of the foam, with further displacement as stronger struts hold out longer.

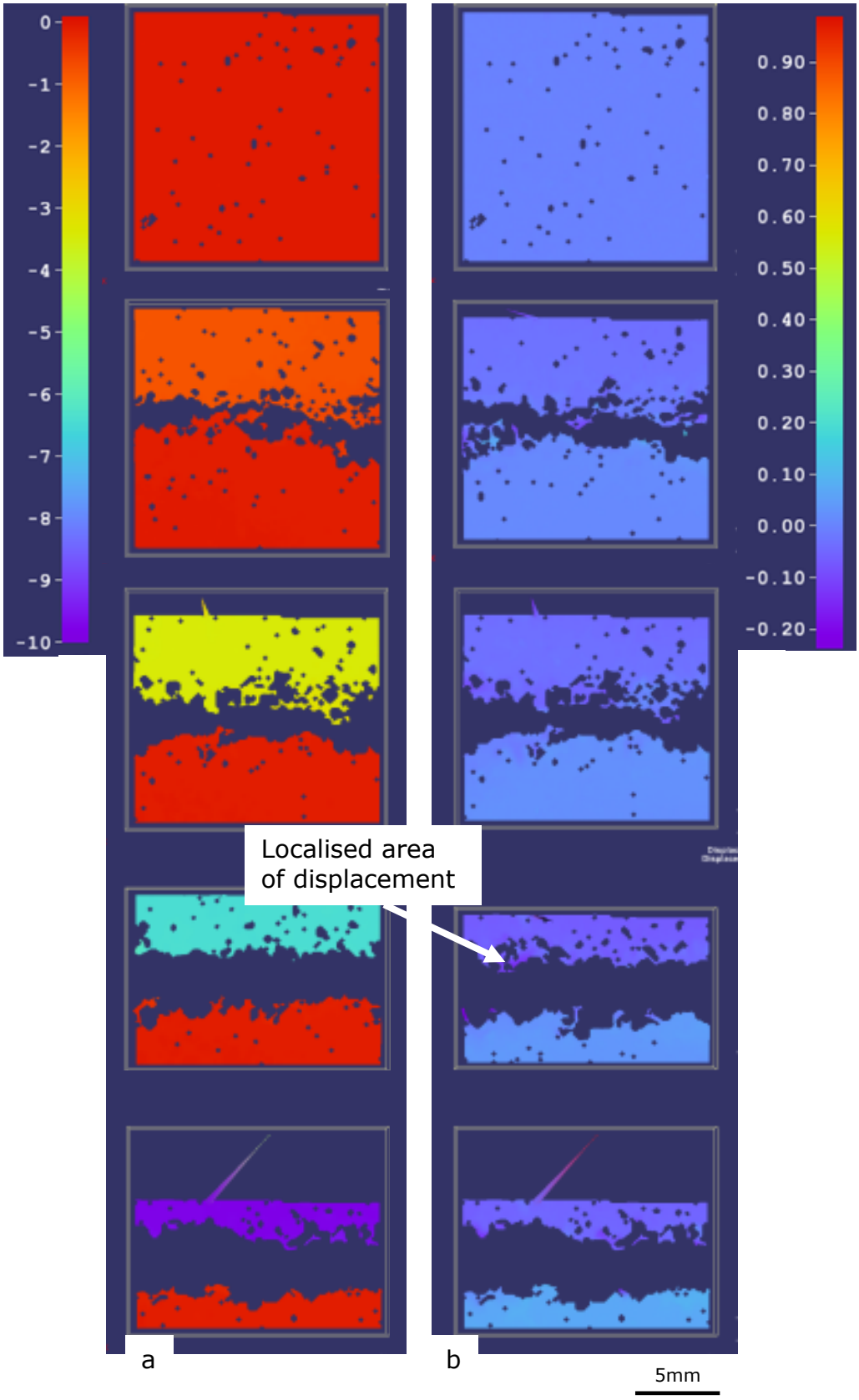


Figure 6-3 Images of the DIC analysis of the 1116 foam sample, ST orientation compression test, with displacement plots (mm) of the Y-axis (a) and X-axis (b).

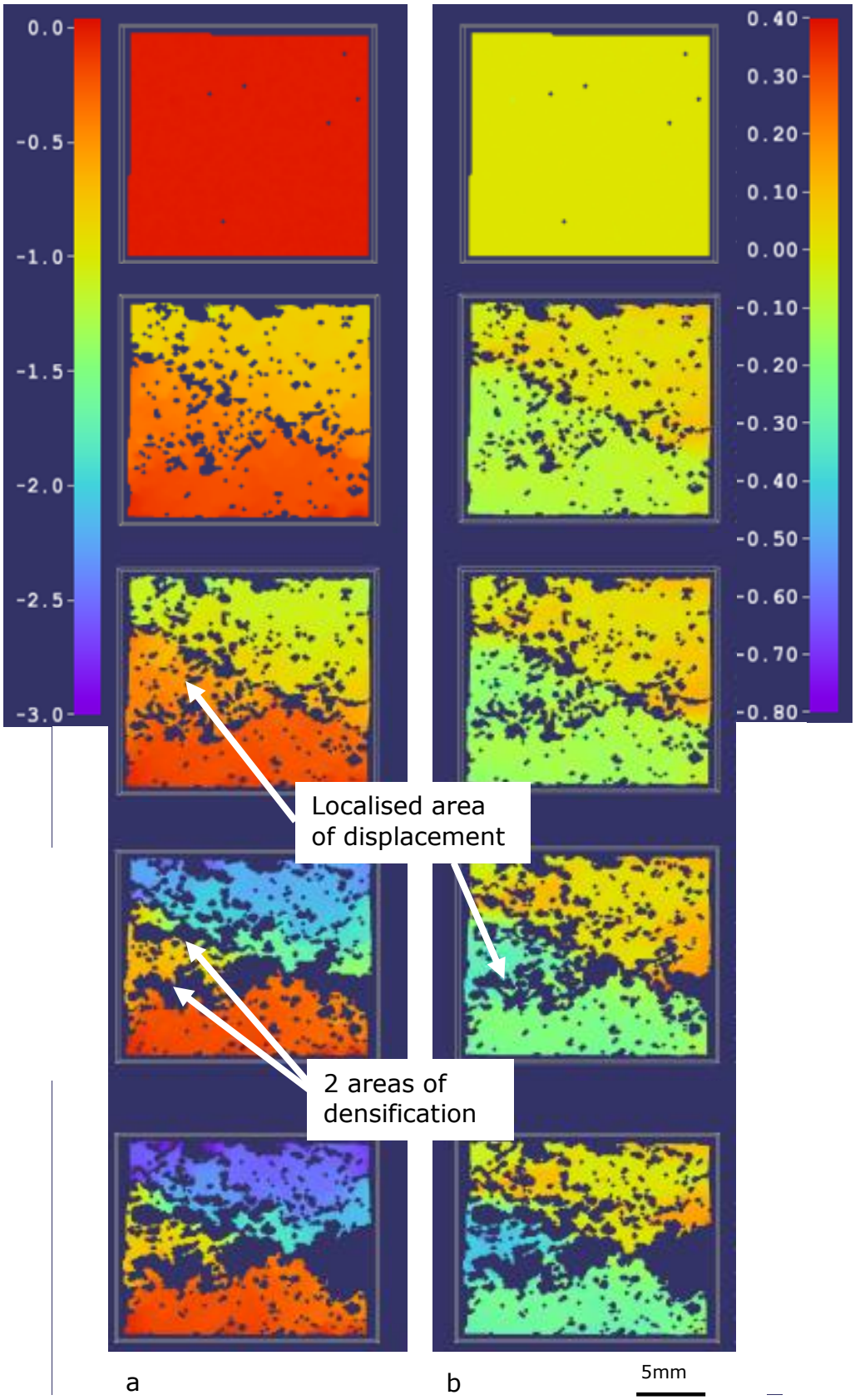


Figure 6-4 Images of the DIC analysis of the 1116 foam sample, LL orientation compression test, with displacement plots (mm) of the Y-axis (a) and X-axis (b).

6.2.3 Tensile Testing 1116 Foam

A sample of 1116 foam was tensile tested in the ST orientation, using the same parameters as the conventional testing. Unfortunately there were no LL orientation samples that could be tested at the same time to perform a comparison.

Figure 6-5 shows images of sample BA6 during ST tensile testing, with the measured displacement (mm) in the Y-axis (a) and X-axis (b) plotted. Similar to the ST compression testing, the failure of the sample is initiated in the "dark band" region, with little displacement in the majority of the foam. Two areas of note were observed during the test. The first was the localised displacement in the bottom half of the sample, that was caused by the failure of the bond between the foam and tab. Once the bond had failed the section of foam above it was now free to move as the sample was pulled. As the surrounding area struts stretched, the localised struts remained the same but moved position. The second area of note was the localised displacement that occurred in the upper half of the sample near the end of the test. After the majority of the struts had failed a few struts held out, which as the sample continued to be pulled caused the foam to stretch along and around their positions.

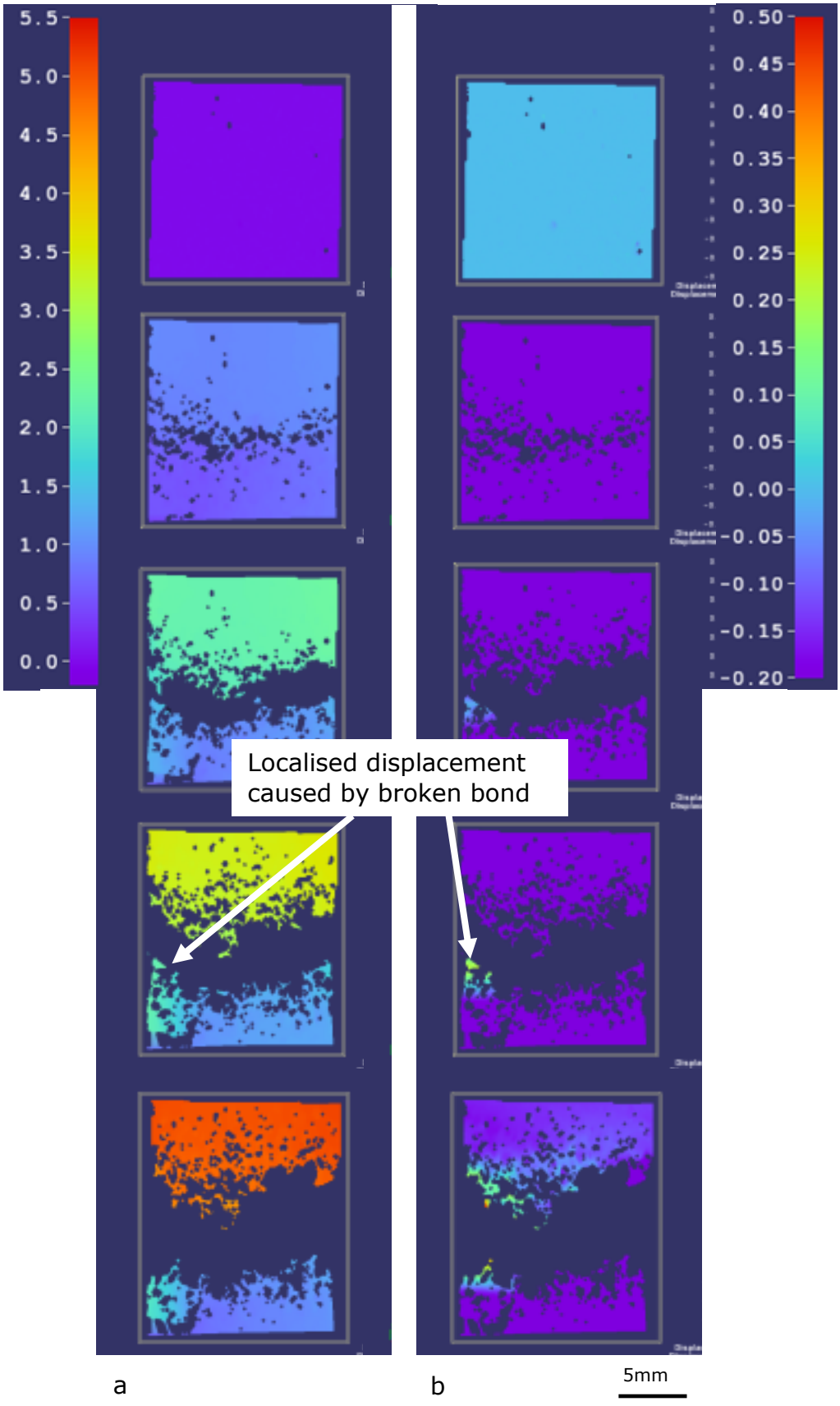


Figure 6-5 Images of the DIC analysis of the 1116 foam sample, ST orientation compression test, with displacement plots (mm) of the Y-axis (a) and X-axis (b).

6.3 CONCLUSIONS

The DIC work undertaken although not exhaustive does complement the conventional mechanical testing that was performed. The main claims made were; that failure in the ST orientation of the foams is initiated in the "dark band" region, with little deformation within the bulk of the foam until further densification occurs; and that in the LL orientation failure occurs across the foam, with densification occurring at the weakest sections of the foam. In both cases the DIC data recorded further highlights these claims.

Ideally more samples wold have been tested using this method, however as previously stated, few samples remained. Further to this a solution to configuring the equipment to perform 3D analysis on the foams would be greatly beneficial, as greater analysis of the failure and movement in the densification zone can be made.

7 CORROSION

Artificial corrosion tests of samples seldom give results that correlate with the performance in the application environment (due to varying conditions encountered affecting the chemistry of reactions). Therefore the tests performed were for qualitative purposes only. The non-brazed material was tested to see whether there was any significant variation in corrosion resistance across the foam sheet. The brazed foam was tested to analyse the effect of the braze on the corrosion resistance.

7.1 NON-BRAZED FOAM

Analysis of the un-brazed foams showed that the Ni-Cr material is highly resistant to corrosion with the bulk of the material being unaffected by the salt spray.

Figure 7-1 shows images taken after the 0, 100, 200 and the final 900th hour for an 1116 sample (images from all the samples tested can be found in Appendix 12). It can be seen that there is a small amount of corrosion located at the edge of the samples, with the bulk of the sample remaining unaffected. This was typical of all of the samples tested in this way. The areas that show corrosion appear to be sites where the material was most likely damaged during the machining process, whilst sectioning, and where the salts have been able to accumulate on the strut surfaces.

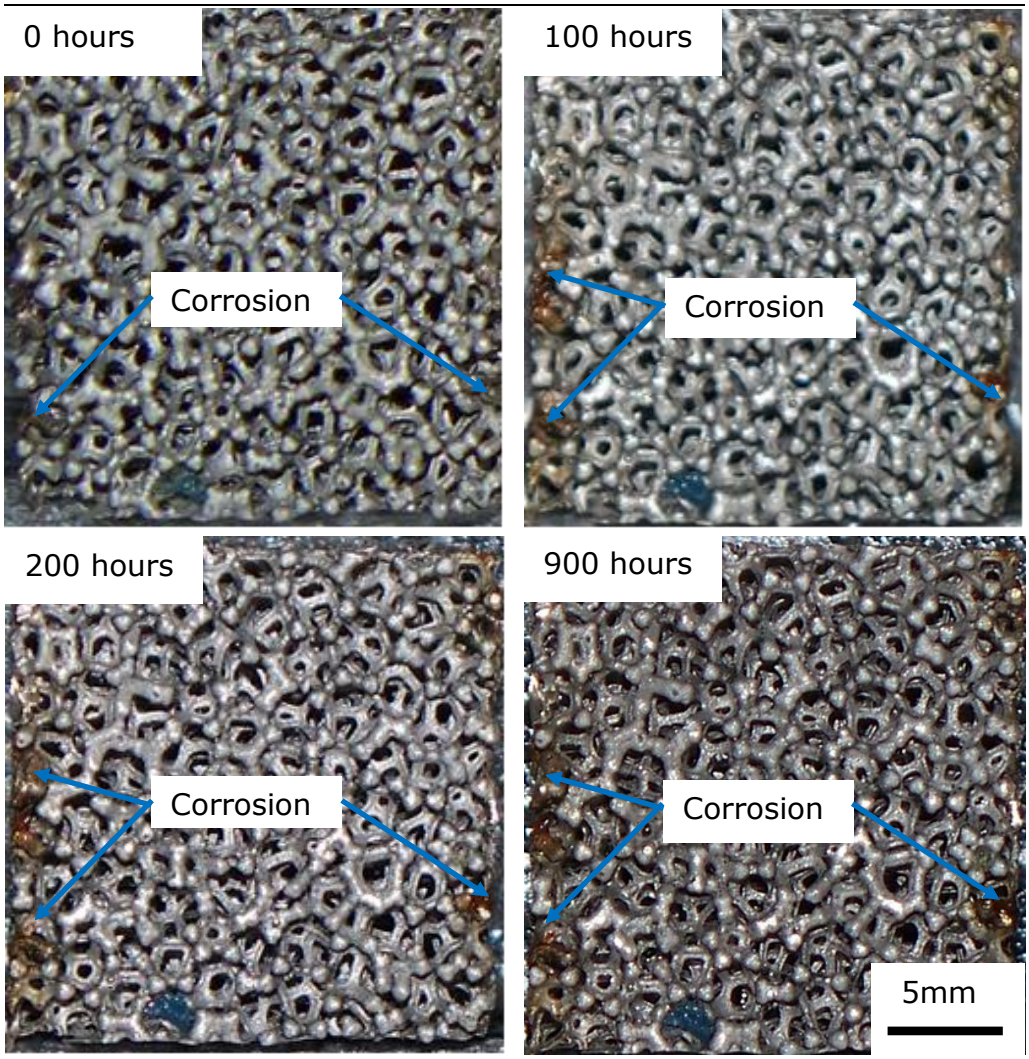


Figure 7-1. Images of an 1116 sample taken at labelled times, showing the location and progression of corrosion during salt spray testing.

Further tests were performed to confirm this by making several cuts as well as filing the samples and arranging them in different orientations, to eliminate the possibility that the corrosion was accelerated in the affected areas by run-off from the salt spray fog alone. Figure 7-2 shows an example of one of the samples.

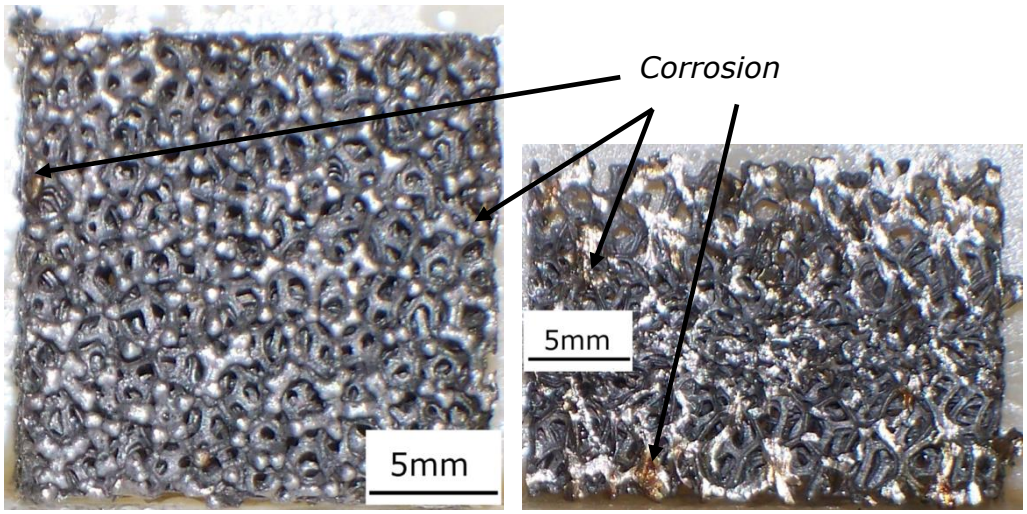


Figure 7-2. Images of two samples which have undergone corrosion testing for 200 hours. Highlighted are the areas where corrosion is visible.

The results were similar to what would be expected of any Ni-Cr material that underwent similar testing, the machined areas were most susceptible to corrosion. As was discussed in the literature review, machining not only damages the Cr-oxide passive layer (which is the main protection), but can also introduce defects or foreign objects into the sample which can act as initiators for pitting and further corrosion. Most importantly, the qualitative analysis showed that there was no large variation in corrosion resistance of the foam across the sheet material.

7.2 CORROSION OF THE BRAZED FOAM

Analysis of the brazed foam samples showed no significant corrosion had taken place within the bulk of the material. Figure 7-3 shows the images taken at the beginning, and after 900 hours, of the salt spray test for two brazed 1116 samples. The samples had their Ni

plates orientated differently in order to ensure any effects were not solely due to the salt spray run off. Both of the samples contained areas where the struts had not bonded to the Ni plate, which also allowed for comparison between the corrosion behaviour of the bonded areas no-bond areas. Figure 7-3(a) shows the images of a brazed sample orientated with the Ni plates orientated above and below the foam. It can be seen how the corrosion has only taken place at the base of the sample. This was typical for the samples tested with some showing corrosion around the top plate as well, but not as severely. It can also be seen in the 900 hours image, how the area where some damage had occurred resulted in the most severe corrosion taking place. Figure 7-3(b) shows the images of the brazed sample orientated with Ni plates at the sides. It can be seen that the surface shows a small amount of corrosion, but that the struts behind do show signs near the top of the sample.

In both samples there does not appear to be any sign of significant corrosion of the bulk of the foam material or Ni-plate, with areas showing signs in areas where the environmental fluids can stagnate causing crevice corrosion. Similar to the non-brazed foam, machining induced defects caused the most severe corrosion. Due to the use of EDM to section the samples, less damage was done to the bulk quantity of struts, which would account for why corrosion didn't occur as predominantly in the foam. As discussed in the literature the EDM process is less likely to introduce foreign objects (which can act as initiation sites) into the cut surface compared to conventional methods. The EDM does create a recast layer that is less resistant to

corrosion, however no significant corrosion due to this was observed.

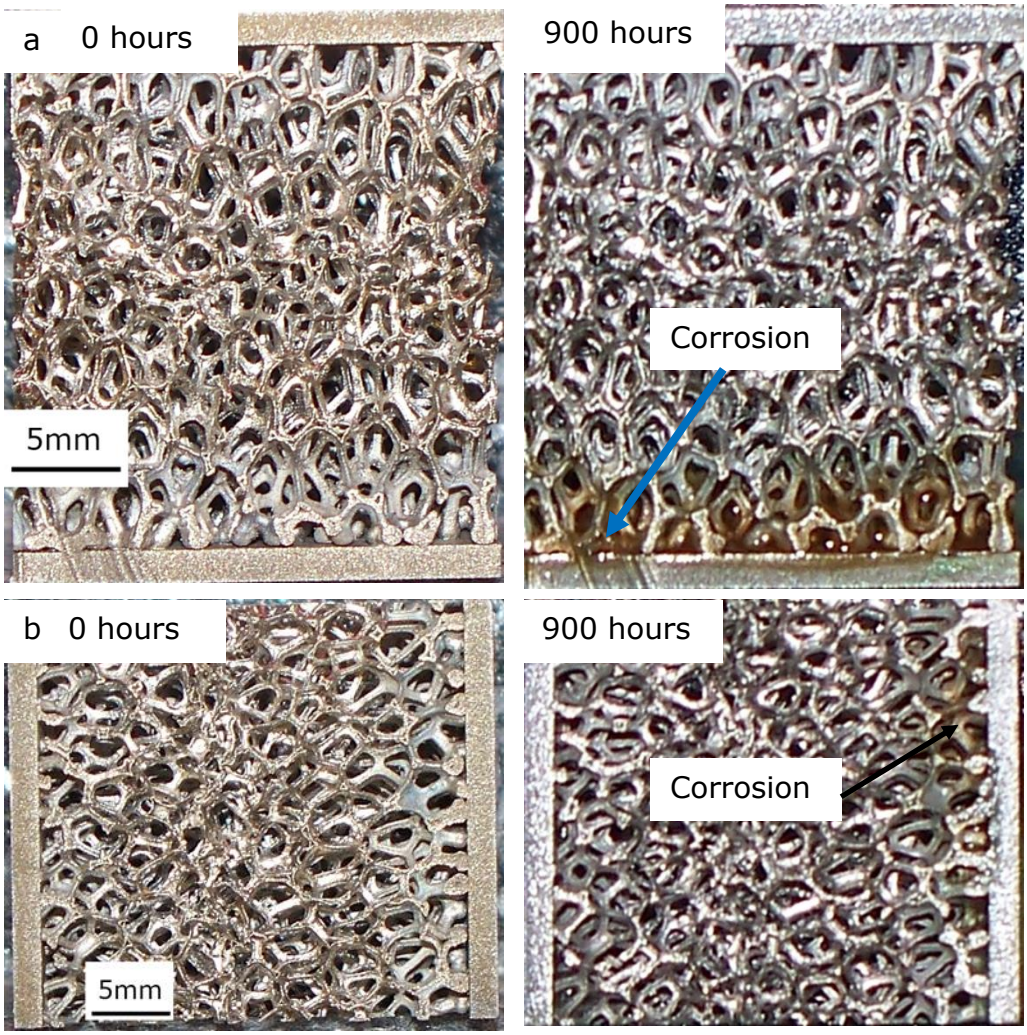


Figure 7-3. Images of brazed samples taken before and after 900 hours of salt spray testing. Samples were orientated with the Ni pates at the top and bottom (a), and with the plates at the sides (b).

Figure 7-4 shows etched images taken of the brazed foam samples after 900 hours of the salt spray test. Figure 7-4(a) shows an image of a strut from within the bulk of the material, which shows no sign of corrosion on its surface. Figure 7-4(b) is an image of a brazed strut from a region where there was no signs of corrosion

(discolouration). There appears to be no signs of braze corrosion around the base of the strut either. Figure 7-4(c) shows an image of a brazed strut from a region that appeared to undergo corrosion. It can be seen that there are two voids within the braze layer, as well as corrosion of the Cr rich phase at the base of the strut. Figure 7-4(d) similarly shows a strut where corrosion had created a void in the braze layer. In comparison with Figure 7-4(b) it can be seen that there was also depletion of the Cr-oxide passive layer on the strut surface. Figure 7-4(e) shows an image from close to the base of a strut, where it is visible that corrosion of the wall had taken place, revealing the Cr rich phase layer. The darkened region between the sample and the filler material (used for polishing) appears to be where salts have accumulated during testing, and which were subsequently removed during the polishing and etching process. This is evidence of crevice corrosion, which has broken down the passive Cr-oxide layer and has started to attack the Cr-rich phase beneath, intergranularly. Figure 7-4(f) is an image of the base of a strut that was not bonded to the Ni plate prior to testing. Whilst the plate, braze attached to the plate, and bulk of the strut appear to be unaffected, the Cr rich phase has been corroded, with severe intergranular corrosion.

These observations confirm what is reported in the literature that Ni-Cr foams are at risk from pitting and intergranular corrosion if the passive oxide film is breached. By preventing the stagnation of the corrosive environment fluids, it is likely that crevice corrosion

will not be as severe and thus the passive layer will not be destroyed so severely.

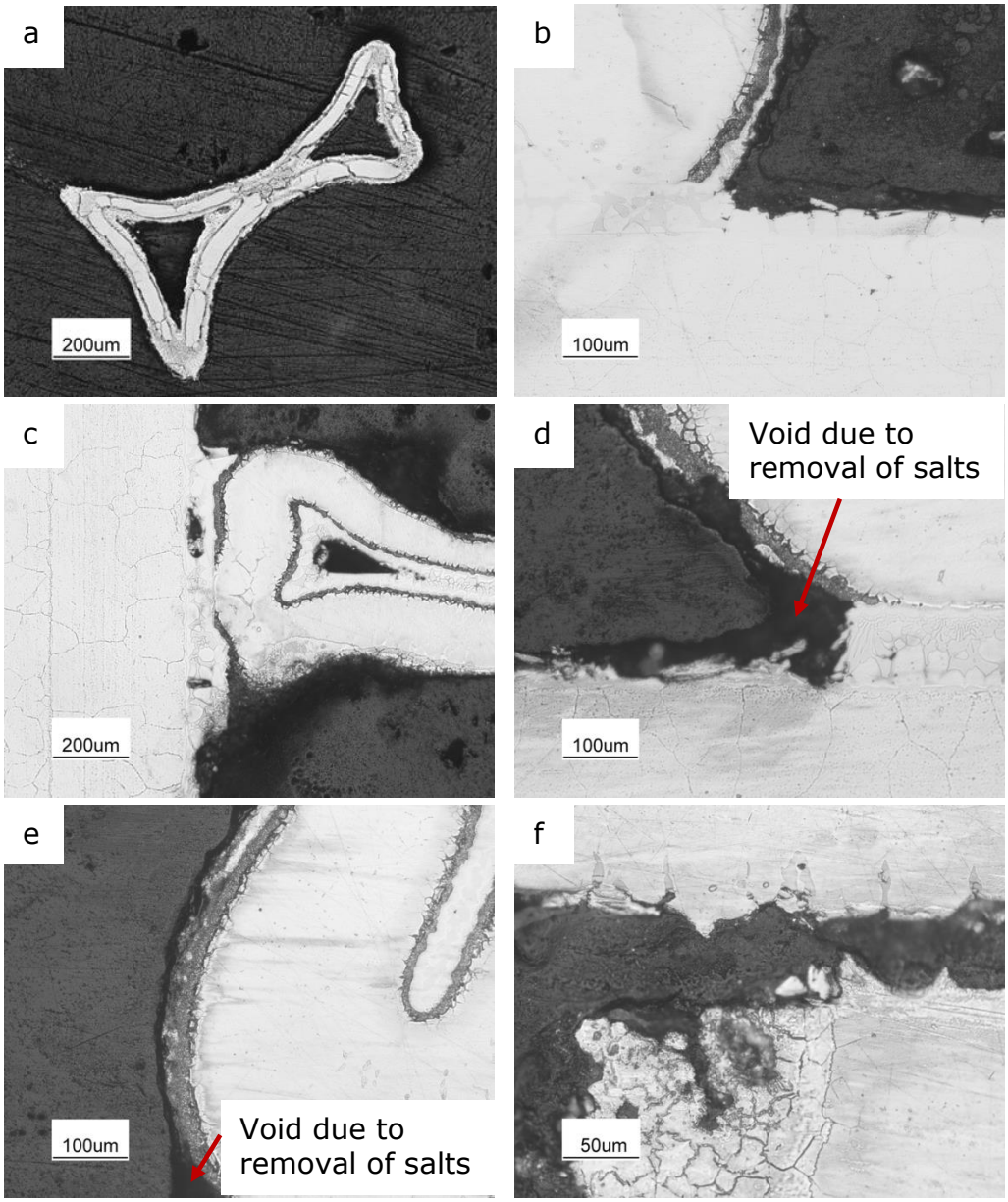


Figure 7-4. Etched sample images after 900 hours of salt spray testing. Showing the corrosive effects on a strut within the bulk of a sample (a), the braze layer (b-d), the strut wall (e), and a strut that had not bonded to the Ni plate (f).

Rolls Royce plans the addition of a filler material for sealing the foam. This should have the beneficiary effect of preventing corrosive

salts from reaching the braze layer within the bulk of the material. However, as they are manufactured with a rough cut and are removable from the casing (leaving gaps between the edges of the tiles and the casing) this will leave the edges susceptible to corrosion still, both in the foam and braze.

7.3 CONCLUSION

The aims of the research undertaken in this chapter were to analyse the corrosion resistance that the foam has (both brazed and non-brazed), to determine whether any significant issues may arise in service.

Corrosion analysis, on un-brazed foam, has shown that there is little variation in resistive properties across the sheet. Sites that showed increased corrosion compared to the bulk were found to be caused by damage sustained during the cutting process.

Corrosion analysis, on brazed material, has shown that the foams are susceptible to pitting and crevice corrosion that can corrode the Cr-oxide passive layer. Once removed the Cr-B phases, present at the base of the struts (strut-plate bond), are attacked through intergranular corrosion, due to their reduced corrosive resistance. The possibility of weakening the bond will therefore have to be considered for the design

8 ANALYSIS OF FILLED FOAM MATERIAL

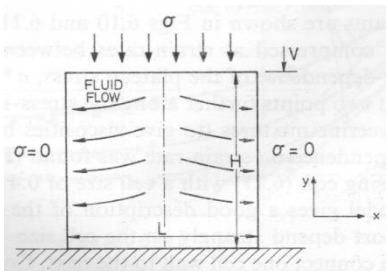
This chapter details the limited analysis which was performed on samples of filled foam. The samples were off-cuts from the manufacturing of the tiles that went into the engine, as well as from when Rolls Royce was investigating how to fill the foams. These samples were to be used in order to ascertain the how to prepare the samples, the testing parameters and the suitability of techniques such as X-ray micro-CT for analysis.

Currently the filler material chosen by Rolls Royce is a syntactic silicone containing 28 wt% hollow glass spheres (in order to reduce the density) as well as graphite particles, and is supplied by Advanced Composite Group (ACG). The density of the material is 0.830g/cc. Rolls Royce, to determine the erosive and abrasive characteristics, has already performed suitability tests on the filler and foam together. The erosion tests showed a considerable improvement over the current abradable material. The abradability tests required the filled foam to create less than 10% blade wear, and produce no pick-up of abradable on the blade which it did. In testing the 1723 foam performed better than the 1116, which would have led to its use as the material of choice. However, due to Recemat not producing the 1723 beyond 10mm thickness, the 1116 material was chosen. It has been noted that if the 1723 or similar fine pore size foam does become available with a 20mm thickness then it would definitely be considered as material of choice. [9]

8.1 MODELLING FILLED FOAM MECHANICAL PROPERTIES

As has been previously mentioned there are few examples of open-cell foams being filled with a resin and their mechanical properties investigated. The literature found focuses on obtaining accurate models of compressive deformation of the foam structures with an elastic filler. The Finite Element models that were created were derived from the Gibson & Ashby model that describes the effect a fluid passing through an open-cell foam on the strength, by modelling the filler as a highly viscous fluid (Equation 8-1), the illustration of the model can be seen in Figure 8-1.

$$\sigma_{fil} = \frac{C\mu\dot{\varepsilon}}{1-\varepsilon}\left(\frac{L}{l}\right)^2 \qquad \text{- Eqn 8-1}$$



σ_{fil} = Contribution to strength

C = Constant of proportionality (of order unity)

μ = Viscosity

$\dot{\varepsilon}$ = Strain-rate

Figure 8-1 Illustration of the model used for determining the contribution to strength by the filler

The stress-strain plots created by the addition of filler material differ from those of unfilled metal foams. As can be seen in Figure 28, the filled foam exhibits five distinct regions compared to the usual three. There is a linear elastic region (I) at low stress, two plateau regions

(II and IV), a transition region between the two plateaus (III) and the densification region (V). This prolonged plateau region results in a higher energy absorption capability. [70, 71]

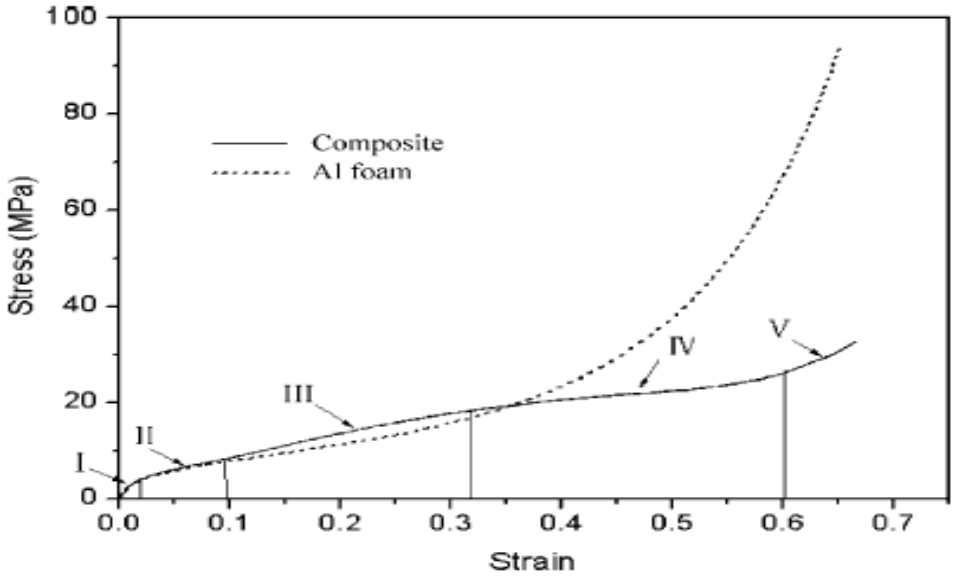


Figure 8-2 Stress-strain plot showing the five regions exhibited by the filled Al foam compared to the three of the unfilled.

8.2 ANALYSIS OF THE FILLED FOAM

Figure 8-3 shows images from a section of the filled tile, which contained a threaded metal piece for attachment to the casing. (a) and (b) are both images of struts. It can be seen that the filler material has surrounded and sealed tight around the strut in image (a), but around the strut in image (b) there is a void. This lack of sealing could be due to lack of wetting of the struts, or due to trapped air during the filling process. Whilst the majority of the sample analysed had filled well, there were several areas were voids were present, as can be seen in Figure 8-4.

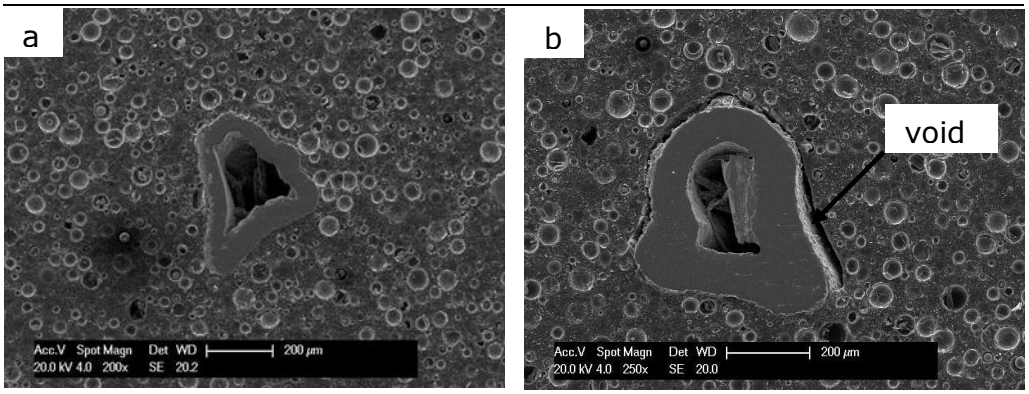


Figure 8-3. SEM images of struts in a filled sample.

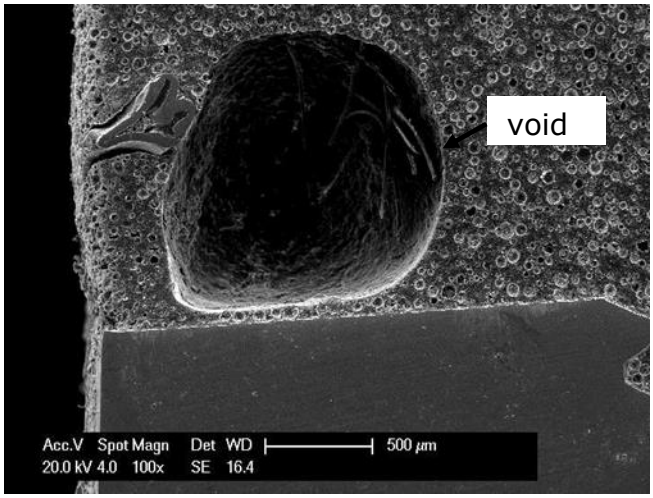


Figure 8-4. SEM image of a filled foam sample, showing a large void in the filler material.

The acoustic dampening properties of the filler material make analysis by ultrasound hard. However a trial was performed which looked at using microCT to locate voids within the samples. Figure 8-5 (a) shows a 2D slice image of a filled sample, which had a 4mm hole drilled into it. It was found that there is a lot of interference in the image from the glass spheres within the filler material, but with thresholding and subsequent contrast and colour manipulation it is

possible to image the hole (b). The resolution at which voids would be visible is something that would have to be determined.

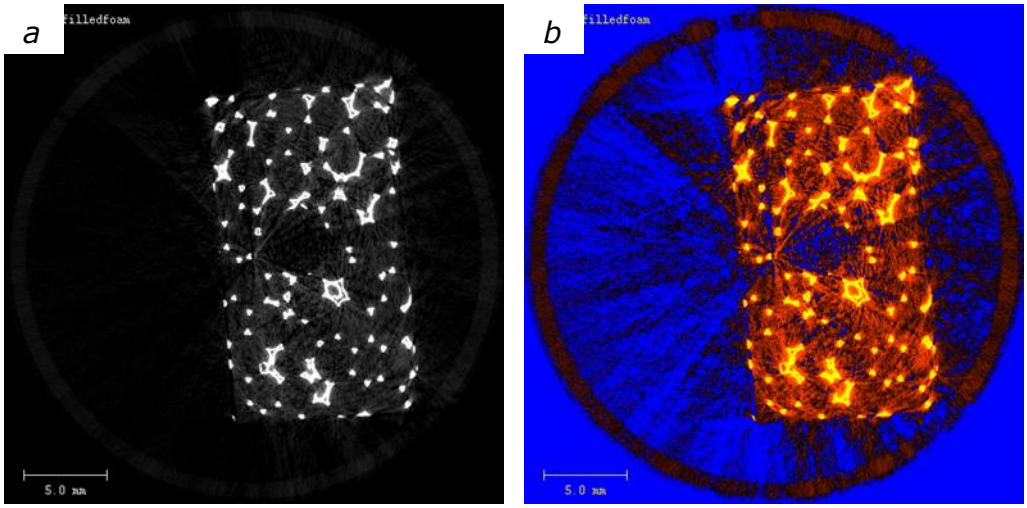


Figure 8-5. Micro- CT 2D slices from CT analysis of a filled foam sample with a 4mm hole drilled through it. Image (a) is the original image, (b) is an image with colour and contrast manipulation

Scanning Electron Microscopy (SEM) analysis of a sample which had the grooved channels machined, showed that at the corners of the channels the glass spheres had been compressed (Figure 8-6 a). This was in contrast to the sides and base of the channel in which the material had cut away without compression. Of note were cracks within the filled material that appeared at the edges of the struts that were near the surface (b).

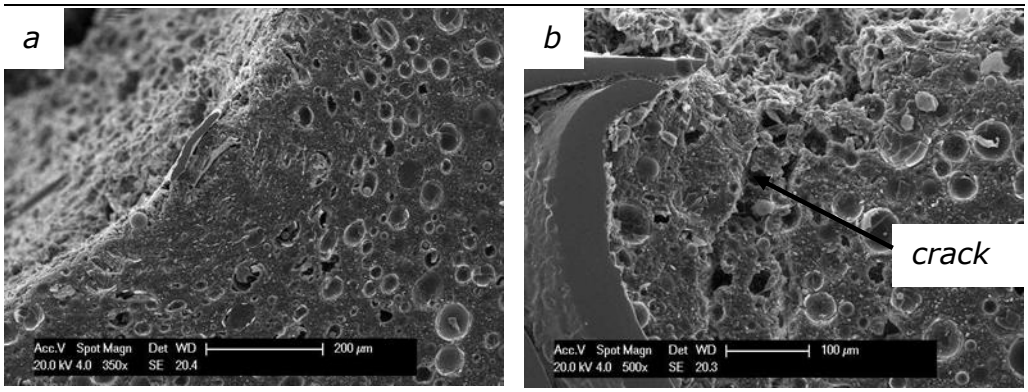


Figure 8-6. SEM images of the machined channels in a filled foam sample, showing crushed glass spheres in the corners (a), and crack at the edge of a strut (b).

8.3 MECHANICAL TESTING OF THE FILLED FOAM

A few samples that the author was given underwent compression testing. Figure 8-7 shows the stress-strain plots for the samples, with I & II being from a different section of material than A, B & C. The plots show that the two material sections appear to have different compressive strengths. Whether this variation is due to the variation in foam properties, or due to the filler being different is unknown, and so too warrants further investigation.

Figure 8-8 shows images taken of the samples during compression. As can be seen in (a) and (b) the samples begin to 'bow' during initial compression. Following this initial 'bowing' the filler material begins to push out through the pores of the foams; this can be seen in (c). Figure 8-9 shows how the material spreads out during compression, as unlike the un-filled foam, there are no voids that can be filled with the compressed material. The expansion causes tearing of the filler material as well as breaking of the struts. In

some places filler has pushed out past the foam struts, whereas in other places the filler has dislocated the struts within it. Figure 8-10 is a cross-sectional image of Figure 8-9, and shows a large void within the centre of the sample, indicating that the filler material has pushed out struts from within the sample.

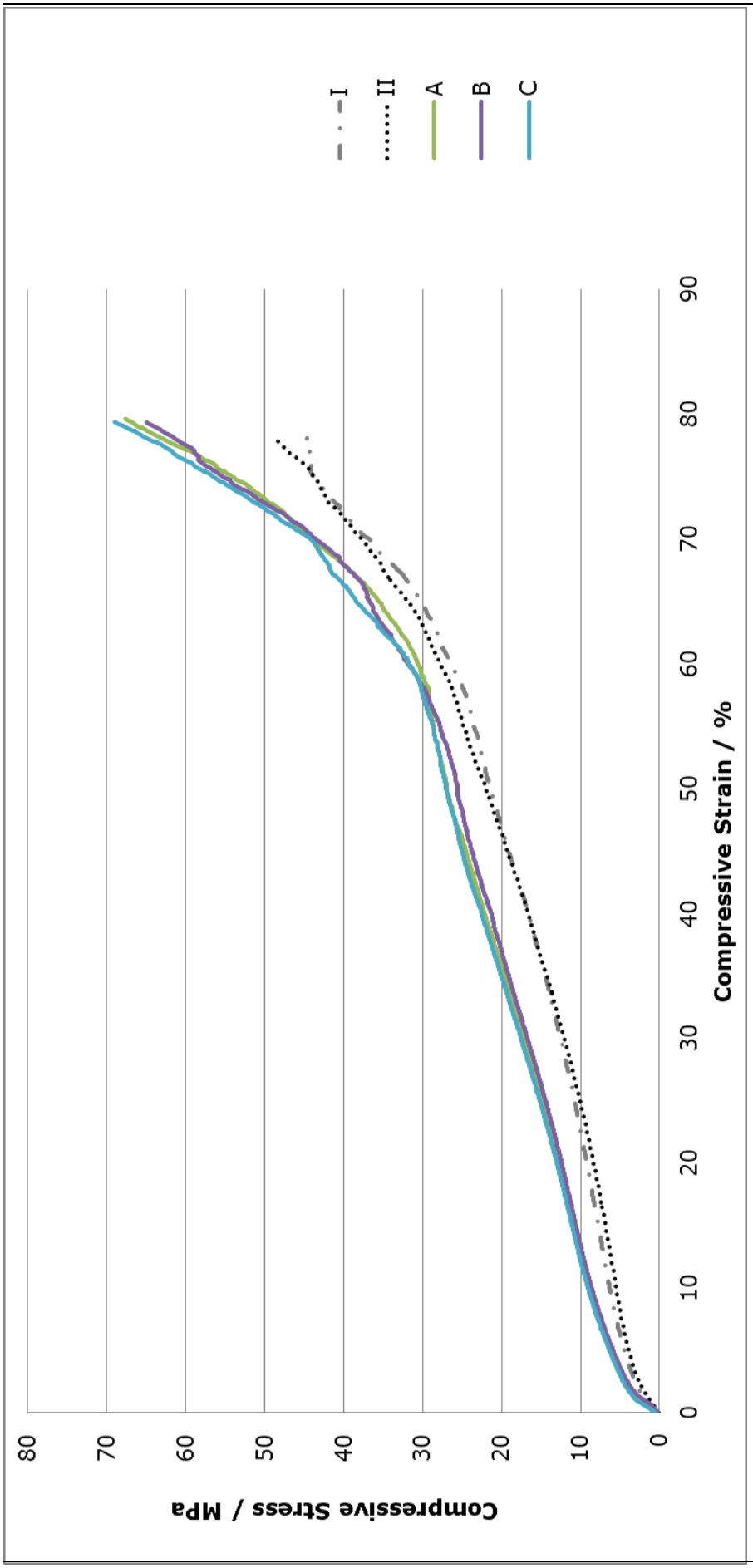


Figure 8-7. Compressive stress-strain plots for filled foam samples.

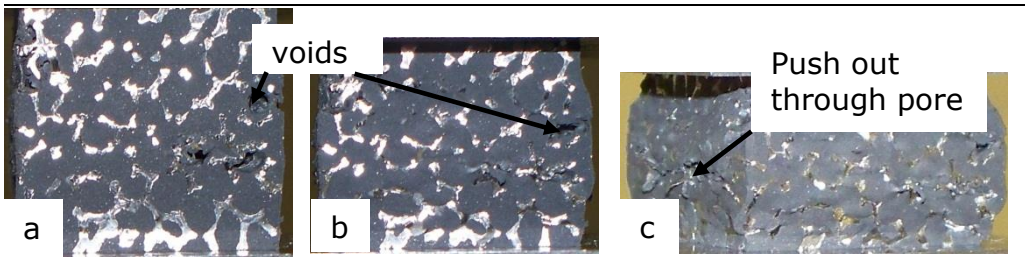


Figure 8-8. Images taken during compression testing of the filled foam material, showing voids present in the material (a-b), as well as the filler material pushing out through the pores (c).

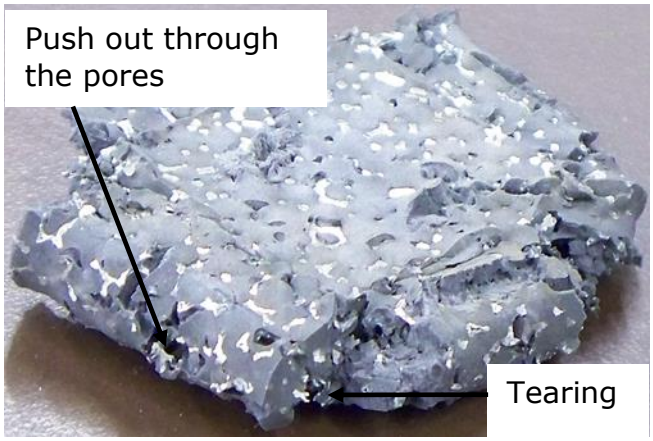


Figure 8-9. Image of a compressed filled sample showing tearing and push-out.

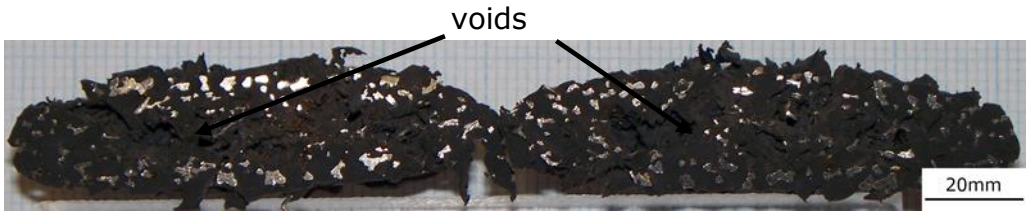


Figure 8-10. Cross-sectional images of a filled foam sample after compression testing, showing voids through the centre of the sample.

8.4 CONCLUSIONS

Initial analysis of the filled foam using microscopy found that voids are present in the filler material. Some large voids are assumed to have formed from trapped gas pockets during the filling process,

whereas voids present as gaps between the filler material and the struts appear to be the result of wetting. The filling process, and the quality of fill produced are therefore areas that should be analysed in future work.

The microscopy investigation also showed that the filler material around areas where the foam had been machined, underwent several forms of deformation, with areas of compression and fracturing present. Further analysis is needed to investigate whether these flaws are caused during filling, or they are due to the machining parameters causing deformation of the struts (as reported for the unfilled foams).

Developing a way to analyse the filled material, by a non-destructive evaluation technique (NDE), is another area worthy of future investigation. The initial work showed that micro-CT shows promise, as it is able to detect the internal struts, and an artificial flaw of 4mm diameter could be detected.

The limited compression testing performed did show a correlation with similar work. It was observed that the filler material dos not just flow around the foam during compression, but can fracture struts and cause tear out. The two small batches of samples tested had differing stress-strain plots, with one batch showing higher strengths than the other. Whether this is an effect of the foam properties or whether this is due to a variation in the filler material is unknown. Further analysis of the compression, as well as tensile and shear, properties is therefore required to properly understand

the process involved during deformation. As well as determining the validity of the theoretical model for predicting failure, and the effect of variation in filler properties.

9 FINAL CONCLUSIONS

This section summarises the key results from the research undertaken in the study of open-cell nickel-chrome metallic foams for an abradable compressor sealing.

A previously un-reported "dark-band" region exists within the as-supplied Recemat foam. This region contains the initial strut failures in the ST orientation during both compression and tensile loading. A section reducing stage during the manufacturing process appears to be the cause of the "dark-band" which results in the detrimental effects on the foam properties.

This thesis has documented the extent of the variation in strength across a foam sheet, and has shown that the edges of the sheet (corresponding to higher density) have higher strength than the bulk of the sheet. Strength is also affected by the amount of Cr diffused into the struts. This is important for the final application as multiple components will be manufactured from a single sheet.

It was found that the current method to determine the brazed bond quality using UT has limitations. Although the method can determine the braze coverage, the strength of the bond was found to be more dependent on the wicking of the braze in and around the base of the struts. Therefore the currently proposed quality/acceptance criteria of using components with the largest area coverage above a (currently arbitrary) UT threshold may give false results as to the strength of the bond.

Though limited, the results from compression testing have indicated that as the filler material is forced through the pores of the foam, in some instances it can damage, even remove, the foam struts. It had previously been assumed by Rolls-Royce that the filler would flow around the strut.

10 FUTURE WORK

The work undertaken for this thesis was to understand the properties of the Ni-Cr open-cell foam that was used by Rolls Royce, as well as determine the effectiveness of the ultrasound NDE method. Whilst the properties of the foam are now better understood, further work is needed to understand the brazing process, and develop an NDE method to be more effective in determining braze quality.

Future work will need to analyse the 1116 sample across an entire sheet, in a similar way to how the 1723 was studied. The 1723 material should also be studied in the LL orientation, as a seal assembly could be manufactured from joining of material in this orientation. Use of the DIC in this future work would be recommended.

In order to better understand the wicking behaviour of the braze material, X-ray micro-tomography scans are performed on samples before and after the brazing process. This will allow observations of the extent to which the braze wicks, and fills, the struts. This will require the use of a larger scanner (with a higher resolution), as the one used for this thesis allowed only a maximum sample size of 20x20mm. Further analysis could be performed by varying the material preparation, amount of braze tape layers used and brazing process times, in order to determine the optimum parameters for producing the strongest bond between the foam and plate, and

further analyse the failure within the braze during tensile and shear loading.

This project was a precursor for testing filled foams. Therefore future work should undertake the same testing procedures with the same foams, only filled. This will allow comparisons to be made between the properties, and the effect of the filler on the foam structure during deformation. Further use of the various NDE methods should also be investigated to determine their effectiveness with the filler present and to help characterise the mechanical failure of the filled foam.

The work undertaken in this thesis was towards the engine programme at Rolls Royce. Considerations of the engine development lead to other areas of future work. One area discussed was the effect of higher temperatures on the seal made of filled foam. One of the initial plans of the project was to investigate this, however the lack of filled foams subsequently forced its removal. Whilst higher temperatures (<~120°C) may have little effect on the mechanical properties of the foam, if the filler becomes less viscous it may flow around the struts during collapse.

Another area of consideration is the possible partial fill of the foam samples. By only partially filling the foams, the seal can be created without the addition of needless weight. How a partially filled foam would collapse would need to be understood.

11 REFERENCES

1. Lefebvre, L. P, Banhart. J. Dunard, D. 'Porous Metals and Metallic Foams: Current Status and Recent Developments'. *Advanced Engineering Materials*. 2008.10. No 9. pp775-788.
2. Duan, D. Li, S. Ding, X. Jiang, S. 'Preparation of Ni-Cr alloy foams by electrodeposition technique'. *Materials Science and Technology*. 2008. Vol 24. No 4. pp 461-466.
3. Onck, P. Van Merkerk, R. Raaijmakers, A. M. De. Hosson. J. 'Fracture of open and closed-cell metal foams'. *Journal of Materials Science*. 40. 2005. 5821-5828.
4. Choe, H. Dunand, D, C. 'Mechanical properties of oxidation-resistant Ni-Cr foams'. *Materials Science and Engineering A*. 384. 2004. pp 184-193.
5. Chan, Y. Buggeln, R. McDonald, H. '3-D Dynamic Labyrinth Seal Analysis Aero Propulsion Laboratory.' *Air Force Wright Aeronautical Laboratories*. AFWAL-TR-87-2009. 1987.
6. Hopkins, N. 'Abradables: ODA Course Notes'. *Surface Engineering Group Rolls Royce*. 2005
7. Andy Moore, Chief of Fans R&T. *Surface Engineering Group Rolls Royce*. Rolls Royce 2005.
8. Ghasripoor, F. 'Abradable Coatings Increase Gas Turbine Engine Efficiency'. *Materials World*. 1997, Vol, 5 no. 6, pp. 328-30
9. Pattinson, G. Gent, J. 'Materials Capability Acquisition Technology Overview Presentation Gate 1: NiCr Abradable Metallic Foam For Compressor Sealing'. *Rolls Royce* 2009

10. Wadley, H. 'Cellular Metals Manufacturing'. *Advanced Engineering Materials*. 2002. 4. No 10. pp 726-733
11. Weber, M. Banhart, J. Baumeister, J. 'Metallic Foams'. *Ullmann's Encyclopedia of Industrial Chemistry*. Sixth Edition. 2000 . Electronic Release.
12. Gibson, L, J. 'Mechanical behaviour of metallic foams' *Annu. Rev. Mater*. Sci. 2000. 30:191–227
13. Banhart, J. 'Manufacture, characterisation and application of cellular metals and metal forms'. *Progress in Materials Science*. 46. 2001. pp 559-632.
14. Ashby, M, F. 'Metal Foams – A Design Guide'. 2000. Butterworth-Heinemann.
15. Kubaschewski, O. 'Oxidation of Metals and Alloys'. Butterworths. London. UK. 1962.
16. Hibner, E. 'Nickel (and Alloys)'. *Corrosion Tests and Standards: Application and Interpretation-Second Edition (MNL20-2ND-EB).* ASTM. Jan. 2005. Chapter 50.
17. Horvath, J. Uhlig, H. 'Critical Potentials for Pitting Corrosion of Ni, Cr-Ni, Cr-Fe, and Related Stainless Steels'. *Journal of The Electrochemical Society*. 1968. Volume 115. Issue 8. pp 791-795.
18. Kritzer, P. 'Corrosion in High-temperature and Supercritical Water and Aqueous Solutions: A Review'. *Journal of Supercritical Fluids*. 2004. Volume 29. pp 1-29.

19. Jakupi, P. Zagidulin, D. Noel, J. Shoesmith, D. 'Crevice Corrosion of Ni-Cr-Mo Alloys'. *ECS Trans*. 2007. Volume 3. Issue 31. Page 259-271.
20. Oldfield, J. 'Test techniques for pitting and crevice corrosion resistance of stainless steels and nickel-base alloys in chloride-containing environments'. *International Materials Reviews*. 1987. Volume 32. pp. 153-172
21. Davis, J. 'Corrosion of Weldments'. ASM International. 2006. Chapter 7.
22. Jangra, K. 'Study of unmachined area in intricate machining after rough cut in WEDM'. *International Journal of Industrial Engineering Computations*. 2012. Volume 3.
23. Newton, T. Melkote, S. Watkins, T. Trejo, R. Reister, L. 'Investigation of the effect of process parameters on the formation and characteristics of recast layer in wire-EDM of Inconel 718'. *Materials Science and Engineering A*. 2009. pp. 208-215.
24. www.recemat.com. Recemat. Accesed September 2008.
25. Hansen, M. 'Constitution of binary alloys'. 2nd Edition. 1958. p1305. McGraw-Hill.
26. Paserin, P. 'CVD Technique for Inco Nickel Foam Production' *Advanced Engineering Materials*. 2004, 6. pp 454-459
27. Choe, H. Dunand, D, C. 'Synthesis, structure, and mechanical properties of Ni–Al and Ni–Cr–Al superalloy foams'. *Acta Materialia*. 52. (2004). pp 1283–1295.

28. Queheillalt, D. 'Synthesis of stochastic open cell Ni-based foams'. *Scripta Materialia 50*. (2004). pp 313–317.
29. Szycher, M. 'Szycher's Handbook of Polyurethanes'. CRC Press. 1999. ISBN: 0849306027.
30. Landrock, A, H. 'Handbook of Plastic Foams: Types, Properties, Manufacture and Applications'. Noyes Publications. New Jersey. 1995. ISBN: 0-8155-1357-7. p 40.
31. Hebner, P, W. 'Polyurethane Foam: Polymer's Cinderella Product'. *Insight 95 International Conference*. October 1995.
32. Paserin, V. 'Superior Nickel Foam Production: Starting from Raw Materials Quality Control'. *Porous Metals and Metal Foaming Technology*. The Japan Institute of Metals 2005. pp 317-320.
33. Liu, P, S. Liang, K, M. 'Preparation and corresponding structure of nickel foam'. *Materials Science and Technology*. 2000. Vol 16. pp 575-579.
34. Harada, K. Yamakawa, A. 'Porous Metals Using Polyurethane Foam Template'. *Porous Metals and Metal Foaming Technology*. The Japan Institute of Metals 2005. pp 301-304.
35. Badiche, X. Forest, S. Guibert, T. Bienvenu, Y. Bartout, D. Ienny, P. Croset, M. Bernet, H. 'Mechanical properties and non-homogeneous deformation of open-cell nickel foams: application of the mechanics of cellular solids and of porous materials'. *Materials Science and Engineering*. 2000. pp 276-288.
36. Di Bari, G. 'Electrodeposition of Nickel, in Modern Electroplating, Fifth Edition'. John Wiley & Sons. USA. 2010.

37. Paserin, V. Shu, J. Marcusson, S. 'Comercial Production and Applications of Nickel-Based Speciality Foams'. *Porous Metals and Metallic Foams : Proceedings of the Fifth International Conference on Porous Metals and Metallic Foams*. September 5-7. 2007. pp 121-124.
38. Gibson, L, J, Ashby, M, F, 'Cellular Solids: Structures and Properties'. 2nd Edition, *Cambridge University Press*. 1997.
39. Cote, F. Deshpande, V. Fleck, N. 'The Shear Response of Metallic Square Honeycombs'. *Journal of Mechanics of Materials and Structures.* 2006. Vol 1. No 7. pp 1280-1299.
40. Jing, L. Wang, Z. Ning, J. Zhao, L. 'The Dynamic Response of Sandwich Beams With Open-Cell Metal Foam Cores'. *Composites: Part B.* 2011. Vol 42. pp 1-10.
41. Jarvis, T. Voice, W. Goodall, R. 'The Bonding of Nickel Foam to Titanium using Ti-Cu-Ni Braze Alloy'. *Materials Science And Engineering: A.*2011. Vol 528. Issue 6. pp 2592-2601.
42. Rakow, F. Waas, A. 'Size Effects in Metal Foam Cores for Sandwich Structures'. *AIAA Journal.* 2004. Vol 42. No 7. pp 1331-1337.
43. Deglurkar, M. Davy, D. Stewart, M. Goldberg, V. Welter, J. 'Evaluation of Machining Methods for Trabecular Metal Implants in a Rabbit Intramedullary Osseointegration Model'. *Journal of Biomedical Materials Research Part B: Applied Biomaterials*. 2006. Vol 80. Issue 2. pp 528-540.
44. Frank, M. Anderson, D. McKinley, T. Brown, T.' "Rapid Manufacturing in Biomedical Materials: Using Subtractive Rapid

Prototyping for Bone Replacement". *Proceedings of the Solid Freeform Fabrication Symposium*. 2008

45. Bram, M. Kempmannn, C. Laptev, A. Stover, D. Wienert, K. 'Machining of Sintered Titanium Foams by Face Milling and Peripheral Grinding'. *Advanced Engineering Materials*. 2003. Vol 5. No 6. pp 441-447.
46. Chen, S. Head, D. Effgen, M. Jawahir, I. 'An Investigation of Sustained Machining Performance for Controlled Surface Quality Requirements in Porous Tugsten'. *IEEE Transactions of Electron Devices*. 2005. Vol 52. No 5. pp 903-908.
47. Bach, F, W. 'Joining of cellular metal parts using foamable filler metal'. *International Conference on Cellular Metals and Metal Foaming Tecnology, 18th -20th June 2001*. Bremen: Verlag MIT Publication. pp 489-494.
48. Bernard, T. Bergmann, H. Haberling, C. Haldenwanger, H. 'Joining Technologies for Al-Foam-Al-Sheet Compound Structures'. *Advanced Engineering Materials*. 2002. 4. No 10. pp 798-802.
49. Longerich, S. Piontek, D. Ohse, P. Harms, A. Dilthey, U. Angel, S. Bleck, W. 'Joining Stratergies for Open Porous Metallic Foams on Iron and Nickel Base Materials'. *Advanced Engineering Materials*. 2009. 9. No 8. pp 670-678.
50. Ma, C. Shi, K, Yu, Z. Xu, P. 'Correlation between brazed joint elevated strength, microstructure and brazing processing parameter of Inconel superalloy'. *Acta Metallurgica Sinica*. 2011. Vol 24. No 3. pp 205-212.

51. Arafin, M. Medraj, M. Turner, D. Bocher, P. 'Transient liquid phase bonding of Inconel 718 and Inconel 625 with BNi-2: Modeling and experimental investigations'. *Materials Science and Engineering A*. 2007. 447. pp125-133.
52. Pouranvari, M. 'Diffusion brazing of a nickel based superalloy part 1 – solidification behavior'. *Metalurgija - Journal of Metallurgy*. 2010. Vol 16. No 4. pp 241-247.
53. Schwartz, M. 'Brazing'. 2003. ASM International.
54. Steward, A, J. 'Vacuum Brazing Trials with Chromised Nickel Metal Foam to Stainless Steel and Nickel Alloy Plates'. *Rolls Royce Materials Function Report*. 2008. MFR45769.
55. Zhang, Q. He, X. 'Microstructural evolution and mechanical properties of a nickel-based honeycomb sandwich'. *Materials Characterization*. 2009. 60. pp 178-182.
56. Collison, I. Wright, D. 'NDE of metallic foam to substrate bond line – preliminary experimental study'. *Rolls Royce Non-Destructive Testing*. 2007. RNE0905.
57. Mix, P, E. 'Introduction to Nondestructive Testing: A Training Guide'. 2005. John Wiley & sons. pp 498-503.
58. Scheffler, M. Colombo, Paulo. 'Cellular Ceramics: Structure, Manufacturing, Properties and Applications'. 2005. Wiley-VCH, Weinheim. pp 259-265.
59. Schladitz, K. Redenbach, C. Sych, T. Godehardt, M. 'Microstructural characterisation of open foams using 3d images'. *Berichte des Fraunhofer ITWM*, Nr. 148. 2008.

60. Buyens, F. Legoupil, S. Vabre, A. 'Metallic foams characterization using X-ray microtomography'. *International Symposium on Digital Radiology and Computer Tomography*. June 25-27. 2007. France.
61. Jacobs, L, J, M. 'Quantitative morphology analysis of polymers foamed with supercritical carbon dioxide using Voronoi diagrams'. *Computational Materials Science*. 38. 2007. pp 751-758.
62. ASTM E 112-96, Standard test method for determining average grain size. *Annual Book of ASTM Standards*. Vol. 03.01. 1999. pp 237–259.
63. ASM Speciality Handbook: Nickel, Cobalt and Their Alloys. ASM. 2000.
64. 'Testing method for compressive properties of porous metals'. *Japanese Industrial Standard*. Japanese Standards Association. 2006.
65. Aly, M. "Tensile Properties of Open-Cell Nickel Foams". *Materials and Design*. 2010. Volume 31. pp 2237-2240.
66. Robinson, J, W. 'Undergraduate Instrument Analysis'. CRC Press. 2004. pp 476-479.
67. Rouessac, A. 'Chemical Analysis: Modern Instrumentation Methods and Techniques'. John Wiley & Sons Ltd. 2007. pp 309-311.
68. 'Cabinet Tests'. *Manual 20, Corrosion Tests and Standards: Application and Interpretation-Second Edition*. ASTM. 2005

69. Khayargoli, P. Loya, V. Lefebvre, P. Medraj, M. "The Impact of Microstructure on the Permeability of Metal Foams". *Proc. CSME Forum, June 1-4, 2004*. London. Ontario. Canada. pp 220-228
70. Cheng, H. Han, F. 'Compressive deformation behaviour and energy absorption characteristic of aluminium foam with silicate rubber'. *Scripta Materialia*. 49. 2003. pp 583-586.
71. Vesenjak, M. 'Experimental Study of Open-Cell Cellular Structures with Elastic Filler Material'. Experimental Mechanics. 2009. 49. pp 501-509.

12 APPENDIX

12.1 APPENDIX 1 – TENSILE RIG DRAWINGS

This appendix presents engineering drawings for designs created by the author of this thesis to produce a tensile rig assembly, specifically to allow for gripping of samples which did not have parallel brazed Ni plates. Figure 12-1 is for the T-section and Figure 12-2 is for the Clamp. 8 M5 bolts are also required.

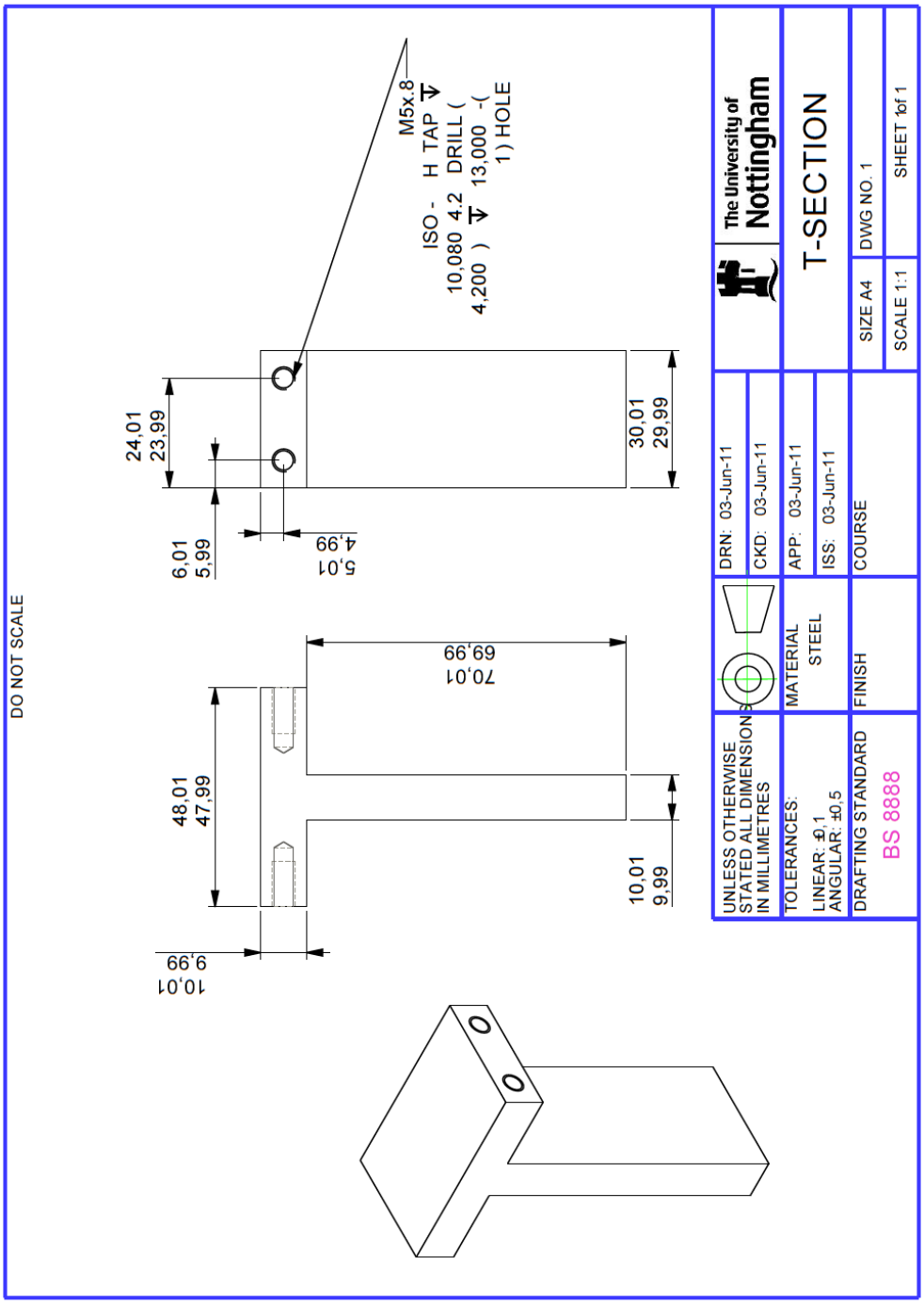


Figure 12-1. Drawings for the T-section for the tensile rig.

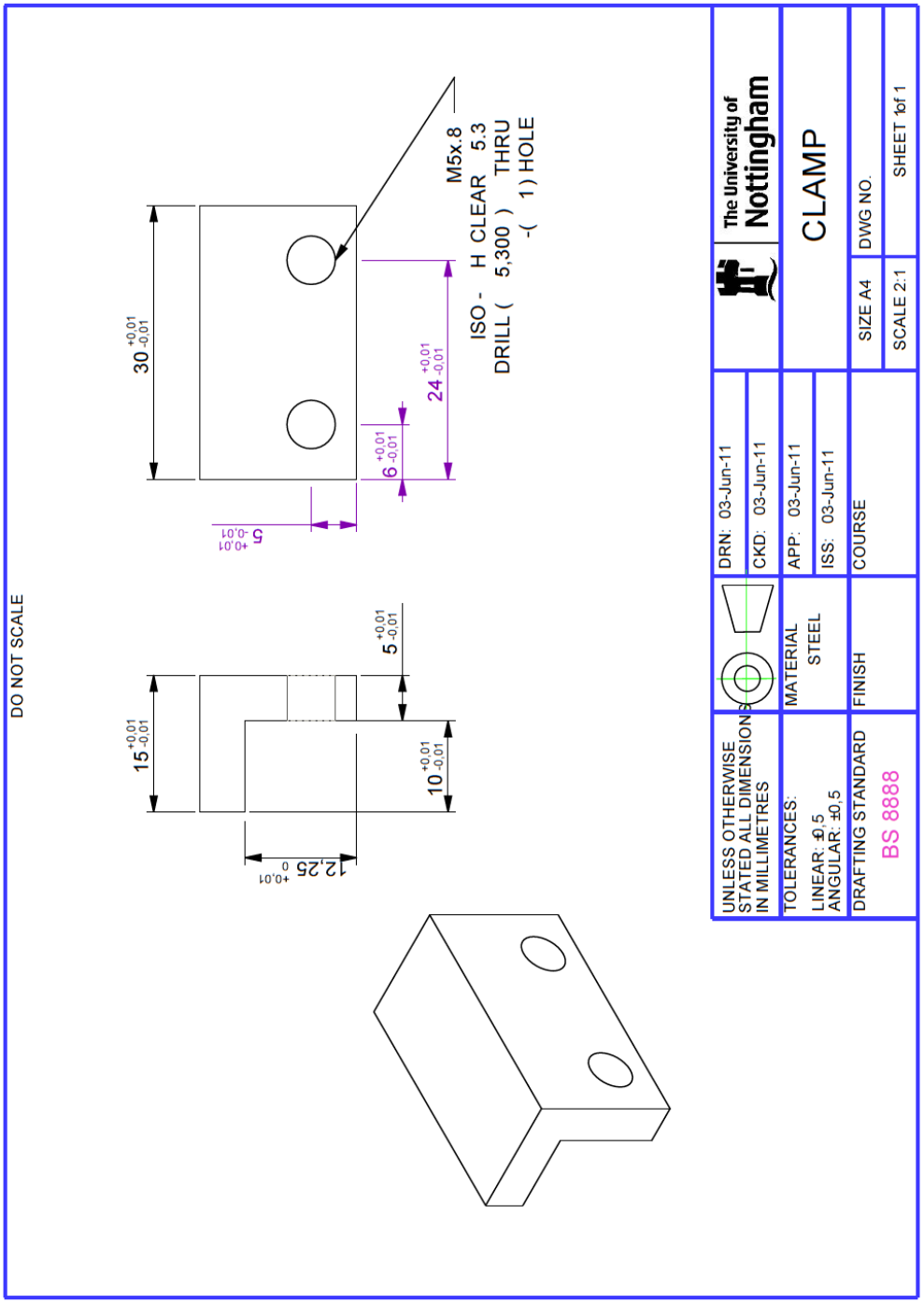


Figure 12-2. Drawing for the clamp of the tensile rig.

12.2 APPENDIX 2 – DENSITY SHEET LAYOUT

This appendix shows the density layout plot for the 1723 samples (Figure 12-3) and the density layout key (Figure 12-4).

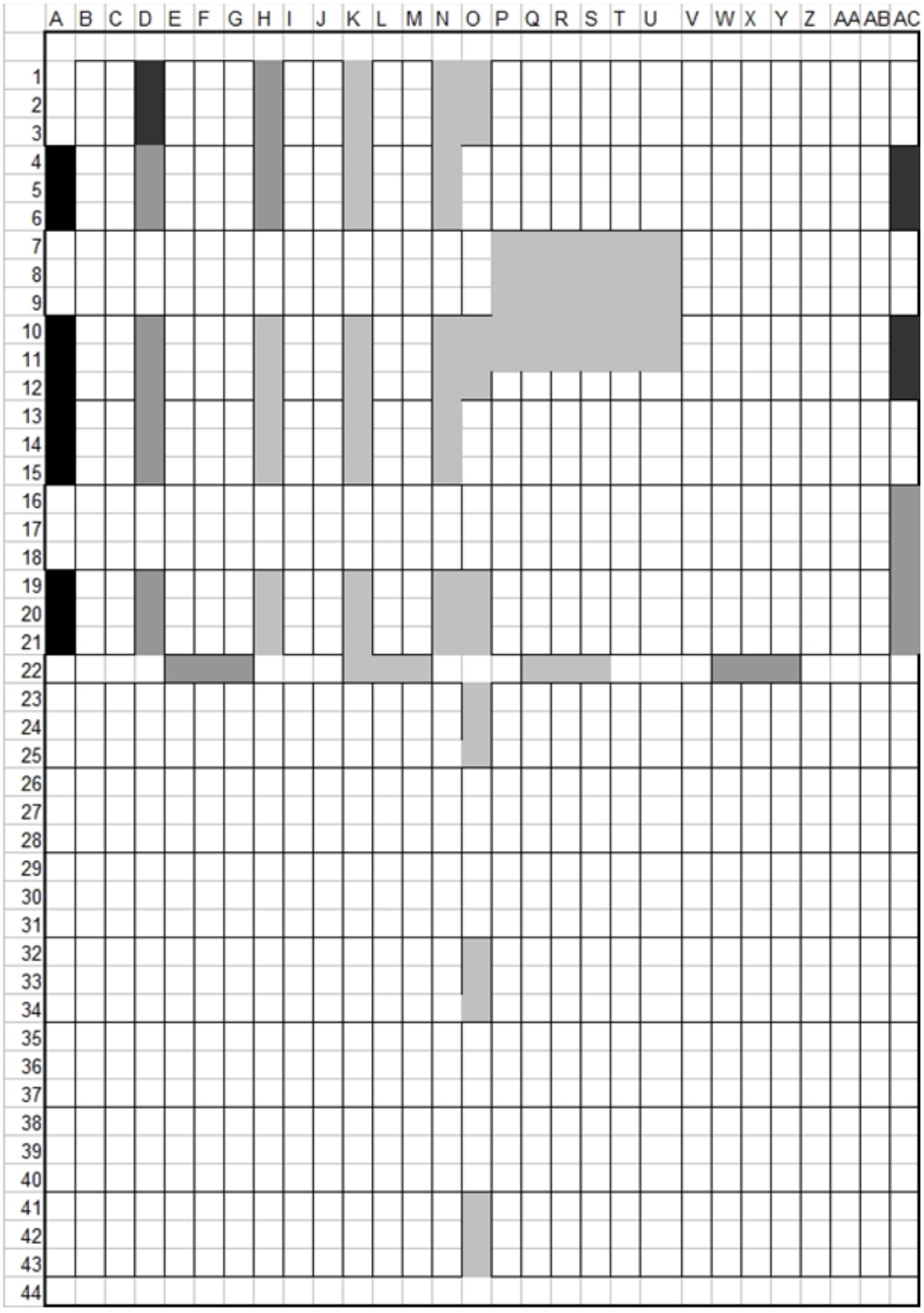


Figure 12-3. Density layout plot for the 1723 samples.

Sample	Density
O20	0.54
O22	0.54
N15	0.55
O44	0.55
O26	0.55
N16	0.55
N13	0.56
N21	0.56
N7	0.56
N22	0.56
N12	0.56
N6	0.56
N14	0.56
O13	0.57
U11	0.58
N5	0.58
U10	0.58
Q8	0.58
K16	0.58
R8	0.58
T8	0.58
R12	0.58
U12	0.58
U8	0.58
Q9	0.58
Q11	0.58
P8	0.58
K21	0.58
T11	0.59
K7	0.59
O35	0.59
P11	0.59
N4	0.59
K15	0.59
P9	0.59
S23	0.59
K13	0.59
S11	0.59
S8	0.59
R11	0.59
M23	0.59
K22	0.59
U9	0.59
P10	0.59
S12	0.59
R10	0.59
Q12	0.59
K12	0.59
T10	0.59
P12	0.59
R9	0.59
T9	0.60

g/cm^3
0.54-0.62
0.63-0.71
0.72-0.80
0.81-0.89

Q10	0.60
H11	0.60
H20	0.60
S10	0.60
T12	0.60
O4	0.60
H16	0.60
N3	0.60
H15	0.60
H21	0.60
S9	0.60
H13	0.61
K6	0.61
H22	0.62
H14	0.62
K3	0.62
K4	0.62
G23	0.63
Y23	0.63
H5	0.65
D16	0.66
H2	0.66
D15	0.67
D11	0.68
D22	0.68
D21	0.68
AC22	0.70
AC19	0.70
AC21	0.70
AC18	0.71
D5	0.71
D2	0.72
AC13	0.75
AC6	0.75
AC7	0.76
AC12	0.76
A7	0.82
A11	0.83
A22	0.83
A13	0.84
A14	0.84
A5	0.85
A21	0.85
A15	0.85
A16	0.85

Figure 12-4. Key to the density layout plot.

12.3 APPENDIX 3 – PYCNOMETRY RESULTS

This appendix shows the Pycnometry table of results, showing density and volume (Table 12-1).

Sample	Volume	Volume Deviation	Density	Density Deviation	Mass	Average Volume	Volume Std Dev	Average Density	Density Std Dev
	cm^3	cm^3	g/cm^3	g/cm^3	g	cm^3	cm^3	g/cm^3	g/cm^3
4	0.1620	0.0003	7.7720	-0.0158	1.2590	0.1617	0.0010	7.7878	0.0481
	0.1611	-0.0005	7.8130	0.0252					
	0.1633	0.0016	7.7114	-0.0763					
	0.1607	-0.0009	7.8335	0.0457					
	0.1612	-0.0004	7.8090	0.0212					
6	0.1653	0.0001	7.7752	-0.0037	1.2854	0.1652	0.0012	7.7788	0.0543
	0.1646	-0.0006	7.8089	0.0300					
	0.1640	-0.0012	7.8377	0.0588					
	0.1652	0.0000	7.7798	0.0010					
	0.1671	0.0018	7.6927	-0.0862					
8	0.1561	0.0008	7.6872	-0.0385	1.1996	0.1553	0.0010	7.7257	0.0487
	0.1541	-0.0012	7.7835	0.0578					
	0.1556	0.0003	7.7105	-0.0152					
	0.1544	-0.0009	7.7708	0.0450					
	0.1563	0.0010	7.6766	-0.0491					
A7	0.2061	-0.0002	7.8040	0.0090	1.6081	0.2063	0.0004	7.7950	0.0157
	0.2070	0.0007	7.7693	-0.0257					
	0.2064	0.0001	7.7907	-0.0043					
	0.2061	-0.0002	7.8039	0.0089					
	0.2060	-0.0003	7.8071	0.0121					
A13	0.2118	-0.0012	7.8676	0.0425	1.6667	0.2130	0.0010	7.8251	0.0351
	0.2135	0.0005	7.8073	-0.0179					
	0.2138	0.0008	7.7949	-0.0303					
	0.2121	-0.0009	7.8586	0.0334					
	0.2138	0.0008	7.7973	-0.0278					
A14	0.2012	-0.0008	7.8586	0.0322	1.5810	0.2020	0.0005	7.8263	0.0185
	0.2021	0.0001	7.8224	-0.0039					
	0.2024	0.0004	7.8124	-0.0139					
	0.2021	0.0001	7.8226	-0.0038					
	0.2023	0.0003	7.8157	-0.0106					
H13	0.1557	-0.0008	7.7618	0.0379	1.2087	0.1565	0.0007	7.7239	0.0359
	0.1571	0.0006	7.6951	-0.0288					
	0.1557	-0.0008	7.7625	0.0385					
	0.1567	0.0003	7.7114	-0.0125					
	0.1572	0.0007	7.6888	-0.0351					
H14	0.1533	-0.0012	7.6896	0.0577	1.1788	0.1545	0.0007	7.6319	0.0333
	0.1545	0.0000	7.6298	-0.0021					
	0.1549	0.0004	7.6098	-0.0221					
	0.1549	0.0004	7.6103	-0.0216					
	0.1547	0.0002	7.6199	-0.0120					
H20	0.1564	-0.0009	7.7106	0.0437	1.2060	0.1573	0.0008	7.6669	0.0390
	0.1572	-0.0001	7.6706	0.0036					
	0.1579	0.0006	7.6392	-0.0277					
	0.1567	-0.0006	7.6971	0.0302					
	0.1583	0.0010	7.6172	-0.0498					
N5	0.1442	-0.0007	7.7783	0.0354	1.1213	0.1448	0.0007	7.7429	0.0373
	0.1441	-0.0007	7.7811	0.0382					
	0.1454	0.0006	7.7134	-0.0295					
	0.1448	0.0000	7.7434	0.0005					
	0.1457	0.0008	7.6984	-0.0445					
N14	0.1324	-0.0013	7.8097	0.0747	1.0342	0.1337	0.0008	7.7349	0.0470
	0.1334	-0.0003	7.7505	0.0156					
	0.1345	0.0008	7.6913	-0.0436					
	0.1341	0.0004	7.7096	-0.0253					
	0.1341	0.0004	7.7136	-0.0214					
O20	0.1430	0.0006	7.8344	-0.0331	1.1200	0.1424	0.0003	7.8675	0.0188
	0.1423	0.0000	7.8701	0.0026					
	0.1421	-0.0002	7.8791	0.0116					
	0.1422	-0.0002	7.8769	0.0094					
	0.1422	-0.0002	7.8770	0.0095					

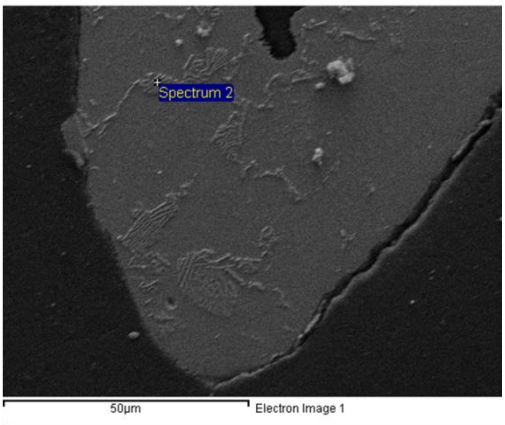
Table 12-1. Complete results of the density and volumes determined by the Pycnometer.

12.4 APPENDIX 4 – EDX ANANLYSIS

This appendix gives some further examples of the EDX analysis performed.

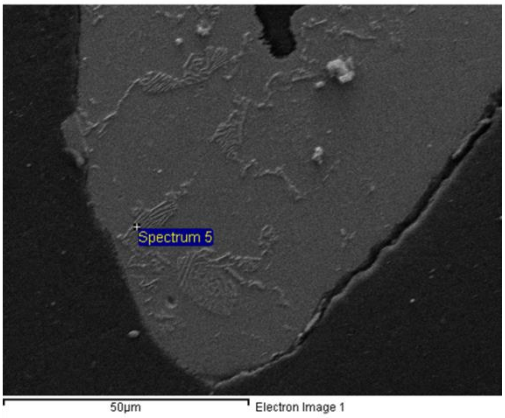
12.4.1 Non-Brazed Foam Second Phase

When analysing the secondary phase, three spot analysis scans were performed in for each section analysed. The following Figures (Figure 12-5, Figure 12-6 and Figure 12-7) shows the results of one area analysed and the three scans performed. The samples were polished, etched and Pt coated prior to analysis



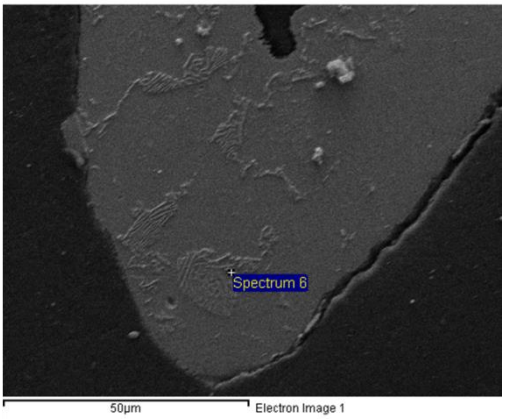
Element	*Weight %*	*Atomic %*
Cr K	*43.32*	*70.50*
Ni K	*4.87*	*7.02*
Pt M	*51.81*	*22.47*
Totals	*100.00*	

Figure 12-5. EDX spot spectrum analysis of a 1116 sample. The image shows the site from where the spectrum was located, and the table shows the results.



Element	*Weight*	*Atomic*
	%	*%*
Cr K	*39.72*	*68.68*
Ni K	*3.31*	*5.06*
Pt M	*56.97*	*26.26*
Totals	*100.00*	

Figure 12-6. EDX spot spectrum analysis of a 1116 sample. The image shows the site from where the spectrum was located, and the table shows the results.

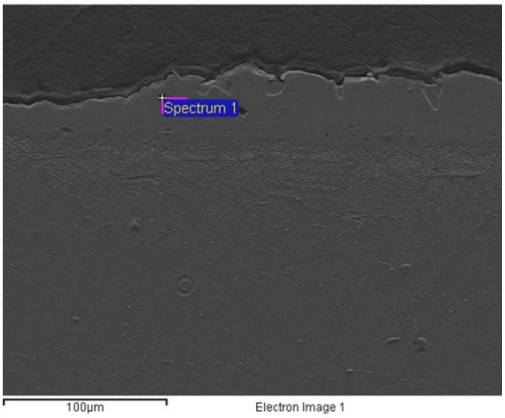


Element	*Weight*	*Atomic*
	%	*%*
Si K	*2.08*	*4.68*
Cr K	*63.51*	*77.27*
Ni K	*9.15*	*9.86*
Pt M	*25.27*	*8.19*
Totals	*100.00*	

Figure 12-7. EDX spot spectrum analysis of a 1116 sample. The image shows the site from where the spectrum was located, and the table shows the results.

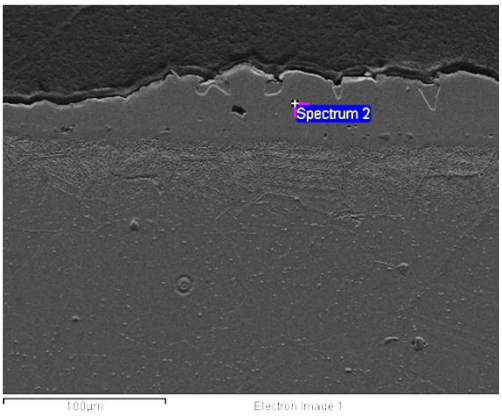
12.4.2 Braze Layer

Similar to the un-brazed chemical analysis, at least three spot analysis scans were performed for each section analysed. Figure 12-8, Figure 12-9 and Figure 12-10 show the results of one phase of the braze layer analysed and the three scans performed. Figure 12-11, Figure 12-12 and Figure 12-13, show examples of analysis that was performed on the other phase within the layer. The samples were polished, etched and Au coated prior to analysis.



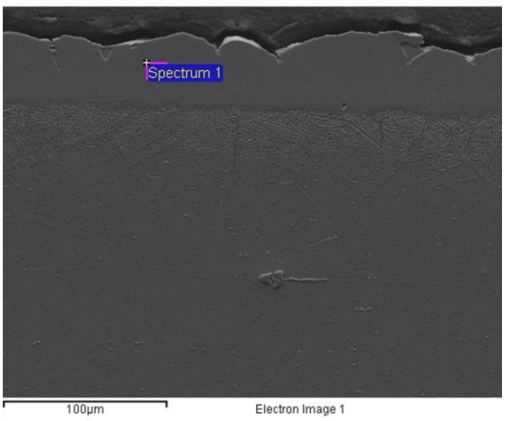
Element	*Weight%*	*Atomic%*
Si K	*3.26*	*8.08*
Cr K	*1.13*	*1.51*
Ni K	*67.45*	*80.04*
Mo L	*1.11*	*0.81*
Au M	*27.05*	*9.57*
Totals	*100.00*	

Figure 12-8. EDX spot spectrum analysis of a brazed sample. The image shows the site from where the spectrum was located, and the table shows the results.



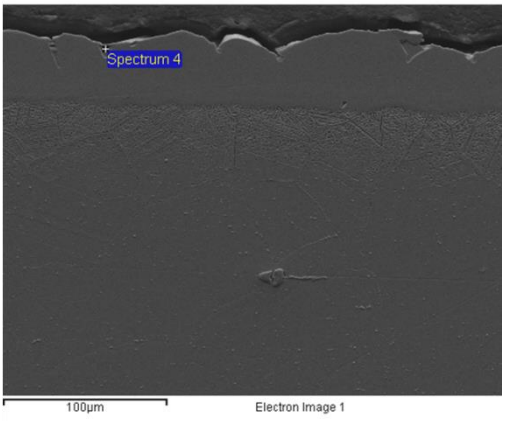
Element	*Weight%*	*Atomic%*
Si K	*3.29*	*8.05*
Cr K	*1.28*	*1.69*
Co K	*0.55*	*0.65*
Ni K	*68.76*	*80.50*
Mo L	*-0.01*	*-0.01*
Au M	*26.12*	*9.12*
Totals	*100.00*	

Figure 12-9. EDX spot spectrum analysis of a brazed sample. The image shows the site from where the spectrum was located, and the table shows the results.



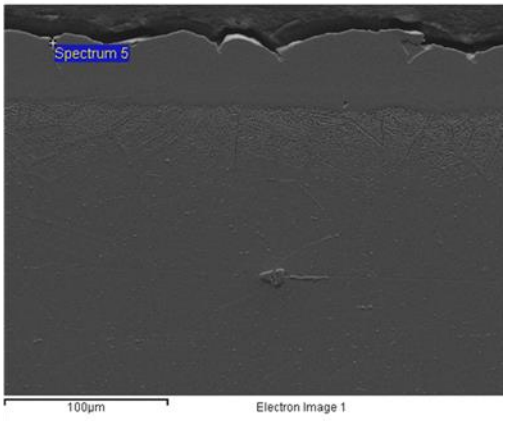
Element	*Weight%*	*Atomic%*
Si K	*3.29*	*8.15*
Cr K	*1.08*	*1.45*
Co K	*0.95*	*1.13*
Ni K	*66.84*	*79.28*
Mo L	*0.42*	*0.30*
Au M	*27.43*	*9.70*
Totals	*100.00*	

Figure 12-10. EDX spot spectrum analysis of a brazed sample. The image shows the site from where the spectrum was located, and the table shows the results.



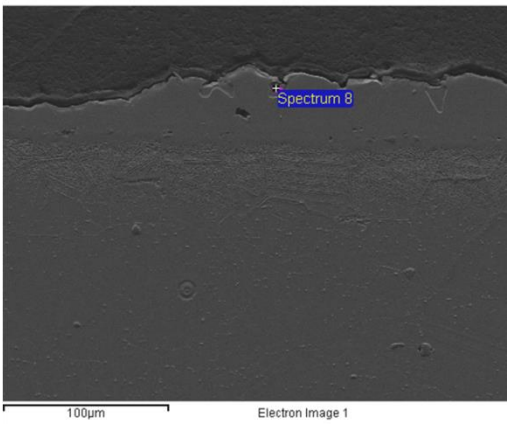
Element	*Weight%*	*Atomic%*
Si K	*0.23*	*0.60*
Cr K	*0.61*	*0.87*
Co K	*0.87*	*1.09*
Ni K	*67.35*	*85.27*
Mo L	*1.21*	*0.94*
Au M	*29.73*	*11.22*
Totals	*100.00*	

Figure 12-11. EDX spot spectrum analysis of a brazed sample. The image shows the site from where the spectrum was located, and the table shows the results.



Element	*Weight%*	*Atomic%*
Si K	*0.62*	*1.62*
Cr K	*0.55*	*0.78*
Co K	*0.91*	*1.13*
Ni K	*67.62*	*84.97*
Mo L	*0.36*	*0.28*
Au M	*29.94*	*11.21*
Totals	*100.00*	

Figure 12-12. EDX spot spectrum analysis of a brazed sample. The image shows the site from where the spectrum was located, and the table shows the results.



Element	*Weight%*	*Atomic%*
Cr K	*0.47*	*0.68*
Ni K	*69.44*	*87.53*
Mo L	*1.24*	*0.96*
Au M	*28.85*	*10.84*
Totals	*100.00*	

Figure 12-13. EDX spot spectrum analysis of a brazed sample. The image shows the site from where the spectrum was located, and the table shows the results.

12.5 APPENDIX 5 – 1723 COMPRESSIVE STRESS LAYOUT PLOTS

This appendix shows the compressive stress layout plots for the 1723 samples. Figure 12-14 is the layout plot for the 0.2% proof stress (Figure 12-15 is the key). Figure 12-16 is the layout plot for the 25% strain (Figure 12-17 is the key). Figure 12-18 is the layout plot for the 60% (Figure 12-19 is the key).

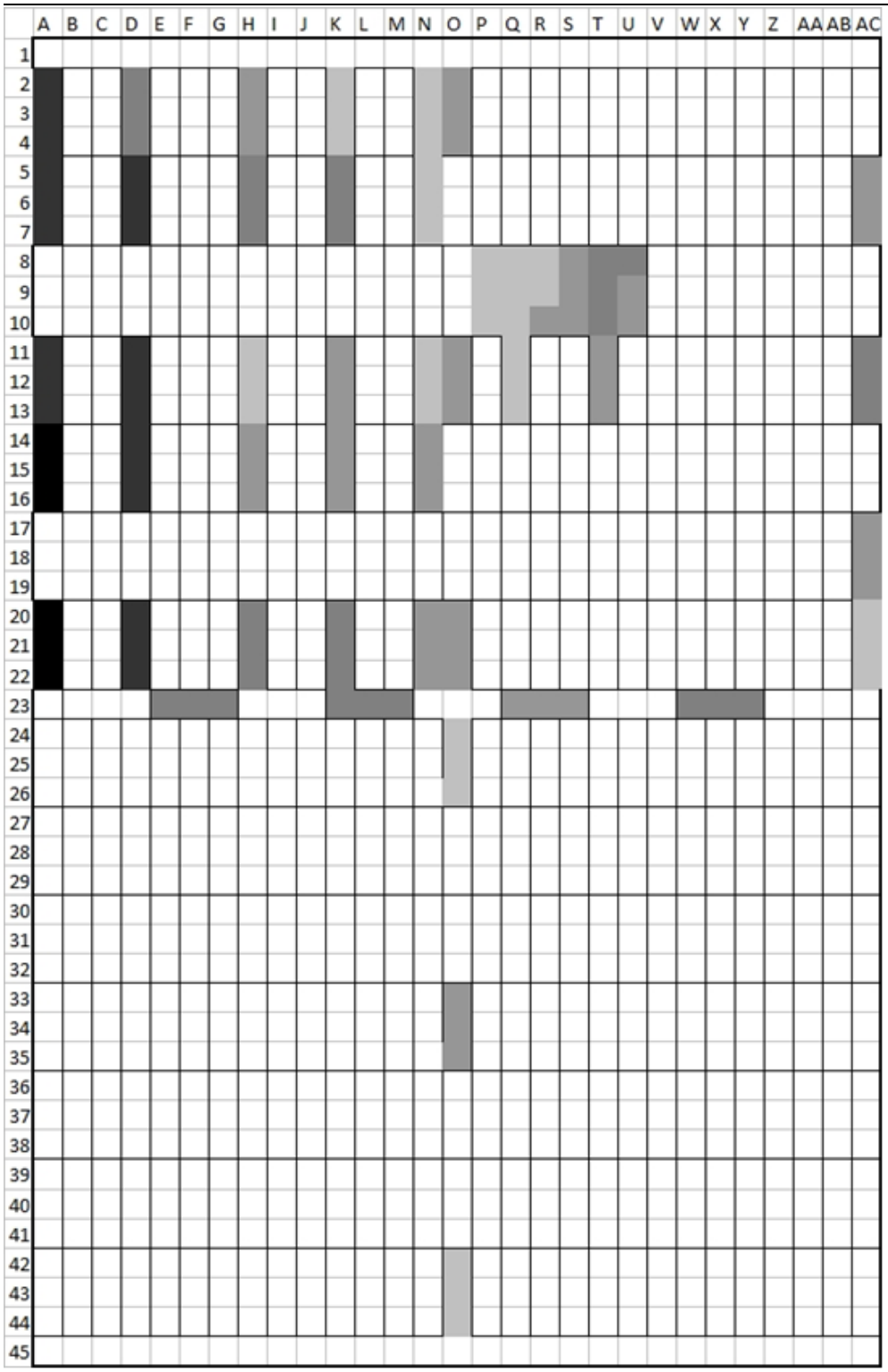


Figure 12-14. Layout plot for the 1723 samples at 0.2% Proof Stress.

SAMPLE	STRESS (Mpa)
AC21	2.96
O44	3.01
N12	3.02
N6	3.02
H11	3.04
O26	3.04
K3	3.07
N3	3.08
K12	3.12
AC6	3.17
O22	3.18
O4	3.19
N15	3.22
N21	3.24
S23	3.30
O13	3.33
H2	3.33
AC18	3.36
O35	3.39
K15	3.40
H15	3.46
Y23	3.50
AC12	3.54
K6	3.55
M23	3.56
H21	3.56
K21	3.61
D2	3.62
G23	3.76
H5	3.80
A2	3.87
D15	3.90
D11	3.95
D21	4.00
D5	4.00
A11	4.04
A5	4.04
A15	4.30
A21	4.31

MPa
2.70-3.08
3.09-3.47
3.48-3.86
3.87-4.25
4.26-4.64

Sample	STRESS (Mpa)
P8	2.78
R8	2.86
P10	2.94
Q10	2.98
Q12	3.03
S10	3.13
R10	3.19
S8	3.27
U9	3.33
T12	3.45
T10	3.53
U8	3.53

Figure 12-15. Key to the layout plot for the 1723 samples at 0.2% Proof Stress.

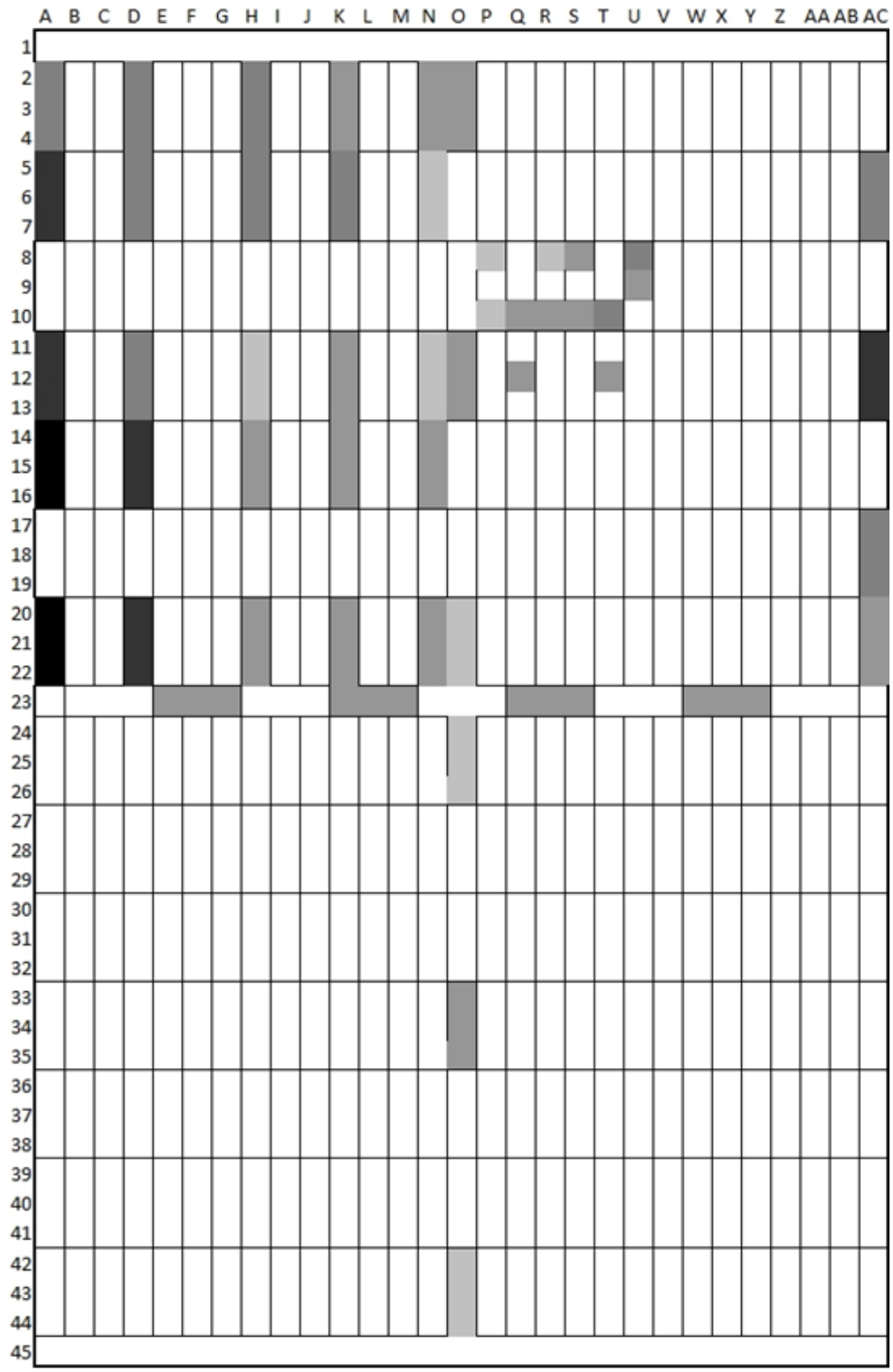


Figure 12-16. Layout plot for the 1723 samples at 25% strain.

SAMPLE	STRESS (Mpa)
O44	5.22
O22	5.33
O26	5.49
N6	5.52
H11	5.62
N12	5.65
N21	5.72
N15	5.76
N3	5.84
O4	5.88
K12	5.96
S23	5.99
O35	6.01
K3	6.15
AC21	6.17
O13	6.21
M23	6.28
K15	6.33
Y23	6.34
G23	6.36
H15	6.36
K21	6.37
H21	6.38
H2	6.48
K6	6.64
AC6	6.71
D2	6.88
AC18	6.92
H5	6.98
D11	7.04
A2	7.08
D5	7.13
D15	7.29
D21	7.50
AC12	7.57
A11	7.59
A5	7.81
A15	8.10
A21	8.16

MPa
4.94-5.70
5.71-6.47
6.48-7.24
7.25-8.01
8.02-8.78

Sample	STRESS (MPa)
P8	5.44
P10	5.67
R8	5.69
Q10	5.82
Q12	6.03
S10	6.09
R10	6.14
S8	6.22
T12	6.40
U9	6.40
T10	6.53
U8	6.55

Figure 12-17. Key to the layout plot for the 1723 samples at 25% strain.

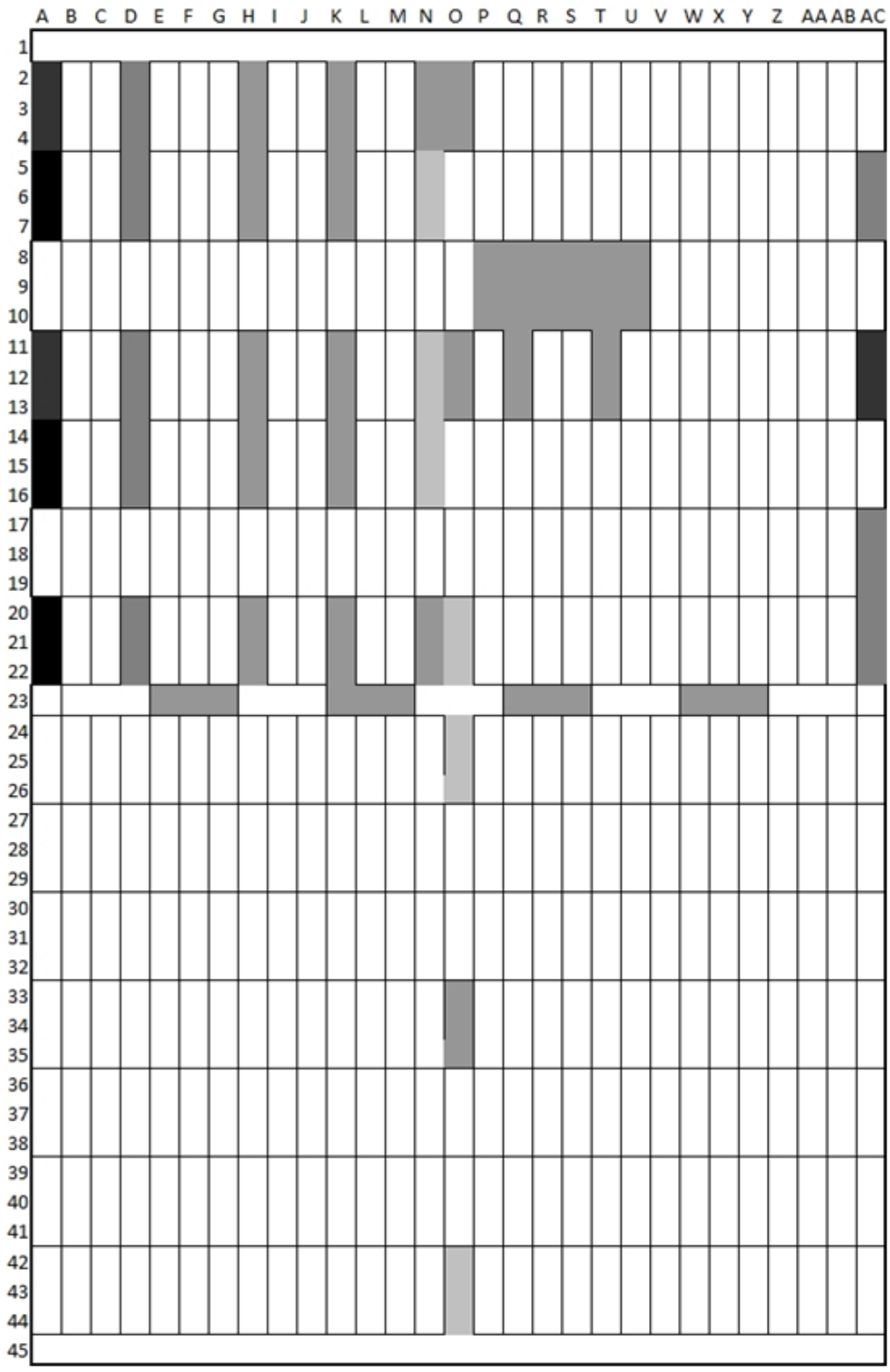


Figure 12-18. Layout plot for the 1723 samples at 60% strain.

SAMPLE	STRESS (Mpa)
O26	13.25
O22	13.31
N12	13.32
N15	13.45
N6	13.55
O44	13.56
H11	13.74
N21	14.07
K12	14.69
O13	14.72
N3	14.87
O4	14.96
K3	15.26
K15	15.29
H15	15.30
S23	15.55
M23	15.69
K6	15.77
K21	15.78
O35	15.92
H21	16.10
H2	16.74
G23	16.76
H5	17.01
Y23	17.02
D11	18.45
D15	18.72
AC21	19.23
D5	19.39
D21	19.69
D2	20.19
AC18	20.19
AC6	20.81
A2	21.52
AC12	22.86
A11	24.31
A5	24.84
A21	26.04
A15	26.71

MPa
9.91-13.60
13.61-17.3
17.4-21.09
21.10-24.79
24.80-28.49

Sample	STRESS (MPa)
P10	14.23
R8	14.31
P8	14.40
Q12	14.71
S8	14.88
Q10	15.08
R10	15.14
U9	15.16
T10	15.23
S10	15.32
U8	15.36
T12	15.53

Figure 12-19. Key to the layout plot for the 1723 samples at 60% strain.

12.6 APPENDIX 6 – 1116 COMPRESSIVE STRESS LAYOUT PLOTS

This appendix shows the compressive stress layout plots for the 1116 samples. Figure shows the layout plots for the short traverse axis. Figure 12-20 (a) is the layout plot for the 0.2% proof stress. Figure 12-20 (b) is the layout plot for the 25% strain. Figure 12-20 (c) is the layout plot for the 60%.

Figure shows the layout plots for the LL axis. Figure 12-21 (a) is the layout plot for the 0.2% proof stress. Figure 12-21 (b) is the layout plot for the 25% strain. Figure 12-21 (c) is the layout plot for the 60%.

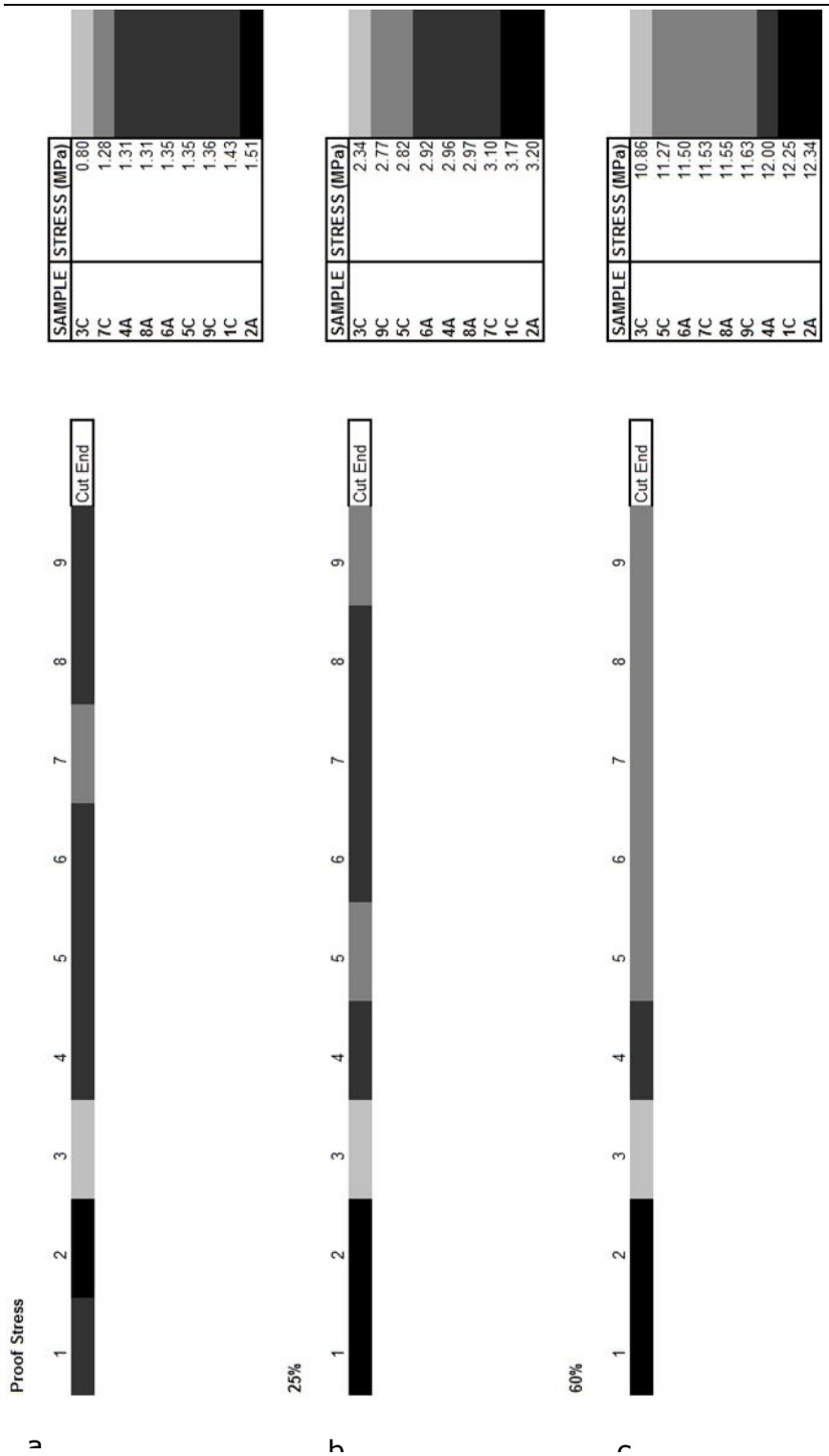


Figure 12-20. Layout plots for the 1116 foam samples in the ST axis, at the proof stress (a), at 25% strain (b) and at 60% strain (c).

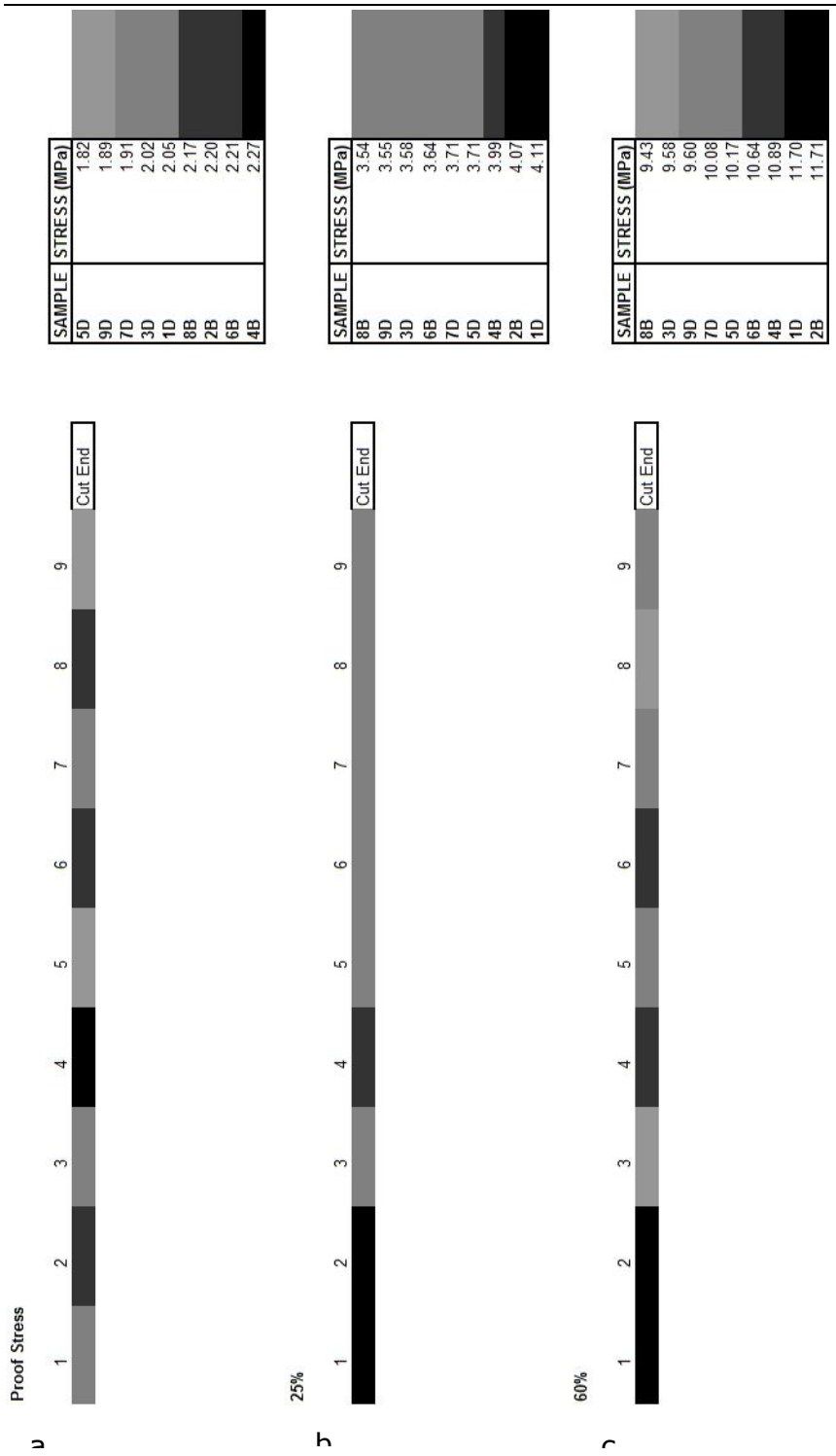


Figure 12-21. Layout plots for the 1116 foam samples in the LL axis, at the proof stress (a), at 25% strain (b) and at 60% strain (c).

12.7 APPENDIX 7 – 1116 ST COMPRESSIVE STRESS-STRAIN

This appendix shows the compressive stress-strain plot for the 1116 samples in the ST axis (Figure 12-22).

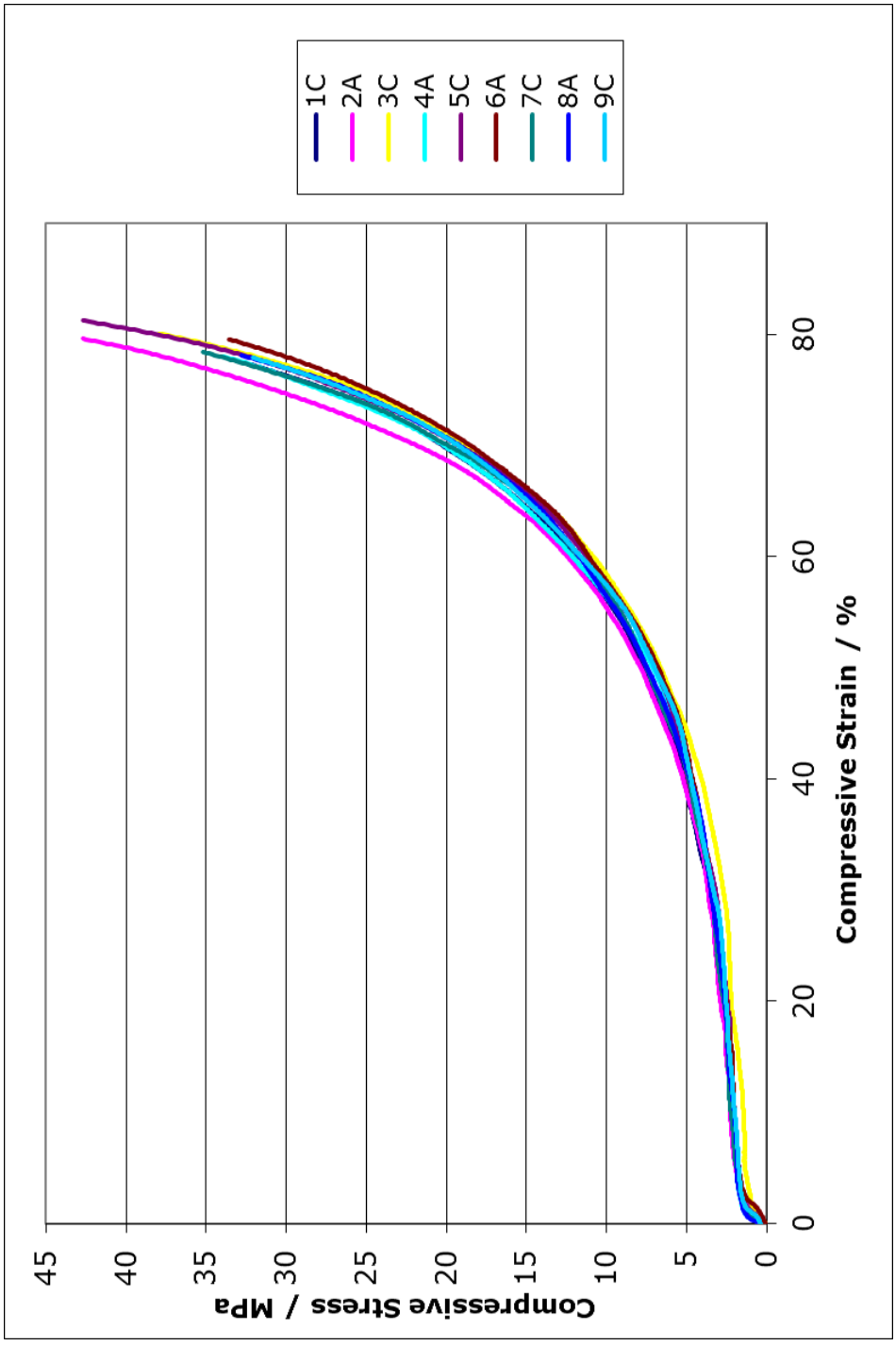


Figure 12-22. 1116 foam, ST compression stress-strain plot.

12.8 APPENDIX 8 - 1116 LL COMPRESSIVE STRESS-STRAIN

This appendix shows the compressive stress-strain plot for the 1116 samples in the LL axis (Figure 12-23).

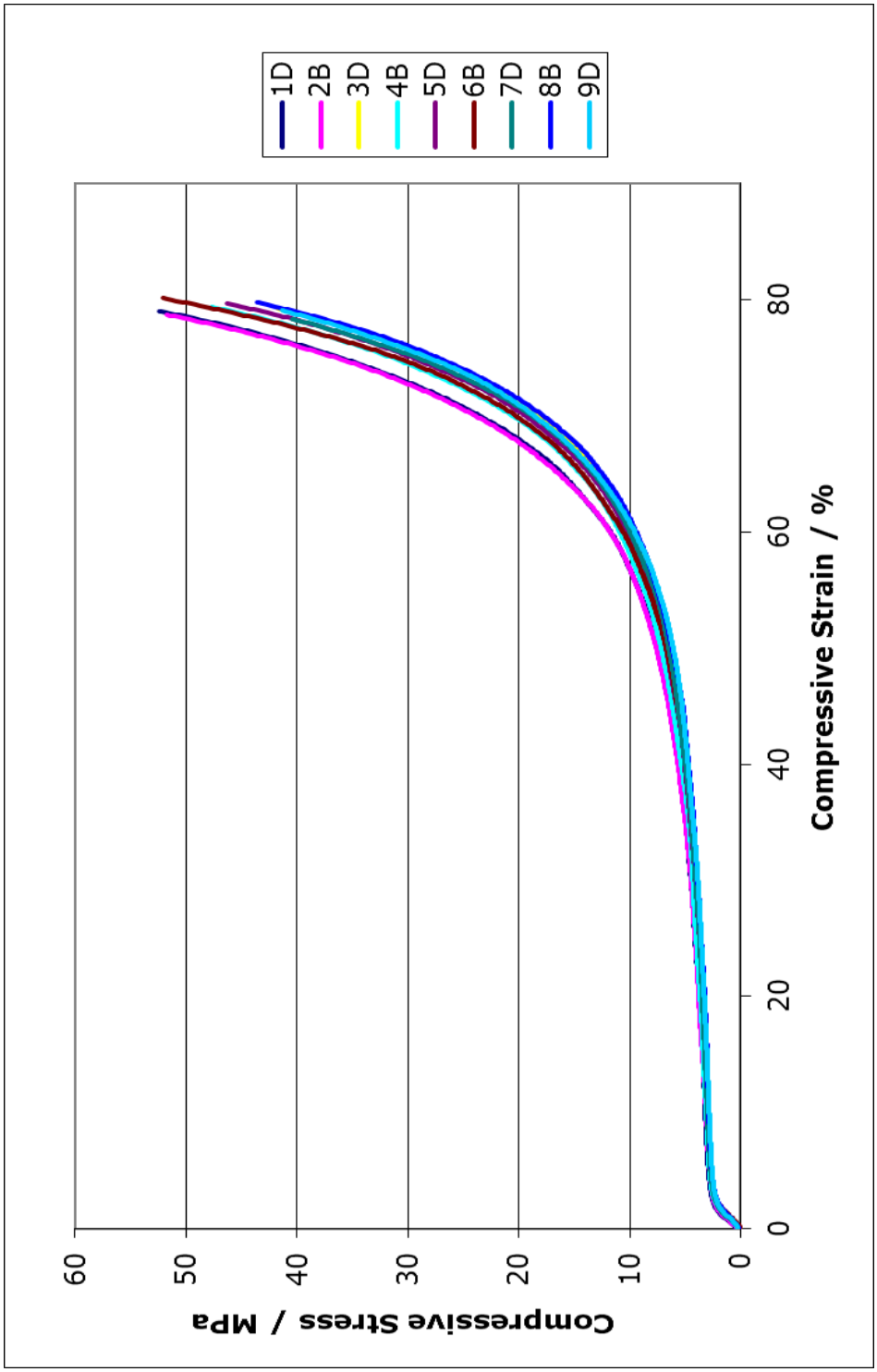


Figure 12-23. 1116 foam, LL compression stress-strain plot.

12.9 APPENDIX 9 – NDE ANALYSIS

This appendix shows the images that were supplied by Rolls Royce, after the samples had undergone NDE analysis, as well as the subsequent image manipulation using ImageJ to determine the braze area. Unless otherwise stated, the samples were tested at 7dB and 10MHz, with a pitch (resolution) of 1mm

12.9.1 Sample 1

Sample 1 consisted of two Ni plates brazed to the 1116 Ni-Cr foam. As there were two brazed faces, two scans were performed. The Side A and Side B C-scan images can be seen in Figure 12-24 and Figure 12-25 respectively, and also show the binary image and area % calculated for each. Most notable in the images was a large area of poor bonding on Side B visible as well as the small area of no braze in Side A (Which was anlaysed with the microCT). Figure 12-26 shows how the material was sectioned, with the top face being Side A. Sample 1A2 was analysed with the microCT, 1A4, 1A5 and 1A6 were used for compression analysis and 1A7, 1A8 and 1A9 were used for corrosion analysis.

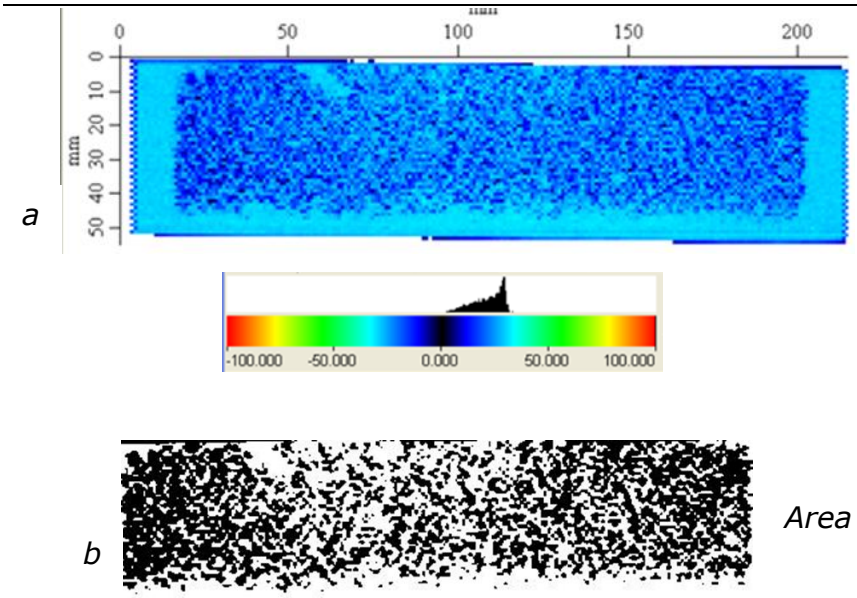


Figure 12-24. Sample 1 Side A ultrasound C-scan image (a), and binary image created using ImageJ to calculate the area% (b).

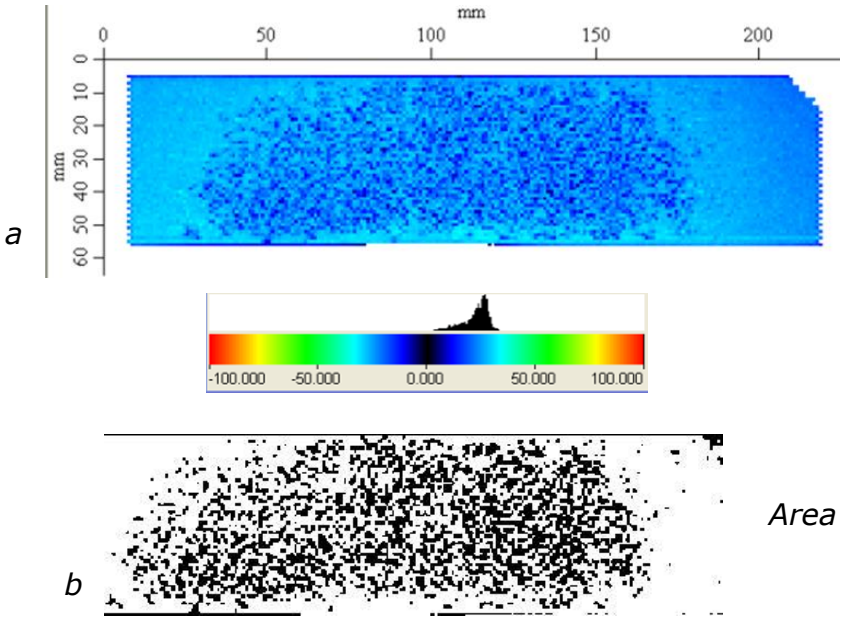


Figure 12-25. Sample 1 Side B ultrasound C-scan image (a), and binary image created using ImageJ to calculate the area% (b).

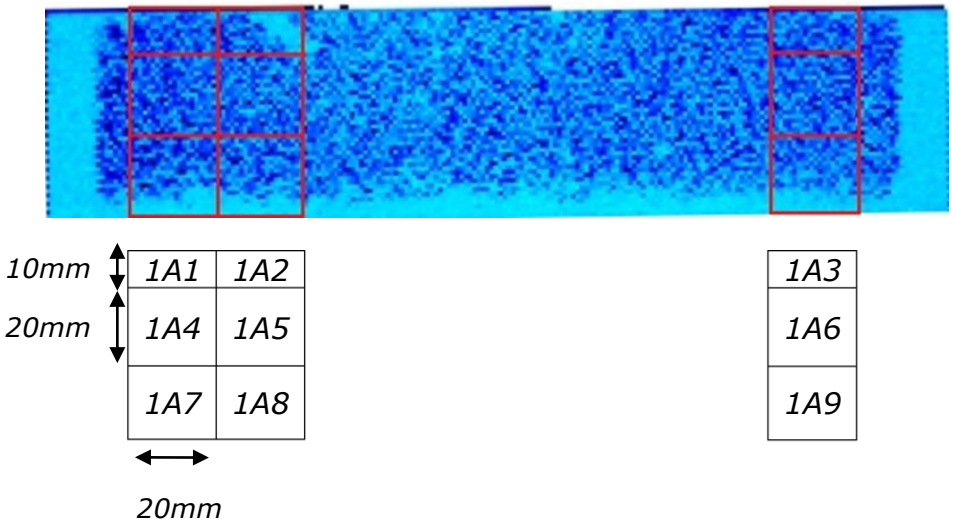


Figure 12-26. Image showing how the material was sectioned and the subsequent sample codes.

12.9.2 Sample 2

Sample 2 was made with only one brazed Ni plate. Figure 12-27 shows the C-scan image for the sample as well as the ImageJ binary image and calculated area. The sample was found to have a good evenly distributed bond, and sections from it (Figure 12-28) were used for microscopy of good braze areas.

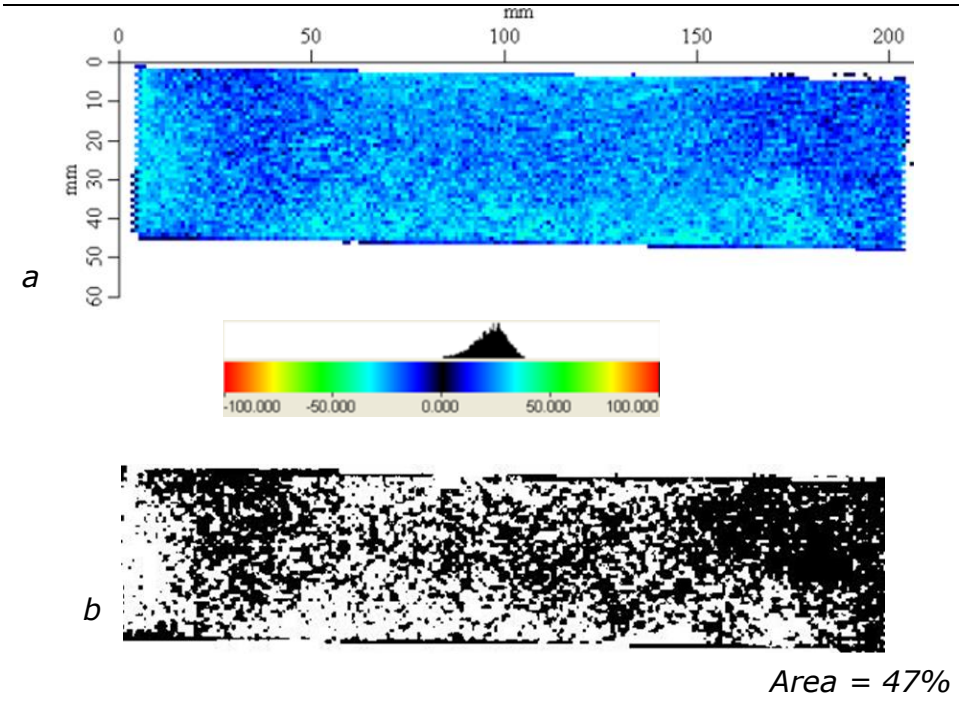


Figure 12-27. Sample 2 ultrasound C-scan image (a), and binary image created using ImageJ to calculate the area% (b).

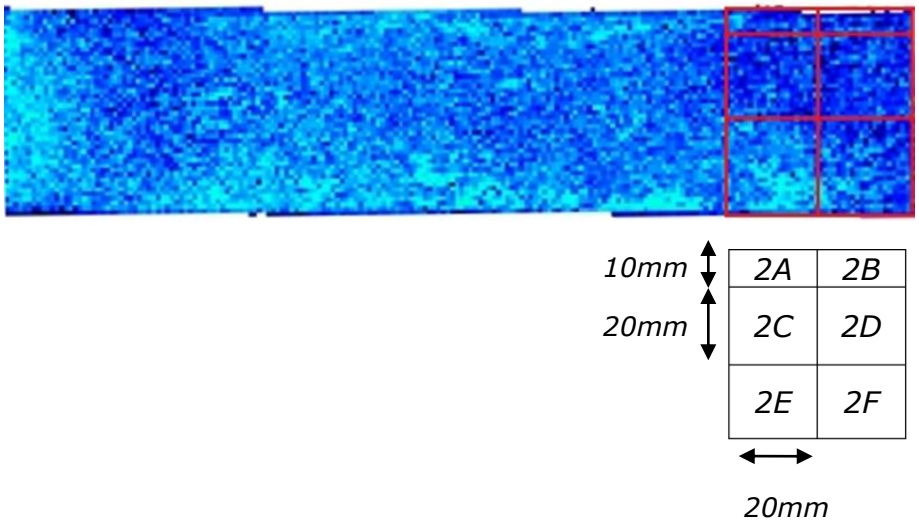


Figure 12-28. Image showing how the material was sectioned and the subsequent sample codes.

12.9.3 Sample 3

Sample 3 consisted of two Ni plates brazed to the 1116 Ni-Cr foam, and was originally a section of Sample 4. Three samples were used to test the rig, and the clear wall, that was eventually used for shear testing. Sample 3 had not been analysed by the NDE method prior to the initial trials, therefore the sectioned material was sent back to Rolls Royce. The three samples were scanned with a pitch (resolution) of 0.5mm instead of the usual 1mm. Figure 12-29 shows the C-scan and binary images for the three samples as well as the calculated areas.

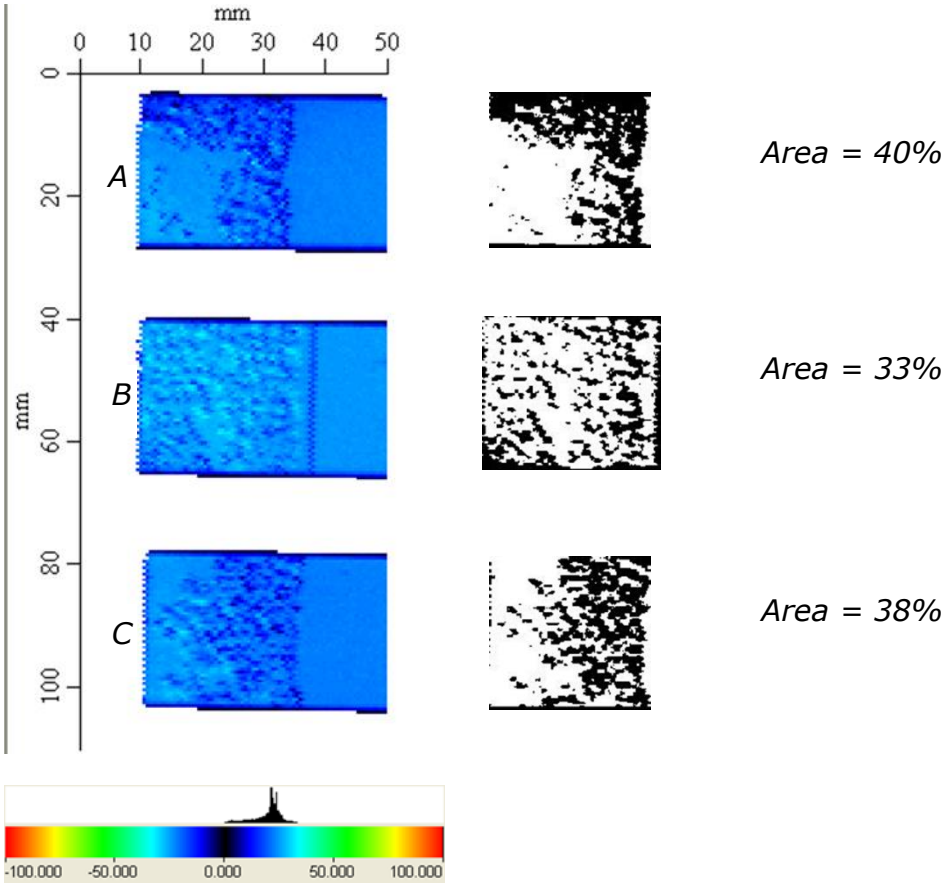


Figure 12-29. Ultrasound C-scan images, and binary images (created using ImageJ to calculate the area%), for Samples A, B and C.

12.9.4 Sample 4

Sample 4 consisted of two Ni plates brazed to the 1116 Ni-Cr foam. As there were two brazed faces, two scans were performed. The Side A and Side B C-scan images can be seen in Figure 12-30 and Figure 12-31 respectively, and also show the binary image and area % calculated for each. Side A was scanned at 17dB in order to image the sample. There was a large area of Side B that had not bonded which meant samples could not be used from there. Figure 12-32 shows where the sectioned samples were located (using Side A as the top face). These samples were used for the shear tests.

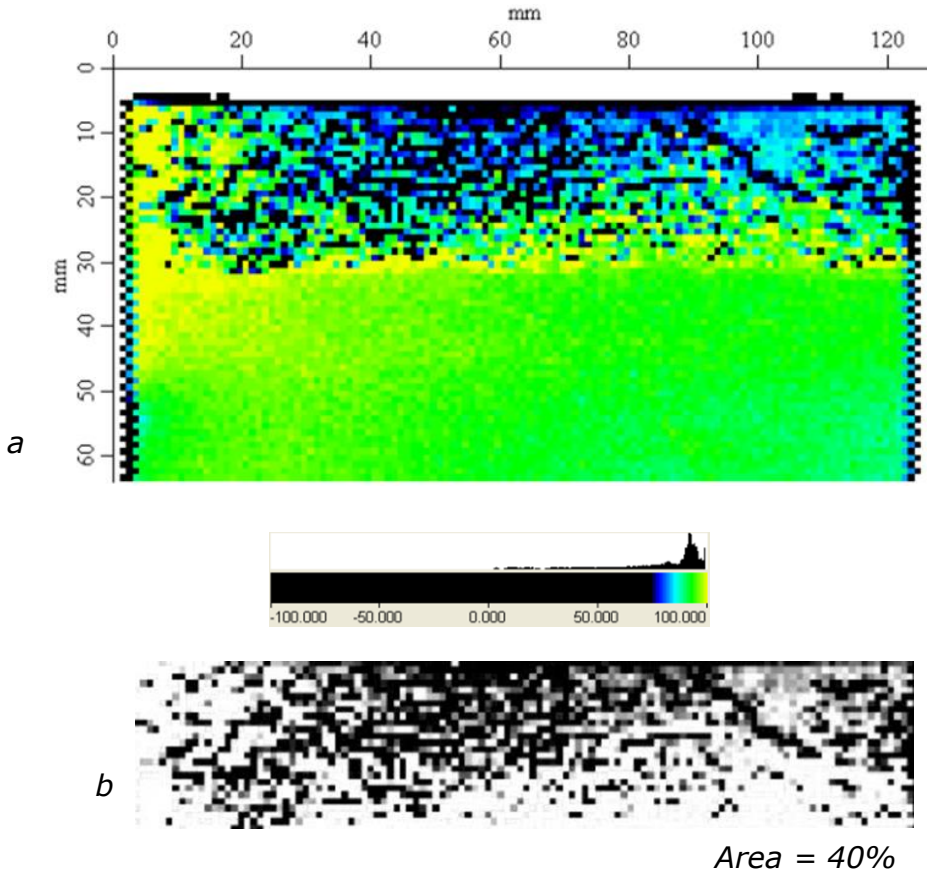


Figure 12-30. Sample 4 Side A ultrasound C-scan image (a), and binary image created using ImageJ to calculate the area% (b).

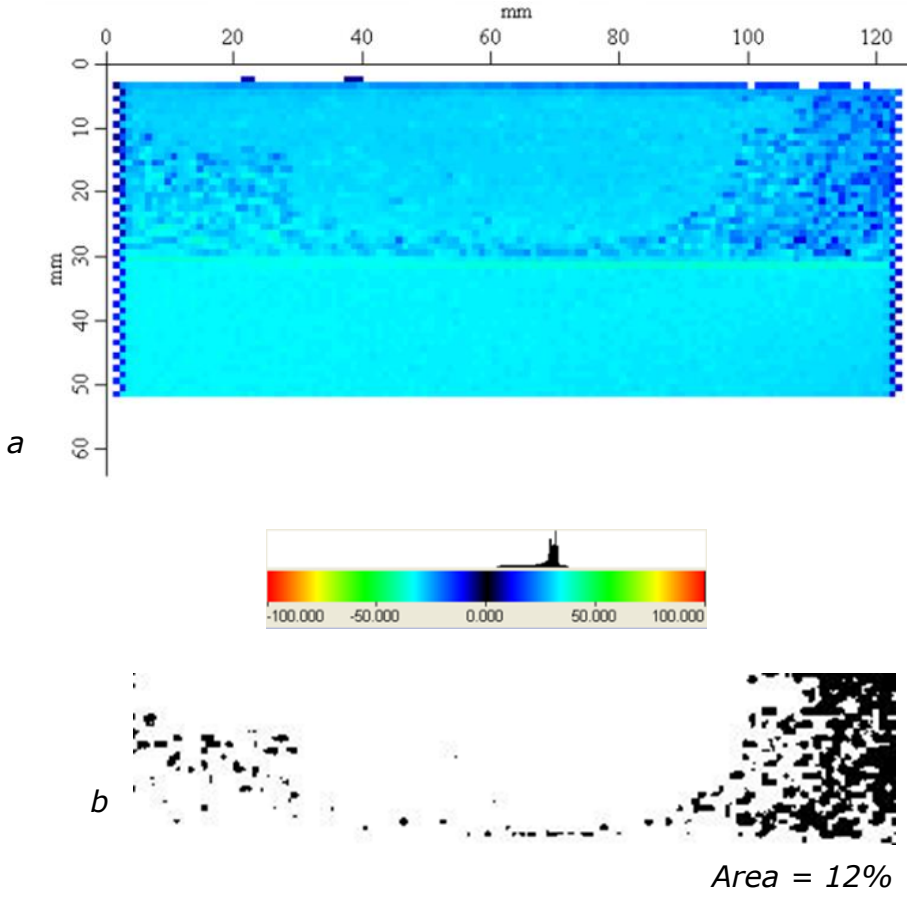


Figure 12-31. Sample 4 Side B ultrasound C-scan image (a), and binary image created using ImageJ to calculate the area% (b).

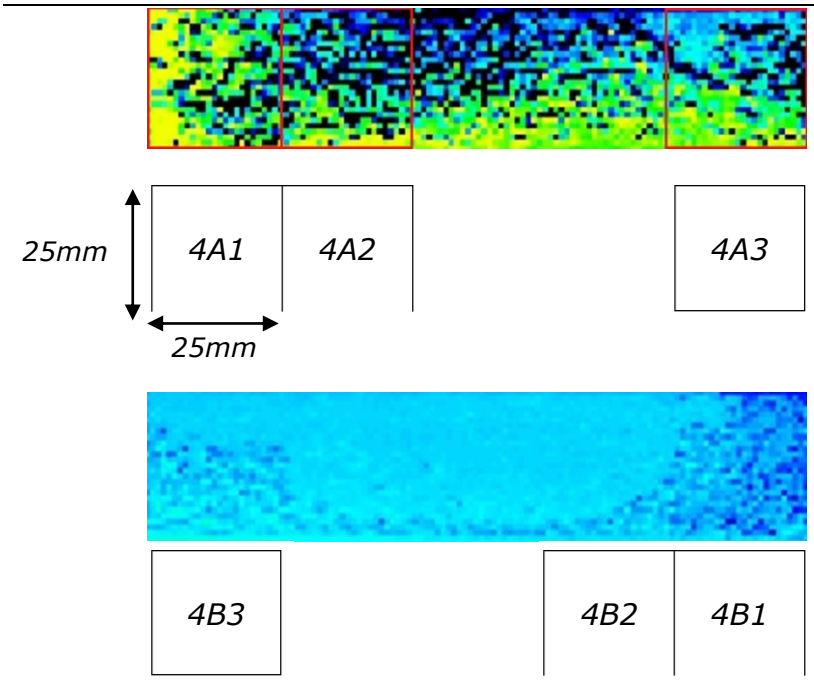


Figure 12-32. Image showing how the material was sectioned and the subsequent sample codes.

12.9.5 Sample A

Sample A consisted of two Ni plates brazed to the 1116 Ni-Cr foam, and the samples were used for tensile testing. As there were two brazed faces, two scans were performed. The Side A and Side B C-scan images can be seen in Figure 12-33 and Figure 12-34 respectively, and also show the binary image and area % calculated for each. Figure 12-35 shows were the sectioned samples were located within the material, with the Side A codes used as the code designation prior to testing.

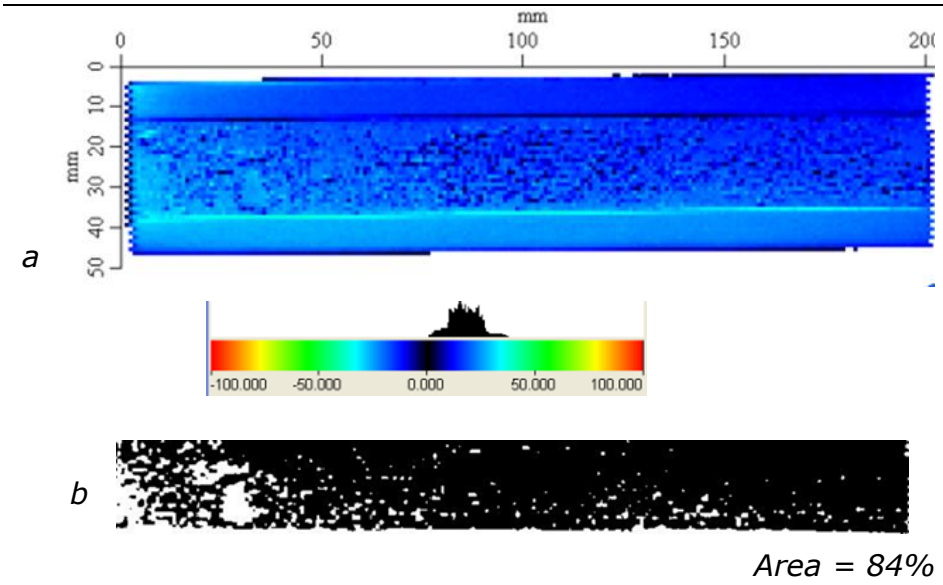


Figure 12-33. Sample A Side A ultrasound C-scan image (a), and binary image created using ImageJ to calculate the area% (b).

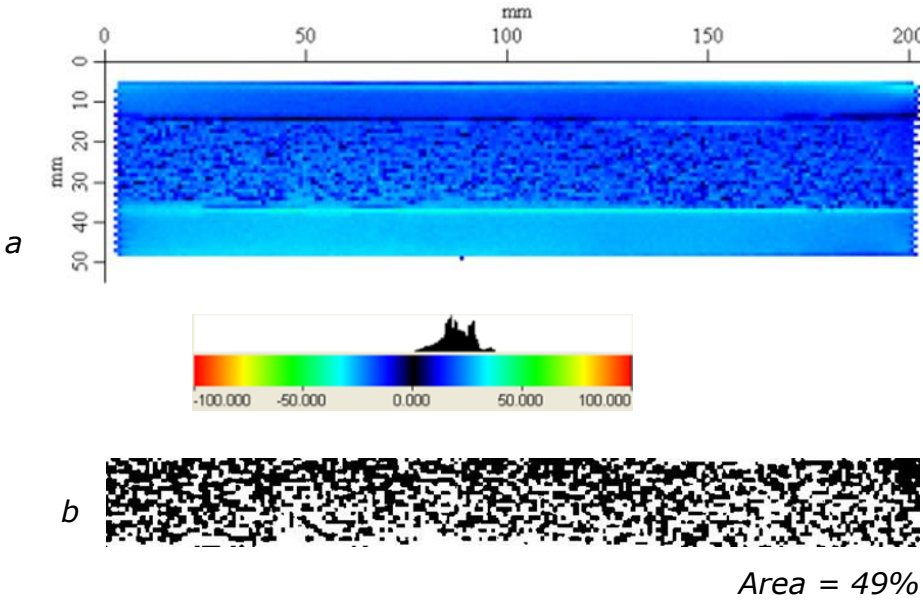


Figure 12-34. Sample A Side B ultrasound C-scan image (a), and binary image created using ImageJ to calculate the area% (b).

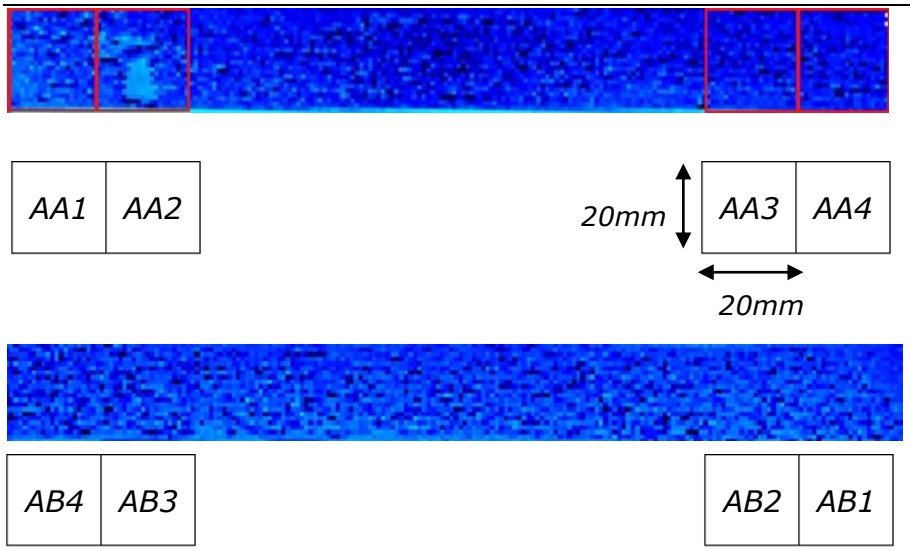


Figure 12-35. Image showing how the material was sectioned and the subsequent sample codes.

12.9.6 Sample B

Sample B consisted of two Ni plates brazed to the 1116 Ni-Cr foam, and the samples were used for tensile testing. As there were two brazed faces, two scans were performed. The Side A and Side B C-scan images can be seen in Figure 12-36 and Figure 12-37 respectively, and also show the binary image and area % calculated for each. Figure 12-38 shows were the sectioned samples were located within the material, with the Side A codes used as the code designation prior to testing.

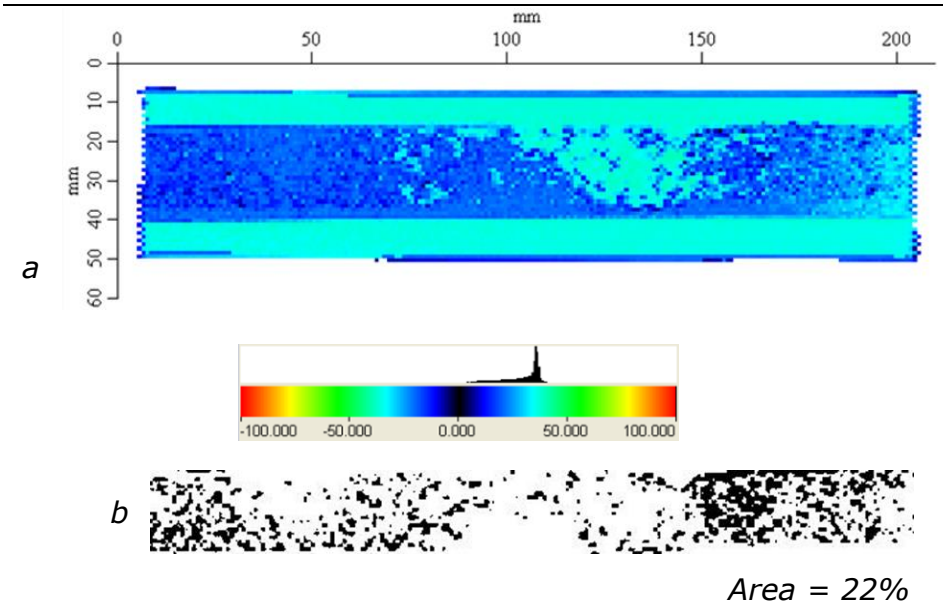


Figure 12-36. Sample B Side A ultrasound C-scan image (a), and binary image created using ImageJ to calculate the area% (b).

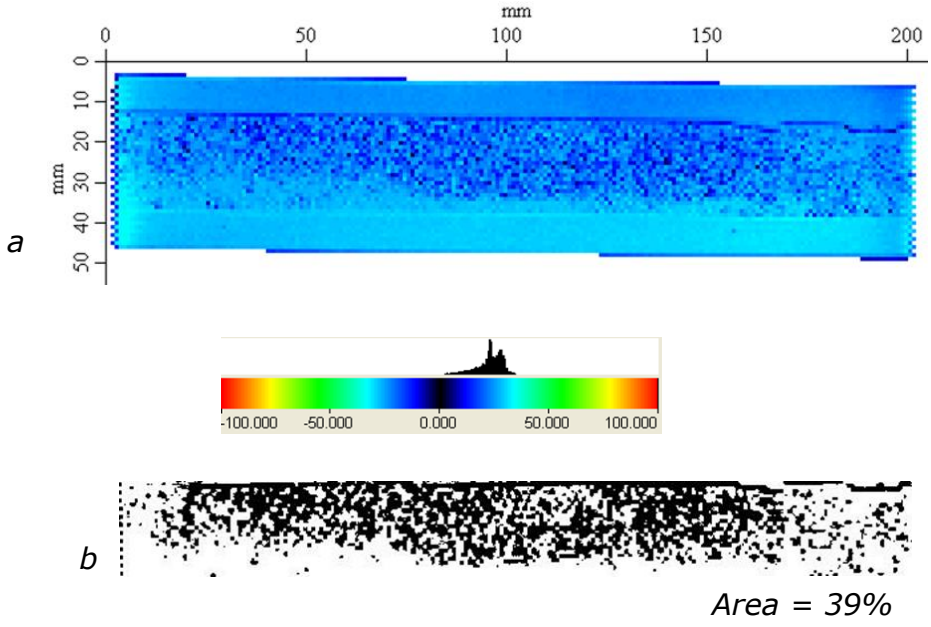


Figure 12-37. Sample B Side B ultrasound C-scan image (a), and binary image created using ImageJ to calculate the area% (b).

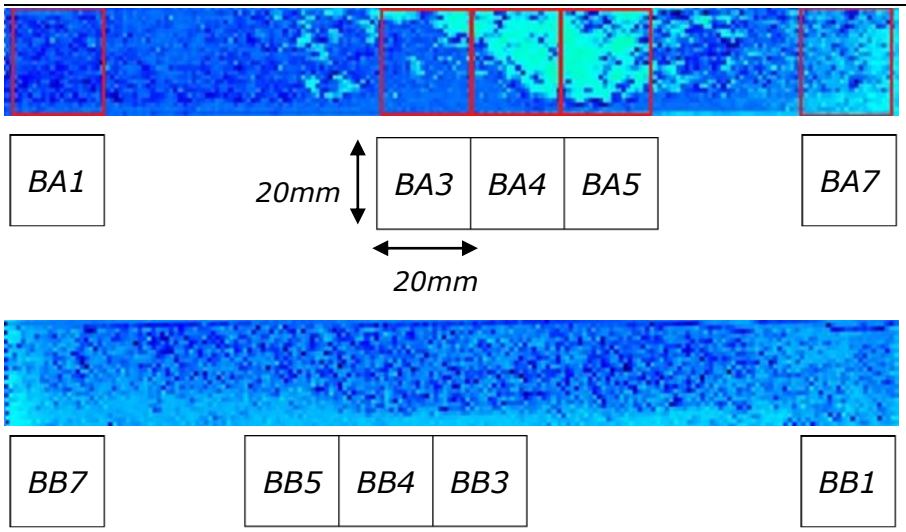


Figure 12-38. Image showing how the material was sectioned and the subsequent sample codes.

12.10 APPENDIX 10 – BRAZED FOAM STRESS-STRAIN PLOT

This appendix shows the complete tensile stress-strain plots for the brazed foam (figure).

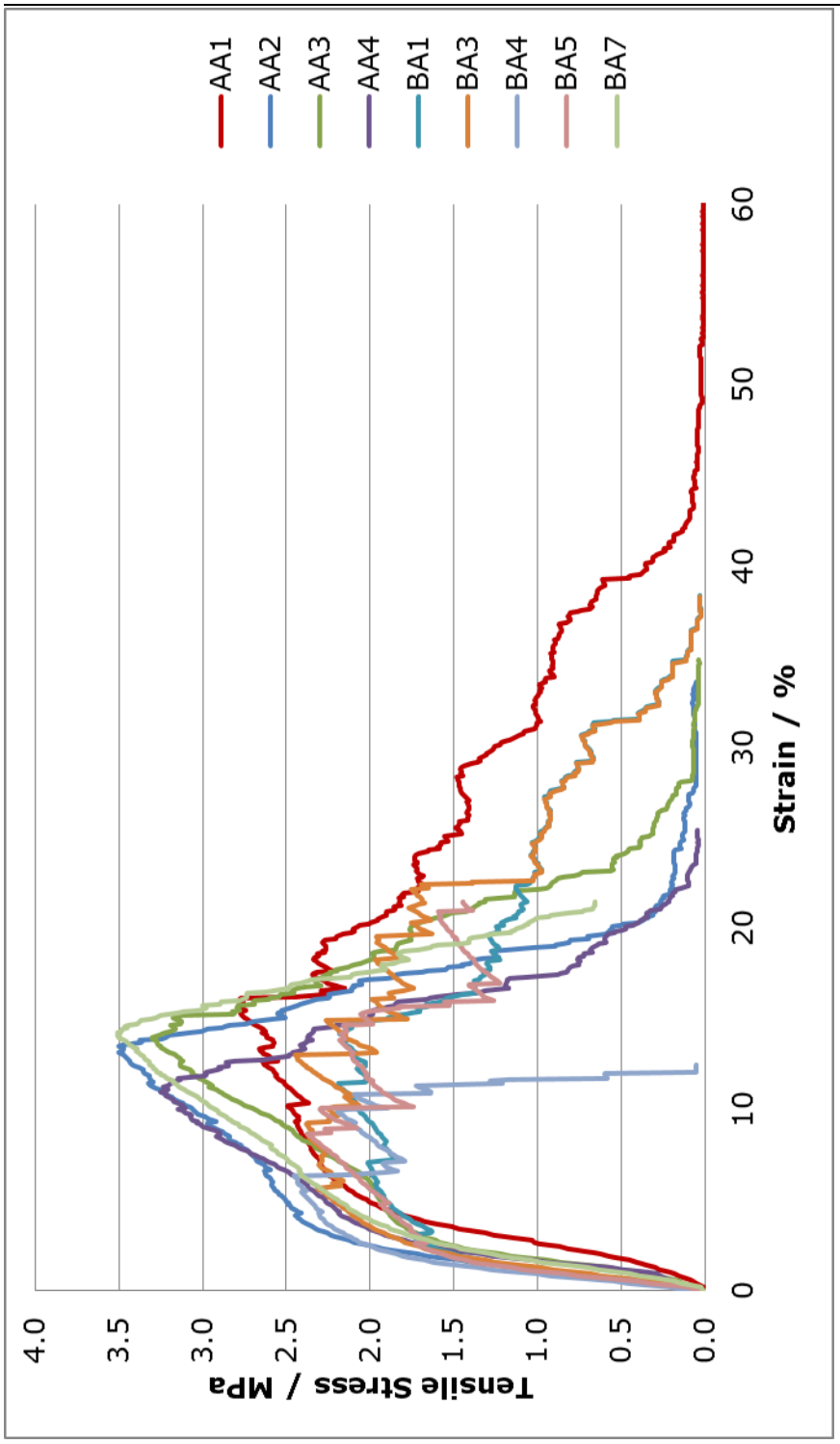


Figure 12-39. Tensile stress-strain plots for the brazed foam samples.

12.11 APPENDIX 11 - BRAZED FOAM STRESS-INCURSION PLOT

This appendix shows the complete shear stress-incursion plot for all the brazed shear samples (Figure 12-40).

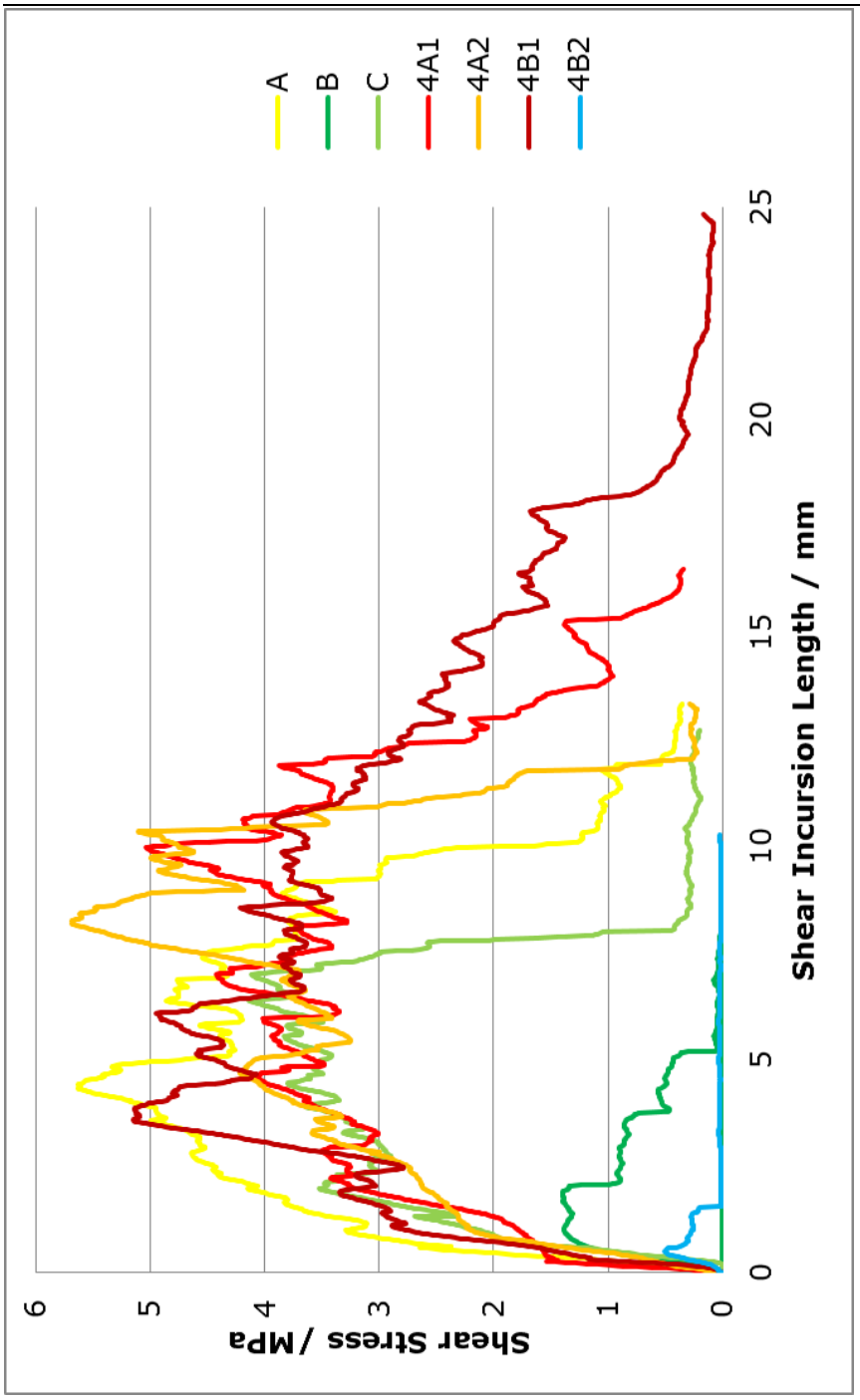


Figure 12-40. Shear stress-incursion plots for the brazed foam material, with the area calculated using the reducing area method.

12.12APPENDIX 12 – CORROSION ANALYSIS IMAGES

This appendix shows images taken of samples that underwent corrosion analysis. Figure 12-41shows images of the 1723 samples after 900 hours in the salt spray cabinet. Figure 12-42 shows the images of the 1116 samples after 900 hours in the salt spray cabinet.

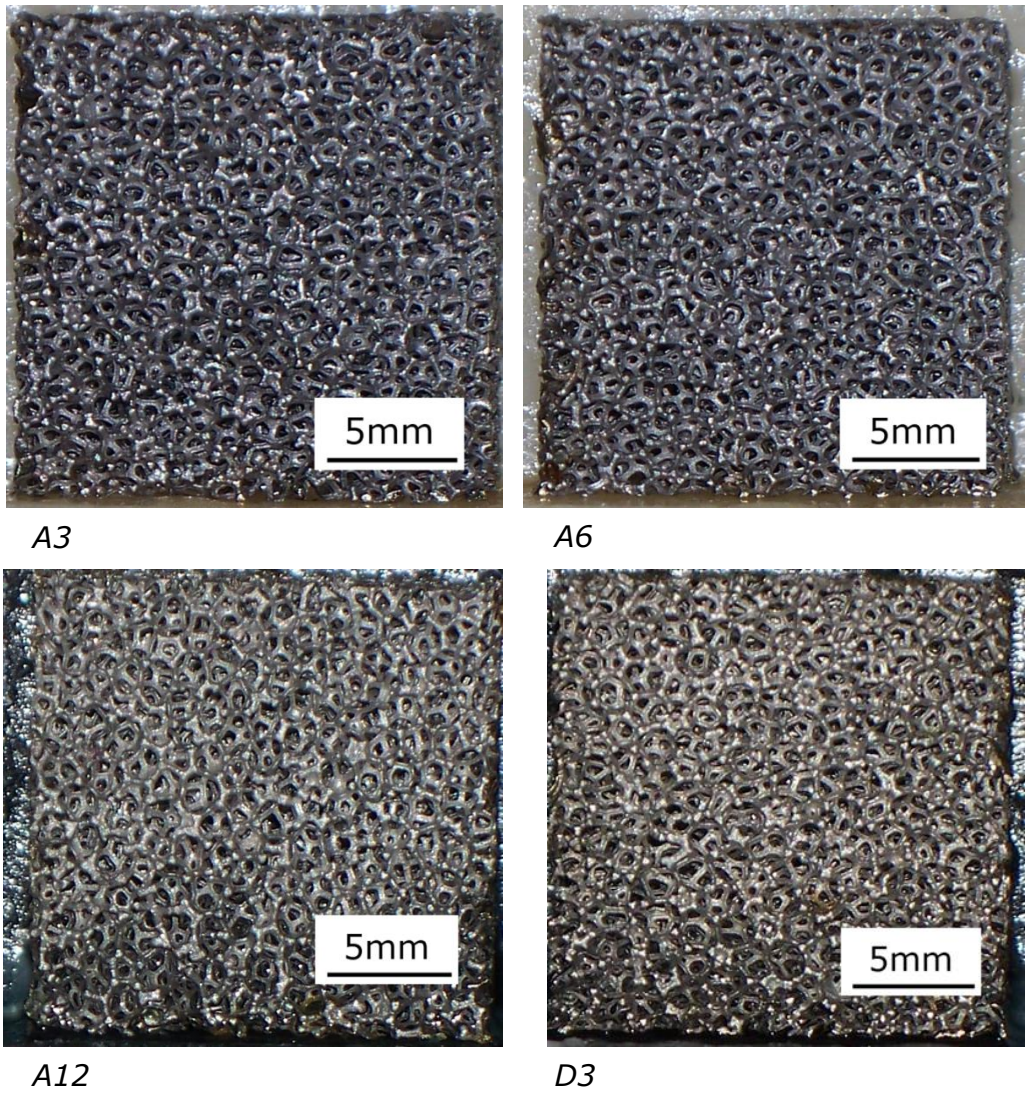
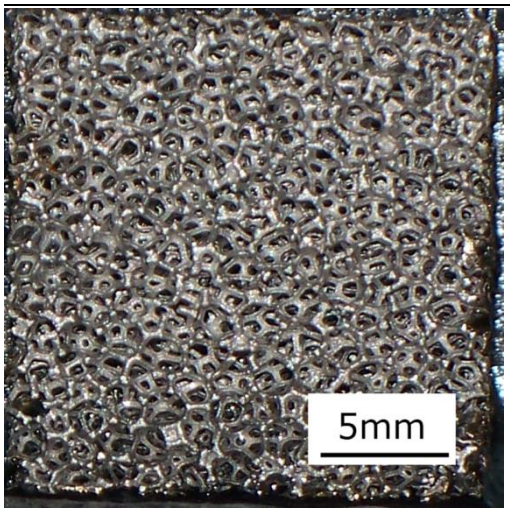
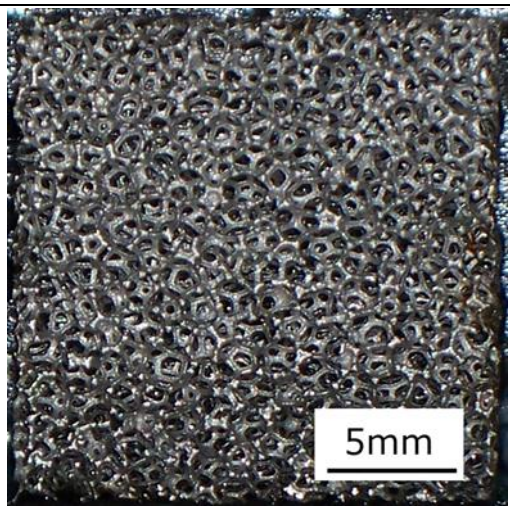


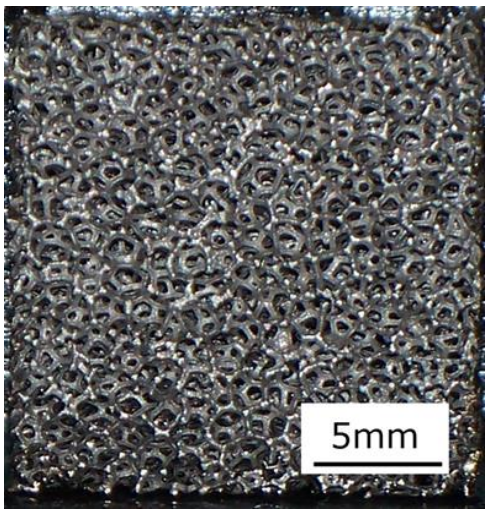
Figure 12-41. Images of 1723 foam samples after 900 hours in the salt spray cabinet.



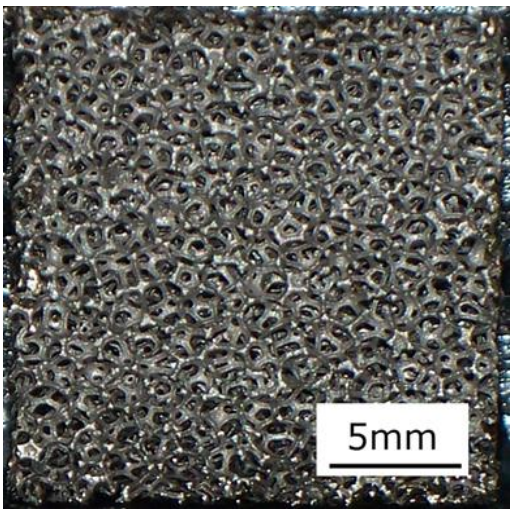
D6



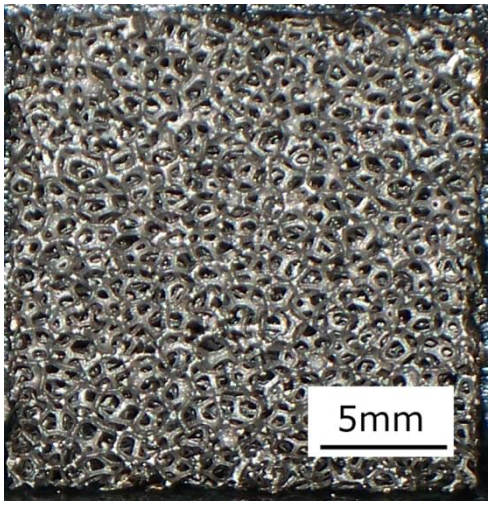
D12



H3

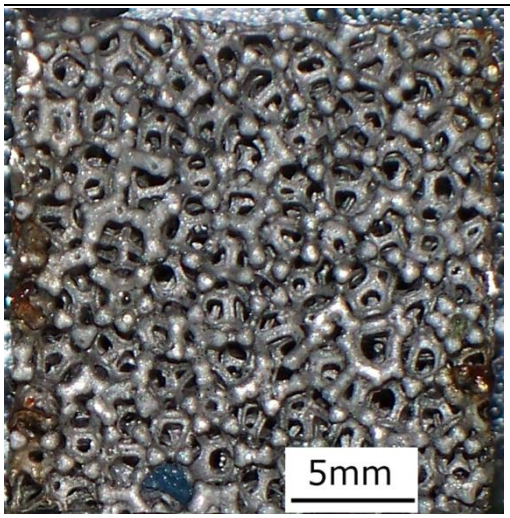


H6

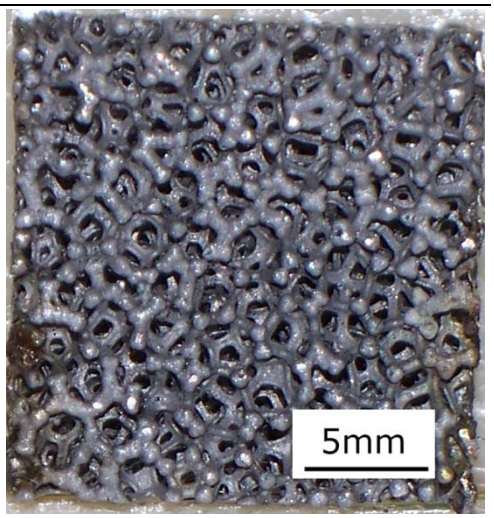


H12

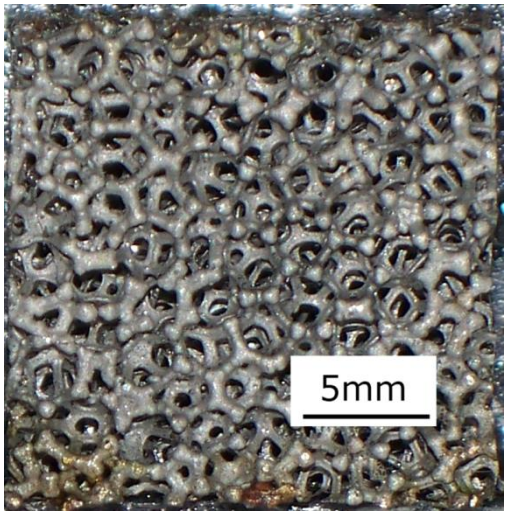
Figure 8-41 Continued. Images of 1723 foam samples after 900 hours in the salt spray cabinet.



1B



5B



9B

Figure 12-42. Images of 1116 foam samples after 900 hours in the salt spray cabinet.

12.13 APPENDIX 13 – YOUNG'S MODULUS

This appendix documents the work done on cyclic loading to determine the Young's Modulus. The tests were conducted wrong, and instead of modulus values being determined along the length of the stress-strain curve they were only performed within the initial yield area. This meant that a plot of the modulus again strain could not be made to define E_0. Unfortunately as the samples set aside for the Young's Modulus test were used in the initial batch of testing it was not possible to perform a proper test

The modulus values defined by the cyclic loading tests enabled both a comparison against the values derived from the literature, as well as a comparison between the compression and tensile properties.

12.13.1 Experimental Procedure

In order to obtain values of Young's Modulus, cyclical loading tests were performed. Samples were prepared in a similar way to the non-brazed tensile test samples, with the same operating parameters.

The samples were loaded and unloaded within the linear elastic region, for five cycles, with the modulus obtained from the stress-strain curves in the last four cycles used to calculate an average. The initial loading cycle was discarded, in accordance with how similar tests have been performed in the literature. It has been found that defects in the sample and strut geometry cause some

cells to deform at lower loads, however subsequent loads are more uniform and a better representative of the sample properties [65].

The loading was performed in both compression and tension, to allow for a comparison between the two deformations to take place.

Comparisons were made with the theoretical model, given in Equation 2-2.

12.13.2 Results

Figure 12-43 shows a stress-strain plot of a sample that underwent compressive cyclical loading. It can be seen that after the initial load, there is good conformity between the loading and unloading cycles. This indicates that some plastic deformation of the samples did occur during the initial loading cycle, but that the following cycles are representative of the linear elastic region of the plot. As was discussed in the experimental procedures it is customary to discard this cycle, and so each load and unload cycle, with the exception of the initial load, had their gradients measured to determine the Young's Modulus. Figure 12-44 is an example stress-strain plot of one of the compressive cycles. From the plot a linear equation was derived from which the gradient could be determined, and as can be seen by the correlation coefficient on the plot (R^2), there was a correlation of greater than 99%.

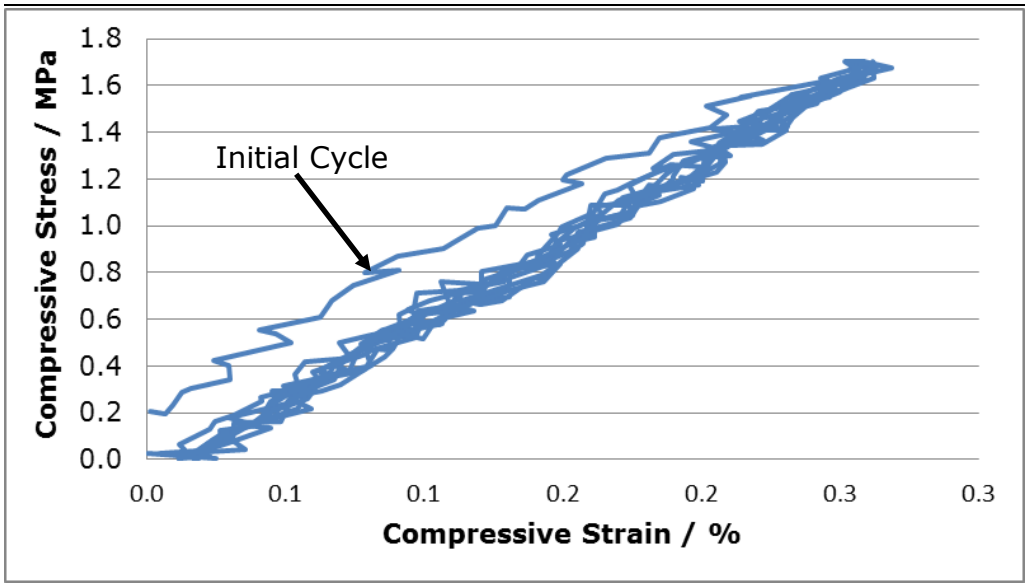


Figure 12-43. Stress-strain plot of a sample undergoing compressive cyclical loading, showing good conformity after initial load.

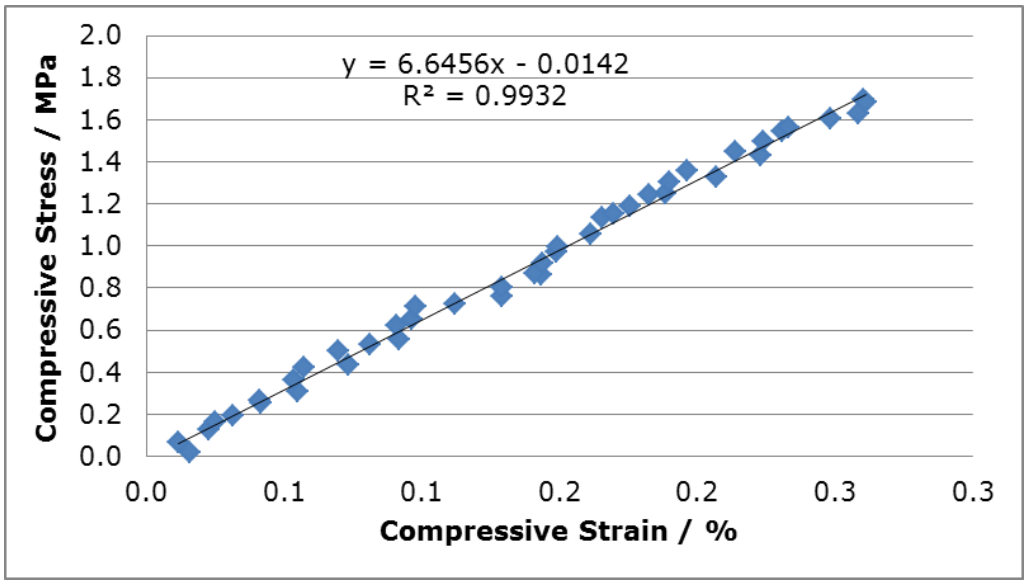


Figure 12-44. The second-cycle compressive stress-strain plot for a sample, showing the equation of linear best fit and the correlation coefficient.

Table 12-2 and Table 12-3 show the average values for Young's Modulus derived from both the compressive and tensile cyclic loading respectively. In both loading configurations it was found that

the 1116 foam in the LL orientation had a higher modulus, and the 1723 foam in the ST orientation had the lowest.

	1116		1723
	ST	LL	ST
Young's Modulus (MPa)	495	692	382
Standard Deviation	11	18	2
Variance (%)	2	3	1

Table 12-2. Average Young's Modulus derived from compressive cyclic loading.

	1116		1723
	ST	LL	ST
Young's Modulus (MPa)	378	675	307
Standard Deviation	6	8	5
Variance (%)	2	1	2

Table 12-3. Average Young's Modulus derived from tensile cyclic loading.

Table 12-4 shows the results of the combined data of the tensile and compressive cycles for the different loading orientations. Comparisons between the different loading conditions shows that whilst 1116 LL foams had ~1% variance the ST orientations were much larger, with ~11% and ~13% variances for the 1723 and 1116 foams respectively.

	1116		1723
	ST	LL	ST
Young's Modulus (MPa)	436	683	345
Standard Deviation	58	8	37
Variance (%)	13	1	11

Table 12-4. Average Young's Modulus derived from the combined compressive and tensile cyclic loading data.

Using the model relationship between the relative modulus and relative density described in Equation 2-2, and using the density values obtained through analysis it was possible to derive values for the Young's Modulus of the samples. The 1116 and 1723 foams were found to have values of 980 MPa and 1080 MPa respectively. Both of these values are much higher than the values obtained through cyclic loading testing. It was expected that the theoretical value would be higher due to the model being for an ideal foam, with a cubic structure. The real foams have a more complex geometric structure and have defects and variations in the dimensions of the pores and struts, as well as variations in the chemical content, that create a reduction in modulus. The deformed mid-section of the ST orientated samples therefore creates a significant modulus reduction.

12.14 APPENDIX 14 – MATERIAL SUPPLY ISSUES

After initial submission of the thesis it was recommended that information, not previously disclosed, about issues that arose during the research for this thesis should be mentioned.

The initial plan for the thesis, which was discussed with Rolls Royce, was to characterise the 1116 and 1723 nickel-chrome metallic foam, in terms of their basic properties, and then compare the results to the same material after it had been filled with a resin containing hollow glass spheres. In all cases material would be supplied by Rolls Royce

Due to how the overall engine design programme was running at Rolls Royce it was agreed that the plan would remain quite flexible, encase any aspects of the project required further investigation, and that all the material required could not be supplied up front at the beginning of the project, due to it being required for manufacturing parts for engine trials. The supply of material is the reason that only the 1723 foam was investigated over an entire sheet, and why the 1116 foam samples could not be directly compared with the 1723 samples in terms of locations.

Two small samples of filled foam material, from two separate batches, were supplied by Rolls Royce in order to perform some initial trials on (the results of which have now been added to the main section of the thesis). These samples were left over sections of manufactured parts for the test engine trials. It was the intention

that when more foam material was ordered and delivered they would apply the filler and supply it for a complete investigation. For whatever reason this was delayed, and despite talks indicating that the material would be supplied, time on the thesis ran out.

After completing the initial tensile tests of the foam samples, it became apparent that the method for attaching the material to a tab for the testing machine would likely not be strong enough to hold the filled material (still assumed to be supplied). It was during discussions about the possibility of getting some brazed samples manufactured that Rolls Royce revealed that only limited testing had been done on the brazed foam material. It was therefore agreed to investigate some brazed sample material, which they would manufacture with some 1116 material remaining, but with unknown locations from within the supplied sheet material. Again delays were met due to issues with their brazing facilities.

Additional to delays during the thesis other aspects of the thesis were questioned during the viva. After the initial discovery of the "dark band" deformed region in the foams, I contacted the foam supplier Recemat to ascertain whether this was a product of a defective sample, or whether this was a common feature. The reply that I eventually received was that as they didn't directly manufacture the foam sheets and they therefore couldn't give me a direct answer.

The second aspect of the thesis was the use of digital image correlation (DIC). As a new piece of equipment to the university, full

knowledge of its capabilities had not been gained. Initial trials run on the samples produced incomprehensible results, and so contact with the software suppliers was made. Unfortunately they were unable to help, and as previous trials by the technician had indicated that large pore foams weren't able to be analysed, it was decided to continue the investigation of the materials using conventional methods. Since then it has been determined that with a different set up it is possible to use the DIC to analyse the foams. Unfortunately due to the lack of remaining material available only a small number of samples could be tested. The results of these additional trials have been included within the thesis for comparative purposes.

Lastly, work done to determine the Young's Modulus of the foam samples by extrapolating data from cyclic loading tests were performed wrong. Instead of modulus values being determined along the length of the stress-strain curve they were only performed within the initial yield area. This meant that a plot of the modulus against strain could not be made to define E0. Unfortunately as the samples set aside for the Young's Modulus test were used in the initial batch of testing it was not possible to perform any subsequent correct tests. The analysis that was performed can be found in the Appendix.

It is hoped these comments clarify why aspects of the thesis are the way they are.